Lehrstuhl für Statik
der Technischen Universität München

Modeling the Interaction of Wind and Membrane Structures by Numerical Simulation

Alexander Markus Kupzok

Vollständiger Abdruck der von der Fakultät für Bauingenieur– und Vermessungswesen der Technischen Universität München zur Erlangung des akademischen Grades eines

Doktor–Ingenieurs

genehmigten Dissertation.

Vorsitzender: Univ.-Prof. Dr.-Ing., Dr.-Ing. habil. G.H. Müller

Prüfer der Dissertation:

1. Univ.-Prof. Dr.-Ing. K.-U. Bletzinger
2. Univ.-Prof. Dr.-Ing. R. Höffer,
   Ruhr-Universität Bochum
3. Prof. R. Löhner, Ph.D.,
   George Mason University, Fairfax, Virginia / USA

Die Dissertation wurde am 11.03.2009 bei der Technischen Universität München eingereicht und durch die Fakultät für Bauingenieur– und Vermessungswesen am 08.05.2009 angenommen.

Modeling the Interaction of Wind and Membrane Structures by Numerical Simulation

Abstract

In the scope of this thesis, a methodology for the numerical analysis of the interaction of wind and membrane structures is developed. The high flexibility of membranes leads to considerably large deformations for external loadings, which makes membrane structures susceptible to wind induced aeroelastic effects.

The focus of this work is the appropriate combination of different physical and numerical disciplines to account for the relevant factors inherent to the coupled simulation of light, flexible structures and highly turbulent air flows. To fulfill these requirements, the occurring wind-structure interaction is modeled by a surface-coupled fluid-structure interaction (FSI) method. This is realized with a partitioned coupling approach in a modular software environment that can be applied to various problems of fluid-structure interaction. In the partitioned coupling approach, the multiphysics problem is separated into a structural part and a fluid part. In the structural part, the stresses and deformations of the construction due to wind loading are computed. The air flow around and the surface pressure on the structure are simulated in the fluid part. The physical coupling between the structural part and the fluid part, i.e. between the membrane structure and the wind flow, is accounted for by means of exchanging the necessary boundary conditions between the two numerical computations.

To derive the initial shape of the prestressed membrane, numerical form finding computations are used. Special care is taken towards the realistic modeling of wind flow in a neutrally stratified Atmospheric Boundary Layer. As a prerequisite for the assessment of aeroelastic problems, the utilization of stable as well as efficient coupling strategies and further aspects of coupled computations are discussed in detail. Already existing single field solvers are modified for the application in coupled simulations. In order to efficiently implement the coupling strategies into the software environment, a central coupling tool is developed, which organizes the data exchange within the coupled computation.

The potential of the developed software environment is illustrated with the simulation of wind induced, aeroelastic effects on the mobile canopy structure ARIES. The significance of the results obtained is discussed and the method is placed in the framework of wind engineering.

Numerische Simulation der Wechselwirkung zwischen Wind und Membranbauwerken

Zusammenfassung

Im Rahmen dieser Arbeit wird eine Methodik zur numerischen Untersuchung von Windeinflüssen auf Membranbauwerke entwickelt. Durch die hohe Flexibilität des Membranmaterials, die zu großen Verformungen infolge externer Lasten führt, hat die Betrachtung von aeroelastischen, windinduzierten Effekten eine große Bedeutung für den Entwurf und die Konstruktion von Membranbauwerken.

Der Schwerpunkt dieser Arbeit liegt in der Kombination unterschiedlicher physikalischer Fragestellungen und numerischer Ansätze, um alle relevanten Effekte der Wechselwirkung von leichten und flexiblen Bauwerken mit einer hochturbulenten Windumströmung abzubilden. Dazu wird die Wind-Bauwerk-Wechselwirkung als ein oberflächengekoppeltes Problem der Fluid-Struktur-Interaktion betrachtet und modelliert. Im Rahmen dieser Arbeit wird eine modulare Berechnungsumgebung entwickelt, die sich für verschiedenste Simulationen von oberflächengekoppelten Problemen anwenden lässt. Zur numerischen Simulation des physikalischen Mehrfeldproblems wird ein partitioniertes Verfahren eingesetzt, das eine separate Betrachtung der einzelnen Teilgebiete, hier die Struktur- und die Strömungssimulation, ermöglicht. Die Kopplung zwischen Bauwerk und Windumströmung erfolgt durch den entsprechenden Austausch von Randbedingungen zwischen den Berechnungsprogrammen.

Zur Ermittlung der Ausgangsgeometrie der vorgespannten Membrankonstruktion werden numerische Formfindungsmethoden eingesetzt. In der Strömungssimulation liegt ein besonderes Augenmerk auf der realistischen Modellierung der neutralen atmosphärischen Grenzschichtströmung. Zur Simulation aeroelastischer Probleme werden stabile und effiziente partitionierte Kopplungsmethoden, neben anderen Aspekten gekoppelter Berechnungen, im Detail vorgestellt. Bestehende Simulationsprogramme werden für den Einsatz in gekoppelten Berechnungen entsprechend erweitert. Für den Austausch der physikalischen Randbedingungen zwischen den Simulationsprogrammen wird ein zentrales Schnittstellenprogramm entwickelt und eingesetzt.

Die Leistungsfähigkeit der numerischen Berechnungsumgebung wird anhand der Untersuchung von windinduzierten Effekten an der mobilen Tribünenüberdachung ARIES gezeigt. Abschließend werden die Anwendbarkeit der Methode und die Aussagekraft der Ergebnisse der Arbeit im Rahmen des Windingenieurwesens diskutiert.

Acknowledgements

This dissertation was written from 2003 to 2009 during my time as research scholar and teaching assistant at the Chair of Structural Analysis (Lehrstuhl für Statik) at the Technische Universität München, Munich, Germany.

First and foremost, I would like to express my gratitude to Prof. Dr.-Ing. Kai-Uwe Bletzinger, who acted as my supervisor and examiner (Doktorvater). His remarkable support and guidance, not only in the scope of research, but in all aspects of university life, helped me greatly to evolve in academics. Prof. Bletzinger initiated the research towards Fluid-Structure Interaction and established a small FSI team collaborating in a constructive research environment. I am particularly grateful for the time he devoted to this topic and my work, as well as for his patience and confidence.

I would like to address special thanks to Prof. Dr.-Ing. Rüdiger Höffer for being part of my examining jury and for spending his time on explanations, suggestions, and discussions on wind engineering and the application of CFD. I am also very thankful to Prof. Rainald Löhner for his advice on my thesis in the fields of CFD and FSI and his readiness to be present in my jury, despite the involved long travel from Virginia to Munich. Furthermore, I want to thank Prof. Dr.-Ing., Dr.-Ing. habil. Gerhard Müller for his commitment to chair the jury.

Working at the Chair of Structural Analysis, I always appreciated the cordial and motivating atmosphere among the colleagues. I am deeply thankful to the former and present colleagues, for providing this excellent working environment. I will always warmly recall the close cooperations, long discussions, and leisure activities. I specially would like to thank Thomas Gallinger, Roland Wüchner, and Ute Israel as core members of the FSI-team, without whose contributions this work would not have been possible. Additionally, I am obliged to Roland Wüchner and Thomas Gallinger for being great and patient room mates.

I would like to thank all friends, who have accompanied me during the completion of this work and gave me their support.

I am especially grateful towards my family, in particular to my parents Hans-Brecht and Therese Kupzok, who provided the basis for my education and were always a great source of encouragement and support.

Finally, I would like to thank my dear fiancée Agnieszka for her tremendous effort and invaluable help in proofreading my thesis, for her understanding and, most of all, for her love, which carried me through all difficult times.

Alexander Kupzok

Contents

List of Figures

Chapter 1

Introduction

1.1 Motivation and Thematic Framework

The demand for sustainable buildings, the application of new construction techniques, and the possibilities due to new construction materials give rise to light and slender structures in civil engineering. Designing these types of structures in such a way, that they resist external loadings typical in civil engineering, the more effort has to be put into analyzing the behavior of the structure, the lighter and more slender it becomes.

In case of wind loads, a detailed analysis is very complicated due to the stochastic nature of wind. However, what Simiu and Scanlan state in [SS96] holds even more for highly optimized constructions: "It is the task of an engineer to ensure the performance of structures subjected to the action of wind will be adequate during their anticipated life from the standpoint of both safety and serviceability."

Membrane Structures

Membrane structures are a good example of extremely light-weight and highly optimized constructions. Due to the constant stress state over the thickness, the material strength is optimally used. In the last years, the use of membranes in structural engineering became more and more common. With the development of new materials, the spectrum of membrane structures became wider, reaching from large span roof and mobile structures to elements for cladding. As a result of spectacular public buildings such as the Allianz Arena in Munich, membrane structures are in the focus of public interest.

Membrane structures are very special types of constructions because of the membrane's properties. Membranes have no or very little bending stiffness. Therefore, their load carrying behavior is based on tension stresses tangential to their surface. In case of tangential compression stresses, the membrane loses its stiffness and starts to wrinkle. External load not tangential to the surface of the membrane causes relatively large deformations. In order to prevent the occurrence of large deformations even for small external loadings, membrane structures are designed as doubly curved geometries and are stabilized by applying prestress. The initial shape of the prestressed membrane is determined by the mechanical property of equilibrium of internal membrane stresses and the dead load. Accordingly, the initial, doubly curved shape is generally unknown and has to be derived by experimental approaches or numerical form finding computations. Typically, the resulting initial shape is a free-form membrane structure, which closes itself to any analytical description.

Analysis of Wind Effects on Membrane Structures

The lightness and flexibility in material and construction of membrane structures brings along a high responsiveness to external loadings. Especially for wind loading, membrane structures show high susceptibility. Moreover, in contrast to other load cases, such as dead or snow load, the wind load on membrane structures can not generally be presumed as a static load case, but in some cases the dynamics of the loading and the structural response have to be considered. Analysis of wind load on membrane structures is further complicated in case of aeroelastic behavior, in which the large deformations of the membrane lead to an interaction between membrane and wind flow.

The usual approach in structural engineering of reducing the complex problem of structures subjected to wind to simpler models by finding appropriate assumptions involves the risk of neglecting essential effects, which result from the interaction of wind and structure. A generic tool to analyze dynamic effects in wind engineering is the experimental simulation in wind tunnels. A basic requirement for this experimental approach is the resemblance of dynamic behavior between reality and model. For small scale models this requirement is difficult to meet, especially in the analysis of aeroelasticity. As a result, corresponding wind tunnel experiments are complicated, as well as elaborate and expensive. Accordingly, Williams [Wil95] described the state of the analysis of membrane structures in 1995 as the following: "The behavior of a membrane structure in wind can be extremely complex. There is no one satisfactory design method and it's a question of combining experimental results with simple theories and experience with similar structures."

Next to the established methods of wind tunnel experiments, the application of numerical methods, namely Computational Fluid Dynamics (CFD), becomes applicable for the analysis of wind effects, as the available computational power steadily increases. The use of CFD methods in wind engineering is a rather young subdomain called Computational Wind Engineering (CWE). Developments in CWE are generally driven along two lines: the correct modeling of the boundary conditions and the correct modeling of the turbulent wind flow.

Numerical Simulation of Wind-Membrane Structure-Interaction

The application of numerical methods to the analysis of wind induced effects on membrane structures provides, among other advantages, the possibility to overcome the limitations of experimental approaches in the modeling of aeroelastic effects. The wind load on the structure can be simulated by a numerical fluid simulation. The responses of the membrane structure, namely the deformations due to the wind loads, result from a numerical structural analysis. Combining fluid and structural analysis leads to a multi-physics approach, which is realized by a coupled simulation of fluid-structure interaction. Within this thesis, numerical methods for the analysis of surface coupled problems are applied to model the interaction between wind and membrane structure.

For a correct modeling of wind-membrane structure interaction, the following requirements for a coupled numerical analysis are identified:

- Availability of form finding methods to determine the proper initial geometry.

- ◇ Correct numerical analysis of the structural behavior of membrane structures with respect to geometrical nonlinearities.
- ◇ Adequate modeling of a complex, highly turbulent wind flow in a neutrally stratified Atmospheric Boundary Layer (ABL).
- ◇ Representation of strong interaction between wind and membrane by appropriate coupling methods of fluid and structural analysis.
- ◇ At the fluid-structure interface, treatment of moving boundaries and accurate transfer of boundary conditions.

Within this thesis, a framework for the simulation of wind-membrane structure interaction, which is able to satisfy these requirements, is developed and presented.

ARIES mobile canopy structure

The capability of the framework developed within this thesis is shown on the example of the mobile canopy structure ARIES, for which the wind-membrane interaction is analyzed.

ARIES is a lightweight, deployable canopy system designed to provide weather protection for modular temporary events seating (see fig. 1.1). It was developed at the University of Dundee [BG05] and the Technische Universität München, [Gen05, Gen04], together with Arena Seating, United Kingdom. A Teaching Company Scheme grant funding was awarded in 2000 for a 2-year programme to develop and construct a prototype, which was completed in 2002. It was developed to combine flexibility and operator safety as well as to significantly reduce operational costs. It can be deployed by only two people, who prepare and erect an entire canopy module.

Figure 1.1: ARIES mobile canopy structure.

The construction is a hybrid tensile restrained structure with a cantilevered free span of 13m and a width of 6m. The completed canopy represents a highly efficient composite post-tensioned tensile structure with an anticlastic membrane supported by aluminum trusses. The trusses are stressed into a curved shape, defined by the supporting cables and A-frames.

The environmental loading was assessed with wind tunnel testing on rigid, small-scale models. The pressure coefficients from the tests, in conjunction with a wind code assessment, gave an indication of the magnitude of the wind loading likely to be experienced by the canopy. However, the question, if and to which extent, an interaction between the flexible canopy structure and the wind flow occurs, remained open.

By using numerical methods of fluid-structure interaction, the wind-ARIES structure interaction is analyzed within this thesis. As ARIES features a prestressed membrane, an appropriate numerical model has to meet all the requirements formulated above.

1.2 Aim of This Thesis and Approach

The aim of this thesis is to develop a software environment as a numerical tool for the analysis of the interaction between wind flow and membrane structures. The wind flow around the structure is modeled by methods of Computational Fluid Dynamics (CFD). The structural behavior is computed using the Finite Element Method (FEM), which includes form finding computations. Structural and fluid simulations are combined in a multi-physics simulation for the modeling of strong physical coupling between wind flow and membrane structure.

Within this work, the analysis of wind effects on membrane structures is performed in a deterministic way for specific setups of wind speed, wind turbulence, and wind direction. Thereby, necessary approximations, mainly in modeling the turbulent air flow, have to be made. As a consequence, the aim of this thesis is not to represent all possible wind induced effects, and, therefore, the results of this work cannot be directly used as design loads. However, possible ways of how to extend the results derived by the numerical computation into design loads for membrane are provided.

In order to meet the requirements identified above as necessary for the numerical analysis of an interaction between wind and membrane structures, a partitioned approach is chosen. In a partitioned approach, the surface-coupled multi-field problem is solved by using individual single field solvers for the different physical fields. In case of fluid-structure interaction, the involved physical fields of structural and fluid analysis can be solved in specialized, well-suited, and tested single field simulation programs. The physical coupling between the single fields is realized by exchanging the specific boundary conditions. Thereby, existing simulation programs for the modeling of the air flow and the structural behavior can be reused. However, several modifications of the existing simulation programs are necessary, in order to realize the coupling methods.

In the current approach, the form finding and the structural part are solved by the research code CARAT, the fluid part by the general purpose Computational Fluid Dynamics

Code CFX-11 of Ansys Inc., and for the coupling, a central coupling tool called COMA is developed.

1.3 Organization of This Thesis

The introductory Chapter 1 presents the motivation for this work and a brief overview about the thematic framework. Due to the complexity of the multi-physics problem and the extension of the field of wind engineering, a review of representative publications describing the state of the art is provided in the respective chapters.

The thesis is structured following the physical decomposition of the partitioned approach into chapters, which discuss the structural field and the fluid field. Within each of the two chapters, the specific problem is discussed, fundamentals about the considered physical field are presented, and the numerical approach for modeling and simulating the physical field is provided. Finally, the numerical methods of the single fields are applied on the ARIES structure.

In Chapter 2, the main characteristics of membrane structures are discussed. Based on these characteristics, appropriate methods for the numerical simulation with the Finite Element Method (FEM) are introduced. These methods are applied to setup a numerical model of the ARIES canopy structure.

Chapter 3 presents the several approaches to analyze wind loads on membrane structures. Fundamentals of fluid mechanics are presented and used to derive the Finite Volume Method (FVM). A strong focus lies on the correct modeling of the ABL flow and the flow for CWE. By using a rigid structural representation, the wind load on the ARIES structure is simulated.

Chapter 4 brings together the simulation of fluid and structural fields. Theory and different approaches for the simulation of multi-physics problems are discussed. Selected aspects of coupled fsi simulations, which are necessary ingredients for the computational setup, are discussed in detail. The concept of the software environment, the necessary modification in the single field solvers, and the newly developed central coupling tool are described. Finally, this software setup is used to analyze the reaction of the ARIES structure to wind loading.

In chapter 5 a summary of the methods developed and the results obtained in this research is presented. The thesis concludes with a discussion, how and to which extent, the tools and results obtained can be used for the design of membrane structures.

Chapter 2

Structural Modeling of Light-Weight Structures

In this chapter, the characteristics of membrane structures are studied. For a detailed analysis of wind loading on membrane structures, an appropriate numerical model, which is able to represent the correct structural behavior, is necessary. Due to the special properties of membranes, suitable methods are needed for numerical modeling and analysis. Throughout the whole thesis, structural modeling is based on the Finite Element Method (FEM). Starting from the basics of continuum mechanics and introducing methods of space and time discretization, the formulation for a generic hexahedral 3-dimensional Finite Element is derived.

For the modeling of membrane structures, a special type of Finite Elements are derived based on the generic hexahedral element. Usually, membrane structures used in civil engineering are prestressed. The consideration of this prestress state requires experimental or computational techniques, commonly referred to as form finding procedures, which are briefly introduced.

All the techniques presented in this chapter are applied to set up the complex structural model of the ARIES mobile canopy structure. In the following chapters, this model is used for further analysis with respect to wind loading, both on a rigid structure (in chapter 3) and with taking into account aero-elastic effects using methods of Fluid-Structure Interaction (in chapter 4).

2.1 Characteristics of Membrane Structures

Shape and physical behavior of fabric structures is very different to those of conventional constructions based on stiff frames. These differences result from the missing bending stiffness of membrane material. Without the possibility of load transfer via bending action, the whole load transfer has to be carried out through stress acting tangential to the membrane surface. This tangential acting stress is referred to as membrane stress. The membrane is able to carry tension stress only. Compression in the membrane leads to a phenomenon of structural instability, the occurrence of wrinkles. According to their properties, membrane structures can be identified as tensile structures.

The lack of bending action implies certain properties for membrane structures. Due to the fact that the distribution of the tangential stress over the membrane thickness is constant, the utilization of the material strength is optimal. However, a strong interaction between shape and structural behavior occurs. In a static configuration the tangential tension stresses of the membrane are in equilibrium at every point. If this equilibrium is disturbed, e.g. by an external load, the membrane will react with deformations in such a way, that the internal membrane stress and the external loading reach a new state of equilibrium. For loads acting perpendicularly to the membrane surface this usually results in large deformations.

The sensitivity of membrane structures with respect to external loadings is determined by their stiffness. This stiffness is mainly a result of two factors: geometry and prestress.

For distributed loads acting not only tangential to the surface, including dead load of the membrane material, the geometry of the membrane needs to be curved in order to enable equilibrium between internal membrane stress and loading. These double curved surfaces can be classified as synclastic or anticlastic, depending on the sign of their Gaussian curvature.

Prestress is introduced in membrane structures to provide the flexible fabric with an additional geometric stiffness and ensure that for all load cases no compressive stress occurs. The initial geometry of the prestress membrane is the shape, for which the membrane forces introduced by the prestress and those due to dead load are in equilibrium. In general, this shape is unknown and form-finding procedures are used to determine the initial shape. These can be conducted as experiments or by numerical computations, the form-finding computations.

For membrane structures, the prestress is realized as mechanical or pneumatic prestress. Since prestress can only be imposed as tension, it is also known as pretension.

◇ **Pneumatically imposed prestress**

Pneumatically imposed prestress is caused by a pressure difference between both sides of the membrane. This leads to overall synclastic shapes with positive Gaussian curvature, such as balloons or cushions. Air supported structures, usually in the form of shallow spherical 'caps' are another typical application. Fig. 2.1 provides examples of synclastic, pneumatically prestressed constructions.

(a) Balloon shape. (b) Cushion shape.

Figure 2.1: Generic synclastic shapes.

◇ **Mechanically imposed prestress**

Mechanically imposed prestress is introduced by tightening the anchorage. Typically, the geometries for mechanically prestressed structures are anticlastic, meaning the sign of their Gaussian curvature is negative. In fig. 2.2 the four generic types of anticlastic surfaces are presented: cone, saddle-surface, hyperboloid and "ridge and valley".

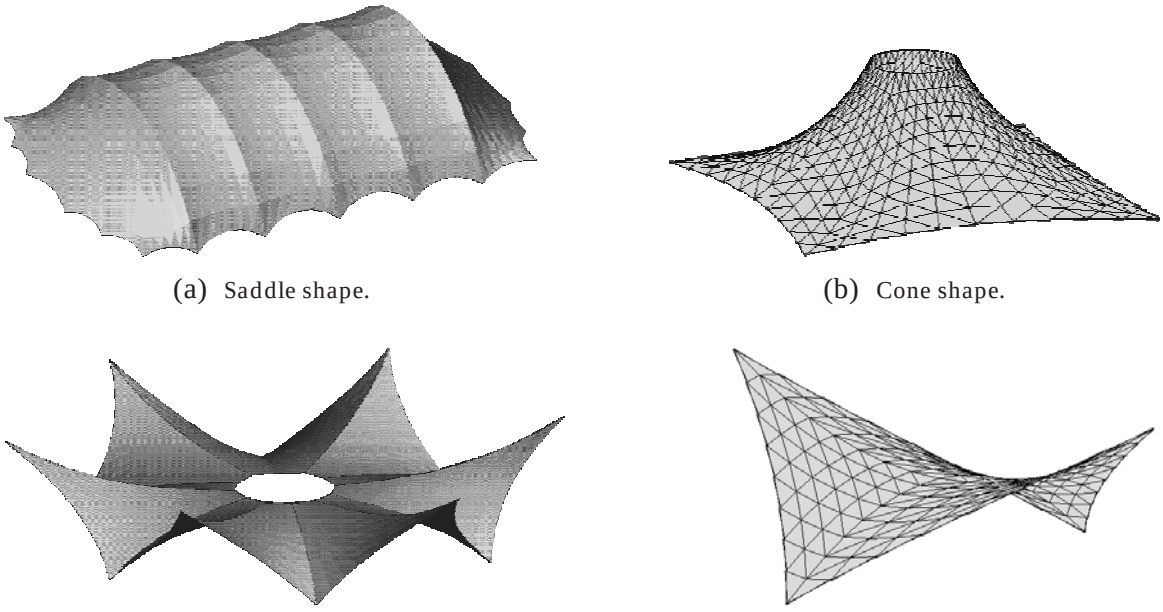

(a) Saddle shape. (b) Cone shape.

(c) 'Ridge & valley' shape. (d) Hyperboloid shape.

Figure 2.2: Generic anticlastic shapes.

In the following, only mechanically prestressed structures shall be considered.

Prestressed membrane structures commonly require continuous support along the edges to maintain a prestressed state. This support can be rigid, such as a stiff beam or anchorage or, more commonly, flexible. Flexible support is realized by cables attached to the edges of the membrane. They are curved due to the (pre-)tension stress of the membrane and, therefore, also subject to (pre-)tension. If the stress at the edges of the membrane acts tangential to the edge cables, the membrane might slide along the cable, which is usually prevented by additional fittings.

For the realization of membrane structures, a variety of synthetic materials with different properties is available. They can be categorized into two groups: fabrics and foils.

◇ **Fabrics**

Fabrics show an anisotropic behavior in the directions of their fibers. Corresponding to the manufacturing process of fabrics, the two directions are called warp and weft. The fabric determines the load carrying behavior. Commonly a coating is applied which protects the fibers from mechanical, chemical, or biological damages and determines the transparency and sealing. Typical examples for these composite materials are PVC

(Polyvinylchlorid) coated polyester fabrics or PTFE (Polyetrafluoroethylene) coated glass fiber fabrics.

◇ **Foils**

Foils have an isotropic material behavior. A typical material for foil constructions in civil engineering is ETFE (Ethylentetrafluoroethylene). ETFE is highly transparent, has a high chemical resistance and a penetrability towards air that is small enough for the usage in pneumatic structures. Compared to fabric materials of the same thickness, foils typically have a lower load carrying capacity. Therefore, foil structures usually have a limited free span.

2.2 Fundamentals of Structural Analysis

2.2.1 Fundamentals of Continuum Mechanics

In the following, a brief introduction to the field of continuum mechanics is given. The presented explanations are restricted to those most relevant to the topic of light-weight structures. Full and detailed derivations can be found, among others, in [BW00], [Hol00], [Par03], [SR04].

2.2.1.1 Differential Geometry

A material point $\mathbf{M}$ of a continuous body $\mathbb{B}$ in a three dimensional space can be identified by its position vector $\mathbf{x}(\theta^1, \theta^2, \theta^3)$. The position vector refers to curvilinear convective coordinates θ^i (fig. 2.3). In the following, the summation convention by Einstein will be used. Latin indices take to values 1 to 3, while Greek indices take values 1 and 2. The base vectors of the curvilinear coordinate system θ^i can be derived as:

$$\mathbf{g_i} = \frac{\partial \mathbf{x}}{\partial \theta^i} \tag{2.1}$$

The elements $\mathbf{g_i}$ are called covariant base vectors. Additional to the covariant basis, a reciprocal (or dual) basis is introduced. The elements of the reciprocal basis are called contravariant base vectors $\mathbf{g^i}$. The two bases $\mathbf{g_i}$ and $\mathbf{g^i}$ satisfy the following condition:

$$\mathbf{g_i} \cdot \mathbf{g^j} = \delta^i_j \tag{2.2}$$

δ^i_j is the (mixed) Kronecker delta. Based on the curvilinear coordinate system θ^i the contravariant base vectors can be derived by the following equation:

$$\mathbf{g^i} = \frac{\partial \theta^i}{\partial \mathbf{x}} \tag{2.3}$$

By using the scalar product on two covariant base vectors, the metric coefficients g_{ij} of the covariant basis are calculated. Same holds for the contravariant base vector and the metric coefficients g^{ij} of the contravariant basis:

$$g_{ij} = \mathbf{g_i} \cdot \mathbf{g_j} \qquad g^{ij} = \mathbf{g^i} \cdot \mathbf{g^j} \tag{2.4}$$

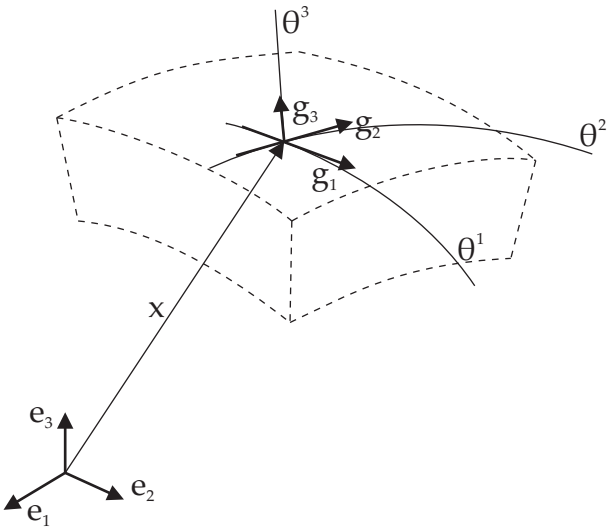

Figure 2.3: Geometry in curvilinear coordinates.

The Unity (or Identity) tensor or Metric tensor of a coordinate system is derived as:

$$\mathbf{I} = g_{ij}\ \mathbf{g^i} \otimes \mathbf{g^j} = g^{ij}\ \mathbf{g_i} \otimes \mathbf{g_j} = \mathbf{g_i} \otimes \mathbf{g^j} = \mathbf{g^i} \otimes \mathbf{g_j} \tag{2.5}$$

with $\otimes$ as the dyadic product.

2.2.1.2 Kinematics

For each material point **M** of a continuum body $\mathbb{B}$ the mapping κ assigns a position **x** at a certain time *t*. The configuration at a defined time $t = t_0$ is called the reference configuration and is the initial configuration of the system. Configurations for $t > t_0$ are called current configurations. In the following, all quantities based on the reference configuration are expressed in upper case letters, while those based on current configurations are expressed in lower case letters.

The motion χ is defined as the transformation from reference to current position at a time *t*:

$$\mathbf{x} = \chi(\mathbf{X}, t) \tag{2.6}$$

Commonly, in structural mechanics, a Lagrangian description is used, in which the coordinate system "sticks" to a material point and changes, when the position of the material point is modified. Therefore, a material point is identified by its Lagrange coordinates $\mathbf{X}(\theta^1, \theta^2, \theta^3)$ and the point in time *t*. The displacement field **d** from reference to current configuration can be expressed as:

$$\mathbf{d}(\mathbf{X}, t) = \chi(\mathbf{X}, t) - \mathbf{X} = \mathbf{x}(\mathbf{X}, t) - \mathbf{X} \tag{2.7}$$

According to the definition of the co- and contravariant base vectors in the current configuration ($\mathbf{g}_i$ and $\mathbf{g}^i$) at a position $\mathbf{x}(\theta^1, \theta^2, \theta^3)$ (eq. 2.1 and eq. 2.3), the co- and contravariant

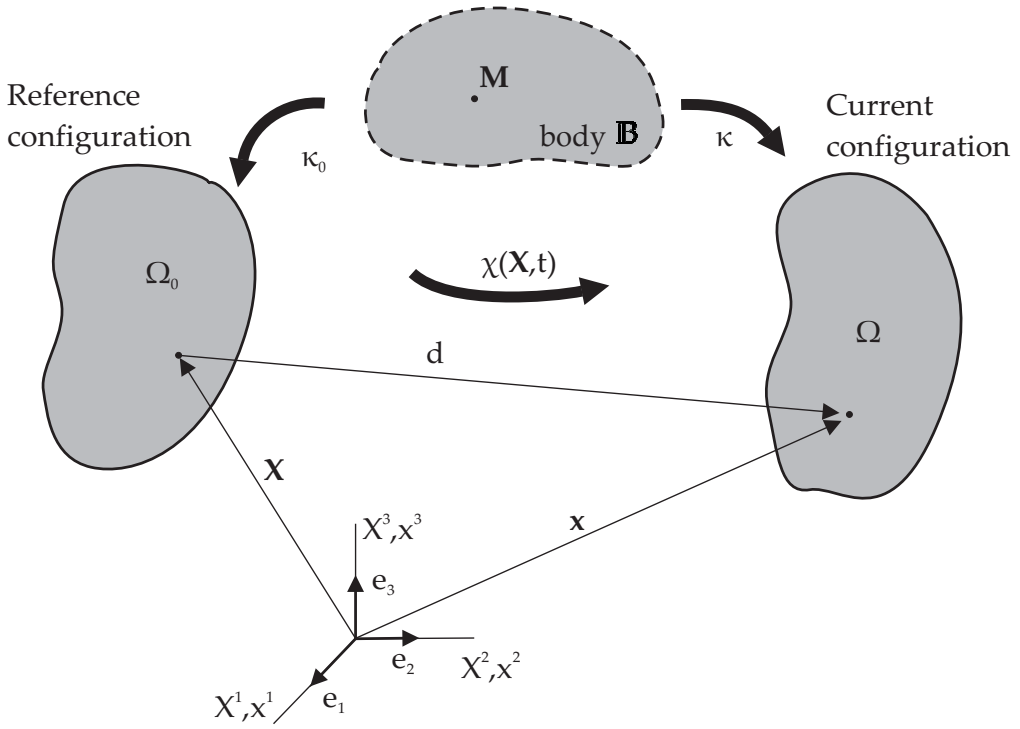

Figure 2.4: Configuration and motion of a continuum body and a material point.

base vectors of reference configuration at a position $\mathbf{X}(\theta^1, \theta^2, \theta^3)$ are:

$$\mathbf{G_i} = \frac{\partial \mathbf{X}}{\partial \theta^i} \qquad \mathbf{G^i} = \frac{\partial \theta^i}{\partial \mathbf{X}} \tag{2.8}$$

The material deformation gradient $\mathbf{F}$ describes the mapping of a differential line element in the reference configuration $d\mathbf{X} = \mathbf{G_i} d\theta^i$ into a line element in the deformed configuration $d\mathbf{x} = \mathbf{g_i}\, d\theta^i$:

$$d\mathbf{x} = \frac{\partial \mathbf{x}}{\partial \mathbf{X}} d\mathbf{X} = \mathbf{F} \cdot d\mathbf{X} \tag{2.9}$$

Commonly, $\mathbf{F}$ is an asymmetric second order tensor. As the mapping of a line element is equivalent to the mapping of a base vector from reference to current configuration the deformation gradient can be used to relate co- and contravariant base vectors in reference and current configuration:

$$\mathbf{g_i} = \mathbf{F} \cdot \mathbf{G_i} \qquad \mathbf{g^i} = \mathbf{F^{-T}} \cdot \mathbf{G^i} \qquad \mathbf{G_i} = \mathbf{F^{-1}} \cdot \mathbf{g_i} \qquad \mathbf{G^i} = \mathbf{F^T} \cdot \mathbf{g^i} \tag{2.10}$$

Accordingly, $\mathbf{F}$ can be derived as:

$$\mathbf{F} = \frac{\partial \mathbf{x}}{\partial \mathbf{X}} = g_i \otimes G^i \qquad \mathbf{F^T} = G^i \otimes g_i \neq \mathbf{F} \qquad \mathbf{F^{-T}} = g^i \otimes G_i \qquad \mathbf{F^{-1}} = G_i \otimes g^i \tag{2.11}$$

The deformation gradient contains information about the complete deformation process, including rigid body deformations. Therefore, it is not objective and cannot be used directly

as a strain measure. Instead, the objective, symmetric Green-Lagrange (**GL**) strain tensor **E** is introduced for the description of large displacements (with **I** as the identity tensor):

$$\mathbf{E} = \frac{1}{2}(\mathbf{F^T F} - \mathbf{I}) = E_{ij}\, \mathbf{G^i} \otimes \mathbf{G^j} = \frac{1}{2}(g_{ij} - G_{ij})\mathbf{G^i} \otimes \mathbf{G^j} \tag{2.12}$$

2.2.1.3 Constitutive Equations

The constitutive equation describes the connection between static and kinematic quantities, thus between stress and strains. The energetically conjugate quality for the Green-Lagrange (**GL**) strain tensor **E** is the symmetric second Piola-Kirchhoff (**PK2**) stress tensor **S**.

GL strain tensor and PK2 stress tensor are used to compute the internal energy of a deformed body. The property of orthogonality of the co- and contravariant metrics are used to ensure that the internal energy is independent of the used metric: the strain tensor is based on the covariant, while the stress tensor is based on the contravariant basis. The PK2 stress tensor is based in the reference configuration and has no physical meaning. A measurement for the real physical stress is the symmetric Cauchy stress tensor σ:

$$\sigma = \sigma^{ij}\mathbf{g_i} \otimes \mathbf{g_i} \tag{2.13}$$

With the use of the deformation gradient, the PK2 stress tensor can be transformed into the Cauchy stress tensor and vice versa:

$$\sigma = (\det\mathbf{F})^{-1}\mathbf{F\ S\ F^T} \qquad \mathbf{S} = \det\mathbf{F}\ \mathbf{F^{-1}}\sigma\mathbf{F^{-T}} \tag{2.14}$$

In the scope of this work, large deformations with small strains are analyzed. The St. Venant-Kirchhoff material law is used, which is a generalization of the linear elastic Hooke's material law for large rotations [BLM00]. Using the strain energy density $W^{int}(\mathbf{E})$, the constitutive relation can be formulated as:

$$\mathbf{S} = \frac{\partial \mathbf{W^{int}}(\mathbf{E})}{\partial \mathbf{E}} \tag{2.15}$$

The fourth order elasticity tensor $\mathbb{C}$ is derived by linearizing the constitutive relation:

$$\mathbb{C} = \frac{\partial \mathbf{S}}{\partial \mathbf{E}} \qquad \text{with} \quad \mathbb{C} = C^{ijkl}\mathbf{G}_i \otimes \mathbf{G}_j \otimes \mathbf{G}_k \otimes \mathbf{G}_l \tag{2.16}$$

and describes a linear relation between the GL strain tensor **E** and the PK2 **S** stress tensor:

$$\mathbf{S} = \mathbb{C} : \mathbf{E} \qquad \text{with} \quad S^{ij} = C^{ijkl}E_{kl} \tag{2.17}$$

The general elasticity tensor has $3^4 = 81$ independent coefficients, which can be reduced to 36 due to the symmetry of the PK2 stress and GL strain tensors. For an isotropic material, two parameters are sufficient to describe the material properties. In a mathematical context usually the Lamé constants λ and μ are used, while in an engineering context Young's modulus E and Poisson's ratio ν are applied.

$$\lambda = \frac{E\nu}{(1+\nu)(1-2\nu)} \qquad \mu = \frac{E}{2(1+\nu)} \tag{2.18}$$

Using the Lamé constants, the components of the elasticity tensor for an isotropic material can be determined by:

$$C^{ijkl} = \lambda G^{ij}G^{kl} + \mu[G^{ik}G^{jl} + G^{il}G^{kj}] \tag{2.19}$$

2.2.1.4 Equilibrium Conditions

Within this work, no velocity dependent physical damping is considered. The momentum balance principle states that inner forces, inertia forces, external forces, and body forces acting on a body and its surface have to be in equilibrium. In the current configuration, this equilibrium is expressed in eq. 2.20, which is known as Cauchy's firsts equation of motion. A detailed derivation can be found in [Hol00].

$$\int_{\Omega} (\nabla \cdot \sigma + \mathbf{b} - \rho \ddot{\mathbf{d}}) d\Omega = \mathbf{0} \tag{2.20}$$

In the reference configuration, the momentum balance principle is formulated as:

$$\int_{\Omega_0} (\nabla \cdot \mathbf{P} + \mathbf{B} - \rho_0 \ddot{\mathbf{d}}) d\Omega_0 = \mathbf{0} \tag{2.21}$$

B and b are vectors of body forces per volume unit, acting in the reference and current configuration respectively. The acceleration field $\ddot{\mathbf{d}}$ is the second derivative of the displacement field with respect to time. $\mathbf{P}$ is the first Piola Kirchhoff (**PK1**) stress tensor, which is asymmetric and defined in both, the current and the reference configuration. Therefore, it is advantageous to exchange it for the PK2 stress tensor using eq. 2.22.

$$\mathbf{P} = \mathbf{F}\,\mathbf{S} \tag{2.22}$$

The equation of motion expressed with the PK2 stress tensor is the following:

$$\int_{\Omega_0} (\nabla \cdot (\mathbf{F}\,\mathbf{S}) + \mathbf{B} - \rho_0 \ddot{\mathbf{d}}) d\Omega_0 = \mathbf{0} \tag{2.23}$$

Since the equation of motion has to be fulfilled for every domain Ω_0 it can be transferred into a local perspective:

$$\nabla \cdot (\mathbf{F}\,\mathbf{S}) + \mathbf{B} - \rho_0 \ddot{\mathbf{d}} = \mathbf{0} \tag{2.24}$$

Together with appropriate initial conditions and boundary conditions, eq. 2.12, eq. 2.17, and eq. 2.24 present the strong form of the elastic dynamic boundary value problem in material description. It is a system of nonlinear coupled hyperbolic partial differential equations. The initial conditions describe position, state of deformation, and state of motion at the initial point in time. Therefore, the displacement field $\mathbf{d} = \mathbf{d_0}$ and the velocity field $\dot{\mathbf{d}} = \dot{\mathbf{d}}_\mathbf{0}$ are to be prescribed at time $t = t_0$ for the whole domain Ω_0 .

The boundary conditions on the body surface Γ consist of the Dirichlet boundary condition Γ_D, which specifies a prescribed deformation $\hat{d}$ of the boundary surface and the Neumann boundary condition Γ_N, which specifies a prescribed force vector $\hat{\mathbf{T}}_\mathbf{N}$ on the boundary.

$$\begin{aligned} d &= \hat{d} \quad \text{for} \quad \Gamma_D \qquad \forall\, t \in [t_0, T] \\ \mathbf{T} &= \hat{\mathbf{T}}_\mathbf{N} \quad \text{for} \quad \Gamma_N \qquad \forall\, t \in [t_0, T] \end{aligned} \tag{2.25}$$

At a specific point of the boundary for a specific degree of freedom, either a Dirichlet or a Neumann boundary condition can be prescribed:

$$\Gamma_N \cap \Gamma_D = 0 \quad \text{with} \quad \Gamma = \Gamma_N \cup \Gamma_D \tag{2.26}$$

2.2.1.5 The Weak Form - the Principle of Virtual Work

For two- or three-dimensional problems, an exact solution of elastic dynamic boundary value problem is in general not possible. In the scope of this work, the well established Finite Element Method is used to solve problems of structural mechanics.

The Finite Element Method is based on variational principles and provides a solution technique in which selected field equations and selected boundary conditions are satisfied in integral form. In contrast to the original differential equation, in the integral formulation the requirements for differentiability of the solution functions are weaker. Therefore, the integral form is referred to as the weak form, whereas the original differential equation is referred to as the strong form of the problem.

The most basic and common variational principle is the principle of virtual work. It is the basis of standard Galerkin finite element models. Using the principle of virtual work, the equilibrium condition and the traction boundary conditions are not exactly satisfied but are approximated in an integral sense. The kinematic equation and the material law are represented exactly.

To derive the principle of virtual work, the first Cauchy equation of motion and the Neumann boundary conditions are multiplied by an arbitrary test function and integrated over the volume of the domain Ω_0 [Bat02],[BLM00],[Hug00]. The test function is chosen as a variation of the displacement field $\delta\mathbf{d}$. This virtual displacement field can be arbitrary but has to be compatible to the Dirichlet boundary conditions. By multiplication of the equation of motion and the Neumann boundary conditions with a virtual displacement field, the existence of a virtual work is assumed. In a state of equilibrium, the virtual work δW, that is performed by the internal and external forces of the system due to the virtual displacement field shall be zero.

$$\delta W = \delta W_{dyn} + \delta W_{int} - \delta W_{ext} = 0 \tag{2.27}$$

The virtual work δW can be separated in contributions due to inertia forces δW_{dyn}, internal forces δW_{int}, and external forces δW_{ext}.

$$\delta W_{dyn} = \int_{\Omega_0} \rho_0 \ddot{\mathbf{d}} \cdot \delta\mathbf{d} \, d\Omega_0 \tag{2.28}$$

$$\delta W_{int} = \int_{\Omega_0} \delta\mathbf{E} : \mathbf{S} \, d\Omega_0 \tag{2.29}$$

$$\delta W_{ext} = \int_{\Gamma_0} \hat{\mathbf{T}} \cdot \delta\mathbf{d} \, d\Gamma_0 + \int_{\Omega_0} \rho_0 \mathbf{B} \cdot \delta\mathbf{d} \, d\Omega_0 \tag{2.30}$$

Equation 2.29 contains the expression of virtual strain $\delta\mathbf{E}$. $\delta\mathbf{E}$ is related to the virtual displacement $\delta\mathbf{d}$ by the following relations:

$$\delta\mathbf{E} = \frac{1}{2}(\delta\mathbf{F}^{\mathbf{T}} \cdot \mathbf{F} + \mathbf{F}^{\mathbf{T}} \cdot \delta\mathbf{F}) \tag{2.31}$$

with

$$\mathbf{F} = \mathbf{I} + \frac{\partial \mathbf{d}}{\partial \mathbf{X}} \qquad \text{and} \quad \delta\mathbf{F} = \frac{\partial(\delta\mathbf{d})}{\partial \mathbf{X}} \tag{2.32}$$

Inserting eq. 2.28, eq. 2.29, eq. 2.30 into eq. 2.27, the weak form of the boundary value problem of nonlinear elastic dynamics based on the principle of the virtual work is formulated:

$$\delta W = \int_{\Omega_0} \rho_0 \ddot{\mathbf{d}} \cdot \delta \mathbf{d} \, d\Omega_0 + \int_{\Omega_0} \delta \mathbf{E} : \mathbf{S} \, d\Omega_0 - \int_{\Gamma_0} \hat{\mathbf{T}} \cdot \delta \mathbf{d} \, d\Gamma_0 - \int_{\Omega_0} \rho_0 \mathbf{B} \cdot \delta \mathbf{d} \, d\Omega_0 = 0 \qquad (2.33)$$

The principle of virtual work is equivalent to the field equations (eq. 2.12, eg. 2.17, and eq. 2.24), as long as the same function spaces are used to solve both system of equations. For the derivation of the principle of virtual work, only the variation of the displacement is performed. There is a practically infinite multitude of alternative variational formulations, containing all possible combinations of weak and strong satisfaction of the field equations and boundary conditions, as well as additional variants that can be obtained by weighted combinations of these basic principles ("parameterized variational principles") [Bis03]. Next to the principle of virtual displacement the most important principles are the Hellinger-Reissner principle and the Hu-Washizu principle. Table 2.1 gives a brief comparison between the most important variational principles in context of the finite element method.

principle	variables	Euler-Lagrange equations (weakly satisfied)	subsidiary conditions strongly satisfied
virtual work	$\mathbf{d}$	equilibrium traction boundary conditions	kinematic equation material law displacement boundary cond.
Hellinger-Reissner	$\mathbf{d}$, σ	equilibrium kinematic equation traction boundary cond. displacement boundary cond.	material law
Hu-Washizu	$\mathbf{d}$, σ, ϵ	equilibrium kinematic equation material law traction boundary cond. displacement boundary cond.	

Table 2.1: Comparison of variational principles, source: [Bis03]

2.2.2 Numerical Modeling

In order to apply the Finite Element Method, the continuous formulation of the boundary value problem of nonlinear elasto-dynamics has to be transformed into a discretized form. Starting from the weak form (eq. 2.33), a time and space wise discretization is conducted. This leads to a non-linear system of equations, which can be solved conveniently in an iterative manner using computer resources. The following sections introduce the fundamental ideas and methods of space and time integration. Further information about the specific element formulations used in the scope of this work are presented in section 2.3.1.

2.2.2.1 Space Discretization

A continuous body **B** is divided into non-overlapping domains Ω_e, the so-called finite elements (eq. 2.34). The quantities of the considered problem, such as displacements or stress, are specified by element wise functions within the finite elements. Thereby, the relevant continuous quantities are transferred to a discrete set of unknowns and thus approximated on a local level.

$$\mathbf{B} \approx \mathbf{B}^h = \bigcup_{e=1}^{n_{ele}} \Omega_e \tag{2.34}$$

In the following, the formulation of a basic three-dimensional brick element shall be derived.

For a finite element Ω_e, the shape functions $N_i(\xi, \eta, \mu)$ for all nodes i of the element are described by the natural coordinates ξ, η, and μ as parameters. For the requirements and effects of different sets of shape functions, see [Bat02], [Hug00], [ZTZ05]. The position vector of the reference and the current configuration of a point can be described as:

$$\mathbf{X} \approx \mathbf{X}^h(\xi, \eta, \mu) = \sum_{i=1}^{n_{nod}} N_i(\xi, \eta, \mu) \cdot \overline{\mathbf{X}}_\mathbf{i} \tag{2.35}$$

$$\mathbf{x} \approx \mathbf{x}^h(\xi, \eta, \mu) = \sum_{i=1}^{n_{nod}} N_i(\xi, \eta, \mu) \cdot \overline{\mathbf{x}}_\mathbf{i} \tag{2.36}$$

The superscript h indicates an approximated quantity. n_{nod} is the number of nodes within the finite element. Assuming that the position vectors of the nodes ($\overline{\mathbf{X}}_\mathbf{i}$, $\overline{\mathbf{x}}_i$) refer to the global Cartesian base, the parameters ξ, η, μ can be identified as the coordinates $\theta^1, \theta^2, \theta^3$. The same coordinates were used in section 2.2.1.1 for the description of the differential geometry. Considering eq. 2.7, the displacement field can be approximated to:

$$\begin{aligned} \mathbf{d}(\theta^1, \theta^2, \theta^3) \approx \mathbf{d}^h(\theta^1, \theta^2, \theta^3) &= \mathbf{x}^h(\theta^1, \theta^2, \theta^3) - \mathbf{X}^h(\theta^1, \theta^2, \theta^3) \\ &= \sum_{i=1}^{n_{nod}} N_i(\theta^1, \theta^2, \theta^3) \cdot (\overline{\mathbf{x}}_\mathbf{i} - \overline{\mathbf{X}}_\mathbf{i}) \\ &= \sum_{i=1}^{n_{nod}} N_i(\theta^1, \theta^2, \theta^3) \cdot \overline{\mathbf{d}}_\mathbf{i} \end{aligned} \tag{2.37}$$

Comparing 2.35, eq. 2.36, and eq. 2.37 it becomes obvious that the same set of shape functions N_i can be used to approximate both: geometry and displacements. This duality in element formulations is known as the iso-parametric concept. As the shape functions are time independent, velocity and acceleration can be derived in eq. 2.38 and eq. 2.39 in discretized form:

$$\dot{\mathbf{d}}^h(\theta^1, \theta^2, \theta^3) = \sum_{i=1}^{n_{nod}} N_i(\theta^1, \theta^2, \theta^3) \cdot \dot{\overline{\mathbf{d}}}_\mathbf{i} \tag{2.38}$$

$$\ddot{\mathbf{d}}^h(\theta^1, \theta^2, \theta^3) = \sum_{i=1}^{n_{nod}} N_i(\theta^1, \theta^2, \theta^3) \cdot \ddot{\overline{\mathbf{d}}}_\mathbf{i} \tag{2.39}$$

Accordingly, with eq. 2.2 and eq. 2.3, the covariant base vectors of the discretized geometry for reference and current configuration are:

$$\mathbf{G}_l^h = \mathbf{X}^h{}_{,l} = \frac{\partial \mathbf{X}^h}{\partial \theta^l} = \sum_{i=1}^{n_{nod}} N_i(\theta^1,\theta^2,\theta^3)_{,l} \cdot \overline{\mathbf{X}}_i \tag{2.40}$$

$$\mathbf{g}_l^h = \mathbf{x}^h{}_{,l} = \frac{\partial \mathbf{x}^h}{\partial \theta^l} = \sum_{i=1}^{n_{nod}} N_i(\theta^1,\theta^2,\theta^3)_{,l} \cdot \overline{\mathbf{x}}_i \tag{2.41}$$

Using eq. 2.40 and eq. 2.41 in combination with eq. 2.11 the discretized deformation gradient and, via eq. 2.12, the discretized Green-Lagrange strain tensor is formulated.

The Bubnov-Galerkin method - that is applied here - uses the same interpolation concept for real quantities of the problem as for assumed test or virtual quantities. The variation of the displacement in the discretized form, according to eq. 2.37, is:

$$\delta \mathbf{d}^h(\theta^1,\theta^2,\theta^3) = \sum_{i=1}^{n_{nod}} N_i(\theta^1,\theta^2,\theta^3) \cdot \delta \overline{\mathbf{d}}_\mathbf{i} \tag{2.42}$$

As the geometry is discretized into non-overlapping finite domains, so-called elements, the principle of virtual work can be expressed on an element level. The integration is performed numerically by applying the Gauss quadrature rule in an element wise manner. Therefore, element based, local coordinate systems are introduced. The change of base from the physical curvilinear coordinate system to the element wise local system has to be incorporated into the integration. Details about the integration procedure can be found in [Hug00],[AM88], and [ZTZ05].

In the following, element based quantities are indicated by the superscript *e*. The contributions of virtual work on all elements sum up to the virtual work of the whole system:

$$\delta W^h = \delta W^h_{dyn} + \delta W^h_{int} - \delta W^h_{ext} = \sum_{e=1}^{n_{ele}} \delta W^e_{dyn} + \sum_{e=1}^{n_{ele}} \delta W^e_{int} - \sum_{e=1}^{n_{ele}} \delta W^e_{ext} \tag{2.43}$$

For the discretization of the virtual work due to forces of inertia, the approximations introduced in eq. 2.39 and eq. 2.42 are used. The contribution of one element is:

$$\begin{aligned}
\delta W^e_{dyn} &= \int_{\Omega^e_0} \rho_0 \, \delta \mathbf{d}^h \cdot \ddot{\mathbf{d}}^h \, d\Omega^e_0 && (2.44)\\
&= \int_{\Omega^e_0} \rho_0 \left(\sum_{i=1}^{n_{nod}} N_i(\theta^1,\theta^2,\theta^3) \cdot \delta \overline{\mathbf{d}}_i \right) \left(\sum_{j=1}^{n_{nod}} N_j(\theta^1,\theta^2,\theta^3) \cdot \ddot{\overline{\mathbf{d}}}_j \right) d\Omega^e_0 && (2.45)\\
&= \sum_{i=1}^{n_{nod}} \sum_{j=1}^{n_{nod}} \delta \bar{\mathbf{d}}_i \cdot \underbrace{\left[\int_{\Omega^e_0} \rho_0 \; N_i(\theta^1,\theta^2,\theta^3) \; N_j(\theta^1,\theta^2,\theta^3) \; \mathbf{I} \, d\Omega^e_0 \right]}_{\mathbf{m}^{e\ ij}} \cdot \ddot{\bar{\mathbf{d}}}_j && (2.46)\\
&= \sum_{i=1}^{n_{nod}} \sum_{j=1}^{n_{nod}} \delta \bar{\mathbf{d}}_i \cdot \mathbf{m}^{e\ ij} \cdot \ddot{\bar{\mathbf{d}}}_j && (2.47)
\end{aligned}$$

Summarizing the nodal degrees of freedom within one element to a vector $\bar{\mathbf{d}}^e$, the mass matrix of an element can be correspondingly expressed as $\mathbf{m}^e$. Using this notation, the contribution of the forces of inertia to the virtual work can be written as:

$$\delta W^e_{dyn} = \delta \bar{\mathbf{d}}^{e^T} \mathbf{m}^e \ddot{\bar{\mathbf{d}}}^e \tag{2.48}$$

For distributed, non-constant external loading on the boundary, the consistent nodal load vector is derived by integration of the load over the element surface using the shape function. In the following, it is assumed, that external loads and body forces are independent of the deformation of the structure: $\hat{\mathbf{T}}^h{}_{,\mathbf{d}} = \mathbf{0}$ and $\mathbf{B}^h{}_{,\mathbf{d}} = \mathbf{0}$ [MWBR99].

$$\begin{aligned}
\delta W^e_{ext} &= \int_{\Gamma^e_0} \hat{\mathbf{T}} \cdot \delta \mathbf{d}^h \, d\Gamma^e_0 + \int_{\Omega^e_0} \rho_0 \, \mathbf{B} \cdot \delta \mathbf{d}^h \, d\Omega^e_0 && (2.49)\\
&= \int_{\Gamma^e_0} \hat{\mathbf{T}} \cdot \left(\sum_{i=1}^{n_{nod}} N_i(\theta^1,\theta^2,\theta^3) \cdot \delta \bar{\mathbf{d}}_i \right) d\Gamma^e_0 + \\
&\qquad \int_{\Omega^e_0} \rho_0 \, \mathbf{B} \cdot \left(\sum_{i=1}^{n_{nod}} N_i(\theta^1,\theta^2,\theta^3) \cdot \delta \bar{\mathbf{d}}_i \right) d\Omega^e_0 && (2.50)\\
&= \sum_{i=1}^{n_{nod}} \delta \bar{\mathbf{d}}_i \cdot \left[\int_{\Gamma^e_0} \hat{\mathbf{T}} \cdot N_i(\theta^1,\theta^2,\theta^3) \, d\Gamma^e_0 + \int_{\Omega^e_0} \rho_0 \, \mathbf{B} \cdot N_i(\theta^1,\theta^2,\theta^3) \, d\Omega^e_0 \right] && (2.51)\\
&= \sum_{i=1}^{n_{nod}} \delta \bar{\mathbf{d}}_i \cdot \mathbf{r}^{e\,i}_{ext} && (2.52)
\end{aligned}$$

Integrating the contribution of the consistent nodal load vectors $\mathbf{r}^{e\,i}_{ext}$ the load vector $\mathbf{r}^e_{ext}$ is derived, which corresponds to the vector of unknown displacements $\bar{\mathbf{d}}^e$ of the problem. Assuming a time dependent load, the element load vector is $\mathbf{r}^e_{ext}(t)$. The discretized form of the virtual work due to time dependent external loading can be written as:

$$\delta W^e_{ext} = \delta \bar{\mathbf{d}}^e \mathbf{r}^e_{ext}(t) \tag{2.53}$$

The contribution of the internal forces is more difficult to be discretized due to the nonlinearity of the Green-Lagrange strain tensor $\mathbf{E}(\bar{\mathbf{d}})$ with respect to displacements $\bar{\mathbf{d}}$. The variation of the Green-Lagrange strain tensor is derived in a discretized form, using $\bar{\mathbf{d}}^e$ as a vector of the unknown displacements:

$$\frac{\partial \mathbf{E}^h(\bar{\mathbf{d}})}{\partial \bar{\mathbf{d}}^e} \, \delta \bar{\mathbf{d}}^e = \mathbf{E}^h{}_{,\bar{\mathbf{d}}^e} \, \delta \bar{\mathbf{d}}^e \tag{2.54}$$

Using this, the contribution of the internal forces can be transformed to:

$$\begin{aligned}
\delta W^e_{int} &= \int_{\Omega^e_0} \mathbf{S}^h : \delta \mathbf{E}^h \, d\Omega^e_0 = \int_{\Omega^e_0} \mathbf{S}^h : \mathbf{E}^h{}_{,\bar{\mathbf{d}}^e} \, \delta \bar{\mathbf{d}}^e \, d\Omega^e_0 && (2.55)\\
&= \delta \bar{\mathbf{d}}^e [\int_{\Omega^e_0} \mathbf{S}^h : \mathbf{E}^h{}_{,\bar{\mathbf{d}}^e} \, d\Omega^e_0] = \sum_{i=1}^{n_{nod}} \delta \bar{\mathbf{d}}^e_i \cdot \mathbf{r}^{e\,i}_{int}(\bar{\mathbf{d}}) = \delta \bar{\mathbf{d}}^e \cdot \mathbf{r}^e_{int}(\bar{\mathbf{d}}) && (2.56)
\end{aligned}$$

Summarizing the contributions of virtual work for one element, the spacial discretized equation of motion is derived.

$$\delta W^e = \delta W^e_{dyn} + \delta W^e_{int} - \delta W^e_{ext} = \delta \bar{\mathbf{d}}^e \cdot [\mathbf{m}^e \, \ddot{\bar{\mathbf{d}}}^e + \mathbf{r}^e_{int}(\bar{\mathbf{d}}) - \mathbf{r}^e_{ext}] = 0 \tag{2.57}$$

The virtual work for the whole system is deduced by assembling the contributions from each element according to 2.43:

$$\delta W = \delta W_{dyn} + \delta W_{int} - \delta W_{ext} = \delta \bar{\mathbf{d}} \cdot [\mathbf{M}\, \ddot{\bar{\mathbf{d}}} + \mathbf{r}_{int}(\bar{\mathbf{d}}) - \mathbf{r}_{ext}] = 0 \tag{2.58}$$

Correspondingly, $\mathbf{M}$ resembles the mass matrix of the system, which has to be computed only once due to the Lagrangian formulation. The vector $\bar{\mathbf{d}}$ contains all unknown degrees of freedom of the system. As well as its variation, the size and location of $\bar{\mathbf{d}}$ and its variation $\delta\bar{\mathbf{d}}$ have to comply with the Dirichlet boundary conditions.

Applying the fundamental lemma of variational calculus, the spacial discretized, non-linear differential equation and the initial conditions are derived:

$$\mathbf{M}\, \ddot{\bar{\mathbf{d}}} + \mathbf{r}_{int}(\bar{\mathbf{d}}) = \mathbf{r}_{ext} \qquad \dot{\bar{\mathbf{d}}}(t = t_0) = \dot{\bar{\mathbf{d}}}_0, \qquad \bar{\mathbf{d}}(t = t_0) = \bar{\mathbf{d}}_0 \tag{2.59}$$

2.2.2.2 Time Discretization

After the spacial discretization in finite elements, eq. 2.59 states the semi-discrete problem. As the next step, time discretization is performed. The continuous time period $[t_0, T]$ is divided into n_t time steps of equal length Δt. The system quantities are not regarded as time wise continuous anymore, but as defined at discrete points in time t_n:

$$t_n = t_0 + \Delta t\, n \quad \text{with} \quad n \in [0, n_t] \tag{2.60}$$

In a time integration scheme the system quantities at the end of the new time step t_{n+1} are computed based on those at the the end of the previous time-steps t_n, t_{n-1}, t_{n-2}, etc. Time integration schemes can be classified into one-step and multi-step schemes, depending on the number of previous time steps used to derive the values for the new time step.

In explicit time integration schemes, the dynamic equilibrium based on the equation of motion is computed at the beginning of the time step. For implicit time integration schemes, the equilibrium is considered at the end of the time step. In an implicit scheme, the state of motion at the end of a time step depends on itself. Thus, for each time-step a system of equations has to be solved.

For the solution of problems concerning structural dynamics, implicit and explicit one-step time integration schemes have proven to be especially well suited . In the simulation of light-weight structures under wind loading, modes with relatively low frequencies are expected. Therefore, considerably large time step lengths are sufficient to capture the physically relevant responses. For the applicable time step length, stability issues of the time integration scheme have to be considered. A time integration scheme is called unconditionally stable, if the stability of the method does not depend on the time step length. Usually, explicit time integration methods are only conditionally stable. For linear structural behavior, established methods based on the Newmark scheme show an unconditionally stable behavior [Bel83], [Hug00]. For the non-linear structural behavior, unconditionally stable time integration schemes are still a topic of ongoing research .

Within this work, small numerical dissipation is applied to ensure the stability of the time integration scheme. Since this proved to be sufficient more elaborate energy conserving schemes could be omitted. Numerical dissipation occurs if the time integration scheme causes an error in computing the amplitude of a dynamic response. This effect is welcome in reducing the nonphysical so-called spurious higher frequency modes that are likely to occur in time integration methods for Finite Element Methods [Hug00]. For the lower frequency modes, which are of interest for the accuracy of the analysis, the influence of numerical dissipation has to be restricted.

In the scope of this work, the Generalized-α time integration scheme is used [CH93], [Cri97], [Hul04]. Thereby, it is possible to control the dissipation on the spurious higher frequency modes and to minimize the dissipation in the lower frequency modes. Compared to the Newmark method [New59], the Generalized-α time integration scheme's advantage is to maintain second order accuracy, providing that the relevant parameters are chosen in an appropriate way.

As in the Newmark scheme, displacements $\mathbf{d}_{n+1}$ and the velocity $\dot{\mathbf{d}}_{n+1}$ at the end of time step $\Delta t = t_{n+1} - t_n$ can be approximated to:

$$\mathbf{d}_{n+1} = \mathbf{d}_n + \Delta t\, \dot{\mathbf{d}}_n + \Delta t^2 \left(\left(\frac{1}{2} - \beta \right) \ddot{\mathbf{d}}_n + \beta\, \ddot{\mathbf{d}}_{n+1} \right) \tag{2.61}$$

$$\dot{\mathbf{d}}_{n+1} = \dot{\mathbf{d}}_n + \Delta t \left((1-\gamma)\, \ddot{\mathbf{d}}_n + \gamma \ddot{\mathbf{d}}_{n+1} \right) \tag{2.62}$$

β and γ are the so-called Newmark parameters. Using the displacements $\mathbf{d}_{n+1}$ as primary variable, velocity $\dot{\mathbf{d}}_{n+1}$ and acceleration $\ddot{\mathbf{d}}_{n+1}$ can be found by transforming eq. 2.61 and eq. 2.62 to:

$$\dot{\mathbf{d}}_{n+1} = \frac{\gamma}{\beta \Delta t} (\mathbf{d}_{n+1} - \mathbf{d}_n) - \frac{\gamma - \beta}{\beta} \dot{\mathbf{d}}_n - \frac{\gamma - 2\beta}{2\beta} \Delta t \ddot{\mathbf{d}}_n \tag{2.63}$$

$$\ddot{\mathbf{d}}_{n+1} = \frac{1}{\beta \Delta t^2} (\mathbf{d}_{n+1} - \mathbf{d}_n) - \frac{1}{\beta \Delta t} \dot{\mathbf{d}}_n - \frac{1 - 2\beta}{2\beta} \ddot{\mathbf{d}}_n \tag{2.64}$$

For the Generalized-α method, two additional shift parameters α_m and α_f are introduced. In the time interval $[t_n, t_{n+1}]$, α_m and α_f are applied for interpolation:

$$\ddot{\mathbf{d}}_\alpha = (1-\alpha_m) \ddot{\mathbf{d}}_{n+1} + \alpha_m\, \ddot{\mathbf{d}}_n \tag{2.65}$$

$$\dot{\mathbf{d}}_\alpha = (1-\alpha_f) \dot{\mathbf{d}}_{n+1} + \alpha_f\, \dot{\mathbf{d}}_n \tag{2.66}$$

$$\mathbf{r}^{int}_\alpha = (1-\alpha_f) \mathbf{r}^{int}_{n+1} + \alpha_f\, \mathbf{r}^{int}_n \tag{2.67}$$

$$\mathbf{r}^{ext}_\alpha = (1-\alpha_f) \mathbf{r}^{ext}_{n+1} + \alpha_f\, \mathbf{r}^{ext}_n \tag{2.68}$$

Inserting eq. 2.61 and eq. 2.62 as well as eq. 2.65 - 2.68 into the semi-discrete equation of motion eq. 2.59, the dynamic equilibrium can be formulated as:

$$\begin{aligned} \tfrac{1-\alpha_m}{\beta \Delta t^2} \mathbf{M} \bar{\mathbf{d}}_{n+1} + (1-\alpha_f) \mathbf{r}^{int}_{n+1} = (1-\alpha_f) \mathbf{r}^{ext}_{n+1} + \alpha_f \mathbf{r}^{ext}_n - \alpha_f \mathbf{r}^{int}_n + \\ \mathbf{M} \left[\tfrac{1-\alpha_m}{\beta \Delta t^2} \bar{\mathbf{d}}_n + \tfrac{1-\alpha_m}{\beta \Delta t} \dot{\bar{\mathbf{d}}}_n + \left(\tfrac{1-\alpha_m}{2\beta} - 1 \right) \ddot{\bar{\mathbf{d}}}_n \right] \end{aligned} \tag{2.69}$$

By the choice of the Newmark parameters β and γ and the interpolation parameters α_m and α_f, the degree of numerical dissipation is controlled. Depending on the spectral radius ρ_∞, the four parameters can be determined as:

$$\alpha_m = \frac{2\rho_\infty - 1}{\rho_\infty + 1} \qquad \alpha_f = \frac{\rho_\infty}{\rho_\infty + 1} \qquad \beta = \frac{1}{4}(1 - \alpha_m + \alpha_f)^2 \qquad \gamma = \frac{1}{2} - \alpha_m + \alpha_f \tag{2.70}$$

For the high frequency range, the numerical dissipation can be evaluated by the spectral radius $\rho_\infty \in [0, 1]$. For $\rho_\infty = 1$ no numerical dissipation is applied, but the computation might face instable behavior for nonlinear problems. A choice of ρ_∞ in the range of $[0.85, 0.95]$ introduces a numerical damping in the high frequency modes, which proved to be sufficient for the examples presented in the scope of this work. However, this method requires the time step to be small enough, so that relevant physical modes are not regarded as spurious and subject to numerical dissipation.

2.2.2.3 Linearization

For the linearization of the problem, eq. 2.69 is transformed into a residual form:

$$\begin{aligned}\mathbf{R}\left(\bar{\mathbf{d}}_{n+1}\right) = \frac{1-\alpha_m}{\beta\Delta t^2}\mathbf{M}\bar{\mathbf{d}}_{n+1} + (1-\alpha_f)\mathbf{r}^{int}\left(\bar{\mathbf{d}}_{n+1}\right) - (1-\alpha_f)\mathbf{r}^{ext}_{n+1} - \\ \alpha_f\mathbf{r}^{ext}_n + \alpha_f\mathbf{r}^{int}\left(\bar{\mathbf{d}}_n\right) - \mathbf{M}\left[\frac{1-\alpha_m}{\beta\Delta t^2}\bar{\mathbf{d}}_n + \frac{1-\alpha_m}{\beta\Delta t}\dot{\bar{\mathbf{d}}}_n + \left(\frac{1-\alpha_m}{2\beta} - 1\right)\ddot{\bar{\mathbf{d}}}_n\right] = \mathbf{0}\end{aligned} \tag{2.71}$$

The solution is computed by a Newton-Raphson iteration [Cri91]. For the iteration, a new index k is introduced, which describes the number of the current iteration. For a specific time step $n+1$, starting from the last computed residuum vector $\mathbf{R}(\bar{\mathbf{d}}^k)$, the new residuum vector $\mathbf{R}(\bar{\mathbf{d}}^{k+1})$ shall be computed. For the linearization the Taylor-series is used:

$$\mathbf{R}(\bar{\mathbf{d}}^{k+1}_{n+1}) = \mathbf{R}(\bar{\mathbf{d}}^k_{n+1}) + \frac{\partial\mathbf{R}(\bar{\mathbf{d}}^k_{n+1})}{\partial\bar{\mathbf{d}}_{n+1}}\Delta\bar{\mathbf{d}}^{k+1}_{n+1} + \mathcal{O}\left(\left(\Delta\bar{\mathbf{d}}^{k+1}_{n+1}\right)^2\right) = \mathbf{0} \tag{2.72}$$

$$\text{with} \qquad \Delta\bar{\mathbf{d}}^{k+1}_{n+1} = \bar{\mathbf{d}}^{k+1}_{n+1} - \bar{\mathbf{d}}^k_{n+1} \tag{2.73}$$

By truncating the Taylor-series after the linear term, a linear system of equations is deduced:

$$\frac{\partial\mathbf{R}(\bar{\mathbf{d}}^k_{n+1})}{\partial\bar{\mathbf{d}}_{n+1}}\Delta\bar{\mathbf{d}}^{k+1}_{n+1} = -\mathbf{R}(\bar{\mathbf{d}}^k_{n+1}) \tag{2.74}$$

Inserting eq. 2.71 into eq. 2.74, the following equation is derived:

$$\begin{aligned}&\left[\frac{1-\alpha_m}{\beta\Delta t^2}\mathbf{M} + (1-\alpha_f)\underbrace{\frac{\partial\mathbf{r}^{int}\left(\bar{\mathbf{d}}^k_{n+1}\right)}{\partial\bar{\mathbf{d}}_{n+1}}}_{\mathbf{K}_T}\right]\Delta\bar{\mathbf{d}}^{k+1}_{n+1} = \\ &-\frac{1-\alpha_m}{\beta\Delta t^2}\mathbf{M}\bar{\mathbf{d}}^k_{n+1} - (1-\alpha_f)\mathbf{r}^{int}\left(\bar{\mathbf{d}}^k_{n+1}\right) + (1-\alpha_f)\mathbf{r}^{ext}_{n+1} \\ &-\alpha_f\mathbf{r}^{ext}_n + \alpha_f\mathbf{r}^{int}\left(\bar{\mathbf{d}}_n\right) + \mathbf{M}\left[\frac{1-\alpha_m}{\beta\Delta t^2}\bar{\mathbf{d}}_n + \frac{1-\alpha_m}{\beta\Delta t}\dot{\bar{\mathbf{d}}}_n + \left(\frac{1-\alpha_m}{2\beta} - 1\right)\ddot{\bar{\mathbf{d}}}_n\right]\end{aligned} \tag{2.75}$$

$\mathbf{K}_T(\bar{\mathbf{d}}^k_{n+1})$ is the tangential stiffness matrix after time step $n+1$ and iteration step k. The term in brackets on the left side of eq. 2.75 can be identified as the effective stiffness matrix $\mathbf{K}_T^{eff}$

$$\mathbf{K}_T^{eff}(\bar{\mathbf{d}}^k_{n+1}) = \left[\frac{1-\alpha_m}{\beta\Delta t^2}\mathbf{M} + (1-\alpha_f)\mathbf{K}_T\left(\bar{\mathbf{d}}^k_{n+1}\right)\right] \tag{2.76}$$

and the term on the right side of eq. 2.75

$$\begin{aligned}\mathbf{r}^{eff}(\bar{\mathbf{d}}^k_{n+1}, \bar{\mathbf{d}}_n) = &-\frac{1-\alpha_m}{\beta\Delta t^2}\mathbf{M}\bar{\mathbf{d}}^k_{n+1} - (1-\alpha_f)\mathbf{r}^{int}\left(\bar{\mathbf{d}}^k_{n+1}\right) + (1-\alpha_f)\mathbf{r}^{ext}_{n+1} + \\ &\alpha_f\mathbf{r}^{ext}_n + \alpha_f\mathbf{r}^{int}\left(\bar{\mathbf{d}}_n\right) + \mathbf{M}\left[\frac{1-\alpha_m}{\beta\Delta t^2}\bar{\mathbf{d}}_n + \frac{1-\alpha_m}{\beta\Delta t}\hat{\mathbf{d}}_n + \left(\frac{1-\alpha_m}{2\beta} - 1\right)\tilde{\mathbf{d}}_n\right]\end{aligned} \tag{2.77}$$

as the effective load vector. Using efficient stiffness and efficient load vector, the linearized nonlinear elastic problem is stated as:

$$\mathbf{K}_T^{eff}(\bar{\mathbf{d}}^k_{n+1})\,\Delta\bar{\mathbf{d}}^{k+1}_{n+1} = \mathbf{r}^{eff}(\bar{\mathbf{d}}^k_{n+1}, \bar{\mathbf{d}}_n) \tag{2.78}$$

Equation 2.78 is solved for $\Delta\bar{\mathbf{d}}^{k+1}_{n+1}$. The solution is used to update $\bar{\mathbf{d}}^k_{n+1}$ by applying eq. 2.73. For a converged solution it holds: $\bar{\mathbf{d}}^{k+1}_{n+1} \approx \bar{\mathbf{d}}^k_{n+1}$. Using a good initial predictor for this Newton scheme, quadratic convergence can be reached. Velocity $\hat{\mathbf{d}}_n$ and acceleration $\tilde{\mathbf{d}}_n$ at the beginning and end of a time step are derived based on eq. 2.61 and 2.62.

2.3 Modeling of Membrane Structures

2.3.1 Numerical Analysis of Structural Behavior of Membrane Structures

Membrane structures are classified as surface structures, since their ratio of thickness h to span L is usually $h/L << 1$. Each material point on the surface can be identified by two Gaussian surface parameters θ^1 and θ^2 at a certain time t in the current configuration $\mathbf{x}(\theta^1, \theta^2)$ and in the reference configuration $\mathbf{X}(\theta^1, \theta^2)$. Using these properties, the equations derived in section 2.2.1 can be simplified by an early semi-discretization in thickness direction θ^3 [Bis99], while the other dimensions stay continuous. Furthermore, based on the spatial load carrying behavior of membranes, the following assumptions are introduced:

- ◇ The thickness of the membrane is considered as constant and comparably thin. In accordance with the behavior of available membrane material the Poisson effect in thickness direction is neglected.
- ◇ Normal stress is constant over the thickness.
- ◇ Only normal and in-plane shear stresses are acting in the mid plane. All stress and strain components with respect to the thickness direction are zero.

Due to the 'in advance' discretization in thickness direction, the element wise contributions of virtual work in the spatially fully discretized system can be simplified for eq .2.44, eq. 2.49, and eq. 2.55 to:

$$\delta W^e_{dyn} = h \int_{A^e_0} \rho_0 \, \delta \mathbf{d}^h \cdot \ddot{\mathbf{d}}^h \, dA^e_0 \tag{2.79}$$

$$\delta W^e_{ext} = \int_{\Gamma^e_0} \hat{\mathbf{T}} \cdot \delta \mathbf{d}^h \, d\Gamma^e_0 + h \int_{A^e_0} \rho_0 \, \mathbf{B} \cdot \delta \mathbf{d}^h \, dA^e_0 \tag{2.80}$$

$$\delta W^e_{int} = h \int_{A^e_0} \delta \mathbf{E}^h : \mathbf{S}^h \, dA^e_0 \tag{2.81}$$

A^e_0 is the area of a finite surface element in initial configuration. With spatial discretization for all dimensions at a certain point in time t, the displacement $\mathbf{d}(\theta^1, \theta^2) = \mathbf{x}(\theta^1, \theta^2) - \mathbf{X}(\theta^1, \theta^2)$ and the virtual displacement $\delta\mathbf{d}(\theta^1, \theta^2)$ for a material point can be approximated as:

$$\mathbf{d}(\theta^1, \theta^2) = \sum_{i=1}^{n_{nod}} N_i(\theta^1, \theta^2) \cdot \bar{\mathbf{d}}_\mathbf{i} \tag{2.82}$$

$$\delta\mathbf{d}(\theta^1, \theta^2) = \sum_{i=1}^{n_{nod}} N_i(\theta^1, \theta^2) \cdot \delta\bar{\mathbf{d}}_\mathbf{i} \tag{2.83}$$

This holds for the time derivative of the displacement vector $\delta\mathbf{d}(\theta^1, \theta^2)$, the velocity vector $\delta\dot{\mathbf{d}}(\theta^1, \theta^2)$, and the acceleration vector $\delta\ddot{\mathbf{d}}(\theta^1, \theta^2)$, respectively.

All stress components normal to the surface are zero, i.e.:

$$S^{i3} = S^{3i} = 0 \quad \text{and} \quad \sigma^{i3} = \sigma^{3i} = 0 \tag{2.84}$$

The strain state can be derived via the strain tensor of the mid surface:

$$\mathbf{E} = \frac{1}{2}(g_{\alpha\beta} - G_{\alpha\beta})\mathbf{G}^\alpha \otimes \mathbf{G}^\beta \tag{2.85}$$

The artificially imposed prestress is taken into account as a residual stress added to the elastic stress in the reference configuration. The resulting PK2 stress tensor $\mathbf{S}$ in reference configuration is the sum of the prestress tensor $\mathbf{S}_{pre}$ and the elastic stress tensor $\mathbf{S}_{el}$:

$$\mathbf{S} = \mathbf{S}_{pre} + \mathbf{S}_{el} = \mathbf{S}_{pre} + \mathbb{C} : \mathbf{E} \tag{2.86}$$

For the usage of foils, an isotropic material behavior can be assumed. Accordingly, the components of the material tensor $\mathbb{C}$ can be derived as:

$$C^{\alpha\beta\gamma\delta} = \overline{\lambda} G^{\alpha\beta} G^{\gamma\delta} + \mu(G^{\alpha\gamma} G^{\beta\delta} + G^{\alpha\delta} G^{\beta\gamma}) \tag{2.87}$$

$$\text{with} \quad \overline{\lambda} = \frac{2\lambda\mu}{\lambda + 2\mu} = \frac{E\nu}{1 - \nu^2} \quad \text{and} \quad \mu = \frac{E}{2(1+\nu)} \tag{2.88}$$

Fabrics initially show an anisotropic, mainly orthotropic behavior in the perpendicular directions of warp and weft. Furthermore, fabrics feature non-elastic, time and load history dependent properties [FM04]. For detailed information about the derivation of the material tensor for fabrics, see for example [MR95], [Rai03].

The procedures for time discretization and the linearization of membrane and cable elements are derived according to those presented in section 2.2.2.2 and section 2.2.2.3.

For the discretization of edge cables, a cable element formulation can be derived by introducing a second early spatial discretization. All stress components perpendicular to the cable axis vanish and the cross section features a constant stress distribution. For a detailed derivation of this element type, see [WB05], [Wüc07].

2.3.2 Form Finding

Already in their initial state, membrane structures are subject to dead load and prestress. As explained above, the geometry of the structure has to ensure an equilibrium of internal membrane forces (including those due to prestress) and loadings. Therefore, the initial geometry of a membrane structure cannot be easily derived, but is the result of experimental or numerical analysis. The resulting shape resembles a free form surface, which generally cannot be generated by analytical methods.

The procedure of deriving the initial shape of a membrane structure is called **form finding**. As the form finding procedure is an both essential and a challenging task in the design of membrane structures, fundamental equations and solution methods are introduced in the following sections.

In a classical structural analysis, deformation and stress of a structure are computed based on the known geometry, the known load conditions, and material parameters. In contrast, the aim of a form finding procedure is to find a geometry for which a certain internal stress state and, in case, an external loading state, are in equilibrium. Additionally, the geometry has to satisfy prescribed geometric boundary conditions. As the geometry is the unknown while the internal and external stress distributions are prescribed, form finding can be identified as an inverse problem.

In experimental approaches, small scale models are used to simulate a certain stress distribution in a flexible material and to record the resulting shapes. If a shape satisfies all requirements, it is upscaled and used as initial geometry for further design processes. Rubber, thin fabrics, or soap films are used as materials in the small scale models.

In a numerical approach, the inverse problem of form finding is solved by computations. An arbitrary initial geometry, which satisfies the geometric boundary conditions, such as placement and type of supports, is chosen. This geometry serves as a known reference configuration (see fig. 2.5(a)). The aim is to derive a new geometry as current configuration, which is in equilibrium for a prescribed prestress state (see fig. 2.5(b)). In the following section, the problematic and solution strategies for a numerical form finding are introduced.

2.3.2.1 Numerical Form Finding

In the following a mechanically prestressed structure is assumed. For form finding considerations, the low self-weight of the membrane itself has little influence on the result compared to the prestress. Therefore, it is neglected as well as all external loads. Performing the

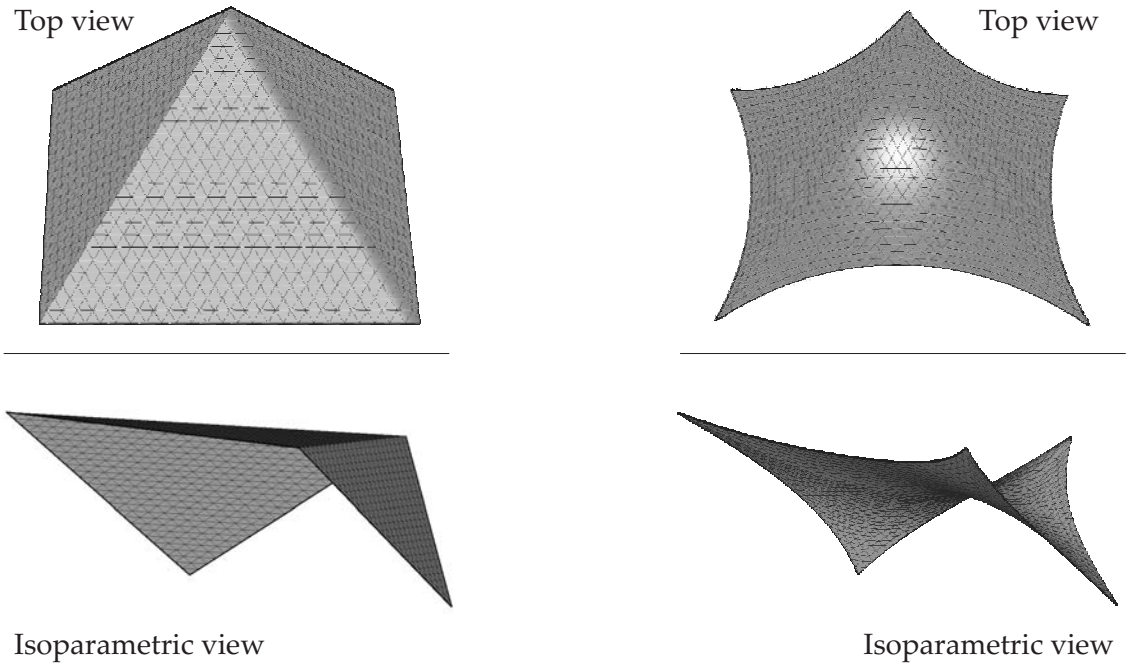

(a) Arbitrary initial shape (reference configuration)

(b) Resulting equilibrium shape (current configuration)

Figure 2.5: form finding computation

form finding procedure without any loading but prestress, the geometry of the membrane solemnly depends on the distribution of membrane prestress and, in case, the ratio to prestress of edge cables. In the design process this fact is utilized. Firstly, the distribution of prestress in the different structural elements is adjusted to derive an acceptable shape. Secondly, while keeping the prestress distribution constant, the level of the prestress is adjusted according to further requirements, such as the capability to withstand design loads.

The state of equilibrium of the internal forces in the membrane can be described by the principle of virtual work in the integral (weak) sense:

$$\delta W_\sigma = h \int_a \sigma : \delta \mathbf{d}_{,\mathbf{x}} \, da = 0 \tag{2.89}$$

This resembles the state of equilibrium in the current configuration $\mathbf{x}$, with σ as the Cauchy stress tensor and a as the area of the membrane surface. The displacement vector $\mathbf{d}$ describes the change of geometry from reference to current configuration, from the assumed initial geometry to the aspired "geometry of equilibrium". $\mathbf{d}_{,\mathbf{x}}$ is the derivative of the displacement vector with respect to the current configuration.

The state of equilibrium can be described in the reference configuration $\mathbf{X}$ equivalently:

$$\delta W_S = h \int_A (\mathbf{F} \cdot \mathbf{S}) : \delta \mathbf{F} \, dA = 0 \tag{2.90}$$

with $\mathbf{S}$ as the second Piola-Kirchhoff stress tensor and A as the area of the membrane surface in reference configuration. The deformation gradient $\mathbf{F}$ connects the reference configuration

to the current configuration:

$$d\mathbf{x} = \mathbf{F} \cdot d\mathbf{X} \tag{2.91}$$

Using the deformation gradient together with further rearrangement [WB05], the principle of virtual work in the current configuration can be transformed to:

$$\delta W_\sigma = h \int_A det\mathbf{F} \, (\sigma \cdot \mathbf{F}^{-T}) \; : \; \delta\mathbf{F} \, dA = 0 \tag{2.92}$$

In the general case, no analytical solution is possible. The Finite Element Method is used to solve the problem in a point wise manner for a discretized geometry. The translational degrees of freedom of the nodes of the finite element mesh are chosen as variables. Using the iso-parametric concept, the discretized geometry $x^h(\theta^1, \theta^2)$ and displacement $d^h(\theta^1, \theta^2)$ of the structure are approximated based on the position of the nodes of the finite element mesh via the shape functions:

$$x^h(\theta^1, \theta^2) = \sum_{k=1}^{n_{nod}} N_k(\theta^1, \theta^2) \cdot \overline{\mathbf{x}}_k \tag{2.93}$$

$$d^h(\theta^1, \theta^2) = \sum_{k=1}^{n_{nod}} N_k(\theta^1, \theta^2) \cdot \bar{\mathbf{d}}_k \tag{2.94}$$

In a Cartesian coordinate system with orthogonal basis $\mathbf{e}_i$, the position $\overline{\mathbf{x}}_k$ and displacement $\bar{\mathbf{d}}_k$ of a node k can be determined by the their coefficients x_k^i and d_k^i:

$$\overline{\mathbf{x}}_k = x_k^1\mathbf{e}_1 + x_k^2\mathbf{e}_2 + x_k^3\mathbf{e}_3 \tag{2.95}$$

$$\bar{\mathbf{d}}_k = d_k^1\mathbf{e}_1 + d_k^2\mathbf{e}_2 + d_k^3\mathbf{e}_3 \tag{2.96}$$

The unknown coefficients of the nodal displacements d_k^i are identified as unknowns of the form finding computation. They are summarized into a vector $\mathbf{b}$ of size n_{dof}, whose components b_r resemble the r-th degree of freedom of the discretized problem. Using the fundamental lemma of variational calculus and the vector of unknowns b_r, the following nonlinear system of equations with n_{dof} equations can be derived:

$$\frac{\partial W_\sigma}{\partial b_r} = h \int_A det\mathbf{F} \, (\sigma \cdot \mathbf{F}^{-T}) \; : \; \frac{\partial \mathbf{F}}{\partial b_r} \, dA = 0 \quad \forall \, r \; \in \; [1, n_{\text{dof}}] \tag{2.97}$$

For the linearization of eq. 2.97 similar procedures to those described in section 2.2.2.1 are applied for the membrane and cable elements introduced in section 2.3.1 [WB05]. Following the common procedure of geometrically nonlinear structural analysis, a direct solution via an iterative Newton-Raphson iteration seems to be possible.

2.3.2.2 Solving the Inverse Problem

Typically, inverse problems are ill posed in contrast to well posed problems, where a known physical situation is modeled. According to the French mathematician Jacques Hadamard (*1865, †1963), a well posed problem is defined by the properties of existence, uniqueness

and stability of its solution. Ill-posed problems usually need to be re-formulated for numerical treatment. Typically this involves including additional assumptions. This process is known as regularization.

Form finding is an ill-posed problem. Especially the non-uniqueness of the solution can be easily explained: An identical surface can be approximated by different sets of nodal coordinates for a finite element discretization (fig. 2.6). This is due to the fact that except for the nodes at the edge, the FE-based nodes can move tangentially to the surface without this movement causing any strain energy. Therefore, the stiffness matrix of the system is singular for tangential movements within the membrane surface. Thus, eq. 2.97 is not solvable in a standard computation. A restriction of the degrees of freedom for the form finding compu-

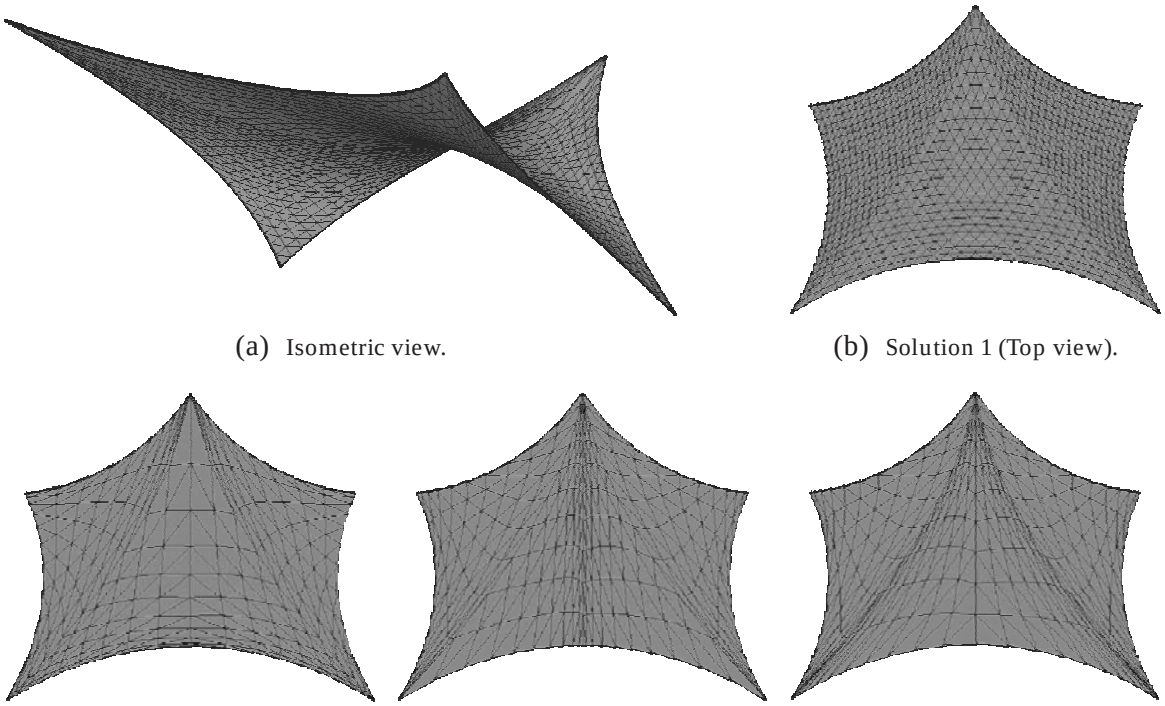

(a) Isometric view. (b) Solution 1 (Top view).

(c) Solution 2 (Top view). (d) Solution 3 (Top view). (e) Solution 4 (Top view).

Figure 2.6: Multiple valid solutions for a form finding problem.

tation to those perpendicular to the membrane surface would enable a simple solution, but is not applicable [Wüc07], since e.g. for flexible cable support, the possibility of tangential movements is necessary for a realistic physical modeling.

Several methods have been developed to overcome the difficulties of the inverse form finding problem. In the following, the basic ideas of the most common methods are presented:

◇ **Modified linearization of the problem**

For the Newton-Raphson type iterative solution of the discretized problem, a not consistently derived, non-singular stiffness matrix is used to approximate the problem [HP72], [AAB74].

◇ **Dynamic Relaxation**

Applying dynamic relaxation, the steady-state form finding problem is transferred into a dynamic problem by adding inertia and damping effects to the system. Thereby, the initially ill-posed problem becomes well-posed. The process of form finding is modeled as decay of an oscillation. The quiescent state serves as resulting geometry of the form finding computation [Bar75], [Bar99].

◇ **Homotopy methods**

General mathematical methods to approach a solution of a singular problem are methods of numerical continuation , also called homotopy methods [Ble97]. A homotopy is a continuous transformation of one function into another. The basic idea to use homotopy in form finding is to modify the originally singular problem by a related well defined one, which fades out as the solution is approached. As an example, a singular problem $f(x) = 0$ is modified by a non-singular problem $g(x) = 0$ to the homotopy $h(x) = 0$ with the homotopy factor $\lambda \in [0;1]$:

$$h(x) = \lambda f(x) + (1-\lambda)g(x) = 0 \tag{2.98}$$

The solution of $h(x) = 0$ approaches the solution of $f(x) = 0$ for λ approaching 1. The method is more successful as the function $g(x) = 0$ is closer to the original function $f(x) = 0$. Applied to the problem of form finding, the original singular function is the formulation of virtual work in the current configuration: $\delta W_\sigma = 0$. The related non-singular function is the formulation of virtual work in the reference configuration with prescribed PK2 stress: $\delta W_S = 0$.

$$\begin{aligned} \delta W_\lambda &= \lambda \delta W_\sigma + (1-\lambda)\delta W_S \\ &= \lambda h \int_A det\mathbf{F}\,(\boldsymbol{\sigma}\cdot\mathbf{F}^{-T}) : \delta\mathbf{F}\,dA + (1-\lambda)h\int_A (\mathbf{F}\cdot\mathbf{S}) : \delta\mathbf{F}\,dA = 0 \end{aligned} \tag{2.99}$$

The stabilizing effect of δW_S is due to the constant and known reference configuration, for which the PK2 stress is prescribed. By increasing λ form 0 to 1 until the solution fails, the geometry derived by the modified problem can be taken as an approximate solution of the original problem. The closer the homotopy factor λ is to 1, the closer the solution of the modified problem is to the solution of the original problem.

Another important property of eq. 2.99 is that the closer the reference configuration is to the current configuration, the better the stabilization term δW_S describes the original problem. This property is used in the Updated Reference Strategy.

– **Updated Reference Strategy (URS)**

The Updated Reference Strategy was developed by Bletzinger [Ble98], [BR99] and uses homotopy introduced above in an iterative manner. The solution of the modified problem (eq. 2.99) is used as reference configuration for the next iteration step. For each iteration step, the desired Cauchy stress σ and second Piola-Kirchhoff stress $\mathbf{S}$ are newly prescribed. The update of the reference configuration by the solution of the modified problem gave name to the Updated Reference Strategy.

With each iteration step, the difference between reference and current configuration decreases and the stabilization term δW_S more accurately describes the original problem. Convergence is reached, if the difference between reference and the current configuration is smaller than a certain threshold. For this solution, $\sigma = \mathbf{S}$ and the solution of the modified problem is identical to the solution of the original problem.

The convergence is independent of the value of the homotopy factor λ, as long as λ is small enough to enable the solution of the modified problem. For a small homotopy factor, the solution procedure is more robust but needs more iterations. For a larger choice of λ, less iteration steps are needed, as long as the solution of the modified problem is possible. In order to increase the performance of the form finding procedure, λ can be increased during the computation.

– **Force Density Method**

Initially, the Force Density Method was developed for the design of cable net constructions for the Olympic Stadium in Munich, Germany [GMSS00]. Meanwhile it has been extended for the application of membrane structures [MM98]. The singular original problem is modified by assuming a constant force density. With this modification, the problem is well-posed and can be solved. In an iterative manner, the solution is used as a new reference configuration [Lin99b], [Lin99a].

The force density can be interpreted as a constant PK2 stress. Accordingly, the Force Density Method is a special form of the URS for $\lambda = 0$. Only the stabilization term $\delta W_S = 0$ is solved as the modified problem. Therefore, the force density method appears to be a consistent part of the more general URS.

2.4 Example: ARIES Mobile Canopy Shelter

In the following, the structural model of the mobile canopy structure ARIES, introduced in section 1.1, shall be created. The aim is to create a structural model that can be used in further analysis with respect to wind loadings. The membrane of the ARIES structure is prestressed, which imposes prestress on the hole structure. Therefore, the setup of the structural model is not trivial and has to incorporate form finding and non-linear analysis.

2.4.1 Initial Considerations

The canopy structure gains its stiffness from the anticlastic prestressed membrane, which is supported by two cantilevers. The prestress is induced into the membrane and the cantilevers by cables at the lower and upper edges of the membrane and the vertical tie-down cable attached to the membrane. The placement of the vertical tie-down cable causes the cone like shape at the front of the membrane. The cantilever beams consist of sections of aluminum trusses and are supported by a pivoting connection at the rear of the grandstand. The cantilevers are interconnected by tubular aluminum purlins. [BG05]

Large displacements of the membrane and the cantilever beams are to be expected. Therefore, the numerical model of ARIES has to take into account non-linear kinematics.

This necessitates a geometrically non-linear analysis. As only small to moderate strains and stresses are expected, a linear elastic material law is applied.

Inherent to geometrically non-linear structural analysis is the load-path dependency of the solution: for multiple load states, the structural deformation and stress state depend on the order in which the load states are applied. Thus, a load superposition is not sufficient for the consideration of multiple load cases. The application of prestress by tensing the respective cables, can be interpreted as an initial load case "prestress". The aim is to find a prestressed shape for the membrane with a uniform stress distribution. This is achieved by a form finding computation.

The setup of an exact prestressed structural model of the ARIES prototype requires detailed information about geometry and stress states. From literature by Gengnagel et al. [Gen05, Gen04],[BG05], and [DB04], the shape of the structure and the dimensions of parts of the structure are known. Detailed data about the initial stress state of the prestressed structural members, in general, and the membrane, in particular, is limited. Therefore, within this work, the ARIES structural model cannot represent the actual ARIES prototype exactly. However, the shape of the membrane resembles the prototype closely, so that later comparisons with results from wind tunnel experiments for this particular membrane shape are possible.

2.4.2 Form Finding Computation

The geometry and topology of the cantilever structures is taken from the original ARIES prototype structure. The lattice structures are modeled by truss elements only. Details can be seen in fig. 2.7, which shows the structural model without the membrane and the edge cables.

During the form finding computations for the membrane and edge cables, the cantilever beams are modeled as flexible and are subject to geometrically non-linear analysis. This is an important feature, as by prestressing the membrane in the form finding procedure, the supporting cantilever beams are stressed as well. The prestress of the cantilever beams has to be included in the model to enable a state of force equilibrium in the initial state for further computations. Furthermore, as the cantilever beams change their geometry due to the prestress-loading from the membrane, the shape of the structure highly depends on the prestress state of the cantilever beams.

For the membrane, PVC type I material with a thickness of 1 mm and a tensile yield strength of 60 kN / m, both in warp and weft direction is used. According to DIN-EN-13782 [Nor05b], the permanent prestress of the membrane has to be limited to 5% of the yield stress. For the PVC type I fabric, this leads to a maximum prestress of 3kN / m.

For form finding computations, the URS algorithm is used. The homotopy factor varies linearly for iteration step 1 to 4 between 0.6 and 0.9. For further iteration steps, the homotopy factor equals 0.9 to ensure quicker convergence. As the prestress distribution in the membrane of the ARIES structure is unknown, an isotropic prestress of 2 kN / m is assumed, which is a realistic choice. The prestress of the cables at the membrane edge between the

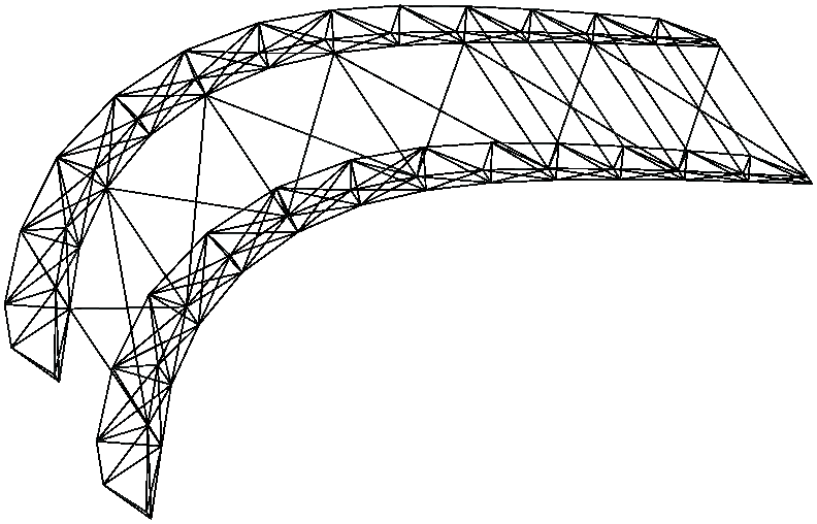

Figure 2.7: Non-prestresses cantilever structure without membrane.

two lattice beams is adjusted to resemble the geometry of the prototype closely. Best approximation was found for a prestress of 3.8 kN in both cables. Fig. 2.8 presents the initial geometry for the form finding procedure, intermediate solution steps, and the converged geometry for the prescribed prestress of 2 kN / m.

A significant difference compared to the prototype structure can be found in the tie-down force of the vertical cable. While in the prototype, a tensile force of 5.0 kN is assumed, by form finding, a tensile force of only 1.0 kN can be considered. This is due to the special character of the form finding computation, which does not take into account any material law (see section 2.3.2.1). In case the prescribed force in the vertical cable is too big to reach equilibrium with the membrane stresses, form finding results in a boundless stretching of the membrane.

To illustrate the process of form finding with respect to the membrane prestress, fig. 2.9 presents the von Mises stress distribution in the membrane after the first and the final form finding step. In the final step, the URS-based form finding results in the uniform stress distribution of 2 kN / m in the membrane and the correct shape of the front and back edge cables.

The convergence of the shape of the structure in the form finding computation requires a considerably large number of form finding steps. The overall shape of the membrane seems to converge quickly, but persistent local changes in the shape cause an overall slow convergence. 50 form finding steps are necessary to achieve sufficient convergence of the geometry for further computations. To illustrate the convergence of the shape during form finding, in fig. 2.10 displacement and von Mises stress of node **A** are plotted over the number of form finding steps.

As presented above, the force in the vertical cable can only be considered as 1.0 kN in the form finding computation. However, the magnitude of the tie-down force proved to be an important variable for the load carrying behavior of the structure. To achieve a more

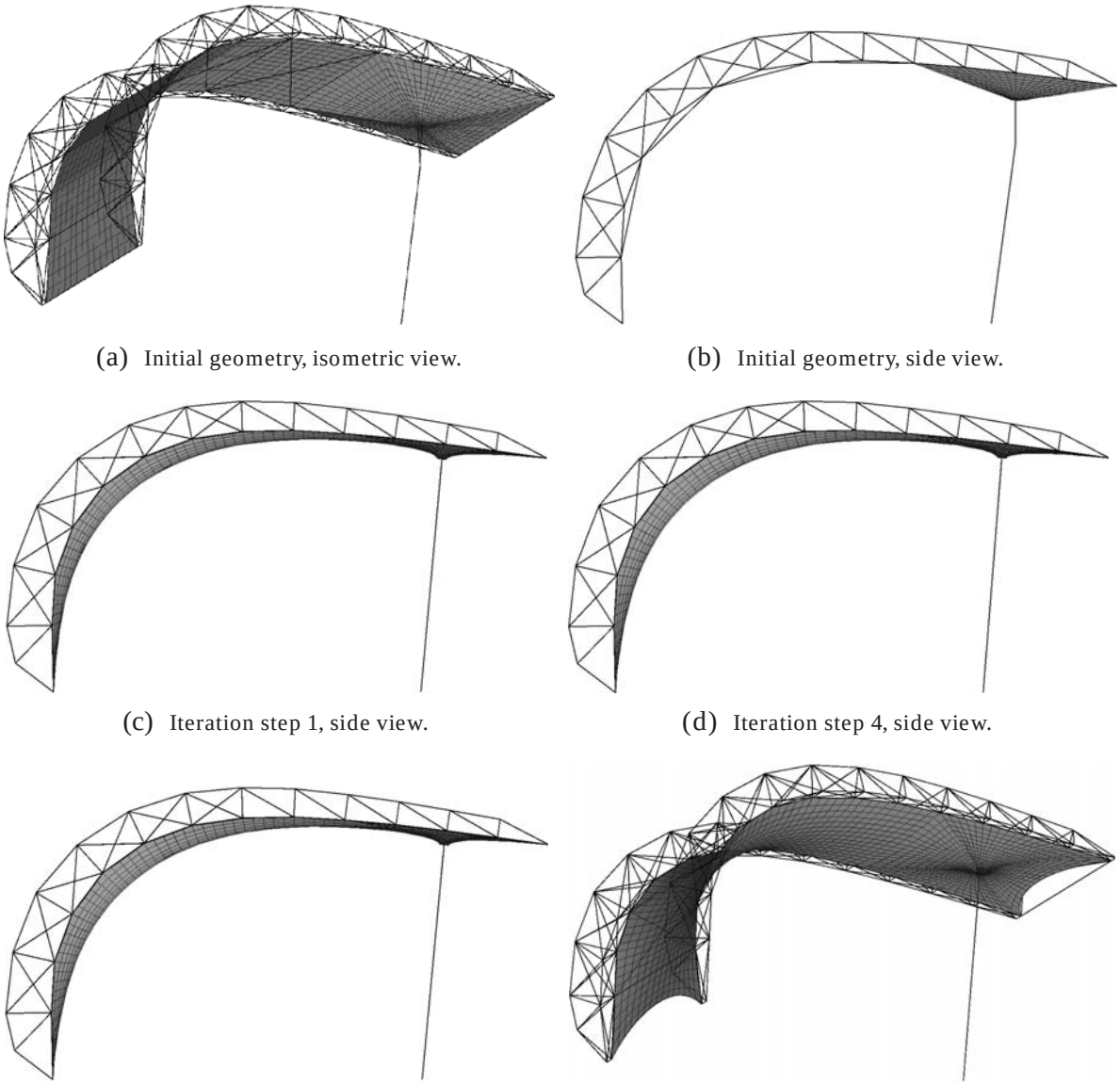

(a) Initial geometry, isometric view.

(b) Initial geometry, side view.

(c) Iteration step 1, side view.

(d) Iteration step 4, side view.

(e) Iteration step 50, side view.

(f) Iteration step 50, isometric view.

Figure 2.8: ARIES form finding

realistic load carrying behavior, the structural model is further prestressed by increasing the tie-down force in the vertical restraint to 4.0 kN in the non-linear structural analysis. Fig. 2.11 presents the von Mises stress distribution for the tie-down force of 4.0 kN. For this prestress state, the maximum stress at the membrane cone exceeds the recommended maximum prestress of 3 kN / m. Therefore, the material has to be reinforced at regions with high stress, which is commonly achieved by the addition of another layer of membrane material. For the following computations, it is assumed that the maximum membrane stress is unproblematic due to this design feature.

With a combination of classical form finding computation and non-linear steady-state structural analysis computation a realistic, prestressed structural model is derived. This model, presented in fig. 2.12, will be used for further analysis.

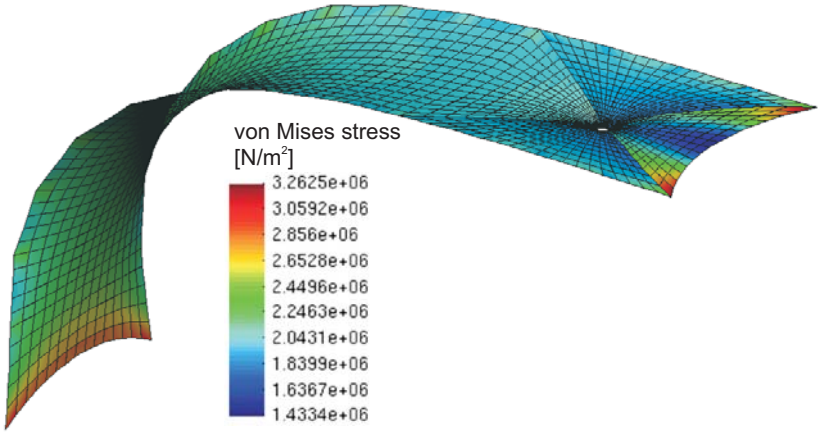

(a) von Mises stress distribution after form finding step 1.

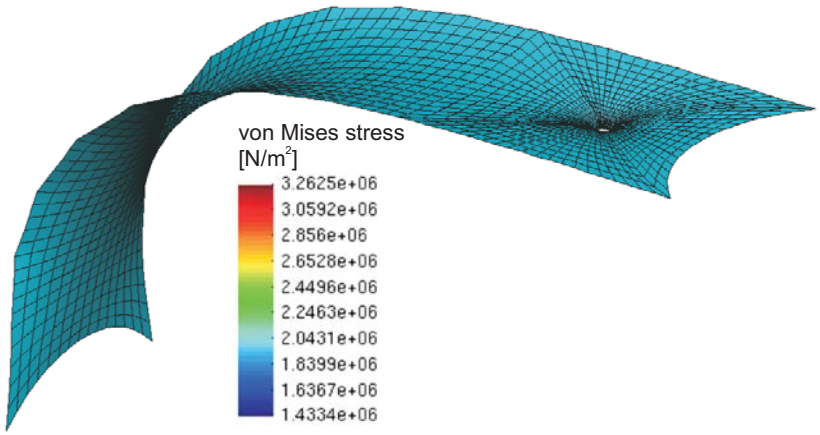

(b) von Mises stress distribution after form finding step 50.

Figure 2.9: ARIES form finding von Mises stress distribution in the membrane

2.5 Summary

From the structural analysis point of view, the missing bending stiffness of membranes demands for additional considerations for the usage in civil engineering. Large deformations are to be expected, which necessitates the consideration of geometrically non-linear effects. Membrane structures react with large deformations to loadings acting perpendicular to their surface. In order to limit the deformations and increase the stiffness of the membrane, it is usually subject to prestress. Due to the typically geometrically non-linear behavior of membrane structures, a load case superposition is not possible. Therefore, the prestress has to be treated as an initial load case. This is done in the form finding computation. The results of the form finding computation are shape and stress state of the prestressed membrane structure, which are used as initial configuration for further analysis.

This chapter presented the fundamentals of numerical structural analysis by the Finite Element Method for cases of small strains and large deformations. Special emphasis lies on the analysis of membrane structures, which includes form finding computations.

With the example of the mobile canopy structure, form finding computation is per-

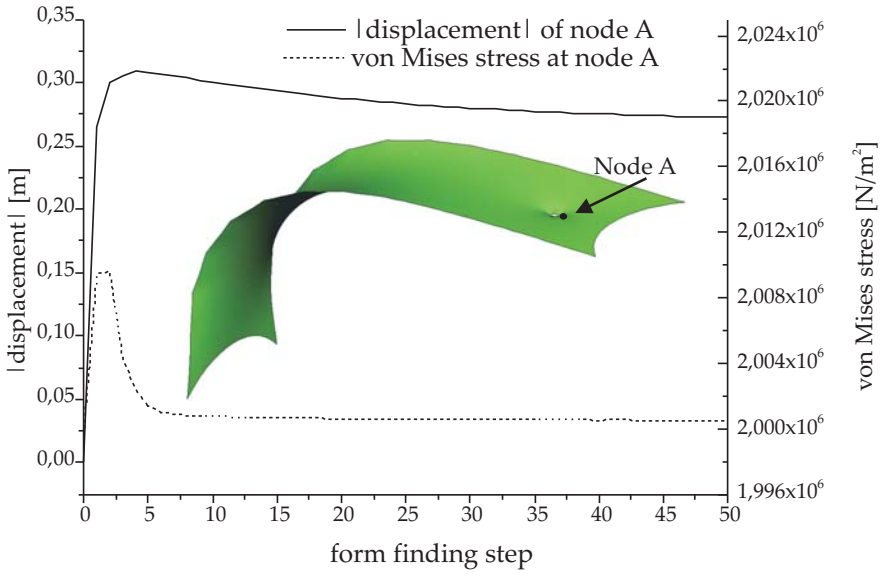

Figure 2.10: Plots of von Mises stress and deformation at node A.

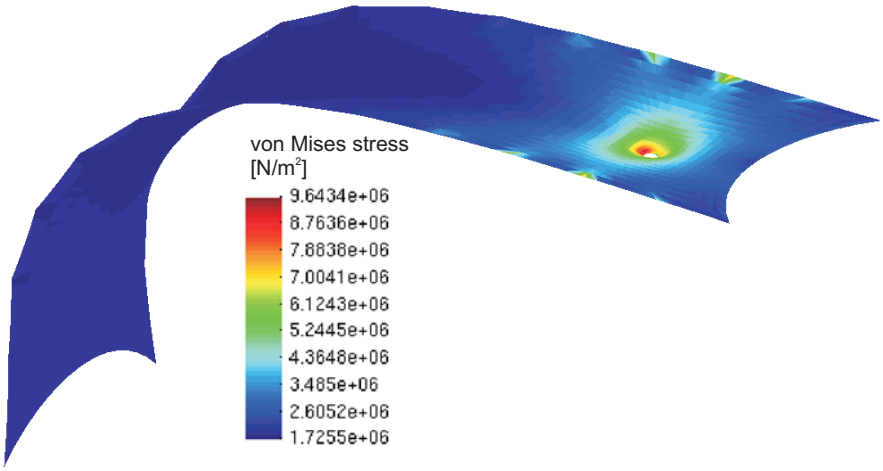

Figure 2.11: von Mises stress distribution in the membrane for a tie-down force of 4.0 kN.

formed and enhanced by an additional geometrically non-linear computation. The resulting structural model is the basis for further analysis of the structure towards wind loadings.

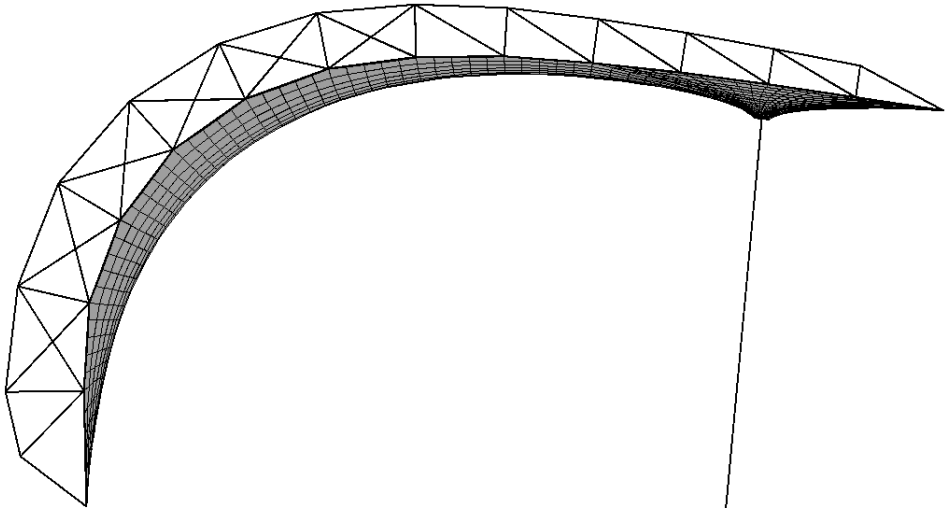

(a) Final prestressed geometry, side view.

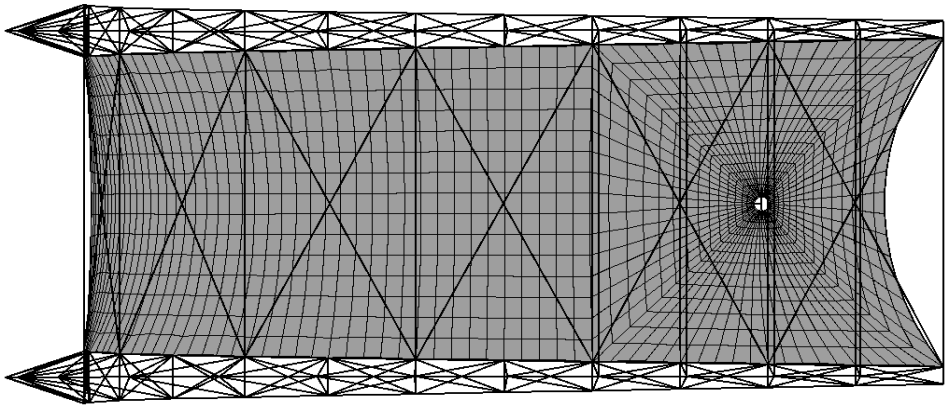

(b) Final prestressed geometry, top view.

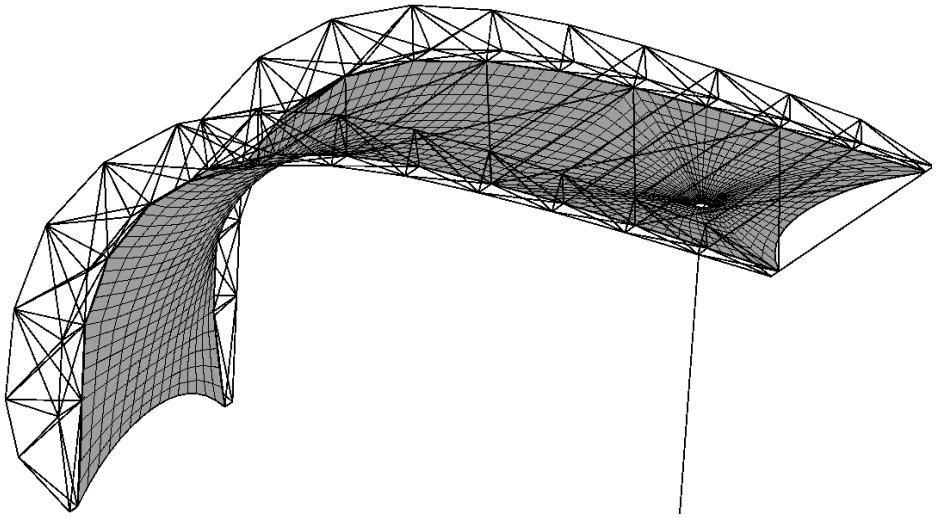

(c) Final prestressed geometry, isometric view.

Figure 2.12: Final prestressed geometry of ARIES structure for further computations.

Chapter 3

Modeling of Wind Loads on Membrane Structures

The prediction of wind effects on membrane structures is difficult due to their complex geometry and load carrying behavior. In the first part of this chapter, methods used to assess wind loading on membrane structures are reviewed in brief.

Within the current work, numerical fluid simulations are used to analyze the air flow around a membrane structure and to calculate loads resulting from this air flow. Therefore, it is necessary to discuss the fundamentals of fluid mechanics with a special focus on the assessment of turbulence modeling, which is done in the second section.

Based on these fundamentals, the Finite Volume Method (FVM) is introduced, which enables a numerical simulation of the fluid flow. To include the possibility of deformations due to wind loadings, enhancements for the modeling with moving boundary conditions are necessary.

Subsequently, the application of numerical fluid simulations in the scope of wind engineering is broadly discussed. Details about the application of the finite volume method with respect to relevant physics and boundary conditions for the simulation of air flow around a membrane are given.

Finally, the geometry of the ARIES membrane structure, derived in section 2.4 is used in a rigid, CFD based numerical model, to assess the mean wind load by the computation of c_p values.

3.1 Wind Loads on Membrane Structures

Wind, especially in the form of an uplift, is regularly the critical load case for membrane and cable stresses in light-weight membrane structures [BD04].

Quasi-static approach

Assuming that no dynamic wind induced effects have to be considered for a membrane structure and that the construction undergoes only deformations, which are small enough to be neglected, wind load can be considered as a static load case. With this assumption,

wind loads can be derived according to building codes, such as EN1991-1-4 [CEN05]. Here, this approach is briefly described at the example of mean wind loads. For computing design loads, in case, additional consideration about the peak wind loads can be necessary.

Applying EN1991-1-4, the mean wind load at a certain point on the surface of a structure is computed as the product of a mean dynamic pressure at a specific point, a dimensionless pressure coefficient, and further coefficients. The distribution of the dimensionless pressure coefficients c_p depends on the geometry of the building and the angle of approach of the wind towards the building. The wind environment around the structure is represented by the mean dynamic pressure value and the further coefficients, which characterize the influences of wind turbulence, topology, terrain roughness, exposure, etc.

c_p values are dimensionless characteristic pressure coefficients, which describe the ratio of the characteristic pressure value p at the point of interest to the dynamic pressure q_{ref} at a specific reference height z_{ref}:

$$p = c_p \, q_{ref} \quad \text{with} \quad q_{ref} = \frac{1}{2} \, \rho \, \overline{u}_{ref}^2 \tag{3.1}$$

$\overline{u}_{ref}$ is the mean velocity at height z_{ref} and ρ is the density of air (≈ 1.2 kg/m^3). For the roof, often the ridge height is taken as reference height z_{ref}. c_p values are usually based on the results of wind tunnel tests using small scale models with similar characteristic shapes [Coo85].

In EN1991-1-4, pressure coefficients are given for surface areas of $1m^2$ or smaller ($c_{pe,1}$) and for surface areas of $10m^2$ or larger ($c_{pe,10}$). For surface areas between $1m^2$ and $10m^2$, values can be interpolated. $c_{pe,10}$ is smaller than $c_{pe,1}$ due to the assumption that a maximum pressure will not appear at each point of a larger surface at the same time. $c_{pe,1}$ is used for cladding or roofing, where the occurring local wind pressure on a small area has to be considered. $c_{pe,10}$ is applied in the calculation of wind loads on larger areas or the whole building.

For the representation of pressure difference between the inside and the outside of a building, c_p values have to be considered both due to internal and external wind pressure. Depending on the building's face and the ratio of area of the surface opening to the total surface area, the internal pressure coefficient c_{pi} can be determined as a fraction of the external pressure coefficient c_{pe} [HK07]. The total loading on the roof and walls of a building has to be calculated by adding the forces from both external and internal wind pressure.

For simply shaped structures, c_p values can be found in building codes and literature, such as [Zur69], [FM04], or [Coo90].

For complex and irregular forms, which differ from the shapes for which data is provided in the literature, wind tunnel tests need to be used to derive c_p values. This is the case for membrane structures, which can have free-form shapes resulting from the requirement of equilibrium of inner forces, as explained in section 2.1. With respect to external and internal c_p-values, it has to be distinguished whether a membrane structure has open or closed sides.

Dynamic effects

Membrane structures have a considerably low natural frequency of typically 0.5 to 1.5 Hz. They are commonly considered as lightly damped structures in terms of their structural damping ratio. This damping results from the crimp interchange of the yarns. An additional damping effect for enclosed and open-sided membrane structures is provided by the air around the membrane. The mass of the air that is moved by the deflection of the membrane is often much larger than the mass of the membrane itself. Due to the inertia of this air, membrane structures show a highly damped behavior in physical experiments.

Generally, membrane structures are considered insusceptible to effects of aerodynamic instability [BD04]. A local flutter behavior can occur at the membrane's edges, where a small change in the wind flow direction relative to the membrane's surface results in a large change of surface pressure. This situation is likely to occur at front edges, where the membrane is more or less parallel to the wind flow. For membrane structures with considerably little prestress and / or small curvature, small traveling waves have been observed. This effect is visible on sails, flags etc. It occurs especially in pneumatic structures, as they often have low Gaussian curvature and little prestress due to a small pressure difference between their inside and outside.

As with most structures and materials, movement and oscillations reduce the lifespan of the material due to fatigue effects. As membrane structures are likely to undergo large deflections, dynamic effects can limit the usability of the structure. Irritating or disturbing visual and acoustic effects can occur.

An additional aspect in safety considerations of a membrane structure in extremely high wind speed conditions is the presence of flying debris. Because of its small thickness and its vulnerability to punctuation and tear, membrane structures can be destroyed by flying objects. An overview and assessment of the threat from flying debris is provided in [Hol01]

Experimental approaches

Typically, wind tunnel experiments are necessary to determine the wind load on membrane structures, due to their individual geometry. The majority of wind tunnel tests for membrane structures are carried out on rigid models, that do not take into account changes in the wind surface pressure, which occur for a deflection of the membrane surface. For experimental wind tunnel data based on rigid structural models, the structural response of the membrane can be computed by numerical structural simulations. Still, this approach neglects the influence that the deformed membrane can have on the wind flow around the structure. Therefore, rigid model tests are limited in the prediction of wind load for deflection sensitive membrane surfaces, but often the only option. Wind tunnel testings using rigid structural models of membrane structures can be found, among many other works, in [RW07] and [BD04]. Extensive investigations have been made for load estimations on stadium roofs: [Nat00], [BBM$^+$06], [BBF07]

For special purposes, more complex aeroelastic replica models are used. In case of membrane structures, replica models are very difficult to build and do not always provide consistent answers [BD04]. The limited accuracy of the results is caused by the strict requirements for similarity in the properties of the small scale model and the full scale structure. In order

to correctly represent aeroelastic effects, this similarity has to hold with respect to flow conditions and dynamic structural properties. An overview of the requirements of similarity for the aeroelastic simulation of membrane structures in civil engineering is provided in [SL85]. Examples of aeroelastic models for membrane structures in wind tunnel experiments can be found in [Kaz98] and [Kai03].

Numerical approaches

A few attempts have been made to apply numerical methods of Computational Fluid Dynamics to the analysis of membrane structures. Examples are the works of Saberi-Haghighi [SH97], and Hübner [Hüb03]. Especially the work of Glück and Halfmann shall be mentioned [GBD$^+$03, GBD$^+$01, Glü02, Hal02], as they analyze membrane-wind-interaction by numerically fully coupled fluid-structure interaction simulation, however, with simplified boundary conditions for the fluid analysis.

Within the current work, numerical fluid simulations are used to analyze the air flow around a membrane structure and to calculate loads due to this air flow. In chapt. 4, the modeling of the air flow around the structure is combined with the structural modeling to account for the membrane-wind interaction. In the following, the necessary fundamentals of fluid mechanics are presented. Subsequently, a special focus is put on the appropriate modeling of the wind flow conditions.

3.2 Fundamentals of Fluid Mechanics

3.2.1 Basic Equations

Fluid mechanic is based on three fundamental principles [And08]:

- ◇ Conservation of mass
- ◇ Newton's second law
- ◇ Conservation of energy

For the derivation of the basic equations, here an isothermally and chemically inert flow is assumed. Therefore, the principle of conservation of energy is not relevant.

Conservation laws can be derived based on a given material point. This Lagrangian description was applied throughout chapter 2. In fluid mechanics, the Eulerian description is widely used. In the Eulerian description, conservation laws are derived based on a certain spacial region, called the control volume, with fixed position and dimension within the fluid domain Ω_F.

In the following, a Newtonian fluid shall be assumed. For Newtonian fluids, the shear stress in the fluid is proportional to the velocity gradient. For a Newtonian fluid, the stress tensor σ acting on a control volume is:

$$\sigma = -\left(p + \frac{2}{3}\mu\nabla\mathbf{u}\right)\mathbf{I} + 2\mu\mathbf{D} \tag{3.2}$$

with μ as the dynamic viscosity, $\mathbf{I}$ as unit tensor, p as thermodynamic pressure and $\mathbf{D}$ as 'rate-of-velocity' tensor:

$$\mathbf{D} = \frac{1}{2}\left[\nabla\mathbf{u} + (\nabla\mathbf{u})^T\right] \tag{3.3}$$

and $\mathbf{u}$ as velocity vector.

The Reynolds transport theorem states that the rate of change of the amount of any scalar, vector, or tensor function $\mathbf{F}(x,t)$ inside a control volume **(CV)** with volume V is equal to the rate of change of the amount of $\mathbf{F}(\mathbf{x},t)$ inside the CV plus the net rate of outwards flux of $\mathbf{F}(\mathbf{x},t)$ due to the mass transport with velocity $\mathbf{u}$ through the surface S enclosing the CV:

$$\frac{D}{Dt}\int_V \mathbf{F}(\mathbf{x},t)\,dV = \int_V \frac{\partial}{\partial t}\mathbf{F}(\mathbf{x},t)\,dV + \int_S \mathbf{F}(\mathbf{x},t)\,(\mathbf{n}\cdot\mathbf{u})\,dS \tag{3.4}$$

with $\mathbf{u}$ as the velocity vector and $\mathbf{n}$ as the unit outward normal vector of surface S.

Conservation of mass

The principle of conservation of mass states that the mass m within a CV shall be constant with time:

$$\frac{Dm}{Dt} = \frac{D}{Dt}\int_V \rho(\mathbf{x},t)\,dV = 0 \tag{3.5}$$

Applying the Reynolds transport theorem to the density field $\rho(\mathbf{x},t)$, eq. 3.5 can be transformed to:

$$\frac{\partial}{\partial t}\int_V \rho dV + \int_S \rho\,(\mathbf{n}\cdot\mathbf{u})\,dS = 0 \tag{3.6}$$

Using gauss divergence theorem [BSMM00], an integral form of eq. 3.6 is derived with ∇ as the spacial gradient operator:

$$\int_V \frac{\partial\rho}{\partial t}dV + \int_V \nabla\cdot(\rho\mathbf{u})dV = 0 \tag{3.7}$$

As eq. 3.7 also holds for infinitesimally small CVs, its differential form can be derived:

$$\frac{\partial\rho}{\partial t} + \nabla\cdot(\rho\mathbf{u}) = 0 \tag{3.8}$$

Conservation of momentum

According to Newton's second law of motion, momentum $m\mathbf{u}$ can be changed by the action of a force vector $\mathbf{f}$:

$$\frac{d(m\mathbf{u})}{dt} = \mathbf{f} \tag{3.9}$$

The change of momentum in the control volume **(CV)** can be described by the Reynolds transport theorem. The quantity subject to transportation $\mathbf{F}(\mathbf{x},t)$ shall now be the momentum per unit mass $\rho\mathbf{u}$. Accordingly, the change of momentum within the CV is:

$$\frac{D}{Dt}\int_V (\rho\mathbf{u})(\mathbf{x},t)\,dV = \frac{\partial}{\partial t}\int_V (\rho\mathbf{u})dV + \int_S (\rho\mathbf{u})\,(\mathbf{n}\cdot\mathbf{u})\,dS = \int_S \sigma\cdot\mathbf{n}\,dS + \int_V \rho\mathbf{b}\,dV \tag{3.10}$$

The right side of eq. 3.10 describes the sum of forces acting on the surface of the CV and the body force **b** per unit mass. Using Gauss divergence theorem, eq. 3.10 can be transformed to:

$$\frac{\partial}{\partial t}\int_V (\rho\mathbf{u})dV + \int_V \nabla\cdot((\rho\mathbf{u})\otimes\mathbf{u})\,dV = \int_V \nabla\cdot\sigma\,dV + \int_V \rho\mathbf{b}\,dV \tag{3.11}$$

Since eq. 3.11 has to be fulfilled for every control volume V, its differential form is:

$$\frac{\partial(\rho\mathbf{u})}{\partial t} + \nabla\cdot((\rho\mathbf{u})\otimes\mathbf{u}) = \nabla\cdot\sigma + \rho\mathbf{b} \tag{3.12}$$

Historically, the equations describing the conservation of momentum in viscous flow were named Navier-Stokes equations after the French engineer and physicist Claude-Louis Navier (*1785, †1836) and the British mathematician and physicist George Gabriel Stokes (*1819, †1903). In modern literature, this terminology has been expanded to include the entire system of equations describing viscous fluid flow. This includes the equations of conservation of momentum, mass and, if applicable, the equations of conservation of energy. The later terminology is used within this work.

The Navier-Stokes equations form a system of non-linear mixed hyperbolic-parabolic partial differential equations. A classification of the partial differential equations can be found in [BSMM00]. In order to solve this initial boundary value problem, initial and boundary conditions are necessary. These are introduced in the following.

Initial and boundary conditions

The vector field of the velocity $\mathbf{u}_0$ at time $t = t_0$ is prescribed on the fluid domain Ω_F. This initial velocity field has to satisfy the principle of conservation of mass.

$$\mathbf{u} = \mathbf{u}_0 \quad \text{in } \Omega_F \text{ for } t = t_0 \qquad \text{with} \quad \nabla\cdot\mathbf{u}_0 = 0 \tag{3.13}$$

As in solid mechanics, the boundaries of the fluid domain Γ are separated into Dirichlet Γ_D and Neumann Γ_N boundary conditions with $\Gamma = \Gamma_N \cup \Gamma_D$ and $\Gamma_N \cap \Gamma_D = 0$. For Neumann boundary conditions the normal component of the stress $\mathbf{t} = \mathbf{n}\cdot\sigma$ on the boundary is prescribed:

$$\mathbf{t} = \mathbf{n}\cdot\sigma = \hat{\mathbf{t}} \quad \text{on } \Gamma_N \quad \forall\, t \in [t_0, T] \tag{3.14}$$

while for Dirichlet boundary conditions a certain velocity $\hat{\mathbf{u}}$ is prescribed:

$$\mathbf{u} = \hat{\mathbf{u}} \quad \text{on } \Gamma_D \quad \forall\, t \in [t_0, T] \tag{3.15}$$

The assumed incompressibility of the flow together with the principle of conservation of mass results in the requirement that for all moments in time the volume entering the domain Ω_F at some region has to flow out of the domain at another region:

$$\int_{\Gamma_D} \mathbf{n}\cdot\hat{\mathbf{u}}\,d\Gamma_D = 0 \quad \forall\, t \in [t_0, T] \tag{3.16}$$

In fluid mechanics, the most common boundary conditions are:

◇ **no-slip boundary condition**

At a solid wall, the velocity of a fluid particle has to be identical to the velocity of the wall $\mathbf{u}_w$. In the usual case of non-moving walls $\mathbf{u}_w = 0$. For $\mathbf{u}_w = 0$ at the wall and $\mathbf{u} \neq 0$ in some distance from the wall, a velocity gradient normal to the wall develops. This effect is known as the law of the wall (see section 3.2.5) and is an ongoing challenge to modeling.

$$\mathbf{u} = \mathbf{u}_w \quad \text{on } \Gamma_D \quad \forall\, t \in [t_0, T] \tag{3.17}$$

◇ **free-slip boundary condition**

For a free-slip boundary condition, only the velocity component normal to the boundary surface is prescribed:

$$\mathbf{n} \cdot \mathbf{u} = \mathbf{n} \cdot \mathbf{u}_w \quad \text{on } \Gamma_D \quad \forall\, t \in [t_0, T] \tag{3.18}$$

◇ **inflow boundary condition**

Inflow boundary conditions are Dirichlet boundary conditions with a prescribed velocity. Usually, the velocity distribution over the boundary surface is specified. Additionally, in case of RANS simulations, the distributions of the turbulent quantities have to be prescribed.

◇ **outflow boundary condition**

The outflow conditions for an arbitrary fluid flow are difficult to predict and also difficult to prescribe. Mostly, simplified assumptions are used. Among others, the "zero gradient" condition [Glü02], average pressure boundary condition and the 'do nothing' boundary condition [Gra03] shall be mentioned here.

◇ **periodic boundary condition**

Assuming an infinite number of identical flow conditions subsequently located one after the other in the periodic direction, the computational effort can be reduced by periodic boundary conditions. At periodic boundary conditions, all variables are assumed to be identical: for example in case of two periodic boundaries at the front and the end of the domain, the flow conditions at the end of the domain are prescribed at the front of the domain again.

◇ **symmetry boundary condition**

In the case of a symmetric flow simulation, the computational domain can be halved and thus the computational effort can be halved as well. Halving a system can only be performed for laminar and RANS simulations. At symmetry boundary conditions, the velocity component normal to the surface, and for all quantities Φ, the gradient normal to the boundary surface, are assumed to be zero.

$$\mathbf{u} \cdot \mathbf{n} = \mathbf{0} \qquad \forall\, t \in [t_0, T] \qquad \text{and} \tag{3.19}$$

$$\nabla\Phi \cdot \mathbf{n} = \mathbf{0} \qquad \forall\, t \in [t_0, T] \tag{3.20}$$

Incompressibility condition

A fluid flow, in which the density of the fluid is constant is called incompressible. This incompressibility is not a characteristic of the fluid, but a characteristic of the flow. Liquid flows are usually treated as incompressible, while gas flows show incompressible behavior under certain circumstances [FP99]. As a rule of thumb, gas flows with a Mach number Ma smaller than 0.3 can be treated as incompressible. The Mach number relates the characteristic velocity u of a flow to the velocity of sound c:

$$Ma = \frac{u}{c} \tag{3.21}$$

Assuming a constant density ρ, the principle of mass conservation in differential form (eq. 3.8) can be simplified to:

$$\nabla \cdot \mathbf{u} = 0 \tag{3.22}$$

Accordingly, the principle of conservation of momentum (eq. 3.12) can be expressed as:

$$\frac{\partial \mathbf{u}}{\partial t} + \nabla \cdot (\mathbf{u} \otimes \mathbf{u}) = \frac{1}{\rho} \nabla \cdot \sigma + \mathbf{b} \tag{3.23}$$

Using eq. 3.22, the constitutive equation eq. 3.2 can be simplified to:

$$\sigma = -p\mathbf{I} + 2\mu\mathbf{D} \tag{3.24}$$

Because the 'rate-of-velocity' tensor $\mathbf{D}$ is a traceless tensor, the pressure p constitutes the mean normal compressive stress in the stress tensor σ. Without boundary conditions prescribing a pressure level, the pressure can only be determined up to a constant [FP99]. In the scope of this work, it is assumed that body forces $\mathbf{b}$ can be neglected.

The index notation is more commonly used in fluid mechanics. Therefore, it will be applied in the following. Neglecting the body forces, the Navier-Stokes equations for incompressible flows (eq. 3.22 and eq. 3.23 together with eq. 3.24) for each spacial direction $i = 1, 2, 3$ are in index notation:

$$\frac{\partial u_i}{\partial x_i} = 0 \tag{3.25}$$

$$\rho \left(\frac{\partial u_j}{\partial t} + u_i \frac{\partial u_j}{\partial x_i} \right) = -\frac{\partial p}{\partial x_j} - \frac{\partial \tau_{ij}^{mol}}{\partial x_i} \tag{3.26}$$

The left side of eq. 3.26 describes the change of momentum over time as the sum of local time dependent change of momentum and the convective transportation of momentum. This has to be in equilibrium with the right side of the equation, which consists of the sum of pressure forces and forces due to the diffusive momentum transport:

$$\tau_{ij}^{mol} = -\mu \left(\frac{\partial u_i}{\partial x_j} + \frac{\partial u_j}{\partial x_i} \right) \tag{3.27}$$

3.2.2 Turbulence

Observing fluid flow, two fundamentally different flow types can be identified. In case of a fluid flow with low velocity and high viscosity, a regular flow field can be observed for a certain stretch along the main flow direction. With increasing fluid velocity and / or decreasing viscosity, the degree of regularity decreases and the flow shows an increasingly chaotic behavior. In this unstable flow, the main velocity field is superimposed by random velocity fluctuations. Such chaotic flow is called turbulent flow. In the following, the main characteristics of turbulent flows are introduced, following the work of Wengle [Wen01].

The phenomenon of turbulence, common in everyday life, is still one of the most difficult problems in modern physics. Difficulties with understanding of turbulent flow are mainly due to two reasons:

◇ **Randomness of turbulence**

The velocity fluctuations seem to occur randomly on a macroscopic level. The flow is unstable and highly sensitive to perturbations. Statistical methods are usually used to quantify turbulent flows.

◇ **Involved scales of turbulence**

The phenomenon of turbulence incorporates an extensive range of scales. The largest scale L can be identified as a characteristic length of the flow condition. The kinetic energy of turbulent velocity fluctuations is introduced at the large scale. The turbulent velocity fluctuations lead to vortices, called eddies. As energy is dissipated in the turbulent flow, the large scale eddies decay into smaller size eddies by loosing energy. Thereby, an energy cascade is formed, the Richardson Energy Cascade. Along the energy cascade, eddies decay into smaller size eddies until finally a stable eddy motion is reached. At this level, the turbulent energy is transferred into thermal energy due to the viscosity of the fluid. This end of the energy cascade is characterized by the small scales of motion, which is known as the Kolmogorov length l_K.

In a turbulent flow, all scales of eddies between L and l_K exist. For a Reynolds number Re_L (based on the length of L), the ratio between large and small scale can be estimated as:

$$\frac{L}{l_K} \sim Re_L^{\frac{3}{4}} \tag{3.28}$$

For a $Re_L = 10^7$ the largest scale L is 177828 times larger than the smallest scale l_K. Corresponding to the minimal spatial length occurring in a turbulent flow, ratio between the largest characteristic time length T and the minimum time length t_K can be specified:

$$\frac{T}{t_K} \sim Re_L^{\frac{1}{2}} \tag{3.29}$$

In principle, the Navier-Stokes equations can be used to describe turbulent flows, as long as the phenomenon is within the limits of continuum mechanics. This holds even for smallest scale turbulence on the Kolmogorov length level. Therefore, all turbulent flow can be described using only the basic Navier-Stokes equations. This approach to use the basic

Navier-Stokes equations for numerical turbulent flow simulation is called Direct Numerical Simulation (DNS). However, for a complete description of turbulent flow, the resolution of all involved scales is necessary. For a three dimensional fluid domain as large as the largest scale eddies of size L and resolving the smallest length scale l_k (e.g. by the Finite Volume Method introduced in section 3.3.1) the number of degrees of freedom can be estimated to:

$$N_S = \left(\frac{L}{l_k}\right)^3 \sim \left(Re_L^{\frac{3}{4}}\right)^3 = Re_L^{\frac{9}{4}} \tag{3.30}$$

Accordingly, the time wise resolution has to be resolved as well, which leads to an estimation of $n_T = \frac{T}{t_k} \sim Re_L^{\frac{3}{4}}$ time steps to simulate one period corresponding to the characteristic time length T [1].

At the current level of computational power, it is not possible to use DNS for the description of turbulent flows with high Re numbers. DNS is mainly used in basic research and for the validation of alternative approaches for the modeling of turbulent flows. Due to the severe limitations to simulate flows of practical relevance with full resolution of turbulence, turbulence models have been suggested. The turbulence models introduce additional assumptions about the turbulent flow to omit the necessity to resolve all spatial and time scales. However, modeling the unresolved scales requires the use of experimental data and introduces additional uncertainties. In the following, the most common types of turbulence modeling are introduced.

3.2.3 RANS-based Turbulence Modeling - Time Averaging

In the Reynolds decomposition, a quantity of the turbulent flow $\Phi(\mathbf{x}, t)$ at a certain position $\mathbf{x}$ and at a certain time t is separated into a mean value $\overline{\Phi}(\mathbf{x}, t)$ and a fluctuating value $\Phi'(\mathbf{x}, t)$:

$$\Phi(\mathbf{x}, t) = \overline{\Phi}(\mathbf{x}, t) + \Phi'(\mathbf{x}, t) \tag{3.33}$$

with

$$\overline{\Phi}(\mathbf{x}, t) = \lim_{\Delta t \to \infty} \frac{1}{\Delta t} \int_{t_0}^{t_0+\Delta t} \Phi(\mathbf{x}, t)\, dt \tag{3.34}$$

$$\overline{\overline{\Phi}}(\mathbf{x}, t) = \overline{\Phi}(\mathbf{x}, t) \qquad \overline{\Phi'}(\mathbf{x}, t) = 0 \tag{3.35}$$

In the case of time-dependent fluid flow, time averaging has to be performed as an ensemble averaging:

$$\overline{\Phi}_T(\mathbf{x}, t) = \lim_{N \to \infty} \frac{1}{N} \sum_{n=1}^{N} \Phi(\mathbf{x}, t) \tag{3.36}$$

[1] In this estimation an optimum Courant number Co of 1 is assumed. The Courant number is defined as:

$$Co = \frac{u\, \Delta t}{\Delta x} \tag{3.31}$$

with Δt as time step length and Δx as characteristic spatial discretization. Accordingly, the number of time steps for full time resolution of one period of the characteristic time length T is:

$$n_T = \frac{T}{t_k} = \frac{L/u}{l_k/u} = \frac{L}{l_k} = Re^{\frac{3}{4}} \tag{3.32}$$

where N is the number of ensembles. N has to be sufficiently large to ensure the elimination of effects of the fluctuation on the mean value.

By inserting Reynolds averaging for velocity and pressure into the Navier-Stokes equations, the Reynolds-averaged Navier-Stokes (RANS) equations are derived.

$$\frac{\partial \overline{u}_i}{\partial x_i} = 0 \tag{3.37}$$

$$\rho\left(\frac{\partial \overline{u}_j}{\partial t} + \overline{u}_i\frac{\partial \overline{u}_j}{\partial x_i}\right) = -\frac{\partial \overline{p}}{\partial x_j} - \frac{\partial}{\partial x_i}\left[\underbrace{-\mu\left(\frac{\partial \overline{u}_i}{\partial x_j} + \frac{\partial \overline{u}_j}{\partial x_i}\right)}_{\tau_{ij}^{mol}} + \underbrace{\rho\overline{u_i' u_j'}}_{\tau_{ij}^{turb}}\right] \tag{3.38}$$

The viscous stress term τ_{ij}^{mol} describes the transfer of momentum at the molecular level. An additional term compared to the basic Navier-Stokes equation is the Reynolds stress tensor τ_{ij}^{turb}, which describes the momentum transfer due to the fluctuating velocity field. For a fully turbulent flow, $\tau_{ij}^{turb} >> \tau_{ij}^{mol}$ is assumed.

In the basic Navier-Stokes system of equations, three components of the momentum equation and the continuity equation are used to determine the four unknowns u_1, u_2, u_3, and p. Due to the Reynolds stress tensor, the RANS system of equations contains six additional variables, without additional equations. This dilemma is known as the closure problem of RANS. It can be explained by a loss of information necessary to fully describe the turbulent flow during the Reynolds averaging process. Applying additional transport equations for the determination of the six unknowns introduces a set of 22 additional unknowns and thus worsens the closure problem.

The aim of RANS-based turbulence models is to close the RANS system of equations by using empirical or half-empirical data. RANS turbulence models can be subdivided into eddy viscosity models and Reynolds stress models.

3.2.3.1 Eddy Viscosity Turbulence Models

The Boussinesq turbulent viscosity assumption, named after the French mathematician and physicist Joseph Boussinesq (*1842, †1929), uses the analogy between momentum transfer at the molecular level, represented by the viscous stress tensor, and momentum transfer by the fluctuating velocity field, represented by the Reynolds stress tensor. Since in laminar flows, the energy dissipation and the transportation of mass and momentum normal to the local flow direction occurs due to the viscosity of the fluid, in turbulent flows, additional dissipation and transport phenomena can be treated by assuming an increased viscosity. Boussinesq assumes a linear relationship between the deviatoric part of the Reynolds stress tensor and the 'rate-of-velocity' tensor for the mean flow:

$$\tau_{ij}^{turb} = -\mu_t\left(\frac{\partial \overline{u}_i}{\partial x_j} + \frac{\partial \overline{u}_j}{\partial x_i}\right) + \frac{2}{3}\delta_{ij}k \tag{3.39}$$

with k as the turbulent kinetic energy defined as:

$$k = \frac{1}{2}\left(\overline{u_i' u_i'}\right) \tag{3.40}$$

The Boussinesq assumption is not generally valid, as the Reynolds stress tensor is not necessarily proportional to the strain rate tensor. For simple flows such as straight boundary layers and wakes, the Boussinesq assumption is valid, but not in complex flows, such as flows with strong curvature, or strongly accelerated or decelerated flows. Even though the Boussinesq hypothesis is the basis of a widespread number of turbulence models and carefully applied, it can provide reasonably good results for a large variety of flows.

Analyzing eq. 3.39, τ_{ij}^{turb} can be separated into an isotropic term $\frac{2}{3}\delta_{ij}k(\mathbf{x},t)$ and an anisotropic term $-\mu_t\left(\frac{\partial \overline{u}_i}{\partial x_j} + \frac{\partial \overline{u}_j}{\partial x_i}\right)$. The isotropic term corresponds to an additional normal stress, and therefore, is usually treated as an additional pressure term. The anisotropic term distinguishes itself from the diffusive term of the laminar flow only due to its different viscosity μ_t. Using this separation, the RANS equation with implemented Boussinesq assumption is:

$$\rho\left(\frac{\partial \overline{u}_j}{\partial t} + \overline{u}_i\frac{\partial \overline{u}_j}{\partial x_i}\right) = -\left[\frac{\partial \overline{p}}{\partial x_j} + \frac{\partial}{\partial x_i}\left(\frac{2}{3}\delta_{ij}k\right)\right] - \frac{\partial}{\partial x_i}\left[-(\mu+\mu_t)\left(\frac{\partial \overline{u}_i}{\partial x_j} + \frac{\partial \overline{u}_j}{\partial x_i}\right)\right] \tag{3.41}$$

Unlike μ, which depends on material properties of the fluid, the turbulent viscosity μ_t is determined by parameters of the turbulent flow. Therefore, μ_t is neither a uniform nor a constant quantity, but depends on position and time: $\mu_t(\mathbf{x},t)$.

In the simplest description, turbulence can be characterized by two parameters, the turbulent kinetic energy k, or equivalently, the average velocity of the eddies u_c and a length scale L. According to the number of equations used to derive these two parameters or their representatives, eddy viscosity models can be subdivided into zero-, one-, or two-equation models.

In the following, two basic two-equation models are introduced.

The standard k-ϵ turbulence model

The standard k-ϵ turbulence model is based on the assumption that in equilibrium turbulent flows, the rate of production and destruction of turbulence are in near-balance. The dissipation rate ϵ is the turbulent kinetic energy of a unit mass that is transferred into thermal energy per time unit. It is assumed that only as much energy can be dissipated as is produced by the largest scales. Accordingly, ϵ, the kinetic turbulent energy k, and the length scale L are related as:

$$\epsilon \approx \frac{k^{\frac{3}{2}}}{L} \tag{3.42}$$

Introducing the constant C_μ, the eddy viscosity μ_t is expressed as:

$$\mu_t = \rho C_\mu \sqrt{k} L = \rho C_\mu \frac{k^2}{\epsilon} \tag{3.43}$$

The turbulent kinetic energy k is determined by the transport equation:

$$\rho\frac{\partial(k)}{\partial t}+\rho\frac{\partial(\overline{u}_j k)}{\partial x_j}=\frac{\partial}{\partial x_i}\left(\Gamma_k\frac{\partial k}{\partial x_i}\right)+P_k-\rho\,\epsilon \tag{3.44}$$

with P_k as the production term of the kinetic energy and Γ_k as the turbulent diffusion coefficient of kinetic energy:

$$P_k=\mu_t\left(\frac{\partial\overline{u}_i}{\partial x_j}+\frac{\partial\overline{u}_j}{\partial x_i}\right)\frac{\partial\overline{u}_i}{\partial x_j}\qquad\Gamma_k=\mu+\frac{\mu_t}{\sigma_k} \tag{3.45}$$

The transport equation for the dissipation rate ϵ is:

$$\rho\frac{\partial(\epsilon)}{\partial t}+\rho\frac{\partial(\overline{u}_j\epsilon)}{\partial x_j}=C_{\epsilon1}P_k\frac{\epsilon}{k}-\rho C_{\epsilon2}\frac{\epsilon^2}{k}+\frac{\partial}{\partial x_j}\left(\Gamma_\epsilon\frac{\partial\epsilon}{\partial x_j}\right) \tag{3.46}$$

with Γ_ϵ as the turbulent diffusion coefficient of the dissipation rate:

$$\Gamma_\epsilon=\mu+\frac{\mu_t}{\sigma_\epsilon} \tag{3.47}$$

Based on extensive experimental examination of turbulent flows, the five parameters of the k-ϵ turbulence model are most commonly chosen to be [Pop00]:

$$C_\mu=0.09\qquad C_{\epsilon1}=1.44\qquad C_{\epsilon2}=1.92\qquad \sigma_k=1.00\qquad \sigma_\epsilon=1.30$$

The k-ϵ turbulence model has been widely applied, extensively tested, and is still a quasi standard for industrial applications [Wil06]. Despite its well-known limitations, it is possible to provide reasonable results for a large variety of applications. Moreover, it has a robust formulation and leads to results with comparably small computational effort.

One deficit of the standard k-ϵ turbulence model is known as the "stagnation point anomaly". In regions with high pressure gradients the production of the turbulent kinetic energy k is overestimated. This leads to wrong results for the pressure distribution within these areas. Several improvements to the standard k-ϵ turbulence model have been suggested to overcome this deficit, e.g. by [Dur96], [MMK+98].

Another deficit are difficulties in the modeling of near-wall flow (see section 3.2.5). This leads to inaccurate predictions of flow separation and thus to problems in the modeling of complex flow conditions.

Research efforts to resolve these deficits have lead to the development of the Renormalization Group (RNG) k-ϵ turbulence model [YO86] and the Realizable k-ϵ (RKE) turbulence model [SLS+95] et al.

The standard k-ω turbulence model

In the k-ω turbulence model besides the kinetic turbulent energy k, the "turbulent frequency" ω is modeled as variable that determines the scale of the turbulence. The inverse of ω resembles the local turbulent time scale. The k-ω turbulence model assumes that the turbulent viscosity is linked to the turbulent kinetic energy and turbulent frequency via the relation:

$$\mu_t=\rho\frac{k}{\omega} \tag{3.48}$$

The transport equation for the turbulent kinetic energy is:

$$\frac{\partial(\rho k)}{\partial t} + \frac{\partial(\rho k \overline{u}_j)}{\partial x_j} = P_k - \beta^* \, \rho \, \omega k + \frac{\partial}{\partial x_j}\left[\left(\mu + \frac{\mu_t}{\sigma_k}\right)\frac{\partial k}{\partial x_j}\right] \tag{3.49}$$

The production rate of the turbulence P_k is the same as for the k-ϵ turbulence model (eq. 3.45). The transport equation for the turbulent frequency is:

$$\frac{\partial(\rho \omega)}{\partial t} + \frac{\partial(\rho \omega \overline{u}_j)}{\partial x_j} = C_{\omega 1} \, P_k \frac{\omega}{k} - \rho \, C_{\omega 2} \, \omega^2 + \frac{\partial}{\partial x_j}\left[\left(\mu + \frac{\mu_t}{\sigma_\omega}\right)\frac{\partial \omega}{\partial x_j}\right] \tag{3.50}$$

For the k-ω turbulence model the following variables are applied:

$$\beta^* = 0.09 \qquad C_{\omega 1} = 0.5555 \qquad C_{\omega 2} = 0.075 \qquad \sigma_k = 2.00 \qquad \sigma_\omega = 2.00$$

The k-ω turbulence model shows a superior performance in the modeling of low Reynolds flows as compared to k-ϵ turbulence models because it features a reduced length scale measure. Near-wall flow can be simulated by using an appropriate resolution without additional modeling. However, the k-ω turbulence model proved to be inaccurate in the simulation of free-stream flows. After the k-ϵ model, the k-ω model is the second most widely used turbulence model.

The k-ω SST turbulence model

The SST-turbulence model introduced by Menter [Men93] is a zonal model which aims at combining the advantages of the k-ϵ model for free flow regions and the k-ω turbulence model's superior performance in near-wall flow. The k-ω turbulence model is used in near-wall regions, while the k-ϵ turbulence model is applied elsewhere. The standard k-ϵ model is transformed into the k-ω form. The transport equations for k and ω are:

$$\frac{\partial(\rho k)}{\partial t} + \frac{\partial(\rho k \overline{u}_j)}{\partial x_j} = P_k - \beta^* \, \rho \, \omega k + \frac{\partial}{\partial x_j}\left[\left(\mu + \frac{\mu_t}{\sigma_k}\right)\frac{\partial k}{\partial x_j}\right] \tag{3.51}$$

$$\begin{aligned}\frac{\partial(\rho \omega)}{\partial t} + \frac{\partial(\rho \omega \overline{u}_j)}{\partial x_j} &= C_1 \, P_k \frac{\omega}{k} - \rho \, C_2 \, \omega^2 + \frac{\partial}{\partial x_j}\left[\left(\mu + \frac{\mu_t}{\sigma_1}\right)\frac{\partial \omega}{\partial x_j}\right] \\ &+ 2\rho(1 - F_1)\frac{1}{\sigma_2 \omega}\frac{\partial k}{\partial x_j}\frac{\partial \omega}{\partial x_j}\end{aligned} \tag{3.52}$$

The last term in the ω transport equation originates from the transformed ϵ equation. It is called the cross-diffusion term and makes the model insensitive to free stream ω [HL97].

The transition between the two turbulence models is performed via a blending function F_1. The constants of the SST model are a linear combination of the constants of the corresponding underlying models:

$$C_1 = F_1 C_{\omega 1} + (1 - F_1) C_{\epsilon 1} \tag{3.53}$$

$$C_2 = F_1 C_{\omega 2} + (1 - F_1) C_{\epsilon 2} \tag{3.54}$$

$$\sigma_1 = F_1 \sigma_{\omega 2} + (1 - F_1) C_{\epsilon 2} \tag{3.55}$$

$$\sigma_2 = F_1 \sigma_{\omega 2} + (1 - F_1) C_{\epsilon 2} \tag{3.56}$$

For the SST turbulence model the following variables are applied [CFX06]:

$$\begin{aligned} \beta^* = 0.09 \qquad C_{\omega 1} &= 0.5555 \qquad C_{\omega 2} = 0.075 \qquad \sigma_k = 2.00 \qquad \sigma_\omega = 2.00 \\ C_{\epsilon 1} &= 0.44 \qquad C_{\omega 2} = 0.0828 \qquad \sigma_{\epsilon 1} = 1.00 \qquad \sigma_{\epsilon 2} = 1/0.856 \end{aligned} \tag{3.57}$$

The blending function F_1 is given by:

$$F_1 = tanh\left(\arg_1{}^4\right) \tag{3.58}$$

with:

$$\arg_1 = \min\left\{\max\left[\frac{\sqrt{k}}{0.5\,\omega y}\,;\frac{500\nu}{\omega y^2}\right];\frac{4C_{\epsilon 1}k}{CD_{k\omega}y^2}\right\} \tag{3.59}$$

$$CD_{k\omega} = \max\left[2C_{\epsilon 1}\omega^{-1}\frac{\partial k}{\partial x_j}\frac{\partial \omega}{\partial x_j}\,;10^{-20}\right] \tag{3.60}$$

where y is the distance to the nearest wall and ν is the kinetic viscosity.

The SST model accounts for the transport of the turbulent shear stress inside the boundary layers by modifying the turbulent eddy-viscosity function. In order to prevent excessive shear stress levels, which are typically predicted with eddy-viscosity models based on the Boussinesq's approximation, an upper limit for the turbulent shear stress is introduced. With this modification, the eddy viscosity is defined as:

$$\mu_t = \frac{C_{\omega 1}\rho k}{\max(\alpha_1\omega;|\Omega|F_2)} \tag{3.61}$$

with $\alpha_1 = 0.31$ and $|\Omega|$ as the absolute value of the vorticity. The bounding function F_2 is constructed as:

$$F_2 = tanh\left(\arg_2^2\right) \tag{3.62}$$

$$\arg_2 = \max\left[2\frac{\sqrt{k}}{0.09\omega y};\frac{500\nu}{\omega y^2}\right] \tag{3.63}$$

This limitation for μ_t significantly improves the performance for adverse pressure gradient boundary flows, as well as the flow with pressure induced boundary layer separation, and thus enables a more realistic simulation of flow separation. The SST turbulence model proved its superior behavior compared to other two-equation RANS models in different comparisons, e.g. [BHC97], [MKL03].

Non-linear two equation models:

In Boussinesq's approximation (eq. 3.39), a linear dependency of the Reynolds stress and the velocity gradients is assumed. As an extension, in non-linear two equation RANS models a non-linear dependency is assumed. Examples for non-linear two equation RANS models can be found in: [Lum70], [Pop75], [Spe87], and [CLS96].

As an example, the constitutive equation of the Reynolds stress according to [CLS96] is given:

$$\rho\overline{u_i' u_j'} = -\mu_t S_{ij} + \frac{2}{3}\delta_{ij}k \tag{3.64}$$

$$+ \quad C_1\mu_t\frac{k}{\epsilon}\left(S_{ik}S_{kj} - \frac{1}{3}S_{kl}S_{kl}\delta_{ij}\right) \tag{3.65}$$

$$+ \quad C_2\mu_t\frac{k}{\epsilon}\left(\Omega_{ik}S_{kj} - \frac{1}{3}\Omega_{kj}S_{ki}\right) \tag{3.66}$$

$$+ \quad C_3\mu_t\frac{k}{\epsilon}\left(\Omega_{ik}\Omega_{jk} - \frac{1}{3}\Omega_{lk}\Omega_{lk}\delta_{ij}\right) \tag{3.67}$$

with

$$S_{ij} = \left(\frac{\partial\overline{u}_i}{\partial x_j} + \frac{\partial\overline{u}_j}{\partial x_i}\right) \tag{3.68}$$

$$\Omega_{ij} = \left(\frac{\partial\overline{u}_i}{\partial x_j} - \frac{\partial\overline{u}_j}{\partial x_i}\right) \tag{3.69}$$

$$\tag{3.70}$$

C_1, C_2, and C_3 are constants derived on measurements. Non-linear turbulence models are reported to provide improved results in case of anisotropic normal Reynolds stresses, e.g. in the prediction of reattachment length of separated regions behind a backwards facing step [CLS96].

3.2.3.2 Second Moment Closure Models

Second moment closure is based on transport equations for the individual Reynolds stresses and fluxes in eq. 3.38. Additional to the four equations for conservation of momentum and the continuity equations, six transport equations for the Reynolds stresses and one transport equation for the dissipation rate ϵ have to be solved. The second moment models provide the most general approach to solve and thereby close RANS equations. Among many others, details can be found in the works of [LRR75] and [SSG91].

Due to their exact modeling of the transport of Reynolds stresses, second moment closure models are qualified for simulating complex flow situation. However, in practice, the results obtained by second moment closure models are not significantly better than those obtained trough other two equation models [WE99, Mur98] for the specific area of interest of this thesis. In addition to this, second moment closure models lead to a highly increased computational effort due to the seven additional transport equations. Out of these reasons, second moment closure models are not considered within this work.

3.2.4 Large Eddy Simulations - Spatial Averaging/Filtering

As stated above, the phenomenon of turbulence includes a large range of scales. The Large Eddy simulation (**LES**) uses the property, that the large and medium scale eddies dominate

transport processes in the flow. The small scale eddies are responsible for the dissipation of energy and have little significant influence on the macro scale structure of the turbulent flow. In an LES turbulence model, the larger scale eddies are resolved by a direct numerical simulation using the NS equations, while the smaller scale eddies are modeled.

In the common filtering approach, space filtering over a small area is applied. This filter is associated with a certain length scale Δ, which is related but not necessarily identical to the grid scale of the computational grid. Eddies larger than the filter length Δ are resolved, while those smaller than Δ are not. The velocity u_j and the pressure p at a certain point are separated in a resolved part $\tilde{u}_j$, $\tilde{p}$ and an unresolved part u'_j, p':

$$u_j = \tilde{u}_j + u'_j \quad , \qquad p_j = \tilde{p}_j + p'_j \tag{3.71}$$

The basic Navier-Stokes equations of the LES are [FP99, Bre02]:

$$\frac{\partial \overline{u}_i}{\partial x_i} = 0 \tag{3.72}$$

$$\rho \left(\frac{\partial \tilde{u}_j}{\partial t} + \tilde{u}_i \frac{\partial \tilde{u}_j}{\partial x_i} \right) = -\frac{\partial \tilde{p}}{\partial x_j} - \frac{\partial \tilde{\tau}_{ij}^{mol}}{\partial x_i} - \frac{\partial \tau_{ij}^{SGS}}{\partial x_i} \tag{3.73}$$

with the tensor for the molecular transport of momentum:

$$\tilde{\tau}_{ij}^{mol} = -\mu \left(\frac{\partial \tilde{u}_i}{\partial x_j} + \frac{\partial \tilde{u}_j}{\partial x_i} \right) \tag{3.74}$$

τ_{ij}^{SGS} is the sub-grid scale (SGS) Reynolds stress and stands for the large scale momentum flux caused by the action of the unresolved scales. Typically, the sub-grid scale Reynolds stress is separated into an anisotropic and an isotropic part. The isotropic part is usually treated as an additional pressure term (see also eq. 3.38), while the anisotropic part τ_{ij} is subject to modeling:

$$\tau_{ij}^{SGS} = \tau_{ij} + \frac{1}{3} \delta_{ij} \tau_{kk}^{SGS} \tag{3.75}$$

Analog to the RANS models, LES models can be structured by the amount of equations used to model τ_{ij}. A common model is the zero-equation Smagorinsky model (1963):

$$\tau_{ij} = 2\mu_t \tilde{S}_{ij} \tag{3.76}$$

with

$$\tilde{S}_{ij} = \frac{1}{2} \left(\frac{\partial \tilde{u}_i}{\partial x_j} + \frac{\partial \tilde{u}_j}{\partial x_i} \right) \tag{3.77}$$

$$\mu_t = C_s^2 \rho \Delta^2 |\tilde{S}| \tag{3.78}$$

and C_s as the model parameter, Δ as the filter length scale and $|\tilde{S}| = \sqrt{\tilde{S}_{ij}\tilde{S}_{ij}}$. C_s is not a constant parameter but subject to the flow conditions. It can vary between values of 0.065 for channel flow and 0.2 for isotropic turbulence [FP99]. In regions close to walls, the values of C_s have to be reduced even further.

Compared to DNS, a much coarser computational grid can be used, since it is not necessary to resolve the eddies down to the Kolmogorov micro scale. Therefore, the simulation of flows with higher Reynolds numbers is possible.

Compared to the RANS models, LES models have the advantage that only the small scale turbulence is modeled. In comparison to modeling the whole turbulent spectrum, modeling of the small scale turbulence is less difficult, since the small scale turbulence to a large degree shows a homogenous and isotropic behavior. Furthermore, with LES the simulation of unsteady, large-scale turbulent structures is possible, and hence can be used to study phenomena such as unsteady aerodynamic load on structures. The computational grid has to be sufficiently well designed to ensure the resolution of the bulk of turbulent energy and thereby avoiding grid dependent results. For statistically useful interpretation, LES is expected to be more computationally expensive by approximately two orders of magnitude for each direction compared to a RANS solution [Pop00]. Computational efforts increase even more, if the resolution of near wall flow is necessary. If the computational grid and the filter are too coarse to resolve 80% of the turbulent energy, the name of Very-large-eddy simulation VLES is used [Pop00]. For VLES a coarser mesh can be used, however, additional care has to be taken in modeling the sub-scale turbulence as it contains a larger fraction of the total turbulent energy of the flow.

The Detached Eddy Simulation (DES) combines Unsteady RANS and LES models. Dependent on the grid resolution and the turbulent length scale, either the RANS turbulence model (in boundary layer flow) or the LES turbulence model (in free stream) is used. Regions near solid boundaries and those in which the turbulent length scale is smaller than the maximum grid resolution are solved using RANS models. In regions in which the turbulent length scale exceeds the grid dimension the LES model is applied. The grid resolution is not as demanding as pure LES. In its original form, DES is formulated for the one-equation Spalart-Allmaras model [SJSA97] and can be seen as LES with a wall model. For two-equation RANS models, DES is a non-zonal approach of hybrid RANS-LES model. However, grid generation is complicated by the different requirements of RANS and LES. Applied to the same mesh, DES and LES models lead to similar results [BJM03].

3.2.5 Law of the Wall

At no-slip boundary wall, strong gradients in the flow variables exist since both mean and fluctuating part of velocity vanish. As a consequence, k and thus μ_{eff} are exactly zero at the wall. At high Reynolds numbers, this results in very large flow gradients near the wall. Moreover solid boundaries selectively damp fluctuations normal to the wall.

Experiments and mathematical analysis have shown that the flow close to a no-slip wall in a two-dimensional turbulent boundary layer without pressure gradient can be divided into different layers. In the inner layer, viscous and turbulent stresses are of importance. In the outer layer, viscous stresses can be neglected and the application of turbulence models introduced above is possible.

In the following, the non dimensional velocity $\overline{u}^+$, the averaged wall shear stress $\overline{\tau_w}$ and the shear velocity u_τ are used. The distance to the wall y is expressed as a non dimensional

wall distance y^+ with the kinematic viscosity $\nu = \frac{\mu}{\rho}$.

$$\overline{u}^+ = \frac{\overline{u}}{u_\tau} \qquad u_\tau = \sqrt{\frac{\overline{\tau_w}}{\rho}} \qquad y^+ = \frac{u_\tau z}{\nu} \tag{3.79}$$

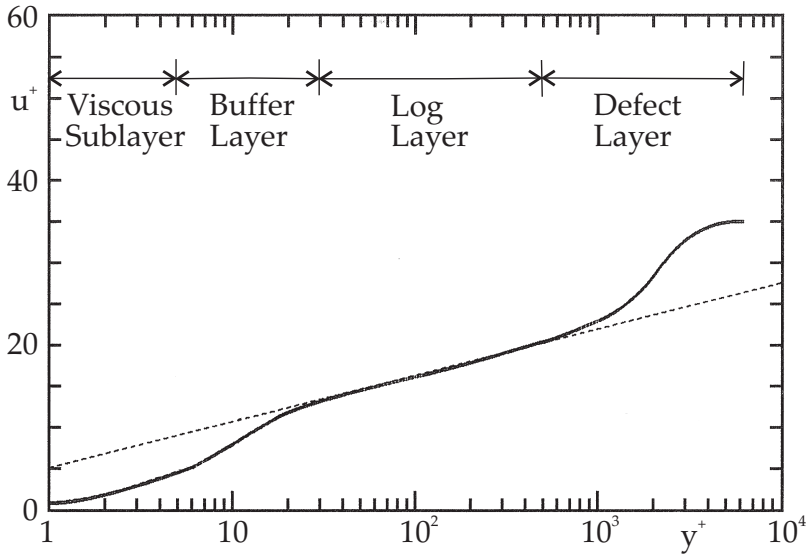

Figure 3.1: Typical velocity profile for a turbulent boundary layer, after [Wil06].

Fig. 3.1 presents the typical velocity profile for a turbulent boundary layer. In a turbulent boundary layer, the following four regions can be identified:

1. Linear (viscous) sub-layer: $y^+ < 5$

   The fluid region is in direct contact with the wall. Laminar, molecular viscosity effects are dominating.

2. Buffer layer: $5 < y^+ < 30$

   Effects of molecular velocity and turbulence are of equal importance.

3. Logarithmic layer: $30 < y^+ < 500$

   Turbulent region close to the wall with Reynolds stresses as dominant effects.

   A logarithmic velocity distribution is assumed:

   $$u^+ = \frac{1}{\kappa} ln(y^+) + C \tag{3.80}$$

   The parameters are the Kàrmàn constant $\kappa = 0.4$ and $C = 5.0$ for hydrodynamically perfectly-smooth walls. For completely rough walls, C varies with the surface sand-grain roughness k_s, with roughness elements of average roughness k_s. For large roughness height with $\frac{u_\tau k_s}{\nu} \gg 1$, C can be calculated by eq. 3.81 [Wil06]:

   $$C = 8.0 - \frac{1}{\kappa} ln\left(\frac{u_\tau k_s}{\nu}\right) \tag{3.81}$$

4. Outer (or defect) layer: $500 < y^+$

   Inertia dominated region far from the wall.

In the modeling of this near wall flow for RANS turbulence models, two approaches are possible.

◇ Low-Re models

In low-Re models the velocity distribution is solved down to the wall. The increasing importance of viscosity is incorporated in the transport equations for k and ω. Low-Re models are much more computationally expensive but provide a more profound analysis in case near wall behavior is relevant. For k-ϵ based turbulence models, low-Re formulations are more difficult to derive and therefore less commonly used [Man08].

◇ Wall functions

Using wall functions, the flow in the near wall region is not resolved but theoretical profiles close to the boundary surface are assumed. These profiles are mainly valid for near-equilibrium boundary layers, which limits the applicability of wall functions. For wall functions, mostly a logarithmic velocity profile is assumed. The computational grids at the wall have to be chosen in such a way, that the necessary boundary resolution required by the wall function is maintained: the y^+ distance of the first node close to the wall should be sufficiently small [Aps06].

3.3 Numerical Simulation of Fluid Flow

The Navier-Stokes equations are a coupled system of nonlinear partial differential equations, which are difficult up to impossible to solve analytically. For the usage of computational methods, the equations have to be transformed and discretized. Therefore, the set of partial differential equations, which are valid in the entire domain, is transferred into a set of discrete algebraic equations, which are valid at specific points in the domain. The simultaneous solution of these interdependent discrete equations provides the numerical solution. The most common discretization techniques for fluid dynamics are:

◇ Finite Difference Method (FDM)

◇ Finite Volume Method (FVM)

◇ Finite Element Method (FEM)

Within this work, the Finite Volume Method is used. It is the most widely used approach in Computational Fluid Dynamics (CFD). In this method, the domain is divided into a grid of finite control volumes (**CV**). The centroids of the CVs represent discrete points, at which the algebraic equations for all flow variables have to be fulfilled. This corresponds to a co-located grid. In the following, the FVM for co-located grids will be introduced. For more detailed discussion see [FP99] or [Sch99].

3.3.1 The Finite Volume Method (FVM)

The FVM is based on the conservation equations in the integral form. To derive the integral form, here, the Reynolds transport theorem for an arbitrary scalar quantity Φ is considered: [2]

$$\underbrace{\rho\frac{\partial\Phi}{\partial t}}_{\text{unsteady term}} + \underbrace{\rho\frac{\partial(\Phi u_i)}{\partial x_i}}_{\text{convective term}} - \underbrace{\frac{\partial}{\partial x_i}\left(\Gamma_\Phi\frac{\partial\Phi}{\partial x_i}\right)}_{\text{diffusive term}} = \underbrace{s_\Phi}_{\text{source term}} \tag{3.82}$$

The quantity Φ represents any of the averaged quantities introduced in section 3.2. By inserting the relevant quantities, the simple NS equations (see tab. 3.1) as well as RANS, URANS, and LES-averaged NS equations can be expressed. Additional to the convective, diffusive, and unsteady term, eq. 3.82 has a source term, which can be found in the transport equations for k, ϵ, and ω introduced in section 3.2.3.

term	Φ	Γ_Φ	s_Φ
conservation of mass	1	0	0
conservation of momentum	u_i	μ	$-\frac{\partial p}{\partial x_j}$

Table 3.1: Terms of NS equations for Reynolds transport theorem

The integral form is derived by integration over the control volume V:

$$\int_V \rho\frac{\partial\Phi}{\partial t}\,dV + \int_V \rho\frac{\partial(\Phi u_i)}{\partial x_i}\,dV - \int_V \frac{\partial}{\partial x_i}\left(\Gamma_\Phi\frac{\partial\Phi}{\partial x_i}\right)\,dV = \int_V s_\Phi\,dV \tag{3.83}$$

Using the Gauss theorem, the volume integral of the convective and diffusive term can be described by an integral over the volume's surface S:

$$\underbrace{\int_V \rho\frac{\partial\Phi}{\partial t}\,dV}_{\text{unsteady term}} + \underbrace{\int_S \rho(\Phi u_i)\,dS_i}_{\text{convective term}} - \underbrace{\int_S \left(\Gamma_\Phi\frac{\partial\Phi}{\partial x_i}\right)\,dS_i}_{\text{diffusive term}} = \underbrace{\int_V s_\Phi\,dV}_{\text{source term}} \tag{3.84}$$

For the discretization, structured and unstructured grids can be used. Figure 3.2 shows a control volume in a structured two-dimensional grid, which will be used in the following. The volume is enclosed by four surfaces S_l with unit normal vector n_l, labeled according to the compass notation as East, West, North, and South.

3.3.2 Approximation of Convective Term

The integral over the surface S of the control volume V can be split into four integrals over the surface parts S_w, S_e, S_n, and S_s. These integrals describe the convective fluxes F^C over the four surfaces:

$$\int_S \rho\,(\Phi u_i)\,dS_i = \sum_{l=w,e,s,n} F_l^C = \sum_{l=w,e,s,n}\int_{S_l} \rho\,n_{l\,i}\,u_i\,\Phi\,dS_l \tag{3.85}$$

[2] In case of NS with turbulence models based on averaging, the averaged velocity $\overline{u}_i$ has to be used instead of u_i.

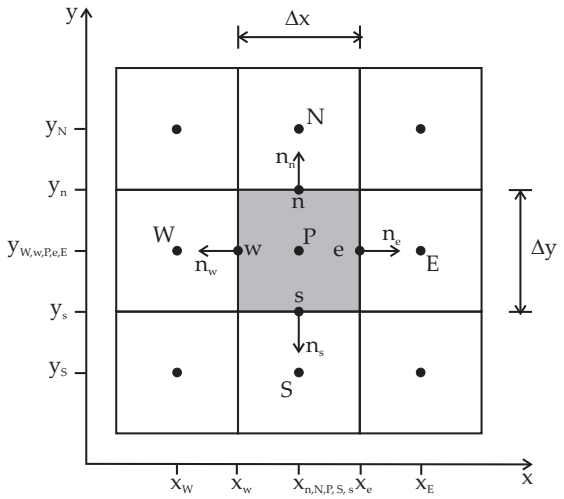

Figure 3.2: Control volume CV with compass notation, after [Fra06].

For computing the integral over the face in direction l, the midpoint rule is applied, which approximates the mean value over the surface as the value in the surface center, Φ_l and u_l. This approximation is of second order accuracy with respect to the grid width. For the East surface, exemplary the flux is approximated as:

$$F_e^C = \int_{S_e} \rho \, n_{ei} \, u_i \, \Phi \, dS_e \approx \rho \, n_{ei} \, u_{ei} \, \Phi_e \, S_e \tag{3.86}$$

The value $u_{l\,i}\Phi_l$ at the center of surface S_l has to be approximated by interpolation, as only the values at the cell centers are known. Here, the three most common interpolation methods are explained based on the East surface S_e of the volume:

◇ Upwind interpolation scheme (UDS)

The UDS is the simplest interpolation scheme and is based on the direction of the flux:

$$\Phi_e^{UDS} = \begin{cases} \Phi_P & \text{for} \quad u_{ei}\, n_{ei} \geq 0 \\ \Phi_E & \text{for} \quad u_{ei}\, n_{ei} < 0 \end{cases} \tag{3.87}$$

The UDS is first order accurate. The truncation error behaves like a diffusion term and contributes to the effect of numerical diffusion. The diffusion coefficient can be calculated as $\Gamma_{\text{num}} = 0.5 u_{ei} n_{ei} \Delta x$. For high Re-numbers, the Γ_{num} can become significantly larger than the physical diffusion coefficient Γ_{mol} in high Re flows. Therefore, the UDS is known as an over-dissipative and generally inaccurate method.

◇ Central interpolation scheme (CDS)

The CDS is a second order interpolation scheme. The value at the face center is a linear interpolation between the cell centers, with the distance to the cell center as weighting factor:

$$\Phi_e^{CDS} = \lambda_e \Phi_E + (1 - \lambda_e)\Phi_P \quad \text{with} \quad \lambda_e = \frac{x_e - x_P}{x_E - x_P} \tag{3.88}$$

CDS does not introduce numerical diffusion into the solution. In regions with high flow gradients and insufficient grid resolution, oscillation occur in the solution. These oscillations can be removed by mesh refinement.

◇ Quadratic Upwind Interpolation for Convective Kinematics (QUICK)

The QUICK is third order accurate for equidistant and second order accurate for non-equidistant grids. For the QUICK interpolation, information of a second node in upstream direction is considered: for $u_{ei}\, n_{ei} \geq 0$, W is considered as additional node, and for $u_{ei}\, n_{ei} < 0$, the centeriod of the next CV east of E is considered. As an example for a flow in direction P to E, the interpolation for equidistant grids is:

$$\Phi_e^{QUICK} = \frac{6}{8}\Phi_P + \frac{3}{8}\Phi_E - \frac{1}{8}\Phi_W \tag{3.89}$$

Even so the QUICK interpolation is slightly more accurate compared to CDS, in practice, differences in convergence and accuracy are small for sufficiently fine grid resolution.

In most CFD software codes apply a combination of high and low order approximation. Thereby, oscillating solutions can be omitted at the cost of small numerical diffusion.

3.3.3 Approximation of Diffusive Term

The diffusive term describes the diffusive fluxes F^D of the the surface S of the control volume V.

$$\int_S n_i \Gamma \frac{\partial \Phi}{\partial x_i}\, dS = \sum_{l=w,e,s,n} F_l^D = \sum_{l=w,e,s,n} n_{l\,i} \int_{S_l} \left(\Gamma \frac{\partial \Phi}{\partial x_i} \right) dS_l \tag{3.90}$$

Similar to the convective term, for the diffusive term the second order midpoint rule is applied to approximate the surface integrals on the surface S_i. For the surface S_e, the approximation is:

$$\int_{S_e} n_{e\,i} \left(\Gamma \frac{\partial \Phi}{\partial x_i} \right) dS_e \approx n_{e\,i} \left(\Gamma \frac{\partial \Phi}{\partial x_i} \right)_e S_e \tag{3.91}$$

This linear interpolation is second order accurate for equidistant grids and first order for non-equidistant grids. Since the derivative $\frac{\partial \Phi}{\partial x_i}$ is unknown at the face center, an additional approximation is necessary. Assuming a linear profile between the derivatives in the points P and E, the same linear interpolation introduced in eq. 3.88 can be used. Accordingly, the local gradient is approximated as:

$$\left(\frac{\partial \Phi}{\partial x_i} \right) \approx \frac{\Phi_E - \Phi_P}{x_E - x_P} \tag{3.92}$$

Another possibility is to first compute the derivative in the cell centers and then interpolate it onto the surface centers, using the same interpolation techniques as for the convective term.

3.3.4 Approximation of Source Term

The source term requires an integration over the whole control volume V. It can be derived assuming a constant or linear profile of the source term and approximated by its value $s_{\Phi,P}$ at the cell center P. This approximation is second order accurate and reads as:

$$\int_V s_\Phi \, dV \approx (s_\Phi)_P \, V \tag{3.93}$$

3.3.5 Approximation of Unsteady Term

Inserting the spatial approximations for the convective and diffusive term together with the source term, eq. 3.84 is discrete in space but still continuous in time. Time discretization is introduced via the unsteady, time dependent-term. Similar to the source term, volume averaging is performed to compute the value at the CV's center.

$$\int_V \rho \frac{\partial \Phi}{\partial t} \, dV \approx \rho \frac{\partial \Phi_P}{\partial t} V \tag{3.94}$$

for an application to wind engineering, considerably large time-steps are sufficient for a time resolution of the relevant physical effects. In order to be able to use larger time-step size, only implicit time integration schemes are considered.

The Euler Backwards time integration scheme is the most simple implicit first order scheme:

$$\left(\frac{\partial \Phi_P}{\partial t} \right)_{t=t_{n+1}} \approx \frac{\Phi_P(t_{n+1}) - \Phi_P(t_n)}{t_{n+1} - t_n} \tag{3.95}$$

A common second order time integration scheme is the Three-Time-Level method:

$$\left(\frac{\partial \Phi_P}{\partial t} \right)_{t=t_{n+1}} \approx \frac{3\Phi_P(t_{n+1}) - 4\Phi_P(t_n) + \Phi_P(t_{n-1})}{2((t_{n+1}) - t_n)} \tag{3.96}$$

Because the right side of eq. 3.95 and eq. 3.96 include the unknown value of Φ at the new time step $n+1$, they has to be solved in an iterative manner for each time step.

3.3.6 Solution Methods

By including the discrete terms derived above in the general transport equation in integral form, for each control volume and each scalar variable Φ, a linear equation of the following type can be formulated:

$$a_P \Phi_P = \sum_{l=w,e,s,n} a_l \Phi_l + q_P \tag{3.97}$$

The value in the cell center depends on the values of the surrounding cell centers and the local source q_P. For the Navier-Stokes equations, these scalar variables are the velocity in three spatial directions and the quantities necessary for turbulence modeling. The unknown pressure requires a special treatment, as no equation exists to directly derive it. The pressure can

be determined through a combination of equations for the conservation of momentum and mass. For the Navier-Stokes equation with a k-ϵ turbulence model, this leads to a coupled system of equations of the following basic type for one CV [Sch04]:

$$\begin{bmatrix} a_{u_1u_1} & a_{u_1u_2} & a_{u_1u_3} & a_{u_1p} & a_{u_1k} & a_{u_1\epsilon} \\ a_{u_2u_1} & a_{u_2u_2} & a_{u_2u_3} & a_{u_2p} & a_{u_2k} & a_{u_2\epsilon} \\ a_{u_3u_1} & a_{u_3u_2} & a_{u_3u_3} & a_{u_3p} & a_{u_3k} & a_{u_3\epsilon} \\ a_{pu_1} & a_{pu_2} & a_{pu_3} & a_{pp} & 0 & 0 \\ a_{ku_1} & a_{ku_2} & a_{ku_3} & 0 & a_{k\epsilon} & a_{kk} \\ a_{\epsilon u_1} & a_{\epsilon u_2} & a_{\epsilon u_3} & 0 & a_{\epsilon k} & a_{\epsilon\epsilon} \end{bmatrix} \cdot \begin{bmatrix} u_1 \\ u_2 \\ u_3 \\ p \\ k \\ \epsilon \end{bmatrix} = \begin{bmatrix} b_{u_1} \\ b_{u_2} \\ b_{u_3} \\ b_p \\ b_k \\ b_\epsilon \end{bmatrix} \tag{3.98}$$

For all N control volumes in the computational domain, the system of equations can be summarized to:

$$\mathbf{A}(\mathbf{\Phi}) \cdot \mathbf{\Phi} = \mathbf{b}(\mathbf{\Phi}) \tag{3.99}$$

with $\mathbf{A}$ as a sparse coefficient matrix for all the conservation laws with the size GxG with $G = N \cdot$ "*number of unknown quantities per cell*" , $\mathbf{\Phi}$ as a vector of all unknowns of size G and $\mathbf{b}$ as the right hand side. Since the entries of matrix $\mathbf{A}(\mathbf{\Phi})$, as well as those on the right hand side $\mathbf{b}(\mathbf{\Phi})$, dependent on the unknowns $\mathbf{\Phi}$, eq. 3.99 is a nonlinear system of equations.

For the solution of the Navier-Stokes equation, two different approaches are possible:

◇ Segregated solution

In a segregated solver, the transport equations for the velocities and turbulent quantities, as well as for the conservation of mass, are solved in a sequential manner. To ensure the coupling of the equations, an iterative procedure is necessary. A certain pressure distribution is assumed for the computation of the remaining unknowns. Once all the other unknowns are computed, the pressure equation is solved and the pressure distribution is corrected. In the next iteration step the corrected pressure distribution is used to derive a solution for the remaining variables.

As pressure is used to correct the solution, this procedure is also known as pressure correction method. A well-known solution algorithm based on this method is the SIMPLE algorithm.

◇ Simultaneous solution

In a simultaneous solver, the system of equations is solved for all unknowns at once. Compared to a segregated solver, this solution method demands for higher computational power and memory and is more robust.

For linearization of the nonlinear system of equations, Newton or quasi-Newton methods are applied. Full Newton methods are restricted to small or special types of applications because of the high effort to compute the derivatives. Accordingly, approximate linearization schemes are more common.

The linearized system can be solved by direct or iterative solvers. Because of the size of the system of equations, iterative methods are preferred. Furthermore, the multi-grid

method is an enhanced solution technique, which is well suited for CFD problems. Applying the multi-grid method, the equation system is solved on grids of different levels of coarseness. Exemplary, in the common 'V-cycle' procedure, the multi-grid solution is started on the grid level with highest resolution. The results from the fine grid are transferred to progressively coarser grids. On the coarser grid, the solution is performed again and results on the coarser grid are transferred back to the finer grid. This procedure is done successively. It enables a fast damping of the small scale oscillations in the numerical solution and thus increases the convergence of the solution.

3.3.7 Moving Boundaries

In many industrial applications the geometric boundaries of the fluid domain are not constant but rather changing in time. In these cases, the computational grid has to be adapted. The capacity to include moving boundaries into the CFD computation is essential for its application to solve surface coupled FSI-problems introduced in the next chapter.

If the boundaries of the fluid domain are modified, such change has to be included into the system of equations. An overview of different methods available for the treatment of moving boundaries in fluid simulations is taken from [WGG+06] and includes:

- ◇ The Immersed Boundary Method [Pes02, MI05]
- ◇ The Distributed Lagrangian Multiplier / Fictious domain [Baa01, vLAdHB05, Zha05]
- ◇ eXtended Finite Element Method (XFEM) [BB99, GW06]
- ◇ Level-set methods [LCB06]
- ◇ Overlapping domain decomposition / Chimera-like methods [SDB83, WGG+06]
- ◇ Arbitrary Lagrangian-Eulerian (ALE) formulation [DHPRF04]

While the first four listed methods belong to the group of fixed-grid methods, in the ALE method, the fluid mesh is adapted to the moving boundaries. These moving boundaries need to be considered in the equations describing the fluid domain.

In the context of this work, moving boundaries are imposed via the continuous Arbitrary Lagrangian-Eulerian (ALE) formulation [DHPRF04]. This formulation brings together the Lagrangian description, as used in section 2.2.1, and the Eulerian description introduced in section 3.2.1. The local change of the boundary condition is spread throughout a certain region of the computational grid, thus causing a change in volume and/or position of the control volumes. Methods how to spread the local change of boundaries into the computational fluid domain are discussed in section 4.4.2.

In the following, the integral form of the general Reynolds transport equation eq. 3.84 is considered. With the ALE extension, volume V and surface S of the CV do not have to remain constant but can be time-dependent values $V(t)$, $S(t)$. This has no influence on the surface integrals in eq. 3.84 since they contain no derivatives with respect to time. They

are evaluated at a specific point in time for which V and S are assumed constant. However, the unsteady term requires modification. With the help of the Leibnitz's law and the Gauss theorem, the time dependent volume integral of the unsteady term can be transformed into two terms:

$$\underbrace{\int_V \rho \frac{\partial \Phi}{\partial t}\, dV}_{A_E} = \underbrace{\frac{d}{dt}\int_V \rho\, \Phi\, dV}_{A_L} - \underbrace{\int_S \rho\, u_{g\,i}\, \Phi\, dS_i}_{K_g} \tag{3.100}$$

A_E is the unsteady term of a fixed CV. A_L is the unsteady term in the modified CV and K_g is the convective flux through the surface of the CV due to its grid velocity $u_{g\,i}$.

In order to describe the conservation of mass with the general Reynolds transport equation eq. 3.84 the following parameters $\Phi = 1, \Gamma = 0$, and $s = 0$ have to be applied. In the case of an incompressible flow, the A_E term vanishes as the mass within a fixed control volume has to be constant. The remaining equation is known as the "geometric conservation law" (GCL) [FLM95, Wal99, Mok01] or the "space conservation law" (SCL) [FP99, Glü02, DP88]:

$$\frac{d}{dt}\int_V dV - \int_S u_{g\,i}\, dS_i = 0 \tag{3.101}$$

The GCL condition states that between two time steps the volume swept over by the movements of the cell boundaries equals the change of volume of the cell. For incompressible problems, violations of the GCL result in artificial mass sources, which can accumulate and compromise the computation [LF96]. The GCL can be introduced as an additional conservation equation [TL79] or can be integrated into the continuum equation [LF96]. The second approach is more common as the GCL is automatically fulfilled, if the grid velocities are consistently derived from the grid position with respect to the time-integration scheme. An example of an implementation in the FV scheme can be found in [Glü02].

The difference between the physical, Eulerian fluid velocity u_i and the velocity of the grid movement $u_{g\,i}$ is the relative fluid velocity of the fluid motion compared to the grid deformation. The conservation equations for scalar quantities are therefore easily derived by replacing the velocity vector in the convective term with the relative velocity $u_c = u_i - u_{g\,i}$.

For moving boundaries, the Reynolds transport equation with the ALE formulation for a scalar quantity Φ reads as:

$$\underbrace{\underbrace{\frac{d}{dt}\int_V \rho\Phi\, dV}_{\text{unsteady term}}}_{\text{Lagrangian}} + \underbrace{\underbrace{\int_{S_i} \rho\Phi u_i\, dS_i}_{\text{convective term}}}_{\text{Eulerian}} - \underbrace{\int_{S_i} \rho\Phi u_{g\,i}\, dS_i}_{\text{convective grid fluxes}} - \underbrace{\int_{S_i} \Gamma_\Phi \frac{\partial \Phi}{\partial x_i}\, dS_i}_{\text{diffusive term}} = \underbrace{\int_V s_\Phi\, dV}_{\text{source term}} \tag{3.102}$$

or further simplified as:

$$\underbrace{\underbrace{\frac{d}{dt}\int_V \rho\Phi\, dV}_{\text{unsteady term}} + \underbrace{\int_{S_i} \rho\left(u_i - u_{g\,i}\right)\Phi\, dS_i}_{\text{convective term}}}_{\text{for moving boundaries (Lagrangian)}} - \underbrace{\int_{S_i} \Gamma_\Phi \frac{\partial \Phi}{\partial x_i}\, dS_i}_{\text{diffusive term}} = \underbrace{\int_V s_\Phi\, dV}_{\text{source term}} \tag{3.103}$$

3.4 Application of CFD to Analyze Wind Loads on Membrane Structures

In this section, the application of the fundamentals of fluid mechanics and the numerical methods for the computation of wind loads on membrane structures is discussed.

Compared to the application of Computational Fluid Dynamics (CFD) in automotive or aviation industry, using CFD in wind engineering is difficult because of the specific physics of the wind flow. In the following, the wind flow is considered as the neutrally stratified atmospheric boundary layer flow, properties of which are presented in section 3.4.3.

The application of numerical methods of fluid mechanics in wind engineering created the rather young sub-discipline of Computational Wind Engineering (CWE), which deals with the application of CFD in the context of the simulation of wind flow around buildings.

3.4.1 Computational Wind Engineering

In Computational Wind Engineering, the numerical simulations are typically based on the Navier-Stokes equations. Recent advances in simulations based on the Lattice-Boltzmann Method [MTB+08], [MCB+07] show very promising results.

For an application in wind engineering, CFD-based methods have the potential to provide the following advantages for the prediction of wind loads, assuming the realistic modeling of the ABL flow:

- ◇ Simulation of wind effects on full scale models.
- ◇ Accessability of all relevant physical quantities in arbitrary points of the simulation field.
- ◇ Flexibility for changes in geometry and design of the structure including the potential for optimization.

State of the art in Computational Wind Engineering

The majority of computations of wind pressure on buildings refer to prismatic building geometries. For these simple shapes, several experimental data is available, both from full scale measurements and wind tunnel experiments. Among others, the famous Silsoe full scale experiment [RHS01] is a valuable source of reference values. In [LM92b] and [LM92a] further data is available based on full scale measurements at Texas Tech. Recent numerical simulations that use prismatic geometries can be found in the works of Robertson et al. [RHRF97], Gao et al. [Gao05], Cheng et al. [CLYS03], and many others. For more complex geometries, fewer examples exists. Among other works, e.g. a CFD-based wind pressure estimation for a complex building geometry was conducted by Suh et al. [SRK+97]. An extensive analysis for a large optical telescope can be found in the work of Mamou et al. [MCB+07, MTB+08].

In the field of computational wind engineering, three major modeling issues have to be resolved:

1. **Generation of atmospheric boundary layer**

   For the generation of the atmospheric boundary layer in a numerical flow summations, several strategies are available. Most common is the generation of averaged velocity profiles and the distribution of the turbulence intensity according to meteorological measurements [PSN97, Kov94]. For the simulation methods including a high resolution in the time domain, instead of the turbulence intensity, the spacial and time-wise correlated velocity fluctuations of the wind can be used [UO99].

2. **Modeling of turbulence**

   Murakami [Mur97] presented a comparison of results in CWE derived from the use of different turbulence models, which is still valid. Dynamic Large Eddy Simulations (LES) show the most promising results in many wind engineering applications. However, LES proved to be a very expensive variant in terms of computational effort. Depending on the application, sufficiently accurate results can be obtained by Reynolds-averaging based turbulence models.

3. **Robustness of simulation with respect to accuracy and reliability**

   Most studies are focused on the flow fields of buildings with prismatic shapes. Generally, good coincidence with experimental results has been achieved in the works listed above. However, most of these simulations were focused on particular cases, partly with experimental results a priori available. The ability to obtain these results cannot be extended to the notion of being able to predict an arbitrary turbulent flow around a complex building geometry. Hence, the applicability of the used techniques and the accuracy of the results has to be evaluated anew for any new setup using CFD-based simulations in wind engineering.

Up to now, wind engineers have been reluctant to use CWE results to compute design loads for buildings. This could change, as with a further increase in computational power, CWE, even with advanced turbulence modeling, comes into the reach of the practicing designer. However, the accuracy of computations and the reliability of the results will always largely depend on the training, experience, and qualification of the practitioner, who conducts the simulations.

In principle, many state of the art CFD simulations have the capability to predict mean wind pressures on buildings with reasonable accuracy. This enables the analysis of quasi-static wind effects, such as the stagnation pressure, and can be used to derive wind loads for cases, in which quasi-static effects are dominant. However, up to now, the modeling of fluctuating and peak pressures is not sufficiently accurate [Hol01]. This limits the application of CFD for cases, in which effects due to fluctuation wind pressure are decisive. The reason for the insufficient representation of pressure fluctuations is primarily the necessity to incorporate simplifying representations of the turbulence in the fluid flow equations, in

order to keep the computational effort manageable (see sections 3.2.3 and 3.2.4). CFD techniques are, however, currently capable of providing useful insights into wind flow around buildings for environmental considerations.

According to Stathopoulos [Sta03], CWE is still in its infancy and in the foreseeable future, CFD simulation will not replace the use of wind tunnel experiments. However, CWE shows a huge potential, if not to replace, then to complement physical experiments.

Guidelines for CWE

To a large extent, CFD is an experience driven method. Besides a well-suited simulation software, the quality of results largely depends on modeling issues. These modeling issues lie in the responsibility of the user, who can handle them in a better or worse manner, depending to his knowledge and experience with CFD. Knowledge about CFD can be taken from literature, especially textbooks and publications. A rich source of information and recommendations are Best Practice Guidelines, which ideally summarize, condense, and discuss the information from publications and textbooks.

Considerations about the discretization and solution of the underlying differential equations are common for all applications of CFD. These aspects depend rather on the underlying flow regime than the specific application. For industrial applications of Computational Fluid Dynamics, several Best Practice Guidelines exist. Among others, here the ERCOFTAC guideline [ERC02], which constitutes generic advice on how to carry out quality CFD calculations, shall be mentioned. Menter proposed an extended version in the scope of the ECORA project in [Mea02]. Further guidelines have been proposed by the Thematic Network for Quality and Trust in the Industrial Application of CFD (QNET-CFD). The EU-funded, collaborative project QNET-CFD provides a collection of CFD-related knowledge and know-how across a range of applications from a wide variety of sources [QNE08].

However, these guidelines are not specific to the application of CFD in the scope of CWE. For the simulation of pedestrian wind in built urban areas, the working group of the COST action C14 proposed a guideline in [FHJ+04]. A further guideline is proposed for the prediction of flow and transport processes in urban or industrial environments by working group COST action 732 [FHSC07]. The German 'Verein Deutscher Ingenieure' (**VDI**) published a guideline on the simulation of micro scale flow fields around obstacles and buildings [Ver05]. Even though these guidelines concentrate mainly on the prediction of wind comfort and the pollution dispersion, they can also be applied to the prediction of wind loading [Fra07]. A guideline including the numerical prediction of wind loading in Japanese [Arc05] and in a short version in English [TNK08] and [TMY+08] is provided by the Architectural Institute of Japan. Additional recommendations on the setup of a numerical model for the simulation of wind loads on buildings was published by Franke in [Fra06].

All specific guidelines for CWE focus on the recommendations for correct physical modeling of the flow condition, the Atmospheric Boundary Layer (**ABL**). In the following, the properties of the air flow within the ABL shall be discussed. Based on the properties of the ABL, modeling aspects specific to CWE are presented. Using the guidelines presented above, together with recent publications, suitable physical models and boundary conditions are identified. Regarding aspects of general CFD, e.g. the required quality and resolution

of the computational grid, the choice of numerical approximations, the time-step size, and the iterative convergence criteria, the general guidelines for CFD computations mentioned above are recommended together with the specific literature.

3.4.2 Definition of the Target Results

For the prediction of wind loads on conventional buildings or its parts, Tamura et al. [TNK08] suggest a classification into two applications with different requirements (see fig. 3.3):

1. **Wind loads on cladding**

   Peak wind pressure coefficients must be calculated from the CFD results (fig. 3.3(a)). Thereby, size effects have to be included. These can be evaluated by a filtering method or spatial integration [Arc04]. However, time history data of the fluctuating wind pressure, which can only be obtained by transient analysis, is necessary.

2. **Wind loads on structural frames**

   For the computation of the structural load, RANS and LES simulations can be used (fig. 3.3(b)). The loadings can be calculated by multiplying wind loads based on a mean flow field with a gust factor [Arc04] or by spectral analysis or time-history response analysis of time dependent data. Alternatively, the load on the structural frame can be computed directly, using methods of fluid-structure interaction.

This separation into a 'larger scale' point of view and a local point of view corresponds to the distinction found in building codes such as the DIN 1055-4 [Nor05a], where the computation of wind loads is separated for small surfaces areas (e.g. for $c_{pe,1}$) and larger surface areas (e.g. for $c_{pe,10}$), as explained in chap. 3.1.

The important consideration, which arises from the two approaches presented in fig. 3.3, is the decision, whether a time-dependent (transient) or a steady-state physical model will be necessary for the analysis. In general, with the use of further interpretation, steady-state results can be retrieved from transient analysis. Moreover, a time-dependent approach is considered to yield more accurate results than steady-state, time averaged simulations [FHJ+04]. Therefore, transient computations can be regarded as advantageous. However, to compute transient results an extremely higher computational effort is necessary compared to steady-state results. Therefore, the requirements of the analysis should be checked as a first step in CWE, in order to decide, which kind of target results shall be obtained from the simulation and what methods are necessary to compute these results.

In the scope of this work, Reynolds-averaged methods are used to describe the turbulent wind flow. As presented in section 3.2.3, the influence of turbulence is modeled by averaged turbulence quantities in RANS methods. Thereby, the effects of turbulence on a building can only be considered in averaged means. Accordingly, small scale fluctuations in wind speed and direction are not explicitly present in the model. Due to the missing representation of statistically sufficient fluctuations of wind turbulence of all important scales, it is not

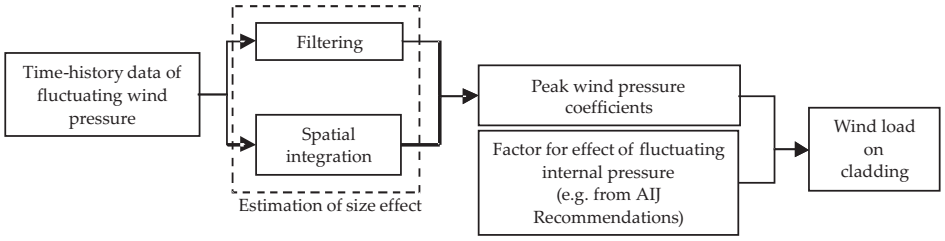

(a) Procedure for estimating wind loads on cladding using CFD.

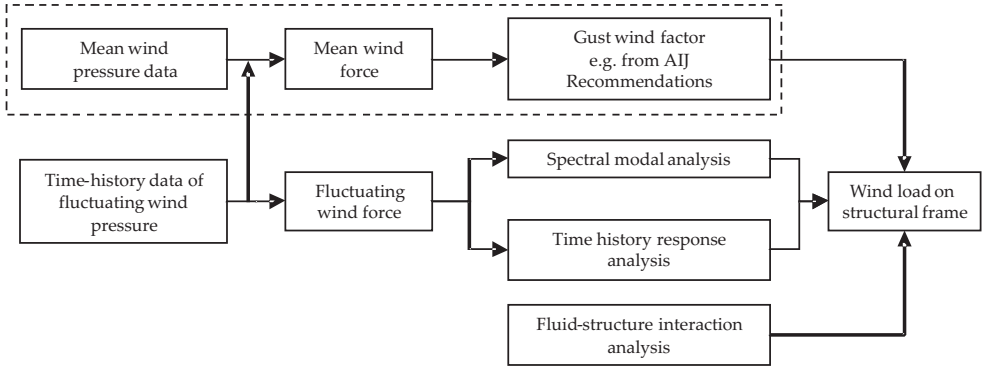

(b) Procedure for estimating wind loads on structural frames using CFD.

Figure 3.3: AIJ recommendation for the prediction of wind loads using CFD. [TNK08]

possible to directly generate design loads based on RANS computations, as illustrated in fig. 3.3.

Therefore, the current work can be considered along the upper line of fig. 3.3b in determining the mean wind load. Within this chapter, this is done by computing c_p values for the membrane structure. Additionally, the computation of dimensionless c_p values enables a comparison with wind tunnel experiments. Further consideration of the significance and applicability of the obtained results are discussed in section 5.2.

3.4.3 Properties of the Neutrally Stratified Atmospheric Boundary Layer

In order to correctly model the wind flow within an Atmospheric Boundary Layer (ABL) in a numerical model, the main characteristics of the ABL wind flow have to be understood. Therefore, preceding further consideration of the CFD models in CWE, in this section, the distribution of velocity, turbulence, and reference wind speed of the ABL is discussed.

The friction of air moving over the ground influences the wind flow, which results in the ABL wind flow. The depth of the atmospheric boundary layer varies between a few hundred meters and several kilometers, depending on wind velocity, roughness of terrain, and angle of latitude [SS96]. The properties of the air flow within the atmospheric boundary layer are essential for wind engineering as buildings are located on the Earth's surface, thus within the ABL. In the following section, the properties of the atmospheric boundary layer shall be analyzed. The focus of the analysis lies on a neutrally or stably stratified atmospheric boundary layer as it is characteristic for strong wind events. The characteristic

of a neutrally stratified atmospheric boundary layer is, that the mechanically produced turbulence is dominant over the convective turbulence produced by an unstable temperature gradient over height [Ver06]. Accordingly, effects due to convective instability and thermal mixing through convection can be neglected. Thereby, the correct prediction of wind effect due to local meteorological events, such as thunderstorms or tornados, is only limited for analysis based on the neutrally stratified ABL.

3.4.3.1 Mean Velocity Profiles

Analyzing the air flow around a building, as a first step, a constant thickness and horizontal homogeneity of the boundary layer flow can be assumed [SS96]. The boundary layer itself can be divided into three different sublayers:

- ◇ laminar / viscose sublayer on the ground
- ◇ Prandl-layer or surface layer
- ◇ the Ekman-layer

The thickness of the Prandl-layer is assumed to be 10-15% of the thickness of the atmospheric boundary layer. Within the Prandl-layer, the deviation of the flow direction to the gradient flow direction, which occurs due to friction of the air flow on the surface and the Earth's rotation, is regarded as constant with an angle between 6° and 30° in the northern hemisphere [Zur69, SS96]. Within the Ekman layer, Lawson [Law80] suggests a linear relation between a decreasing effect of this deflection and an increasing height. As a consequence, except for super tall buildings, the deflection of the wind flow over height, and thus, the change of wind direction over the height of a building, has a negligible influence on the wind load assumptions [Hol04, SS96].

The logarithmic law

With the knowledge about the distribution of wind speed over height, the wind speed at any specific height in the ABL can be determined, if a reference wind speed at a specific height is specified. According to the World Meteorological Organization (WMO), the reference mean wind speed is measured at a height of $10m$. To describe the wind speed distribution over height, two approaches are common: the power law and the logarithmic law. Currently, the logarithmic law is regarded as superior to represent strong wind profiles in the lower atmosphere. The effects of the earth's rotation, the Coriolis force, and the molecular velocity are neglected [Hol01].

Similar to the boundary layer flow over an arbitrary even surface, the wind velocity distribution over the ground can be described by a logarithmic law using eq. 3.104. Thereby, the logarithmic law has a profound theoretical basis for fully developed flow over homogeneous terrain. However, the supposed ideal flow and surface conditions are rarely met in practice.

$$\overline{u}(z) = \frac{u_\tau}{\kappa} ln(\frac{z}{z_0}) \tag{3.104}$$

Eq. 3.104 describes the mean wind speed $\overline{u}(z)$ depending on the height z over ground, z_0 as the roughness length, and κ as the Kàrmàn's constant, which is generally assumed as $\kappa \simeq 0.4$. u_τ is the frictional velocity and related to the ground roughness. It can be determined by using eq. 3.105:

$$\tau_0 = \rho u_\tau^2 \tag{3.105}$$

with τ_0 as the ground shear force and ρ as the density of air. For practical purposes, eq. 3.106 can be derived from eq. 3.104 in order to relate the wind speed at a certain height to the reference wind speed:

$$\frac{\overline{u}(z)}{\overline{u}(z_{ref})} = \frac{ln(z/z_0)}{ln(z_{ref}/z_0)} \tag{3.106}$$

The logarithmic law is only valid, if the height of the roughness elements is finite. Otherwise, a modification of equation 3.104 is necessary: the logarithmic velocity distribution is applied including an offset to the ground:

$$\overline{z} = z_g - z_d \tag{3.107}$$

where z_g is the height above the ground and z_d is a length known as the zero plane displacement. The quantity $\overline{z}$ is called the effective height and used instead of z in eq. 3.104 and in eq. 3.106 respectively (see fig. 3.5).

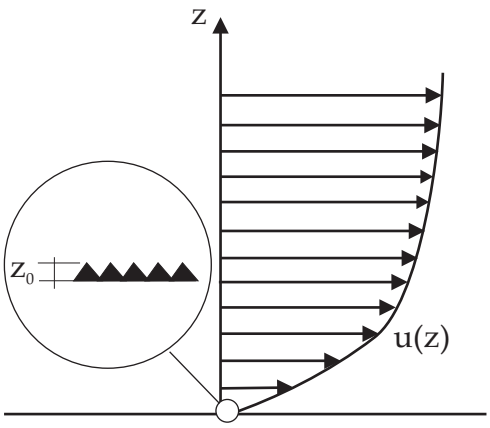

Figure 3.4: Velocity distribution in the boundary layer [Huc02]

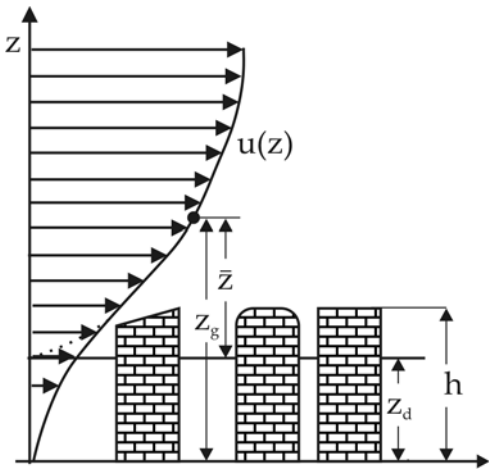

Figure 3.5: Roughness and effective height

The parameters z_0 and z_d are empirical and depend on the nature, height, and distribution of the roughness elements. The roughness length z_0 is a measure of the eddy size at the ground. Based on extensive full-scale measurement, the values in table 3.2 are suggested by [SS96] for surface roughness length z_0 (in conjunction with the assumption $z_d = 0$).

The zero plane displacement z_d can be estimated by a fraction of the height of the roughness elements, which is $\frac{z_d}{h} = \frac{2}{3}$ according to [Huc02], or $\frac{z_d}{h} = \frac{3}{4}$ according to [Hol01]. For practical purposes, the concept of the effective height introduces complications in that the logarithmic function can not be evaluated for a height z_g that is smaller than z_d and is difficult to integrate.

Type of Surface	z_0[m]
Sand	0.001-0.01
Snow surface	0.01-0.06
Mown grass (0.01 m)	0.01-0.1
Low grass, steppe	0.1-0.4
Fallow field	0.2-0.3
High Grass	0.4-1.0
Palmetto	1-3
Pine forest (mean tree height: 15 m; one tree per m^2)	9-10
Sparsely built-up suburbs	2-4
Densely built up suburbs, towns	8-12
Centers of large cities	20-30

Table 3.2: Values for surface roughness length [SS96]

Change of Terrain

When strong winds in a fully-developed boundary layer encounter a change of surface roughness, an adaptation of the flow occurs. After a certain transition zone, the shape of the velocity distribution has the characteristics of the new terrain. The length of the transition zone is in the range of several hundred meters to several kilometers. Detailed approaches with regards to the size of the transition zone and the velocity distribution within this zone can be found in [Hol01, SS96, Soc94].

3.4.3.2 Turbulence in the ABL Flow

The wind over the ground is not homogenous in time and space. At a certain height, the wind is subject to local variations of speed and direction. Momentary increases in wind speed are called wind gusts. Due to this fluctuating behavior, properties of wind within the atmospheric boundary layer are described by statistical methods. Wind speed in the three spacial directions x, y, z is divided into constant mean wind speeds $\overline{u}_i$ and time-dependent turbulence components u_i' representing the fluctuation in wind speed:

$$u_i(t) = \overline{u}_i + u_i' \tag{3.108}$$

The mean wind speed $\overline{u}_i$ is calculated as:

$$\overline{u}_i = \frac{1}{\Delta T} \int_{t_0}^{t_0+\Delta T} u_i(t)\, dt \tag{3.109}$$

with $\overline{u_i'(t)} = 0$. $\overline{u}_i$ is dependent on the averaging time interval ΔT. For a smaller averaging time, a higher maximum wind velocity is determined.

Turbulence Intensity:

The ratio of the standard deviation σ_{u_i} of the fluctuating component and the mean wind speed is known as the turbulence intensity of that component:

$$I_i = \frac{\sigma_{u_i}}{\overline{u}_i} \tag{3.110}$$

with $\sigma_{u_i} = \sqrt{\frac{1}{\Delta T}\left(\int_0^{\Delta T} [u_i(t) - \overline{u}_i]^2 \; dt\right)}$ and ΔT as averaging time interval.

As the frictional effect of the surface roughness decreases with increasing height, so does the turbulence intensity. Approximately, I_1, the turbulence intensity in longitudinal direction at a certain height z, can be determined by eq. 3.111.

$$I_1 = \frac{1}{ln(z/z_0)} \tag{3.111}$$

The lateral and vertical turbulence intensities I_2 in lateral direction and I_3 in vertical direction are usually smaller than the longitudinal turbulence intensity I_1. Estimated ratios for the turbulence intensities in different directions are presented in table 3.3.

Source	I_1	I_2	I_3
[Soc94]	1	0.75	0.5
[Hol01]	1	0.88	0.55

Table 3.3: Ratio of longitudinal to lateral and vertical turbulence intensity.

For a time-dependent numerical analysis, the fluctuation of the velocities has to be explicitly represented in the numerical model. Therefore, additionally to the turbulence intensity, the following characteristics of the ABL flow have be be considered:

◇ **Spectrum of turbulence**

The energy of turbulence varies over the frequency of the turbulent effect. The spectral density of turbulence is used to describe this distribution of turbulent kinetic energy over a frequency range. The spectral energy distribution of the wind turbulence is of high interest for a comparison with building eigenfrequencies, in order to assess the possible excitation of vibrations due to buffeting effects.

◇ **Spatial correlation of turbulence**

The spatial correlation of wind turbulence enables the determination of gust sizes by relating the velocity at two different points in space, e.g. two points on the surface of a building. This is an important quantity for the calculation of fluctuating wind loads for big size constructions, such as large roofs or tall towers.

3.4.3.3 Determination of the Reference Wind Speed

In section 3.4.3.1 and section 3.4.3.2, the relative distribution of velocity and the turbulence intensity in the ABL were presented. However, no indication has been provided about the scale of the occurring wind speeds.

For making a rational decision in the design process on the magnitude of wind loads, the extreme wind conditions, which might affect the structure during its lifetime, have to be estimated. Procedures for estimating extreme winds are based on probabilistic methods applied on parent data measured by meteorological stations. According to extensive measurements, the total population of wind speed is usually fitted by a Weibull-type distribution [Soc94, Hol01, Law80]. The asymptotic extreme value distribution for the Weibull parent distribution is the Gumbel (extreme value type I) distribution. However, since the events of high wind speeds measured in the parent data are generally not statistically independent , it proved to be advantageous to consider only the annual maxima of the wind speed and fit these measurements to an appropriate probability distribution [Soc94, Hol01].

Within this work, the reference wind speed of the German DIN 1055-4:2005-3 [Nor05a] is used as average wind speed at a height of 10 m. In DIN 1055-4:2005-3, the map of Germany is divided into four zones with different reference wind speeds. For each wind zone, a specific reference wind speed u_{ref} is given. u_{ref} is derived by averaging the wind speed in a time-interval of 10 minutes at a height of 10 m for a terrain category II, which corresponds to a surface roughness length of $z_0 = 0.05$ (see tab. 3.2). The probability of exceedance of the mean wind speed within one year is 0.02, which corresponds to return period of 50 years. It should be noted, that u_{ref} is not the design wind speed according to DIN 1055-4:2005-3.

3.4.4 Definition of the Physical Model

In virtually all practical aerodynamic problems, the fluid can be assumed to be Newtonian [And08]. Density fluctuations in conservation of mass equation are ignored, since the considered flow is substantially subsonic [PSN97]. Navier-Stokes equations for Newtonian fluid and non-compressible flow condition can be applied (eq. 3.25, 3.26).

CWE features a fluid with a low viscosity in large domains at moderate fluid velocities. This postulates a highly turbulent flow with high Re-numbers. Therefore, Direct Numerical Simulation (DNS) is not possible, since in practice, the resolution of all relevant scales of turbulence is not possible.

RANS based turbulence modeling

The most widely used approach for turbulence model in CWE is RANS, based on the Reynolds averaged Navier-Stokes equations (eq. 3.38) introduced in section 3.2.3. The use of the standard k-ϵ turbulence model in its original form is not recommended due to the stagnation point anomaly discussed above. Improved models such as the renormalization group (RNG) k-ϵ turbulence model [YO86] (e.g. applied in [ZGZ05]), the realizable k-ϵ turbulence model [SLS$^+$95] (e.g. applied in [SvBRO02]), or the SST k-ω turbulence model [Men93] (e.g.

applied in [LAF08]) are preferable. Besides the choice of turbulence modeling, the adjustment of the parameters used in these models can significantly increase their performance [Lóp02], [YQX+08]. Nonlinear eddy viscosity models are expected to provide better results, as they are able to model anisotropy in the Reynolds stresses [FHJ+04]. In a comparison of non-linear models, Ehrhard et al. [EKM00] found only one model suitable for application to ABL flow and ascribed this fact to a lack of calibration towards CWE of the other models. Reynolds stress models showed higher computational effort due to additional transport equations and to the requirement of high quality computational grids [FHJ+04]. Comparisons of the performance of different RANS based turbulence models can be found among others in [Mur97], [RHS01], [Sta97], [Unh04], [Eas00], [LAF08]. These comparisons come to different, sometimes contradicting conclusions about the performance of RANS models for different types of applications.

Models used for statistically steady RANS can be extended for time dependent simulations to Unsteady RANS (URANS) models. This allows for simulating temporal changes in the flow field. Since URANS requires a rather high spatial resolution, LES and DES simulations are usually preferred for unsteady simulations [FHSC07].

LES based turbulence modeling

Recent increase in computational power as well as algorithmic improvements are providing the possibility of carrying out LES simulations for flow around actual shaped buildings within a reasonable computational time [TNK08]. For bluff body flows, LES or hybrid methods such as DES are expected to provide better results at higher computational costs compared to RANS models [Rod97] [FHJ+04] [XC06]. In contrast to RANS, in an LES / DES simulation, not only data about the mean flow field, but also more detailed information about fluctuations in the flow are acquired. This enables a detailed analysis, especially with respect to extreme values. However, in order to derive highly detailed results, boundary conditions with the same level of detail are required. Otherwise, for example for insufficient modeling of inflow turbulence, Tamura et al. [TNK08] found LES simulations to give worse results, as compared to RANS. The requirement of highly resolved and well documented boundary conditions is difficult to meet, as data of this quality is rarely available in CWE [FHSC07].

3.4.5 Definition of the Computational Domain.

The setup of the computational domain defines the area in which the CFD analysis is conducted. For a detailed discussion and literature review of the definition of the computational domain, see [FHJ+04], [Fra06], or [FHSC07].

The real world ABL extends for a considerable distance over the Earth's surface and has a height of several hundreds of meters. Because of limitations in computational resources and the complexity of the required meteorological models, a CFD simulation can only represent a smaller finite horizontal distance and a limited height in the computational domain. This computational domain has to be big enough to enclose the area of interest and large enough to contain the largest energetically relevant flow structure [FHSC07]. The

environment around the computational domain has to be represented or approximated by appropriate boundary conditions.

Obstacles, such as buildings, topology, or large plants in front of the area of interest shall be explicitly modeled, if their distance to the building of interest d_n is smaller than $6-10$ times their height H_n [FHSC07].

3.4.5.1 Size of the Computational Domain

Since the computational domain can be seen as the resemblance of an experimental wind tunnel, requirements similar to those for experimental wind tunnels can be identified. In the following, a computational domain with a rectangular floor plan is assumed.

The cross-section of the computational domain around the area of interest has to be large enough, so that it does not influence the flow conditions at the buildings. According to [Fra06], the distance above the area of interest is recommended to be $5-6H_{max}$ with H_{max} as the maximum height of the buildings. For the lateral direction, a distance of $5H_{max}$ is recommended. For a building with a quadratic cross section (height = width), this leads to a cross section area of the computational domain of

$$A_{QS} = (5-6)H_{max} \cdot ((2 \cdot 5H_{max}) + H_{max}) = 55 - 66H_{max}^2 \tag{3.112}$$

and to a blocking ratio of

$$H_{max}^2 / A_{QS} \cdot 100\% = 1.5\% - 1.8\%. \tag{3.113}$$

Generally, in CFD a minimum blocking ratio of 3% is recommended, which is more than fulfilled for the cross-section dimensions recommended here. In case the cross-section of the building's windward side is considerably large in its width as compared to its height, the cross-section of the domain should resemble this width / heigth-ratio.

In case of comparison with wind tunnel experiments, the computational domain should be chosen to represent the wind tunnel. Thereby, the CFD model can accurately resemble the geometry of the experiment. However, if the wind tunnel cross-section dimensions are larger than the dimensions given above, the size of the computational domain can be reduced.

If the inflow conditions are well-known, a distance of $5H_{max}$ between inflow boundary and area of interest should be kept. For unknown inflow conditions, the usage of a longer distance can allow a realistic flow establishment. Depending on the outflow boundary condition, the outflow boundary should have a distance of $10-15H_{max}$ from the area of interest to allow for flow development. Fig. 3.6 visualizes these required distances.

3.4.5.2 Level of Details

Details of buildings, such as facades and small structural members are of secondary interest compared to the overall mass distribution of the building and its surroundings. The level of

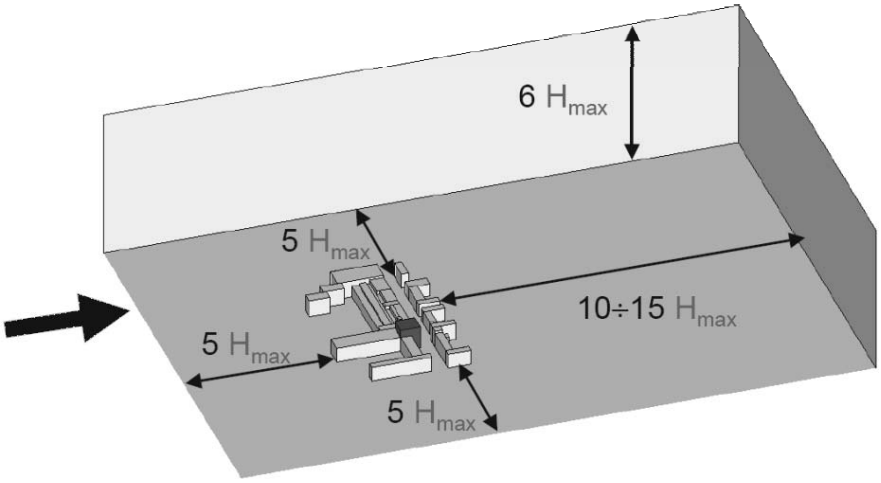

Figure 3.6: Recommendation for the dimension of the computational domain. [Fra06]

detail required for the surrounding can decrease with increasing distance from the area of interest. Generally, the required level of detail depends on the application and the specific area of interest. For example, modeling surface pressures on a roof has higher demands for level of detail than modeling of pollution dispersion from a high stack. The level of detail also depends on the possible grid resolution. General recommendations with respect of the level of detail are not feasible and, in case, sensitivity should be checked by a set of similar examples with different detail level.

3.4.5.3 Boundary Conditions

In contrast to wind tunnel experiments, the real world wind flow near the surface is not enclosed by boundaries other than the ground and can develop along a considerable distance to a neutrally stratified Atmospheric Boundary Layer (**ABL**). In a simulation, the appropriate boundary conditions have to account for the influence of the shorter length on flow development and the artificial surroundings limiting the modeled domain. The correct choice of the boundary conditions is crucial for the accuracy of the solution. However, these boundary conditions are usually not fully known. Therefore, the distance between the boundary and the area of interest has to be large enough, so that the uncertainties in the boundary conditions do not influence the solution [FHSC07].

Inflow boundary conditions

Information about the wind speed at the reference height can be taken from meteorological measurements or building codes. At the inflow condition, the flow of a fully developed, neutrally stratified ABL should be described, which corresponds to upwind terrain and can be characterized by the upstream surface roughness length z_0 introduced in section 3.4.3. To prescribe an ABL flow, the distribution of the mean velocity and also the distribution of turbulent quantities, e.g. for RANS simulations, the turbulent energy k and the dissipation rate ϵ, have to be included. For the standard k-ϵ turbulence model, Richards and Hoxey

[RH93] proposed the following distributions for a fully developed, neutrally stratified ABL:

$$u = \frac{u_*}{\kappa} ln\left(\frac{z+z_0}{z_0}\right) \tag{3.114}$$

$$k = \frac{u_*^2}{\sqrt{C_\mu}} \quad \text{with} \quad u_* = \sqrt{\frac{\tau_w}{\rho}} \tag{3.115}$$

$$\epsilon = \frac{u_*^3}{\kappa(z+z_0)} \tag{3.116}$$

with $\kappa = 0.4$ as the von Kàrmàn's constant, $C_\mu = 0.09$ as a constant of the turbulence model and τ_w as the shear stress, which is assumed constant throughout the boundary layer. In the case of comparison with wind tunnel results, the distributions measured in the experiment can be used.

For the accuracy of the simulation, it is essential, that the prescribed ABL flow-profiles are maintained up to the area of interest. With the use of standard turbulence models and wall functions this is generally not possible as velocity and turbulence profiles decay, even in the absence of obstacles [HW06]. This decay in velocity and turbulent quantities is mainly due to the roughness length used in the wall functions and the top boundary condition (see below). In order to achieve constant distributions of velocity and turbulent quantities over the length of the domain, the profiles obtained in a preliminary simulation of an empty domain with identical computational grid and periodic boundary conditions can be prescribed at the inflow boundary [WE99]. The parameters of this empty domain simulation have to be adjusted so that the resulting profiles fit the meteorological measurements. Additionally, roughness elements can be introduced into the empty domain to enhance the comparability with turbulence generation in wind tunnel experiments.

For unsteady simulations such as LES and URANS, time dependent inflow boundary conditions are required. Using periodic boundary conditions for the simulation of an empty fetch [TMP06] or a fetch with roughness elements [NT02] have been applied for LES simulations with success. Another possibility is to use statistical data based on measurements to generate a corresponding artificial inflow data [KMM97], [FKB$^+$08].

Wall boundary conditions

In wind engineering, the surface roughness is usually specified by the roughness length z_0. For the simulation of rough walls, many general purpose CFD codes use the roughness height k_s as measurement for the sand-roughness of a surface. For a fully rough surface and a logarithmic velocity profile, the relation of k_s and z_0 can be assumed as [FHJ$^+$04], [BSC07], [Fra06]:

$$k_s \approx 30 z_0 \tag{3.117}$$

Using this relation, the roughness height of flow in suburban ($z_0 = 0.3$ m) and urban ($z_0 = 1.0$ m) environment is in the range of $k_s = 9\text{ m} - 30\text{ m}$. In order to maintain the correct profile of the boundary layer flow, this roughness height should be maintained.

However, for the use of wall functions, the cell center closest to the wall is required to have distance larger than k_s to the wall. For ABL flow in urban territory, this leads to an

extremely large grid resolution close to the ground. Consequently, for the use of standard boundary conditions a dilemma between using the correct roughness height to maintain the ABL flow profiles and achieving an adequate grid resolution near the surface exists.

Hargreaves and Wright [HW06] used the commercial CFD codes Ansys CFX and Ansys Fluent with standard k-ϵ turbulence model and standard wall functions to analyze this problem. For the relation $k_s \approx 20z_0$, which allows for slightly better resolution than the ratio presented above, a significant change in the distribution of the turbulent kinetic energy along the flow direction of an empty fetch was found. Hargreaves and Wright state that this problem can only be resolved by the introduction of modified wall functions, e.g. those suggested by Richards and Hoxey [RH93]. Blocken et al [BSC07] experienced similar deviation of flow profiles and suggest several remedial measures for improvement.

Top boundary condition

The real world ABL flow is driven by the geostrophic wind, while its energy is removed by friction over the ground. For a neutrally stratified ABL this results in a constant shear stress of the height. Ideally, the flow in the computational domain should resemble this constant shear stress along the fetch. To achieve this, at the top boundary condition a constant shear stress, which corresponds to the chosen inflow velocity profile, is recommended [FHSC07]. Blocken et al. [BSC07] suggest prescribing the top values of the inflow profile to the top boundary along the whole domain.

Lateral and outflow boundary conditions

Lateral and outflow boundary conditions have to be chosen in an appropriate way, so that they don't influence the flow at the area of interest. Usually symmetric boundary conditions for the lateral boundaries are sufficient, if the distance between them and the area of interest is large enough.

Different boundary conditions can be used for the outlet boundary, assuming that the distance to the area of interest is large enough for the flow to develop.

3.4.6 Validation and Application

Assuming a well tested and certified software, the verification of the software and the numerical modeling is necessary. This includes studies on the domain size, mesh resolution, and applicability of turbulence modeling. To quantify numerical errors from the grid resolution, Franke et al. [FHSC07] suggest a systematic grid convergence study using Richardson extrapolation. If restrictions of the computational capacities limit a uniform refinement, studies on local grid refinement should be carried out. Generally, at least computations with two different settings of unknown or unsure modeling aspects should be tried in order to assess the sensitivities [Mea02], [Ver05]. Before the simulation over obstacles is done, analysis should be carried out, whether the chosen grid and boundary conditions are consistent and no substantial change in the specified ABL boundary profiles occurs [FHSC07].

Even in case of a well verified software and an experienced user, CFD-based results still have to be checked for correct physical modeling. Due to the uncertainties in the CFD simulation, especially for problems of wind engineering, as presented above, the validation of

the solution is an essential requirement. In the scope of design loads, CFD results without validation by experiments are still regarded as critical. Validation has to be carried out with respect to target values defined for the problem. Relative or absolute values can be compared. As a possibility to assess the difference between values from physical and numerical experiments, a hit rate is suggested by the VDI guideline [Ver05].

For the validation of CFD-based results, two possibilities exist:

- **Comparison with wind tunnel experiments**

  For the comparison with wind tunnel experiments, small scale models are simulated by CFD computations. The physical experiments have to fulfill certain criteria, with respect to completeness and accuracy of the measured data, to enable the comparison with CFD results. The well controlled conditions of the wind tunnel provide the possibility to derive steady-state results for the comparison with RANS models and time-dependent results for the comparison with URANS and LES models. The database CEDVAL [Met04] at the Hamburg University compiles high quality wind tunnel experiments for the validation of numerical dispersion models and is available online.

- **Comparison with full scale experiments**

  The comparison with full scale experiments is more difficult, since boundary conditions are most likely unknown or have large uncertainties. For the comparison with steady-state results, a constant flow condition is necessary, which is naturally only given for a time span of few minutes. This excludes to some degree the possibility for the validation of RANS models, which are based on time-averaging [TNK08]. The numerical simulation of highly turbulent wind flow around full scale buildings also requires an elaborate validation of the physical models used, as high computational effort poses limits to the computational domain and / or resolution.

Validated and, in case, adjusted simulations offer the possibility to extend the analysis based on the small scale wind tunnel models beyond the limits of physical wind tunnel experiments, e.g. more detailed analysis of the flow conditions or direct simulation of fluid-structure interaction. Parameter studies for modified geometries within some limits are also possible.

Furthermore, for similar problems with respect to geometry and flow regime, the modeling aspects of a validated problem can be extended to a slightly modified setup, enabling parameter studies on geometrical changes as well as reducing the validation effort for new examples. However, with decreasing similarity between the settings, the uncertainties about the modeling aspects increase.

3.5 Example: Static Wind Load Analysis of ARIES Using Ansys CFX

The numerical principles of Computational Fluid Dynamics, which have been introduced in section 3.3, are now applied to compute the wind loading on the ARIES canopy structure.

Thereby, the modeling aspects for the neutrally stratified atmospheric boundary layer flow in general and their application to wind engineering in particular are applied. For the flow simulation, the CFD software Ansys CFX 11 is used.

3.5.1 Ansys CFX Software Package

Ansys CFX is a commercial multipurpose CFD solver. Its originates in the program CFX-4, formerly known as Flow3D. Its developement started as an in-house code of the United Kingdom Atomic Energy Authority (UKAEA) as early as the late 1980s and was commercialized in the mid 1990s. Before becoming part of Ansys Inc. in 2006, CFX was developed by AEA Technology.

Ansys CFX is applied for a large range of applications, from analyzing flow around ship hulls to aircraft turbines. Computations in the scope of wind engineering, in which CFX is used, can be found, among others, in the works of Easom [Eas00], Knapp [Kna07], Yang et al. [YQX+08], and Wevers [Wev08]

For this research, CFX was chosen on basis of the following reasons:

- ◇ CFX has state of the art features of CFD computations.
- ◇ CFX is widely used in industry and thus has been validated for different test cases in various application areas.
- ◇ CFX is subject to steady development and rapid implementation of new models and methods for CFD simulation.
- ◇ CFX software support, formerly performed by AEA Technology and later by Ansys Inc., enabled the implementation and realization of a multi-physics environment using the in-house CSD code CARAT.

In contrast to the standard discretization scheme for the Finite Volume Method (FVM), presented in section 3.3.1, the control volumes (CVs) used by CFX are not identical to the grid volume elements. CFX uses the grid nodes as centroids of its CVs, which is illustrated in fig. 3.7 for a 2D case.

Surface and volume integrals are evaluated for the surface and volume parts, in the 2D case in fig. 3.7 on the four gray surface parts. Ansys CFX uses a co-located (non-staggered) grid layout. In order to avoid oscillations in the pressure field caused by the decoupling of the pressure field, the advection velocity at each integration point is modified. More details about the CFX solver theory are available in the respective documentation [CFX06].

CFX offers several options for the discretization of the convective term. In the following computations, a first solution was obtained using the Upwind Advection Scheme. This solution was used for preconditioning further simulations as initial value data. All final results were computed using the High Resolution Scheme, which is first order accurate near discontinuities and otherwise second order accurate.

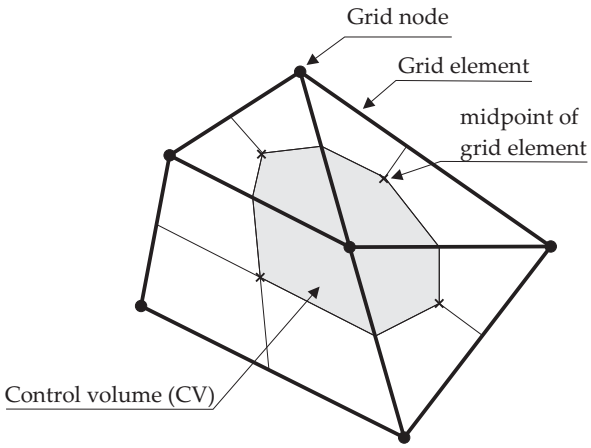

Figure 3.7: Control volume definition in Ansys CFX.

Fig. 3.8 shows a flowchart of the solution scheme used by CFX in the case of moving meshes. The coefficient iteration loop is the solver loop and the time-step loop runs over all time-steps, until the specified maximum simulation time is reached. The solution of the mesh displacement for the ALE approach, as explained in section 4.5.2, can be performed before every new time-step or before every coefficient interaction step. This feature will be elaborated on in section 4.5.2.

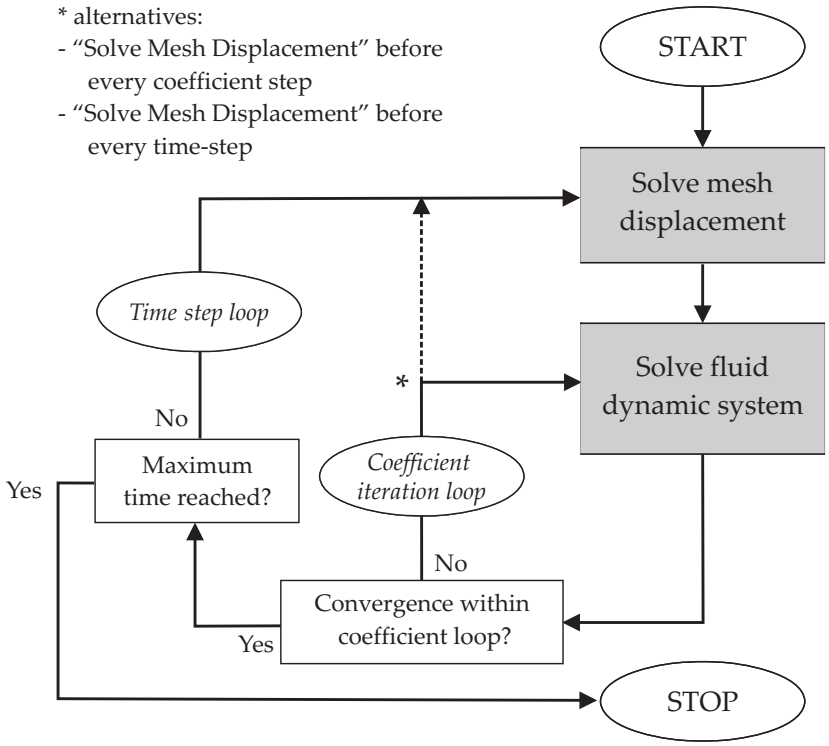

Figure 3.8: Solution scheme of Ansys CFX.

3.5.2 Example Setup

The wind effect on the ARIES canopy structure shall be analyzed using CFX. The best practice guidelines, which have been introduced above, are followed to realize an appropriate ABL flow.

Numerical full scale analysis

As the structure should be subject to analysis of fluid-structure interaction, the usage of a downscaled structural model, such as used in the wind tunnel, is not possible. This is due to the model laws, which have to be fulfilled for a small scale model, if it should represent the static and dynamic behavior of the structural model. Even so, the setup of an equivalent small scale model in a numerical way is much easier than the one for a physical experiment, it still introduces further complications and uncertainties. Therefore, a full scale structural model, which was already introduced in section 2.4, is applied.

The geometry of the full scale structural model is used for the resemblance of the rigid canopy structure in the CFD computation. The lattice cantilevers supporting the membrane are not modeled in the CFD computation. Only the membrane and the tribune resemble the canopy structure. Within this work, it is assumed that the flow conditions around the membrane structure do not significantly change whether the lattice structures are included or not. For considerations about the wind pressure on the lattice structure, which arise for the computations of fluid-structure interaction, it is further assumed, that the majority of the loads are due to the wind effects on the membrane. Thus neglecting the cantilever structures is expected to have a limited effect on the results. The tribune is included in the CFD model, since it has a crucial influence on the flow conditions at the lower end of the membrane.

Wind directions and conditions

Same as in the wind tunnel experiments, in the CFD computation the wind direction of interest is parallel to the axis of symmetry of the ARIES structure. The wind directions are named "wind from the front" and "wind from the back" with respect to the canopy structure. The "wind from the back" situation is with main fluid flow in positive x-direction, and "wind from the front" with the main fluid flow against the positive x-direction with respect to fig. 3.10.

Upstream of the canopy structure, no large objects are assumed. The canopy is placed on a terrain category 1 according to DIN EN1055-4.2005-03 [Nor05a]. This corresponds to the location next to a large lake or on a flat countryside without large obstacles. The upstream roughness length is assumed to be $z_0 = 0.01\text{m}$. The location is chosen to be in Germany in wind zone II, which provides a reference wind speed of $u_{ref} = 25\ \text{m/s}$ for a 10 minute-average measurement at a height of 10 m above the ground with the exceedance probability of 2% in one year (see section 3.4.3.3).

3.5.2.1 The Computational Domain

The general idea in setting up the computational grid for the CFD simulation is to introduce two domains with different discretizations:

- ◇ One larger outer domain with coarse discretization and hexahedral control volumes.
- ◇ One smaller inner domain, which contains the canopy structure, with finer discretization and tetrahedral as well as prism type control volumes.

For the analysis of the two wind directions of interest, the same outer domain is used. The inner domain is rotated by 180° around the vertical axis. Thus, without major changes in the setup of the computational domain and its discretization, both wind directions can be analyzed.

Outer domain

A coarser discretization is applied in the outer domain. On the one hand, this enables a reduction in computational effort, as less finite volume elements are used, and therefore, less degrees of freedom need to be computed. On the other hand, the requirement for the correct functioning of the wall functions concerning the distance of the first CV centroid from the rough wall is met by a coarse discretization at the lower boundary of the domain. For the discretization of the outer domain only hexahedral elements are used. Close to the boundaries of the inner domain, the element size is reduced, while towards the inlet and the outlet boundary, the element size in longitudinal direction is increased.

The outer domain is created large enough to minimize the influence on the boundaries, as explained in section 3.4.5.1. Compared to fig. 3.6, the recommended distance to the lateral boundaries is slightly decreased, while a blocking ration of $\approx$ 1.7% is reached. Fig. 3.9 presents the dimensions of the outer domain and a resemblance of the computational grid.

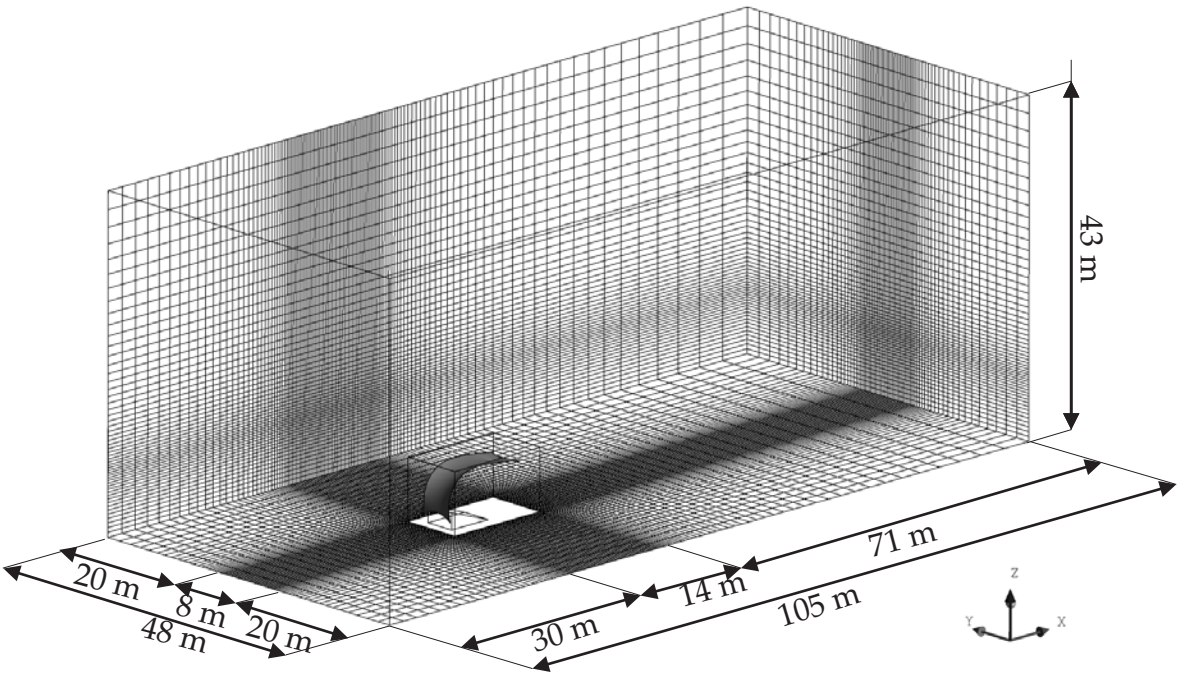

Figure 3.9: Outer domain: dimensions and discretization for "wind from the back"-setup

Inner domain

In the inner domain, a fine mesh resolution is applied. As explained above, for the CFD computation, the lattice cantilever beams supporting the structure are neglected and thus only the membrane itself and the tribune are modeled. The complex, doubly curved membrane geometry motivates the use of tetrahedral finite volume elements. Close to the membrane and the tribune, surface layers consisting of prism elements are applied to ensure a sufficient resolution of the boundary layer for a good prediction of flow separation. The dependency of the solution was checked for three different grid densities.

Fig. 3.10 shows the inner domain and the surface discretization of the membrane, tribune, and floor. In fig. 3.11, a cross-section through the middle of the inner domain is presented, showing the computational grid with boundary resolution by prism layers. Fig. 3.12(a) provides a detailed view of the boundary layer resolution of the membrane, while fig. 3.12(b) shows the surface discretization of the upper side of the membrane at the cone.

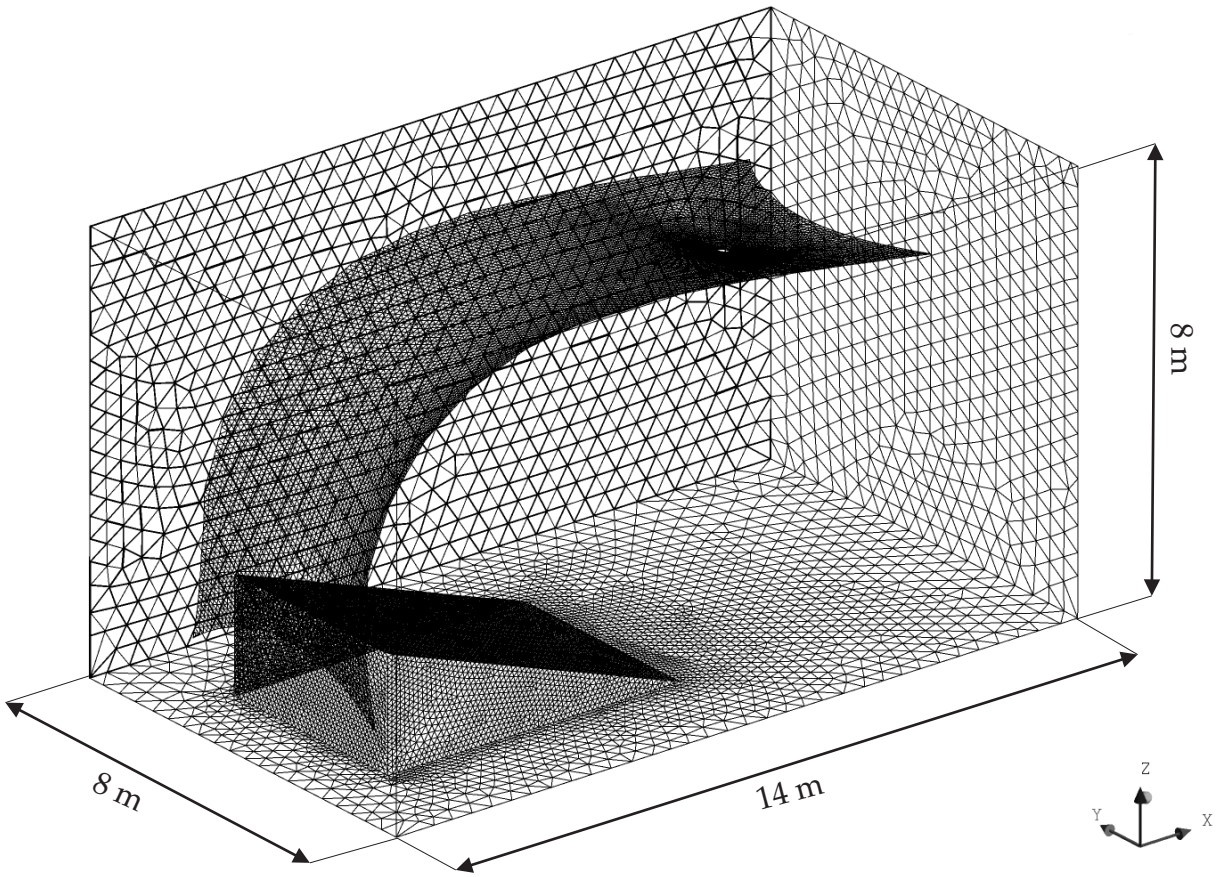

Figure 3.10: Inner domain: dimensions and selected surface discretization.

Inner and outer domains are connected via General Grid Interface (GGI) function, available in the CFX solver. GGI allows to connect multiple fluid domains for one computation with non-matching grid interfaces. Therefore, these domains can feature different mesh

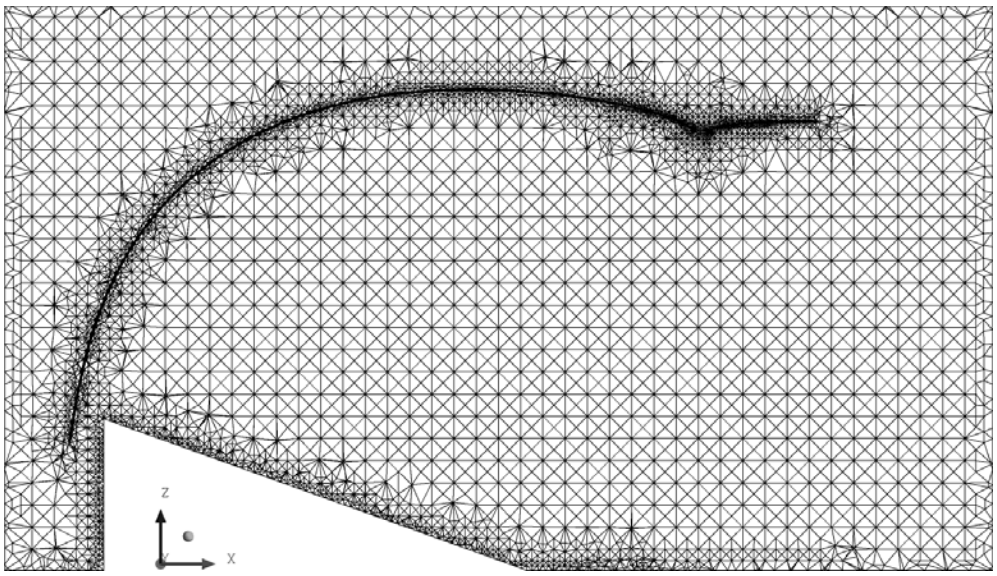

Figure 3.11: Inner domain: cross-section with discretization.

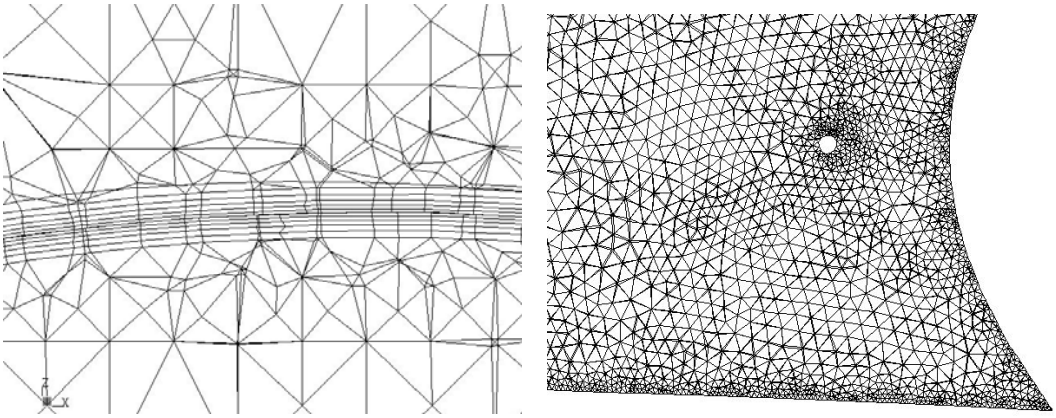

(a) Inner domain: boundary layer resolution

(b) Inner domain: surface resolution of the membrane

Figure 3.12: Inner domain: detailed views of the computational mesh.

topologies and allow for the selection of the best suited meshes for different parts of the geometry. The GGI interface treatment claims to be conservative with respect to fluxes across the interface surface, such as mass, momentum, energy, etc. Further details about the GGI domain interface function can be found in [CFX06]. The GGI interface function is applied on the respective five interface sides between the outer and the inner domains.

3.5.2.2 Boundary Conditions

The boundary conditions are selected to create and maintain an ABL flow along the computational domain.

At the inflow boundary condition, velocity and turbulence are prescribed according to Richards and Hoxey [RH93]:

$$u_{x,\text{inlet}}(z) = \frac{u_*}{\kappa} ln\left(\frac{z+z_0}{z_0}\right) = 3.61912\ ln(100\ z+1)\ \left[\frac{m}{s}\right] \tag{3.118}$$

$$k_{\text{inlet}} = \frac{u_*^2}{\sqrt{C_\mu}} = 6.9856\ \left[\frac{m^2}{s^2}\right] \tag{3.119}$$

$$\epsilon_{\text{inlet}}(z) = \frac{u_*^3}{\kappa\ (z+z_0)} = \frac{7.5845}{z+0.01}\ \left[\frac{m^2}{s^3}\right] \tag{3.120}$$

where z is the height over ground, u_x the velocity component in x-direction, u_y and u_z are prescribed as 0 m / s at the inflow boundary. [3]

The top boundary of the outer domain is modeled not as a wall but as an inlet boundary condition. The velocities $u_x = u_{x,\text{inlet}}(z_{max})$, with z_{max} being the height of the domain and $u_y = u_z = 0$, are prescribed. Furthermore, $k_{\text{inlet}}(z_{max})$ and $\epsilon_{\text{inlet}}(z_{max})$ are prescribed. As explained in section 3.4.5.3, the ABL flow profile is better maintained using this modeling, as compared to a simple wall boundary condition at the top of the domain.

At the outflow boundary, an average static pressure of 0 Pa is prescribed. The lateral side boundaries are modeled as symmetry boundary conditions.

At the bottom of the outer domain, a no-slip wall boundary condition with a roughness height of $k_s = 30 \cdot z_0 = 0.3$ m is specified (see section 3.4.5.3). The height of the first element close to the ground in the outer domain is chosen as 0.6 m , in order to ensure the applicability of the rough wall function. In the inner domain, a smooth no-slip wall boundary is assumed for the bottom of the domain.

The membrane's upper and lower sides are modeled as no-slip wall boundaries.

3.5.2.3 Applied Models

The $k-\omega$ Shear Stress Transport (SST) turbulence model introduced in section 3.2.3.1 is used. A rough wall function is applied at the bottom of the outer domain. [4] For non-slip walls of the inner domain, a "Scalable Wall Function" is used. This wall function provides the possibility of a fine boundary layer discretization by limiting the application of a wall function, if the first node close to the wall lies within the viscous sub-layer.

The fluid is air with a density of $\rho = 1.185$ kg / m^3 and a dynamic viscosity of $\mu = 1.831\ 10^{-5}$ kg / (m s). The density of the fluid is assumed constant and thus the fluid flow is incompressible. The reference pressure is set to 0 Pa.

The computation is steady-state. Accordingly, a steady-state inflow is assumed with time averaged turbulence quantities. The convergence criterion is the RMS of the transport quantities and the convergence limit is set to 10^{-5}.

[3] u_* is determined by solving eq. 3.114 with u_x(z=10 m) = 25 m / s.

[4] The rough-wall function based on the k-ω turbulence model exists only as a beta feature and was applied with the help of Ansys Support.

3.5.3 Results and Discussion

For the analysis of the canopy structure towards wind loadings, the quantity of prime interest is the surface pressure on the membrane. The surface pressure is described by computing dimensionless pressure coefficients, the c_p-values. This enables the comparison with data from experimental wind tunnel testing.

In order to be able to judge the quality of the simulation results with respect to the accurate representation of the atmospheric boundary layer, a preliminary analysis was carried out using an empty domain. Subsequently, the same discretization as for the empty domain was applied to model the flow conditions around the ARIES structure.

3.5.3.1 Preliminary Analysis Using Empty Domains

In the full setup, including the membrane structure and the tribune, quality of the flow with respect to the fully developed, neutrally stratified ABL is very difficult to assess, as flow effects caused by the obstacle overlay the ABL flow. Therefore, as discussed in section 3.4.5.3, a preliminary analysis of the empty domain was carried out. In order to account for the influence of the specific computational grid in this preliminary analysis, the same spatial discretization as for further computations is used. For the outer domain exactly the same computational grid is applied. In the inner domain, the membrane and the tribune were treated as non-existing and the prism-layers around the surfaces were removed. Otherwise, the grid in the inner domain remained unchanged, still featuring the unstructured computational grid adapted to the shape of the membrane structure.

For the qualitative analysis of the neutrally stratified ABL flow through the empty channel, the development of the turbulent kinetic energy k, the dissipation rate ϵ, and the velocity component in flow direction u_x are plotted. Fig. 3.13 shows the position of the significant vertical lines located in the symmetry plane in x-z-direction of the channel. Along these lines, the relevant quantities are plotted in fig. 3.14, fig. 3.15, and fig. 3.16. The figures with index (a) provide a plot over the full height of the channel, and those with index (b) give a detailed view in front and within the inner domain.

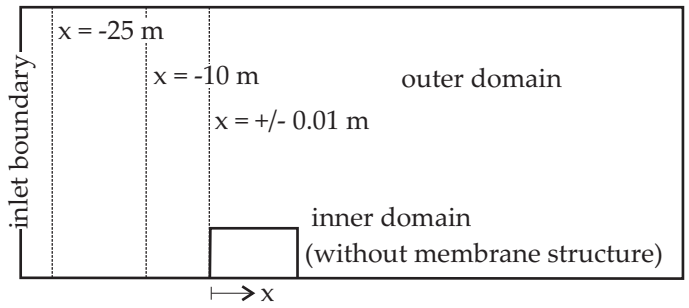

Figure 3.13: Location of lines for evaluation of flow quantities in the empty domain.

Up to the beginning of the inner domain, the velocity profile u_x in the main flow direction is equally well preserved over the complete height and in the detailed view. Compared to

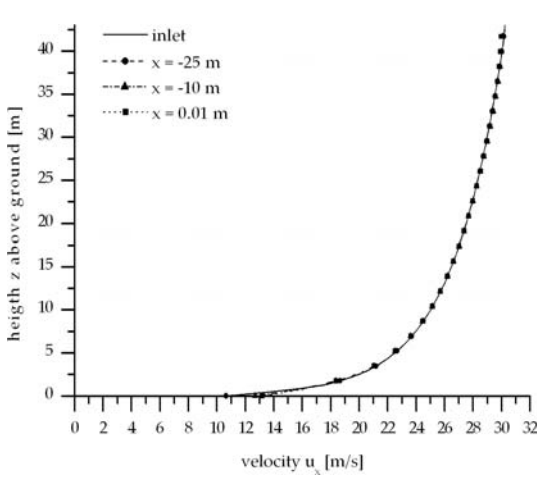

(a) Profiles upstream of the inner domain.

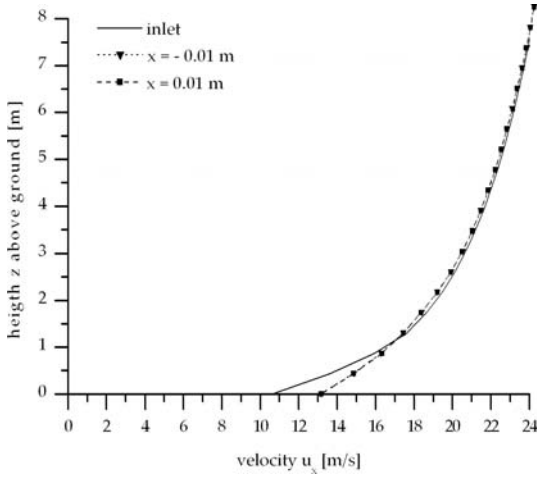

(b) Detailed profiles at the inner / outer domain interface.

Figure 3.14: Changes in the profile of the velocity u_x in the main flow direction.

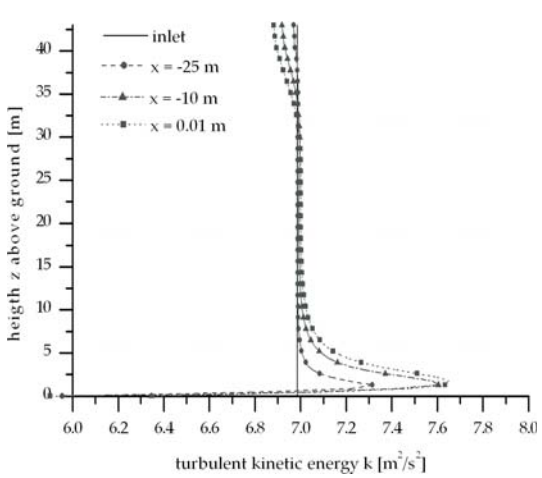

(a) Profiles upstream of the inner domain.

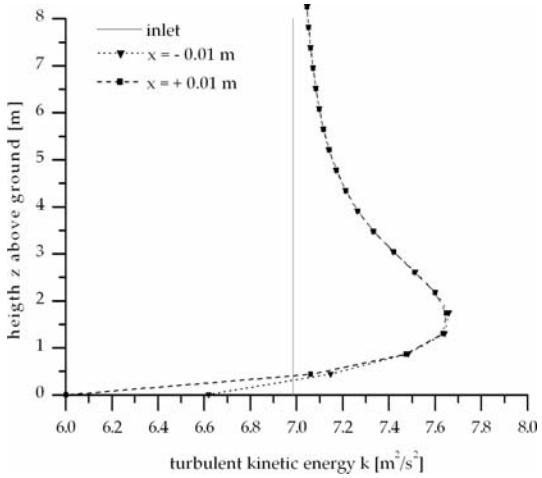

(b) Detailed profiles at the inner / outer domain interface.

Figure 3.15: Changes in the profile of the turbulent kinetic energy k.

the velocity profile at the inlet, in 3.14(b) , a slight increase in the velocity gradient du_x / dz is noticeable. It is caused by the wall function used at the bottom of the outer domain.

In the ideal fully developed, neutrally stratified ABL, the distribution of the turbulent kinetic energy over the height of the channel is considered as constant (see section 3.4.5.3). In the computation, the profile of the turbulent kinetic energy k shows a significant peak close to the ground in fig. 3.15(a) . The peak increases with the distance to the inlet boundary. This distortion of the profile is commonly noticed in the application of generic RANS-based turbulence models with wall-functions and resembles an over production of turbulence by the wall function. Similar results can be found, among many others, in [BCS07], [HW06], and

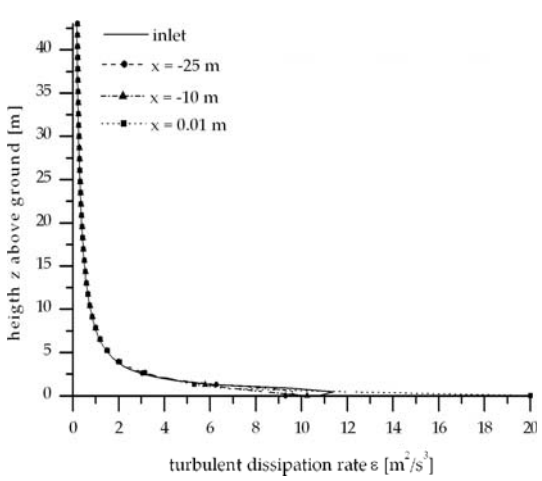

(a) Profiles upstream of the inner domain.

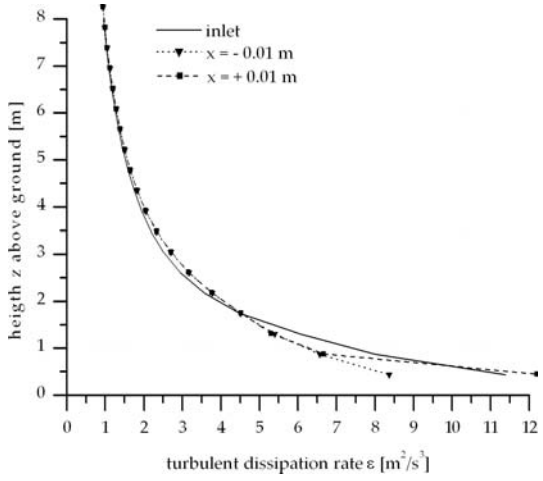

(b) Detailed profiles at the inner / outer domain interface.

Figure 3.16: Changes in the profile of the dissipation rate ϵ.

[YQX+08]. The detailed view of fig. 3.15(b) shows, that the over production of turbulence is significant in the lower parts of the flow. The maximum distortion, compared to k of the fully developed, neutrally stratified ABL, is 15.6 %. With greater distance to the ground, the profile of the turbulent kinetic energy returns to the expected value and only slightly differs at the end of the domain.

The turbulent energy dissipation rate ϵ shows a typical singular behavior towards the ground in fig. 3.16. Overall, the profile of ϵ is assumed as well preserved in the channel.

Within the inner domain, the flow quantities change rapidly as a result of the smooth wall boundary condition specified at the bottom of the inner domain. Behind the inner domain, the velocity u_x and dissipation rate ϵ quickly regain similar profiles compared to those presented in fig. 3.14 and fig. 3.16. Further distortions are visible in the turbulent energy k in and behind the inner domain.

To overcome the deterioration of the profile of flow quantities compared to those of the fully developed, neutrally stratified ABL, in section 3.4.5.3, different techniques were discussed. For the current application the author regarded the flow profiles as sufficiently accurate for further computations.

3.5.3.2 Visualization of the Flow Field Around the Structure

Following the preliminary analysis of empty domains, the flow around the rigid ARIES structure is simulated. Here, selected results from the CFD computation are visualized and briefly discussed. As it is generally the case in wind engineering, surface pressures, which act as suction, have a negative sign, while those "pushing" on the surface have a positive sign.

Wind from the back side of the ARIES structure

As results from the simulation of wind from the back side of the structure, velocity vectors in the symmetry plane and the surface pressure on the upper side of the membrane are shown in fig. 3.17. Fig. 3.17 gives an overview of the pressure distribution around the membrane, mapped on the symmetry plane.

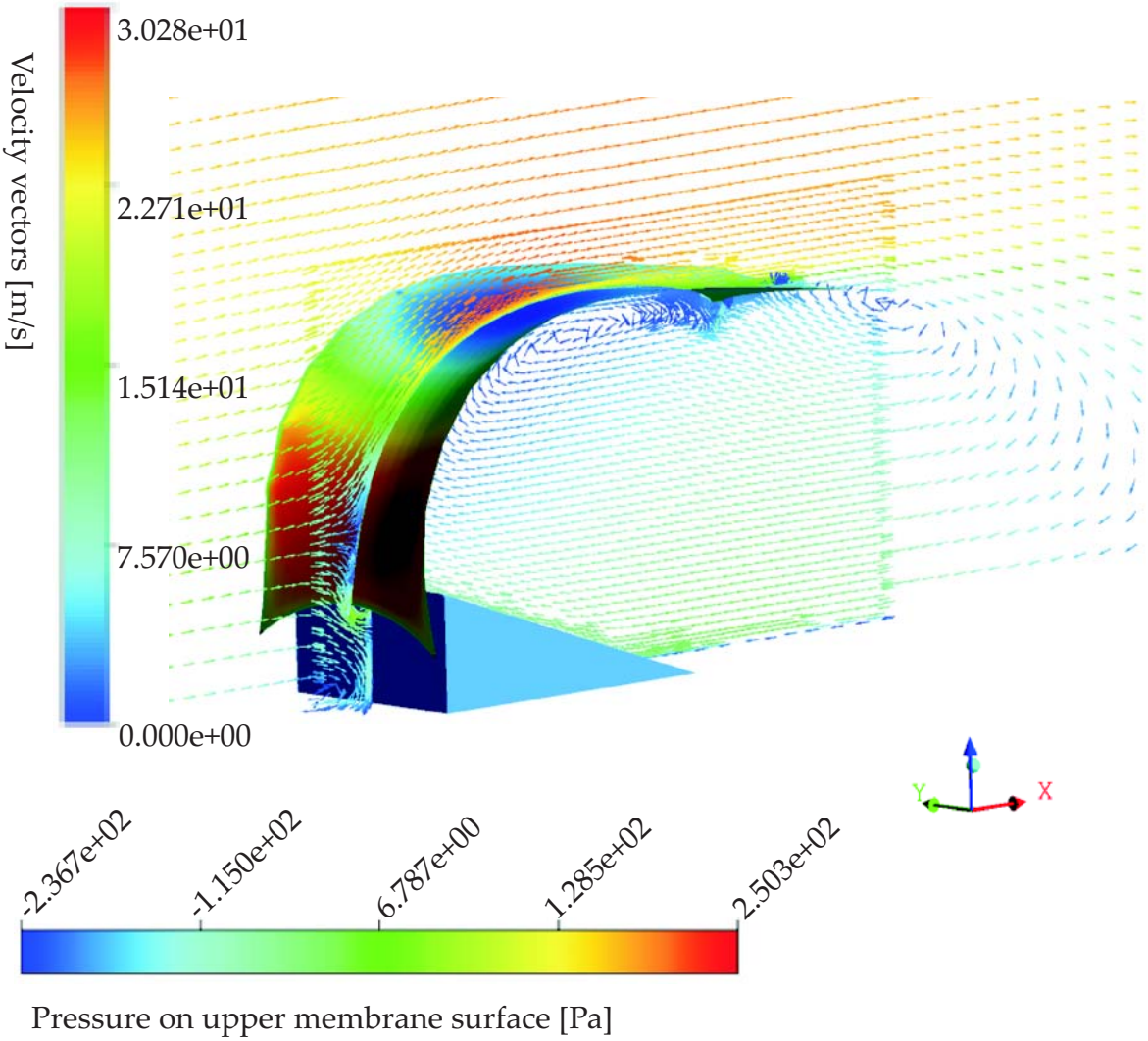

Figure 3.17: Wind from back side: velocity vectors close to the structure.

The air flow is deflected by the ARIES membrane surface and mostly circumvents the construction over the top or to the sides. A small portion of the flow enters under the membrane through the gap between the membrane and the tribune and through the hole in the center of the membrane cone.

On the upper side of the membrane, the flow separates, which results in a change of sign of pressure on the membrane surface in fig. 3.18. Below and behind the membrane, a complex recirculation zone is observed.

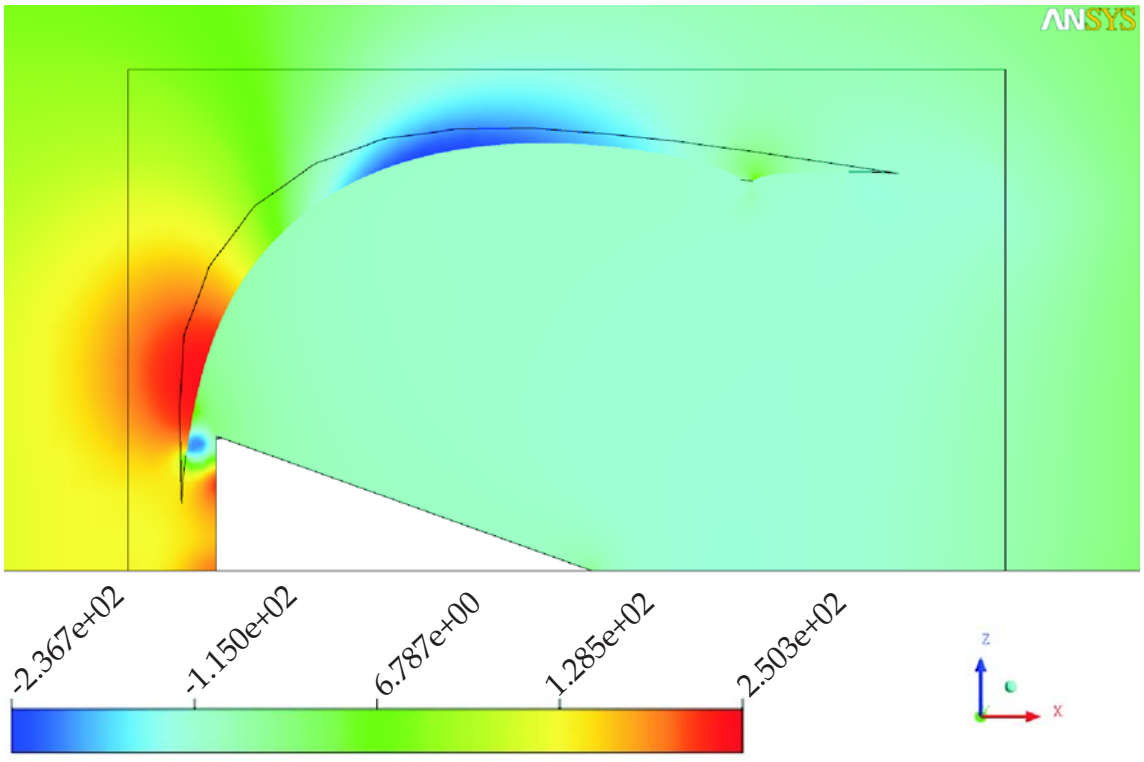

Figure 3.18: Wind from back side: Pressure distribution around the membrane structure.

Regarding the surface pressure on the membrane, the dynamic pressure on the back of the structure results in a positive pressure up to a certain height. After the flow separation, strong suction forces are observed on the upper parts of the membrane. Below the membrane, due to the recirculation, moderate suction in detected. The flow between the gap of the membrane and the tribune results in local suction within the gap.

Wind from the front side of the ARIES structure

For wind flow from the front of the structure, in fig. 3.19 the velocity vectors on the symmetry plane are visualized. Fig. 3.20 presents the pressure distribution around the structure in the symmetry plane and on the upper side of the membrane.

In this setup, the airflow enters the ARIES structure from its "open side". The flow separates above the membrane and at the lateral edges. According to the flow separation, recirculation occurs behind the construction.

The entering of the flow underneath the membrane results in high pressure forces on the lower membrane side. This results in lifting effects, which are increased in the rear part of the membrane, where negative pressure acts on the upper membrane side. Small local suction forces are observed in the gap between the membrane and the tribune.

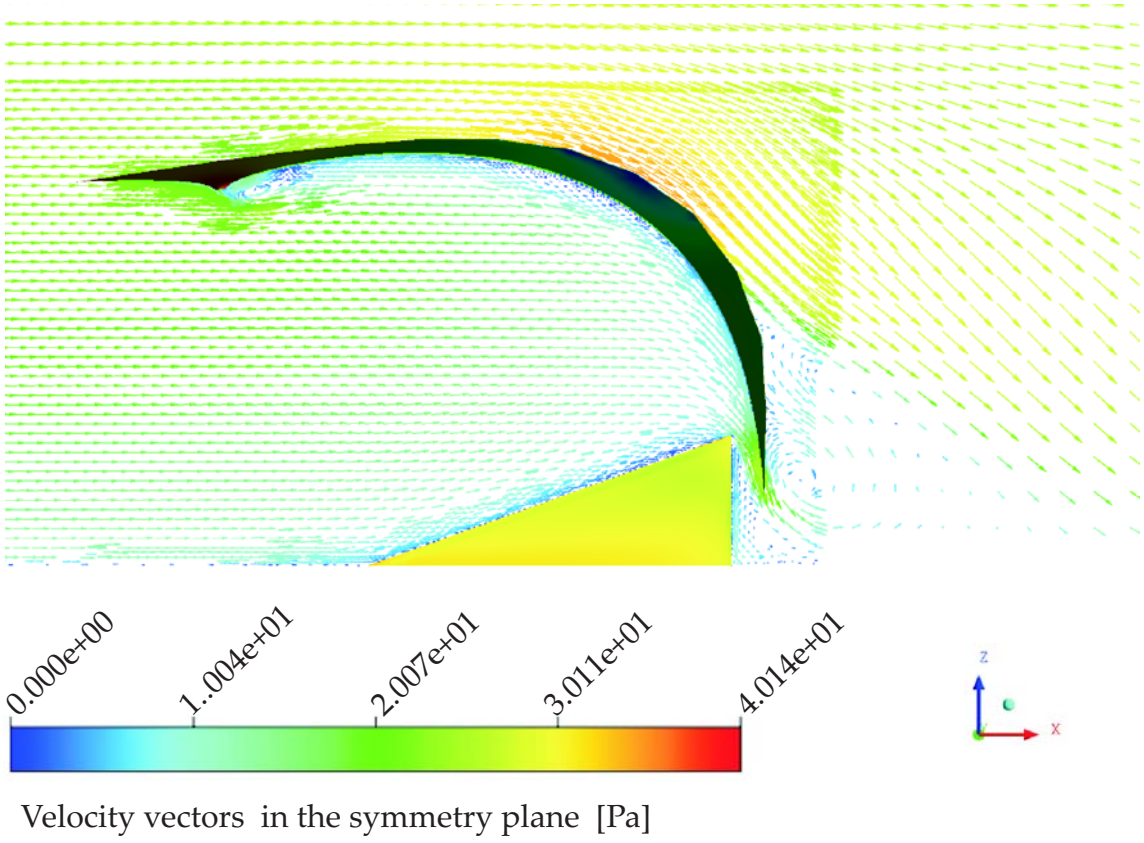

Figure 3.19: Wind from front side: Velocity vectors in the symmetry plane.

Brief parameter study regarding details of the ARIES construction

In a parameter study, the influence of the gap between the membrane and the tribune, as well as the influence of the hole in the center of the membrane cone, have been analyzed. For the magnitude of the surface pressure on the membrane, an easing effect was observed due to the existence of both openings. As these openings are also part of the prototype construction, they are included in the numerical model. However, for a worst case setup with respect to surface pressure the openings should be considered as closed.

3.5.3.3 c_p-values

The surfaces pressure on the membrane is the primary quantity of interest. As common in civil engineering, c_p values, introduced in section 3.1, are used to describe the surface pressure on the membrane. The maximum height of the middle line of the surface $z_{ref} = 6$ m was chosen as reference height z_{ref} for the computation of c_p. The distribution of the c_p-values showed no dependency on the wind speed at reference height, which was analyzed for a wind speed range from 5 m/s up to 25 m/s.

The c_p values are evaluated at 12 points on the membrane's surface in its symmetry axis. The location of points is shown in fig. 3.21. These 12 points have been chosen in accordance

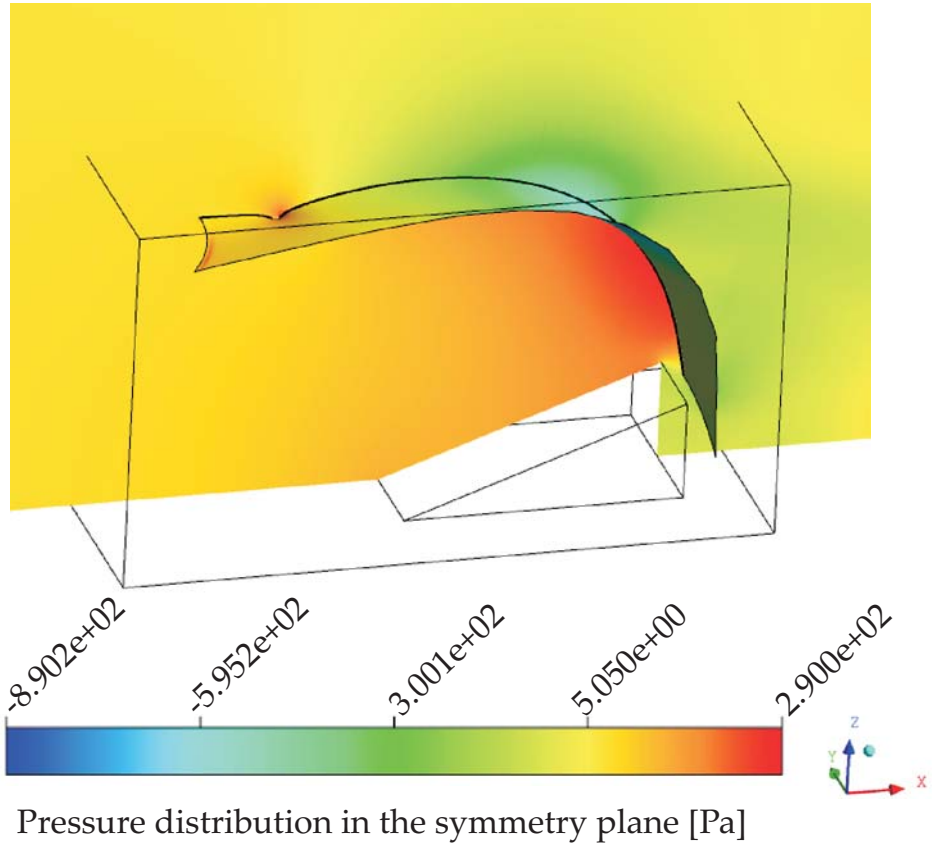

Figure 3.20: Wind from front side: Pressure distribution around ARIES structure.

with the location of the monitoring points in the wind tunnel experiment. Thereby, it is possible to directly compare the results of the wind tunnel experiment and the numerical simulation.

For each of these 12 points, two c_p values are specified: c_{pe} describes the normalized pressure on the upper/outer side of the membrane, c_{pi} describes the normalized pressure on the lower/inner side of the membrane. $c_{p\,\mathrm{net}}$ is defined as $c_{pe} - c_{pi}$ and thus, positive values of $c_{p\,\mathrm{net}}$ describe a net pressure from the outside of the construction towards the inside.

Experimental results are taken from wind tunnel testing published in [Bag01] and [DB04]. Unfortunately, no precise data about the condition of the wind tunnel experiments is available. Fig. 3.22 presents a picture of the rigid, small scale model of ARIES structure in the wind tunnel experiment. Only values for c_{pe} are available from the wind tunnel experiments. The c_p values derived are summarized in tab. 3.4 for wind from the back side of the structure and in tab. 3.5 for wind from the front side.

Comparing the results of wind tunnel experiments and numerical analysis, several observations can be made:

- The general distribution of the pressure coefficients on the upper side of the membrane is consistent for both the experiment and the numerical computation.

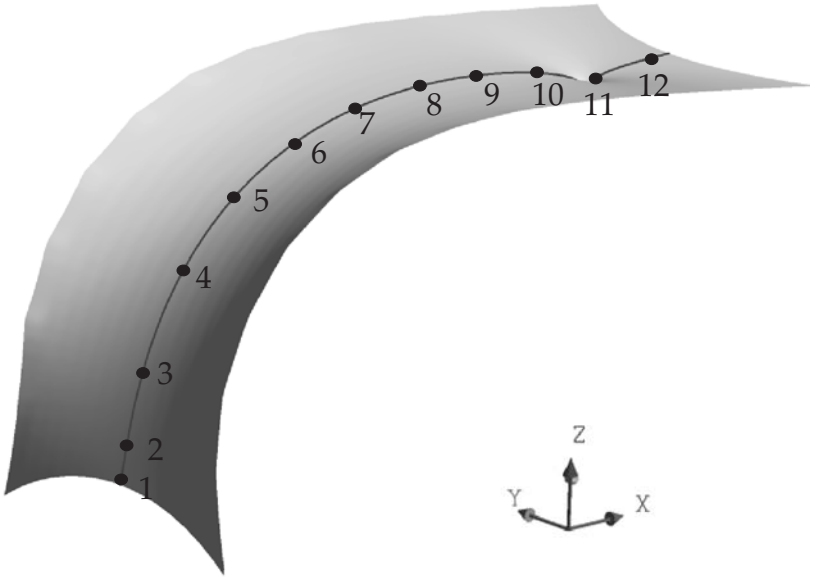

Figure 3.21: Points at which c_p values are determined.

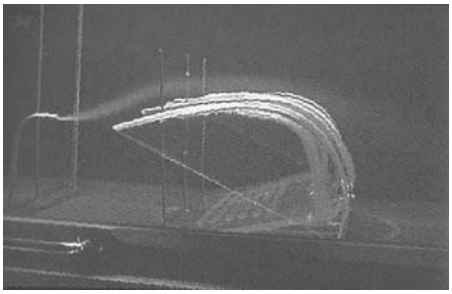

Figure 3.22: Wind tunnel tests of the ARIES structure. [DB04]

- ◇ The numerical simulation results show slightly larger values for positive pressure, such as in points 1 to 4 for wind from the back side. This corresponds to the over-prediction of turbulent kinetic energy by RANS models (see section 3.2.3.1).
- ◇ Negative pressure is slightly underestimated in the numerical computation.

Regarding the difference between results from experiment and numerical computation, beside modeling issues of the CFD based computation, several other factors have to be considered:

- ◇ Without the availability of further data about the setup of the wind tunnel experiment, especially with respect to the ABL modeling and to the surface roughness of the model, the quality of the wind tunnel experiments is difficult to judge.
- ◇ In the development of the ARIES structure, wind tunnel testing was conducted early to assess the wind loads as decisive factor for the design process. Therefore, it is not clear,

		experimental results	results from numerical analysis		
Point Nr.	x-coord [m]	c_{pe} [-]	c_{pe} [-]	c_{pi} [-]	$c_{p\ \mathrm{net}}$
1	0.92	0.50	0.71	-0.23	0.94
2	0.99	0.44	0.77	-0.22	0.99
3	1.27	0.00	0.79	-0.20	0.99
4	1.98	-0.42	0.34	-0.26	0.60
5	2.90	-0.94	-0.27	-0.29	0.02
6	4.01	-1.10	-0.68	-0.31	-0.37
7	5.17	-0.96	-0.74	-0.32	-0.42
8	6.36	-0.88	-0.66	-0.33	-0.34
9	7.52	-0.62	-0.56	-0.33	-0.23
10	8.69	-0.54	-0.42	-0.33	-0.09
11	9.84	-	-0.21	-0.36	0.14
12	11.01	-	-0.30	-0.33	0.03

Table 3.4: Wind from back side: c_p values for specified points on the ARIES membrane.

		experimental results	results from numerical analysis		
Point Nr.	x-coord [m]	c_{pe} [-]	c_{pe} [-]	c_{pi} [-]	$c_{p\ \mathrm{net}}$
1	0.92	-0.62	-0.38	-0.32	-0.06
2	0.99	-0.62	-0.27	0.36	-0.63
3	1.27	-0.66	-0.35	0.79	-1.14
4	1.98	-1.16	-0.32	0.84	-1.16
5	2.90	-1.44	-1.24	0.71	-1.95
6	4.01	-1.34	-1.44	0.57	-2.02
7	5.17	-1.03	-1.06	0.52	-1.58
8	6.36	-0.78	-0.69	0.45	-1.14
9	7.52	-0.54	-0.40	0.46	-0.86
10	8.69	-0.31	-0.13	0.28	-0.41
11	9.84	-	0.28	0.42	-0.14
12	11.01	-	0.08	0.16	-0.08

Table 3.5: Wind from front side: c_p values for specified points on the ARIES membrane.

to which extent the geometry used in the wind tunnel represents the prototype. This uncertainty exists also with regard to the question, whether or not the gap between the membrane and the tribune as well as the hole in the center of the membrane cone have been considered in the experimental approach.

Concluding, the computation of dimensionless pressure coefficients enables the comparison of wind tunnel experiments and numerical simulation towards mean wind loading. In the specific analysis of the ARIES structure, comparing experiment and simulation is done in a qualitative way. For a more specific, quantitative analysis, further details about the wind tunnel testing need to be obtained.

3.6 Summary

In this chapter, a brief summary of approaches for the analysis of wind load in membrane structures is given. The fundamentals of fluid mechanics, including turbulence modeling and near wall flow have been presented. By introducing the Finite Volume Method, a method of computational fluid dynamics (CFD) was introduced.

The application of CFD in wind engineering falls in the young subdiscipline of Computational Wind Engineering (CWE). Within CWE, not only the methods used, but more the modeling techniques are essential for deriving high quality results. Therefore, the properties of the neutrally stratified Atmospheric Boundary Layer (ABL) flow were discussed and simulation aspects have been presented, to correctly model the ABL flow by methods of CFD.

The appropriate methods of CFD together with the essential modeling aspects were used to setup a numerical model for the analysis of wind flow around the ARIES canopy structure. Special care was put into assuring the quality of the ABL flow. As results, c_p values have been derived for wind directions from the front and from the back side. These values have been compared with those derived from wind tunnel experiments.

In the following chapter, the numerical CFD model derived for the rigid ARIES structure is used to simulate the fluid part in the partitioned analysis of the interaction of the ARIES structure with wind.

Chapter 4

Coupling Fluid and Structural Analysis

In the previous chapters, the fundamentals, numerics, and applications of structural and fluid problems have been introduced, drawing a focus on the simulation of wind influence on membrane structures. The structural and the fluid simulation were treated as independent single field problems. In the following, they are considered together as one multi-physics problem, consisting of a fluid and a structural part. For a multi-physics analysis, the term coupled analysis is also common, since the coupling between multiple physical fields is considered.

4.1 Wind - Membrane Structure Interaction in Coupled Problem Analysis

As explained in section 2.3, due to their missing bending stiffness, membrane structures react to forces acting perpendicular to their surface with large deformations. These deformations can become large enough to influence the flow conditions around the structure.

An every-day example for wind-structure interaction is the behavior of a flag in the wind: as the wind changes its direction and/or speed, the flag immediately changes its shape. This change in shape strongly influences the flow conditions around the structure. Accordingly, the surface pressure on the flag's surface will change, as the flag changes its shape. The change of the load condition, in turn, results in a new shape of the structure, and so on. For the example of a flag in the wind, the interaction of flow and structure results in a highly chaotic and unstable behavior.

The interaction of inertial and elastic forces with aerodynamic forces, such as described in the flag-in-the-wind example, is also referred to as an aeroelastic problem.

For the application of wind engineering, it is necessary to evaluate, in which way the interdependency of flow and structure necessitates a multi-field analysis. For rigid structures of limited height, such as small houses or low buildings, the geometry of the structure does not change due to wind loading or if it does, then only to a very small degree. Therefore, the separate analysis of the flow condition around the structure and the deformation of the

structure due to surface pressure from the wind is sufficient. For high, slender constructions, such as towers, stacks, or pylons, as well as for bridges, wind effects can lead to large enough deformations so that a multi-physics analysis has to be considered. Depending on the size and effect of the deformation, techniques based on linear assumptions, such as field elimination techniques, or semi-analytical methods can be applied.

In case of flexible and light-weight membrane structures the application of simplified methods is quite limited due to the magnitude of the changes in shape and the non-linearity of the structural behavior. Here, multi-physics analyses have the potential to give better prediction of wind effects. Within this work, for the analysis of wind effects on membrane structures, a fluid simulation is used to analyze the flow conditions around the structure and to compute the surface load due to the air flow. This surface load is used as a load condition for the structural computation, which computed the reaction of the structure. In order to represent the physical coupling of fluid and structure, the fluid simulation has to take into account the change of the structure's geometry.

The wind-membrane structure interaction is a surface coupled problem with the structure's surface separating the fluid and the structural domain. The domains are non-overlapping. The fluid-structure interface Γ is the part of the structure's surface that is in contact with the fluid, and vice versa, the part of the fluid domain, which is in contact with the structure. Within this work, the fluid-structure interaction is represented using an ALE approach in which the deformation of the structure's wetted surface is used to update the boundaries of the computational fluid domain. This coupling can be identified as Dirichlet-Neumann coupling. The Dirichlet boundary condition for the fluid is determined by the structural displacement $\mathbf{d}_{\Gamma}^{\Omega_S}$. For the structural domain, the fluid loads on the domain $\mathbf{f}_{\Gamma}^{\Omega_F}$ are interpreted as Neumann boundary conditions.

The simulation of wind-membrane interaction is complicated due to the strong non-linearities of the coupled problem. This non-linearity is caused by the non-linearity of the inertia term in the fluid solution, the moving boundaries of the fluid domain and the large structural displacements.

4.2 Strategies to Solve Multi-Physics Problems

For the treatment of non-linear multi-physics problems, two general approaches can be identified:

- **Simultaneous analysis**

  In simultaneous analysis, also referred to as monolithic analysis, the entire multi-physics problem, with all physical fields involved, is summarized in one set of equations, discretized, and solved as one. Examples for simultaneous solution of multi-physics problems can be found among many others in [MHvBdB04], [HWD04], [Hei04], [BCZH06], [Tez07].

◇ **Partitioned analysis**

In partitioned analysis, the physical fields are solved independently. The term 'partitioned' refers to a spatial decomposition, which in the case of fluid-structure interaction means the decomposition into a structural and a fluid domain. The coupling of the individual fields is realized by the exchange of boundary conditions. Examples for partitioned analysis are, among many others, the works of [FL00], [Wal99], [MW01], [GV03], [MS03], [LTM01], [PFO01], [TSS06].

Different aspects inherent to the two approaches will be briefly discussed in the following:

◇ Simultaneous analysis of multi-physics problems shows superior performance with respect to convergence and accuracy of the solution.

◇ Simultaneous approaches usually need to use an identical spatial discretization for all involved fields. In contrast, by using an individual spatial discretization in a partitioned analysis, the best suited spatial discretization can be used for the involved physical fields. To solve different single field problems, different time step sizes may be necessary. In a simultaneous analysis, the smallest necessary time-step has to be used to solve the complete problem. In partitioned analysis, sub-cycling can be used to choose different time-step length and therefore to reduce the computational effort.

◇ A simultaneous solution has to include all unknowns in one large system of equations. Depending on the computational resources, this can lead to a limitation of the problem size. In a partitioned analysis, the whole problem is separated according to the physical fields in smaller 'partitions' and each physical field is solved separately.

◇ Due to the varying nature of the involved single field problems the complete system of equations for a simultaneous approach can be severely ill-conditioned. This potentially ill-conditioned system of equations has to be solved by a single solver. In contrast, in a partitioned analysis, several systems of equations exist, each describing a single physical field. These systems of equations can be solved by specialized solution approaches.

◇ Partitioned analysis enables a highly modular setup, because different specialized solvers for the single physical fields can be combined. This modular setup enables the reuse of existing, well-proven, and specialized software.

Due to the advantages of the partitioned analysis, especially with respect to realization, most multi-physics analyses are conducted using partitioned techniques. With respect to accuracy, simultaneous solution strategies remain the reference. Due to their requirements and limitations, applications of simultaneous analysis are limited to small scale or academic problems.

In the case of fluid-structure interaction, different requirements for spatial discretizations, both with respect to grid topology and grid density, have to be met for the structural

and the fluid field. Typically, the fluid field requires a much finer discretization as compared to the structural field, because of special requirements for boundary resolution. These differences in spatial requirements can be best met in a partitioned analysis.

As discussed in the previous chapter, computational wind engineering typically leads to fluid problems with a very large number of unknowns. Furthermore, to model air flow at high Reynolds numbers, sophisticated methods for modeling of turbulence and wall flow are necessary. Considering the structural side of the application, in section 2.3.1 numerous requirements of a structural solver for simulating the behavior of membrane structures were presented. Considering these special demands of the single field solvers, the possibility to use already existing, highly specialized solvers in a partitioned analysis seems to be the only promising approach to realize the simulation of wind-membrane structure interaction. Therefore, within this work partitioned analysis strategies are used to solve the problem of wind-structure interaction.

4.3 Partitioned Analysis of Multi-Physics Problems

In the following, requirements for the partitioned analysis are identified. On the basis of these requirements, two coupling approaches, *weak coupling* and *strong coupling*, are introduced and discussed.

4.3.1 Requirements for Partitioned Analysis Strategies

In a partitioned approach, the exchange of boundary conditions between the single field solvers represents the coupling of the physical fields. The *coupling algorithm* determines, when the single field problems are solved as well as when, how, and in which form the boundary conditions are exchanged. To ensure the correct representation of the physical coupling in the partitioned coupled computation, several conditions have to be met by the coupling algorithm. These demands are discussed in the following by focusing on problems of fluid-structure interaction:

- ◇ Stability of the computation, even for arbitrary non-linear problems.
- ◇ Accuracy of the results with respect to the 'real' physical problem.
- ◇ Robustness of the method for the usage in different applications.

To achieve stability and accuracy in coupled computations, several requirements, which are based on the physics of the coupled fluid-structure problem, have to be met by the coupling algorithm:

Conservation of volume

At the fluid-structure interface, no volume has to be generated or discreated due to the partitioned analysis strategy. In case of incompressible flows, this corresponds to the requirement of a conservation of mass in the fluid domain. For the fluid simulation alone,

this requirement has already been introduced as the Geometric Conservation Law (GCL) for moving boundaries in section 3.3.7. In the context of coupled computations, the conservation of volume leads to the requirement, that the fluid and the structural domain have to stick together at the interface. Therefore, any deformation of the fluid-structure interface has to be identical for the fluid and the structural domain at any time t:

$$\mathbf{d}_\Gamma^{\Omega_F}(t) = \mathbf{d}_\Gamma^{\Omega_S}(t) \tag{4.1}$$

Conservation of momentum

For the entire coupled problem, no additional momentum $\Delta\mathbf{m}_\Gamma$ can be created at the interface, nor any momentum can be lost [Mok01]. Momentum can only be transferred through the interface from one domain to the other. Therefore, the sum of momentum transferred from the fluid domain to the interface and from the interface to the structural domain and vice versa has to be zero in a certain time period $t^{n+1} - t^n$.

$$\begin{aligned}
\Delta\mathbf{m}_\Gamma^{\Omega,n\to n+1} &= \Delta\mathbf{m}_\Gamma^{\Omega_F,n\to n+1} + \Delta\mathbf{m}_\Gamma^{\Omega_S,n\to n+1} \\
&= \int_{t^n}^{t^{n+1}} \left(\int_\Gamma \sigma_{\text{cauchy},\Gamma}^{\Omega_F}(t)\ \mathbf{n}_\Gamma^{\Omega_F}(t)\ dA \right) dt \\
&\quad + \int_{t^n}^{t^{n+1}} \left(\int_\Gamma \sigma_{\text{cauchy},\Gamma}^{\Omega_S}(t)\ \mathbf{n}_\Gamma^{\Omega_S}(t)\ dA \right) dt = \mathbf{0}
\end{aligned} \tag{4.2}$$

with $\mathbf{n}_{\Gamma,F}$ and $\mathbf{n}_{\Gamma,S}$ as the surface normal vector at the interface. This condition can only be fulfilled, if the Cauchy stress tensor at the interface is equal in the fluid domain and the solid domain:

$$\sigma_{\text{cauchy},\Gamma}^{\Omega_F}(t)\ \mathbf{n}_\Gamma^{\Omega_F}(t) = \sigma_{\text{cauchy},\Gamma}^{\Omega_S}(t)\ \mathbf{n}_\Gamma^{\Omega_S}(t) \tag{4.3}$$

Assuming an identical spatial discretization of the fluid-structure interface in both domains, the integral of the Cauchy stresses over the interface can be interpreted as forces $\mathbf{f}_\Gamma^{\Omega_i}(t)$ acting on the nodes of the discretized interface Γ_d. The requirement for the conservation of momentum can be expressed as:

$$\mathbf{f}_{\Gamma_d}^{\Omega_F}(t) = \mathbf{f}_{\Gamma_d}^{\Omega_S}(t) \tag{4.4}$$

Conservation of energy

Similar to the first two requirements, the requirement of the conservation of energy states that no energy should be created or dissipated at the boundary. The sum of the transferred energy at the boundary with a certain time period has to be zero:

$$\begin{aligned}
\Delta E_\Gamma^{\Omega,n\to n+1} &= \Delta W_\Gamma^{\Omega_F,n\to n+1} + \Delta W_\Gamma^{\Omega_S,n\to n+1} \\
&= \int_{t^n}^{t^{n+1}} \left(\int_\Gamma \sigma_{\text{cauchy},\Gamma}^{\Omega_F}(t)\ \mathbf{n}_\Gamma^{\Omega_F}(t)\ \dot{\mathbf{d}}_\Gamma^{\Omega_F}(t)\ dA \right) dt \\
&\quad + \int_{t^n}^{t^{n+1}} \left(\int_\Gamma \sigma_{\text{cauchy},\Gamma}^{\Omega_S}(t)\ \mathbf{n}_\Gamma^{\Omega_S}(t)\ \dot{\mathbf{d}}_\Gamma^{\Omega_S}(t)\ dA \right) dt
\end{aligned} \tag{4.5}$$

$$= \int_{t^n}^{t^{n1}} \left(\mathbf{f}_\Gamma^{\Omega_F}(t)\ \dot{\overline{\mathbf{d}}}_\Gamma^{\Omega_F}(t) + \mathbf{f}_\Gamma^{\Omega_S}(t)\ \dot{\overline{\mathbf{d}}}_\Gamma^{\Omega_S}(t) \right) dt = \mathbf{0} \tag{4.6}$$

with $\dot{\mathbf{d}}_\Gamma$ as the time derivative of the displacement of the interface and $\overline{\dot{\mathbf{d}}}_\Gamma$ as its discretized form (see section 2.2.2.2). Using eq. 4.4, eq. 4.6 can be simplified to:

$$\Delta E_\Gamma^{\Omega,n\rightarrow n+1} = \int_{t^n}^{t^{n1}} \mathbf{f}_\Gamma^{\Omega_F}(t) \left(\overline{\dot{\mathbf{d}}}_\Gamma^{\Omega_F}(t) - \overline{\dot{\mathbf{d}}}_\Gamma^{\Omega_S}(t) \right) dt = \mathbf{0} \tag{4.7}$$

which can only be fulfilled, if

$$\overline{\dot{\mathbf{d}}}_\Gamma^{\Omega_F}(t) = \overline{\dot{\mathbf{d}}}_\Gamma^{\Omega_S}(t) \tag{4.8}$$

Influence of time discretization

For a semi-discrete problem, which is discretized in space but continuous in time, eq. 4.1 and eq. 4.8 can be treated as one condition. In a partitioned analysis, typically different time discretization schemes are used, as introduced in section 2.2.2.2 for the structural problem and in section 3.3.5 for the fluid problem. For time integration schemes, usually one primary variable is used, while the other time dependent variables are computed depending on this primary variable. In the structural problem, the primary variable is typically the displacement **d**, while in the fluid domain, the primary variable is typically fluid velocity **u**. Also, for the use in different time integration schemes, the primary variables can be evaluated at different times within one time-step. Therefore, only for special pairs of time-integration schemes, such as the Bossak-α method for the structural problem and the Backward-Euler method for the fluid problem, eq. 4.1 and eq. 4.8 can both be satisfied.

In case eq. 4.1 and eq. 4.8 cannot be satisfied simultaneously, eq. 4.8 is likely to be violated, as eq. 4.1 absolutely has to be fulfilled with respect to the conservation of volume. The violation of eq. 4.8 results in an error in the energy conservation. Mok [Mok01] discusses that this error is similar to errors introduced by time discretization, both with respect to size and order. More specific, this error is expected to be of the same order as the time integration schemes used for the single field problems. In test computations performed by Mok et al. [Mok01], the error proved to have little influence on the stability and accuracy of partitioned computations compared to simultaneous computations.

Coupling conditions

Based on the requirements of the conservation of volume, momentum, and energy discussed above, two coupling conditions (also named 'interface continuity conditions' or 'transmission conditions') , which have to be fulfilled at any time t on the discretized fsi interface Γ_d can be identified:

- ◇ Kinematic continuity condition

$$\overline{\mathbf{d}}_{\Gamma_d}^{\Omega_F}(t) = \overline{\mathbf{d}}_{\Gamma_d}^{\Omega_S}(t) \tag{4.9}$$

- ◇ Dynamic continuity condition

$$\overline{\mathbf{f}}_{\Gamma_d}^{\Omega_F}(t) = \overline{\mathbf{f}}_{\Gamma_d}^{\Omega_S}(t) \tag{4.10}$$

4.3.2 Sequentially Staggered / Weak Partitioned Coupling

Fig. 4.1 represents a simple staggered fluid-structure interaction problem, in which the fluid part is solved (1), the loads are transferred to the structural domain (2), the structural field is solved (3), and finally, the structural deformation is transferred to the fluid domain (4). Subsequently, the next time-step begins.

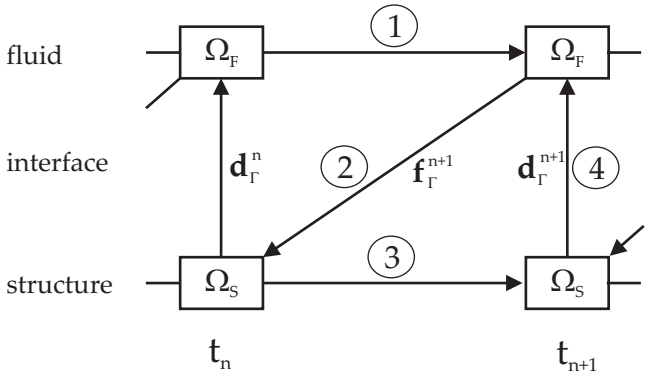

Figure 4.1: Sequentially staggered / weak / explicit coupling scheme.

The single field solvers run in a staggered scheme. Within one time step, boundary conditions are only exchanged once between the structural domain Ω_S and the fluid domain Ω_F and no iteration over the single field solvers is performed. The one-time solution of the single field problems within one time-step can be done in a sequential ("sequentially staggered scheme") or parallel ("parallel staggered scheme") manner. As simple staggered coupling schemes without iteration over the single field problems cannot represent the interaction between the physical single field problems correctly, they are also referred to as weak coupling systems. Taking an analogy to time integration, due to their explicit nature, weakly partitioned schemes are also known as "explicit coupling schemes".

As the coupling information is exchanged only once per time-step, for at least one single field, the boundary conditions from the other single field(s) are only known at the beginning $t = t^n$ of the common time-step $t^n \rightarrow t^{n+1}$. Therefore, not all coupling conditions can be satisfied at the end of the time-step $t = t^{n+1}$, hence one single field problem will not have the correct boundary condition at $t = t^{n+1}$. In the coupling algorithm suggested in fig. 4.1, the fluid loads are known at the end of the time-step as boundary conditions for the structural solution. For the solution of the fluid field, the boundary condition posed by the structural field, namely the structure's geometry, is only known at the beginning of the time-step and therefore, eq. 4.9 cannot be satisfied at the end of the time-step. Since in the coupled problem the solutions of the single field problems are interdependent, the solution of both single fields cannot be exact.

The effects for the coupled solution, that arise from not fully satisfying the coupling conditions, depend on the actual coupling algorithm and the application. Within every time step, a small error in the energy, which is transferred at the boundary, is introduced. This error is likely to sum up over several time-steps, leading to an instable simulation

and / or decay in accuracy. Weak coupling is regarded to be only conditionally stable and only first order accurate with respect to time, even if the time integration schemes of the single fields have higher orders of accuracy. For coupled problems of fluid-structure interaction in compressible flows with low fluid densities, e.g. in aeronautics, simple staggered schemes proved to be sufficiently stable and accurate [FL00]. In fsi problems with incompressible flows, simple staggered schemes show an instable behavior, which will be further discussed in section 4.3.4.

To decrease the error made in satisfying the coupling conditions, predictions for the transferred boundary conditions, typically for the displacements, have been suggested [Pip97],[PF01]. These predictors are used to obtain a more accurate estimation of the fsi interface geometry, which is expected at time $t = t^{n+1}$. The "predicted" interface geometry is applied as modified boundary condition for the fluid simulation for $t = t^n$. The usage of structural predictor might improve weak coupling with respect to stability and accuracy in case of compressible flows.

4.3.3 Iteratively Staggered / Strong Partitioned Coupling

Fig. 4.2 shows an instance of an iteratively staggered coupling algorithm applied to a problem of fluid-structure interaction. In an iterative manner, each single field problem is solved multiple times within one time-step. The single field problems are continuously updated with the boundary conditions resulting from the other field(s). In the following, one sequence of fluid-solution (step 1), transfer of interface loads (step 2), structural solution (step 3), and transfer of displacements (step 4) will be referred to as one step in the *inter-field iteration*. These inter-field iterations are also known as outer-loop iterations.

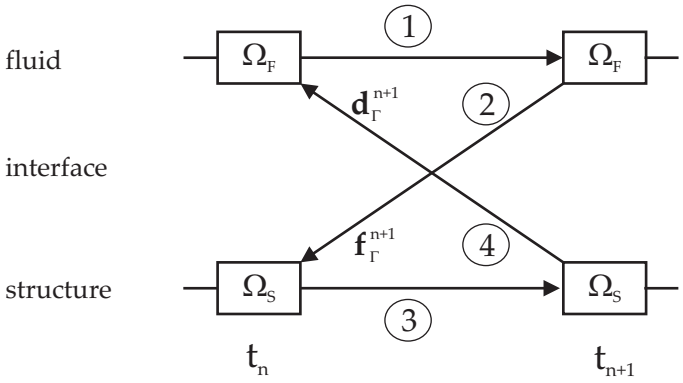

Figure 4.2: Iteratively staggered / strong / implicit coupling scheme.

In case of convergence of the inter-field iterations, the iterative scheme converges towards the solution of a simultaneous approach. Since these coupling schemes represent the strong coupling of the physical fields, they are also named strong partitioned coupling schemes. Within this coupling approach, the coupling conditions are satisfied at the end of each time-step $t = t^{n+1}$, therefore these schemes are also called implicit coupling methods.

Compared to the weak partitioned coupling schemes, strong partitioned coupling schemes show a superior behavior with respect to stability and accuracy. The weak coupling can be interpreted as strong coupling with only one inter-field iteration step. A full iteratively coupled solution has the same properties with respect to order of accuracy and stability as the single field problems. However, strong coupling requires a considerably higher effort compared to weak coupling. As each field is solved multiple times within one time-step, the computational effort multiplies as well. Convergence within one time-step can be limited or slowed down due to the "artificial added mass effect", which is discussed in section 4.3.4.

To simplify the following discussion of iterative staggered fsi coupling schemes, the single field problems are expressed using the coupled degrees of freedom on the interface, namely the interface loading $\mathbf{f}_\Gamma$ and the interface displacement $\mathbf{d}_\Gamma$. Now, the structural problem is abbreviated as a non-linear function S, which, at time step t^{n+1}, relates the interface loads received from the fluid $\mathbf{f}_\Gamma^{n+1}$ to the displacements on the interface $\mathbf{d}_\Gamma^{n+1}$.

$$\mathbf{d}_\Gamma^{n+1} = S\left(\mathbf{f}_\Gamma^{n+1}\right) \tag{4.11}$$

Accordingly, the fluid problem can be seen as a non-linear function F using the interface displacements $\mathbf{d}_\Gamma^{n+1}$ to compute the interface loading $\mathbf{f}_\Gamma^{n+1}$.

$$\mathbf{f}_\Gamma^{n+1} = F\left(\mathbf{d}_\Gamma^{n+1}\right) \tag{4.12}$$

Using eq. 4.11 and eq. 4.12, the coupled fluid-structure interaction is contained in the following non-linear system of equation:

$$\mathbf{d}_\Gamma^{n+1} = S\left[F\left(\mathbf{d}_\Gamma^{n+1}\right)\right] = S \circ F\left(\mathbf{d}_\Gamma^{n+1}\right) \tag{4.13}$$

or equivalently as:

$$\mathbf{f}_\Gamma^{n+1} = F \circ S\left(\mathbf{f}_\Gamma^{n+1}\right) \tag{4.14}$$

Iteratively staggered coupling schemes can be classified according to their general approach of solving eq. 4.13 or eq. 4.14 into *methods based on fixed-point iteration* and *Newton-based methods*, which will be explained in the following. An overview of the available iteratively staggered coupling schemes can be found, e.g. in [Sch06].

4.3.3.1 Methods Based on Fixed-point Iteration

Fixed-point iteration based methods are widely used in the scope of partitioned simulation of fluid-structure interaction [LTM01], [Mok01]. Equation 4.13 is treated as a fixed-point problem to find the fixed-point $\mathbf{x}^*$ for which holds:

$$\mathbf{x}^* = \Phi\left(\mathbf{x}^*\right) \tag{4.15}$$

The fixed-point problem can be solved using a fixed-point iteration. It starts with an initial value $\mathbf{x}_0$ and uses eq. 4.16 to create a sequence $\{\mathbf{x}_0, \mathbf{x}_1, ...\}$, which converges to the fixed-point $\mathbf{x}^*$, if the spectral radius of operator Φ is smaller than 1.

$$\mathbf{x}_{k+1} = \Phi\left(\mathbf{x}_k\right) \tag{4.16}$$

Transferred to the FSI-context, the fixed-point iteration is formulated as: by using eq. 4.17 and an initial interface displacement $\mathbf{d}_{\Gamma,0}^{n+1}$, a sequence of interface displacements $\{\mathbf{d}_{\Gamma,0}^{n+1}, \mathbf{d}_{\Gamma,1}^{n+1}, ...\}$ is created, which converges to the "equilibrium interface displacement" $\mathbf{d}_{\Gamma}^{n+1}$ at time $t = t^{n+1}$.

$$\mathbf{d}_{\Gamma,k+1}^{n+1} = S \circ F \left(\mathbf{d}_{\Gamma,k}^{n+1} \right) \tag{4.17}$$

To create this sequence, the structural problem S and the fluid problem F have to be solved sequentially with updated boundary conditions. The coupling algorithm for a problem of fluid-structure interaction is presented in Algorithm 1. The interface displacement $\mathbf{d}_{\Gamma,0}^{n+1}$ at the beginning of each time-step is enhanced by a predictor according to [Pip97],[PF01].

Algorithm 1 is the well-known Gauss-Seidel method. To improve the stability as well as the efficiency of the Gauss-Seidel method, under-relaxation techniques have been introduced. The under-relaxation can be applied to displacements or loads transferred at the fluid-structure interface. For the under-relaxation of the interface displacements, in Algorithm 1, step 4 is replaced and an additional fifth step is introduced. These changes are shown in Algorithm 2, which is known as the Richardson iteration. For $\omega = 1.0$, Algorithm 2 resembles the Gauss-Seidel method again.

Exemplary for interface displacements, the concept of under-relaxation shall be explained here. The increment of the interface displacement from iteration step k to iteration step $k+1$ is:

$$\Delta\mathbf{d}_{\Gamma,k+1}^{n} = \tilde{\mathbf{d}}_{\Gamma,k+1}^{n} - \mathbf{d}_{\Gamma,k}^{n} \tag{4.24}$$

The non-under-relaxed interface displacement $\tilde{\mathbf{d}}_{\Gamma,k+1}^{n}$, which results directly from the structural computation, is labeled with a tilde to distinguish it from the under-relaxed interface displacement $\mathbf{d}_{\Gamma,k+1}^{n}$. The value of the under-relaxation parameter $\omega \leq 1$ determines, which fraction of the increments $\Delta\mathbf{d}_{\Gamma,k+1}^{n}$ is added to the displacement of the previous iteration step $\mathbf{d}_{\Gamma,k}^{n}$, to compute the under-relaxed interface displacement for the inter-field iteration step $k = k+1$:

$$\mathbf{d}_{\Gamma,k+1}^{n+1} = \mathbf{d}_{\Gamma,k}^{n} + \omega_{k+1}\Delta\tilde{\mathbf{d}}_{\Gamma,k+1}^{n} = \omega_{k+1}\tilde{\mathbf{d}}_{\Gamma,k+1}^{n+1} + (1-\omega_{k+1})\,\mathbf{d}_{\Gamma,k}^{n+1} \tag{4.25}$$

For a small value of ω, e.g. $\omega = 0.05$, the change in displacement between the iteration steps is very small. This usually results in a more 'stable behavior' of the coupled computation, compared to higher values for the under-relaxation factor. However, with a small increment, the solution converges slower because typically more iteration steps are necessary to reach convergence. The challenge posed by using under-relaxation is to find the largest parameter ω, for which the coupling algorithm converges. Usually, the optimal value of ω cannot be determined a priori, but is based on experience or can be the result of a parameter study. Furthermore, the optimal under-relaxation value is expected to change during the inter-field iteration: the increment in the interface displacement becomes smaller as the coupled computation converges and, therefore, less under-relaxation is needed to stabilize the computation.

1. For k as the number of current inter-field iteration: Start with $k = 0$ and predict the interface displacement $\mathbf{d}_{\Gamma,k}^{n+1}$ for $k = 0$:

   Predictor of 0-th order:

   $$\mathbf{d}_{\Gamma,0}^{n+1} = \mathbf{d}_{\Gamma}^{n} \tag{4.18}$$

   Predictor of 1-st order:

   $$\mathbf{d}_{\Gamma,0}^{n+1} = \mathbf{d}_{\Gamma}^{n} + \delta t \, \dot{\mathbf{d}}_{\Gamma}^{n} \tag{4.19}$$

   Predictor of 2-nd order:

   $$\mathbf{d}_{\Gamma,0}^{n+1} = \mathbf{d}_{\Gamma}^{n} + \delta t \left(\frac{3}{2} \dot{\mathbf{d}}_{\Gamma}^{n} - \frac{1}{2} \dot{\mathbf{d}}_{\Gamma}^{n-1} \right) \tag{4.20}$$

2. Solve the fluid problem:

   $$\mathbf{f}_{\Gamma,k+1}^{n+1} = F\left(\mathbf{d}_{\Gamma,k}^{n+1} \right)$$

3. Solve the structural problem:

   $$\mathbf{d}_{\Gamma,k+1}^{n+1} = S\left(\mathbf{f}_{\Gamma,k+1}^{n+1} \right)$$

4. Check for convergence of the fixed-point iteration:

   $$Res = C_{\mathrm{Tol}}\left(\mathbf{d}_{\Gamma,0}^{n+1}, ..., \mathbf{d}_{\Gamma,k}^{n+1}, \mathbf{d}_{\Gamma,k+1}^{n+1}, \mathbf{f}_{\Gamma,0}^{n+1}, ..., \mathbf{f}_{\Gamma,k}^{n+1}, \mathbf{f}_{\Gamma,k+1}^{n+1} \right) \leq \epsilon_{\mathrm{Tol}} \tag{4.21}$$

   with C_{Tol} as a function, with which a certain value is computed to judge the convergence (see section 4.4.3), and ϵ_{Tol} as a tolerance limit for the value Res calculated according to C_{Tol}.

   If $Res > \epsilon_{\mathrm{Tol}}$:

   $$\mathbf{d}_{\Gamma,k}^{n+1} = \mathbf{d}_{\Gamma,k+1}^{n+1} \qquad k = k + 1$$

   go to step 2 (to begin a new step in the outer iteration loop)

   Else if $Res \leq \epsilon_{\mathrm{Tol}}$:

   $$\mathbf{d}_{\Gamma}^{n+1} = \mathbf{d}_{\Gamma,k+1}^{n+1} \qquad n = n + 1 \qquad k = 0$$

   go to step 1 (to begin a new time step)

Algorithm 1: Gauss-Seidel method

It is worth mentioning that the choice of the under-relaxation parameter in a strongly coupled approach only influences the stability of the computation and the number of necessary inter-field iteration loops. In case the inter-field iterations converge, the solution is independent of the choice of the under-relaxation parameter. This effect is shown in [WKB07]

1. For k as the number of current inter-field iteration: Start with $k = 0$ and predict the interface displacement $\mathbf{d}_{\Gamma,k}^{n+1}$ for $k = 0$ according to eqs. 4.18-4.20

2. Solve the fluid problem:

$$\mathbf{f}_{\Gamma,k+1}^{n+1} = F\left(\mathbf{d}_{\Gamma,k}^{n+1}\right)$$

3. Solve the structural problem:

$$\tilde{\mathbf{d}}_{\Gamma,k+1}^{n+1} = S\left(\mathbf{f}_{\Gamma,k+1}^{n+1}\right)$$

4. Check for convergence of the fixed-point iteration:

$$Res = C_{\text{Tol}}\left(\tilde{\mathbf{d}}_{\Gamma,0}^{n+1}, ..., \tilde{\mathbf{d}}_{\Gamma,k}^{n+1}, \tilde{\mathbf{d}}_{\Gamma,k+1}^{n+1}, \mathbf{f}_{\Gamma,0}^{n+1}, ..., \mathbf{f}_{\Gamma,k}^{n+1}, \mathbf{f}_{\Gamma,k+1}^{n+1}\right) \leq \epsilon_{\text{Tol}} \qquad (4.22)$$

   If $Res \leq \epsilon_{\text{Tol}}$:

$$\mathbf{d}_{\Gamma}^{n+1} = \tilde{\mathbf{d}}_{\Gamma,k+1}^{n+1} \qquad n = n+1 \qquad k = 0$$

   go to 1 (to begin a new time step)

5. Choice of the under-relaxation parameter ω_{k+1}

6. Apply under-relaxation to interface displacements

$$\mathbf{d}_{\Gamma,k+1}^{n+1} = \omega_{k+1}\tilde{\mathbf{d}}_{\Gamma,k+1}^{n+1} + (1-\omega_{k+1})\,\mathbf{d}_{\Gamma,k}^{n+1} \qquad (4.23)$$

   and update the interface displacements with under-relaxed values

$$\mathbf{d}_{\Gamma,k}^{n+1} = \mathbf{d}_{\Gamma,k+1}^{n+1} \qquad k = k+1$$

   go to 2 (to begin a new step in the inter-field iteration loop)

Algorithm 2: Richardson iteration

on an example from the wind-engineering context.

Applying under-relaxation to the interface displacements is the common technique in the simulation of fluid-structure interaction. However, the under-relaxation can also be applied to the loads transferred at the interface. Algorithm 3 represents the modified coupling algorithm for under-relaxation of interfaces loads, in which step 3 is divided into several sub-steps, while step 1, 2 and 4 remain unchanged. With respect to stability and efficiency, the same considerations apply to the under-relaxation of the interface loads as to the under-relaxation of the interface displacements.

To overcome the trade-off between stability and efficiency in the choice of ω, using an adaptive choice of ω is advantageous. This extension is known as dynamic or adap-

1. For k as the number of current inter-field iteration: Start with $k = 0$ and predict the interface displacement $\mathbf{d}_{\Gamma,k}^{n+1}$ for $k = 0$ according to eqs. 4.18-4.20

2. Solve the fluid problem:

$$\tilde{\mathbf{f}}_{\Gamma,k+1}^{n+1} = F\left(\mathbf{d}_{\Gamma,k}^{n+1}\right)$$

3. (a) Choice of under-relaxation parameter $\omega_{f,k+1}$

   (b) Apply under-relaxation to interface loadings:

$$\mathbf{f}_{\Gamma,k+1}^{n+1} = \omega_{f,k+1}\tilde{\mathbf{f}}_{\Gamma,k+1}^{n+1} + \left(1-\omega_{f,k+1}\right)\mathbf{f}_{\Gamma,k}^{n+1} \tag{4.26}$$

   (c) Solve the structural problem:

$$\mathbf{d}_{\Gamma,k+1}^{n+1} = S\left(\mathbf{f}_{\Gamma,k+1}^{n+1}\right)$$

4. Check for convergence of the fixed-point iteration:

$$Res = C_{\mathrm{Tol}}\left(\mathbf{d}_{\Gamma,0}^{n+1}, ..., \mathbf{d}_{\Gamma,k}^{n+1}, \mathbf{d}_{\Gamma,k+1}^{n+1}, \tilde{\mathbf{f}}_{\Gamma,0}^{n+1}, ..., \tilde{\mathbf{f}}_{\Gamma,k}^{n+1}, \tilde{\mathbf{f}}_{\Gamma,k+1}^{n+1}\right) \leq \epsilon_{\mathrm{Tol}} \tag{4.27}$$

   If $Res > \epsilon_{\mathrm{Tol}}$:

$$\mathbf{d}_{\Gamma,k}^{n+1} = \mathbf{d}_{\Gamma,k+1}^{n+1} \qquad k = k+1$$

   goto 2 (to begin a new step in the inter-field iteration loop)

   Else if $Res \leq \epsilon_{\mathrm{Tol}}$:

$$\mathbf{d}_{\Gamma}^{n+1} = \mathbf{d}_{\Gamma,k+1}^{n+1} \qquad n = n+1 \qquad k = 0$$

   goto 1 (to begin a new time step)

Algorithm 3: Gauss-Seidel method with under-relaxation of interface loads

tive under-relaxation and its two most common methods are introduced below for under-relaxation of interface displacements. Other methods to choose the under-relaxation factor exist, e.g. as presented in [Dep04] and [KW07]. To the knowledge of the author, their performance is at best equal to the methods introduced here.

Choice of under-relaxation parameter ω by the steepest descent method

The adaption of the well-known steepest descent method for coupled problems was introduced in [WMR99] and [WMR00] and revisited in [KW07]. The optimum search direction for the solution on the interface displacement $\mathbf{d}_{\Gamma}^{n+1}$ is the negative gradient direction, given by the residuum vector $\mathbf{r}_{\Gamma,k}$:

$$\mathbf{r}_{\Gamma,k}^{n} = \tilde{\mathbf{d}}_{\Gamma,k+1}^{n} - \mathbf{d}_{\Gamma,k}^{n} \tag{4.28}$$

The under-relaxation parameter is determined by:

$$\omega_{k+1} = -\frac{\left(\mathbf{r}^n_{\Gamma,k}\right)^T \mathbf{r}^n_{\Gamma,k}}{\left(\mathbf{r}^n_{\Gamma,k}\right)^T \mathbf{J}^n_\Gamma \, \mathbf{r}^n_{\Gamma,k}} \tag{4.29}$$

with $\mathbf{J}^n_\Gamma$ as the Interface-Jacobian

$$\mathbf{J}^n_\Gamma = \mathbf{J}^n_\Gamma\left(\mathbf{d}_\Gamma\right) = \frac{\partial \mathbf{r}^n_\Gamma\left(\mathbf{d}_\Gamma\right)}{\partial \mathbf{d}_\Gamma} \tag{4.30}$$

For the solution of eq. 4.29, the Interface-Jacobian, which is not explicitly available, has to be computed. It can be determined by specially enhanced fluid solvers. For black-box fluid solvers, the Interface-Jacobian can be computed by a finite difference method (e.g. [KW07]) or by solving a simplified fsi-problem [Mok01]. Both methods require the additional solutions of the structural and the fluid field to determine the under-relaxation parameter.

Choice of under-relaxation parameter ω by the Aitken's Δ^2-method

Aitken's method has been proposed and successfully used for coupled problems of fluid-structure interaction in [WMR99] and [MW01], a recent revisiting can be found in [KW07]. The original Aitken's method was developed for scalar problems. For the usage of fixed-point iterations with vectors, [IT69] extended the original method to the Aitken's Δ^2 method. FSI solver based on the Aitken's Δ^2 method proved to be simple to implement, while effective with respect to stability improvements and reduction of computational effort.

In Aitken's method, the under-relaxation factor ω is determined based on the previous two iteration steps. The relaxation parameter ω is computed recursively according to:

$$\begin{aligned} \omega_{k+1} &= -\omega_k \frac{\Delta\mathbf{d}_{\Gamma,k+1} \cdot \left(\Delta\mathbf{d}_{\Gamma,k+1} - \Delta\mathbf{d}_{\Gamma,k}\right)}{\left|\Delta\mathbf{d}_{\Gamma,k+1} - \Delta\mathbf{d}_{\Gamma,k}\right|^2} \\ \text{for} \qquad \Delta\mathbf{d}_{\Gamma,k+1} &= \tilde{\mathbf{d}}_{\Gamma,k+1} - \mathbf{d}_{\Gamma,k} \end{aligned} \tag{4.31}$$

For the computation of ω_{k+1}, only the deformations on the interface, which are naturally available, need to be evaluated, and no additional solution of the single field problems is necessary. Here, Aitken's Δ^2-method is applied for the under-relaxation of the interface displacements. Equally, it can be used to compute an under-relaxation factor for the transferred interface loads.

As the data of two previous steps is necessary to compute the relaxation parameter for the current iteration step, the under-relaxation parameter ω_1^{n+1} for the first iteration step within each time-step cannot be determined. Different solutions are possible to choose ω_1^{n+1}. Using of the last under-relaxation value ω^n from the previous time-step is sensible. However, this can cause problems with respect to the convergence of the single field solvers for the first step of the inter-field iteration loop for high values of ω^n. Therefore, in [KW07], it is suggested, to limit the ω_1^{n+1} by ω_{max}:

$$\omega_1^{n+1} = max\left(\omega^n, \omega_{max}\right) \tag{4.32}$$

To avoid problems, not only with ω_1^{n+1} being too high to ensure convergence, but also with ω_1^{n+1} being too low at the beginning of a new time-step for efficient computation, the author suggests the usage of a fixed value based on an educated choice, e.g. 0.2, for ω_1^{n+1}.

4.3.3.2 Newton-based Methods

In contrast to the fixed-point iteration, the Newton-based methods are adapted from the residuum formulation of the surface coupled problem:

$$\begin{aligned} \mathbf{r}_k &= \tilde{\mathbf{d}}_{\Gamma,k+1} - \mathbf{d}_{\Gamma,k} \\ &= S \circ F\left(\mathbf{d}_{\Gamma,k}\right) - \mathbf{d}_{\Gamma,k} \\ &= \Phi\left(\mathbf{d}_{\Gamma,k}\right) - \mathbf{d}_{\Gamma,k} \end{aligned} \tag{4.33}$$

with the aim to find an interface residuum for which $\mathbf{r}\left(\mathbf{d}_{\Gamma,k}\right) = 0$.

A general Newton method for solving non-linear problems, known as the Newton-Raphson method, is to find $f(x^*) = 0$ by starting from an initial solution x_0 and applying the iteration rule

$$x_{k+1} = x_k - \frac{f(x_k)}{f'(x_k)} \tag{4.34}$$

until $f(x_{k+1}) < Tol$ and thus $x^* \approx x_{k+1}$ within the given tolerance limit of the iteration Tol.

Transferred to the fsi context, this means finding an interface displacement $\mathbf{d}_\Gamma$, for which $\mathbf{r}\left(\mathbf{d}_\Gamma\right) = 0$ by using the iteration rule:

$$\begin{aligned} \mathbf{d}_{\Gamma,k+1} &= \mathbf{d}_{\Gamma,k} - \mathbf{r}'\left(\mathbf{d}_{\Gamma,k}\right)^{-1} \mathbf{r}\left(\mathbf{d}_{\Gamma,k}\right) \\ &\quad \text{with} \quad \mathbf{r}'\left(\mathbf{d}_{\Gamma,k}\right) = \frac{\partial \mathbf{r}\left(\mathbf{d}_{\Gamma,k}\right)}{\partial \mathbf{d}_{\Gamma,k}} \end{aligned} \tag{4.35}$$

$\mathbf{r}'\left(\mathbf{d}_{\Gamma,k}\right)$ is the tangent operator, which again resembles the Interface-Jacobian $\mathbf{J}_\Gamma$ introduced in eq. 4.30.

A realization of a basic Newton algorithm coupling scheme for the solution of fsi problems is presented in Algorithm 4. The difficulty in this approach, which arises due to the non-linear nature of the fsi-problem, is to determine the tangent operator $\mathbf{r}'\left(\mathbf{d}_{\Gamma,k}\right)$. This non-linearity is caused by the non-linearity of the inertia term in the fluid solution, the moving boundaries of the fluid domain and the large structural displacements. Only for special type of problems, the Interface-Jacobian can be derived analytically [FM05]. Several methods have been suggested to approximate the Interface-Jacobian of the interface problem. Thereby, the computational effort for solving eq. 4.35 can be reduced at the price of a slower convergence in the inter-field iteration loop, depending on the quality of the approximation. Another approach is to solve eq. 4.36 by using an iterative matrix free Newton-Krylov formulation [KAT03].

In the following, a brief summary of the most fsi solution schemes related to the Newton method is given.

- ◇ **Approximated Block-Newton by finite difference method**

  The finite difference method can be used to compute the Jacobian, which results in a high computational effort [SM00], as the residuum of the coupled computation $\mathbf{r}_k$

1. For k as the number of current inter-field iteration: Start with $k = 0$ and predict the interface displacement $\mathbf{d}_{\Gamma,k}^{n+1}$ for $k = 0$ according to eqs. 4.18 - 4.20

2. Solve the fluid problem:

$$\mathbf{f}_{\Gamma,k+1}^{n+1} = F\left(\mathbf{d}_{\Gamma,k}^{n+1}\right)$$

3. Solve the structural problem:

$$\tilde{\mathbf{d}}_{\Gamma,k+1}^{n+1} = S\left(\mathbf{f}_{\Gamma,k+1}^{n+1}\right)$$

4. Compute the increment displacement $\delta\mathbf{d}$ based on the Newton method

   (a) Compute the residuum

$$\mathbf{r}_k = \tilde{\mathbf{d}}_{\Gamma,k+1}^{n+1} - \mathbf{d}_{\Gamma,k}^{n+1}$$

   (b) Solve the equation

$$\mathbf{r}'\left(\mathbf{d}_{\Gamma,k}^{n+1}\right)\delta\mathbf{d}_k = -\mathbf{r}_k \tag{4.36}$$

   (c) Update the interface displacements

$$\mathbf{d}_{\Gamma,k+1}^{n+1} = \tilde{\mathbf{d}}_{\Gamma,k}^{n+1} + \delta\mathbf{d}_k \tag{4.37}$$

5. Check for convergence of the fixed-point iteration:

$$Res = C\left(\delta\mathbf{d}_k\right) \leq \epsilon_{\text{Tol}} \tag{4.38}$$

   If $Res > \epsilon_{\text{Tol}}$:

$$\mathbf{d}_{\Gamma,k}^{n+1} = \mathbf{d}_{\Gamma,k+1}^{n+1} \qquad k = k+1$$

   go to 2 (to begin a new step in the inter-field iteration loop)

   Else if $Res \leq \epsilon_{\text{Tol}}$:

$$\mathbf{d}_{\Gamma}^{n+1} = \mathbf{d}_{\Gamma,k+1}^{n+1} \qquad n = n+1 \qquad k = 0$$

   go to 1 (to begin a new time step)

Algorithm 4: Basic Newton algorithm

needs to be computed several times, depending on the order of finite difference interpolation and the number of interface degrees of freedom. The approximated derivatives computed by the finite difference methods depend on the size of the increment, which describes the variation of the interface displacements. Therefore, an additional

parameter is needed, which is likely to influence convergence and accuracy of the computation.

Suggested improvements are to limit the usage of the finite difference method to blocks of the tangent operator [MS03, MNS06] and to speed up the computation, at the cost of limiting the accuracy, by using only one solution step in the fluid solver [Ste02].

◇ **Approximated Block-Newton by simplified fluid and/or structural model**

Gerbeau et al. [GV03] suggest the following simplification of the fluid and the structural model: the fluid domain is fixed, the structure problem is linearized, based on the current configuration. The viscous and inertia terms are neglected in the fluid problem, which effectively reduces the fluid problem to a Poisson's equation. This simplified model is not sufficient to describe the original fsi problem, but useful to determine the tangent operator in the block-Newton algorithm and, therefore, to solve eq. 4.36. This approach is modified by extending the simplified fluid problem in [Dep04].

◇ **Approximated Block-Newton by Jacobi-free Krylov method**

Michler et al. [Mic05, MvBdB05] and van Brummelen et al. [vBdB05] suggest the use of fixed-point iterations as preconditioner to a Newton-Krylov method (GMRES), which is applied to the interface degrees of freedom. By combining Newton and GMRES, the reuse of Krylov vectors in subsequent solutions during the inter-field iterations is possible. Thereby, a reduction in computational effort is expected for sufficiently linear systems. Up to now, this method has been applied to academic problems and still has to prove its applicability for real world problems.

◇ **Approximated Block-Newton by constructed fluid model**

Vierendeels et al. [VLDV07] suggests a method to approximate the Jacobian by using reduced order models, which are constructed during the coupled inter-field iterations. One of the advantages of this approach is the fact that black-box fluid solvers can be used. In case the structural code can be modified, only a reduced order model for the fluid solver is needed. During the coupled computation, the reduced order model is gradually constructed by pairing interface displacements and corresponding interface load states. The updated fsi interface displacements are computed by solving the structural problem, while using the reduced order model as boundary condition, instead of the original fluid problem. The interface loading computed by the fluid solution for the updated boundary displacements is used to enhance the reduced order model. This iteration loop over the structural solver, the reduced order fluid model, and the original fluid model is repeated until convergence is reached. In the case of a black-box structural solver, the method can be extended by using two reduced order models.

4.3.4 Instabilities in Partitioned Analysis of Incompressible Flows

In the simulation of fsi with incompressible flows, sequentially staggered, weakly coupled fsi schemes have been observed to face problems with respect to stability of the computa-

tion [Mok01]. Iteratively staggered, strongly coupled schemes don't show these instabilities, but problems with convergence of the solution within one time-step can occur. This phenomenon is known as the "artificial added mass effect", as it can be traced back to the fluid masses, which surround the structure at the fsi interface, acting as additional mass in the system of equations of the structural problem. However, the "artificial added mass effect" discussed here is only relevant to the computation of the coupled solution. It has to be clearly distinguished from the added mass effect in aeroelastic problems, which is also caused by the mass of a fluid surrounding a structure and is known to damp oscillations but also to cause aeroelastic instabilities, e.g. for bridge cross-sections.

The artificial added mass effect is widely known and has been subject to several analyses, among others in [Mok01],[LTM01], [Nob01]. Causin et al. [CGN05] created a simple, linear model problem to express the influence of the fluid problem in the fsi computation by an additional mass in the structural problem, introducing an "added mass operator". For simplified problems, the added-mass effect can be well described using analytical analysis [CGN05], [FWR07]. However, for real-world fsi problems, the analysis and prediction of the artificial added-mass effect proved to be difficult due to the nonlinearities in fluid and structural problem and additional influences, which are introduced by discretization and approximations.

In the context of the artificial added mass effect, the unstable behavior results in unphysical results for weak coupling schemes, which can be observed in interface loadings and/or displacements as spurious high frequency oscillations and/or extremely high amplitudes, as compared to the expected results. For strong coupling schemes, the occurrence of instability is more likely to be found in the convergence behavior within one time-step rather than in the converged results of the inter-field iterations [CGN05]. In the case of under-relaxed fixed-point iterations, this requires a small under-relaxation factor for a stable, but slow convergence. Depending on the actual formulation, Newton-Krylov-based methods show superior behavior with respect to the number of necessary inter-field iterations and computational effort for simulations affected by the artificial added mass effect [KW07, KW09]

The degree of instability can be assessed by the magnitude of disturbance introduced into the system and by the simulation time, after which this instability occurs. Using these criteria, the correlation of the following parameters for coupled computations with the added mass effect were observed:

- ◇ The ratio of the densities of fluid and structure has the most significant influence. A higher mass ratio ρ^F / ρ^S worsens the instability. This is due to the fact, that by decreasing the structural mass, the destabilizing added mass effect caused by the fluid mass around the structure is increased.

- ◇ For simply staggered coupling schemes, decreasing the time step size could be expected to limit instabilities due to the explicit character of weak coupling schemes. However, decreasing the time-step size worsens the instability. This holds also for iteratively staggered, strongly coupled schemes. It can be explained by the fact, that

in eq. 2.69 the influence of the mass related terms becomes increasingly dominant, as compared to the stiffness related terms, the smaller the time-step size is.

- ◇ The stiffness of the structure has an easing effect on the instability. This easing effect can be increased, e.g. by introducing pre-stress into the structure. A higher fluid viscosity seems to worsen the artificial added mass effect.
- ◇ For explicit coupling schemes, the usage of a higher order predictor for the interface geometry increases the influence of the added mass effect. Best results are achieved by using no predictor for weak coupling with incompressible flows.
- ◇ The usage of higher order time integration schemes used in fluid simulation also seems to worsen the added mass effect.

In order to limit the artificial added mass effect in coupled computations, several remedies have been suggested. Tezduyar et al. [TSKS06] suggest to increase the structural mass on the left side of eq. 2.69 while leaving the right hand side unmodified. Fernández et al. [FGG07] developed an approach using projection scheme for the inter-field iterations. In [PF01] load and motion transfer have been modified to increase stability. A practical approach is to respect a lower limit of the time-step size, and thus, postpone the onset of the added mass instability beyond the end of the time interval of interest. However, this approach is limited by the time-step size necessary to resolve the physical effects of interest. Furthermore, an upper limit of the time-step size can exist due to the Courant-Friedrichs-Lewy condition. Thus, the interval of possible time-step sizes might be very limited or even empty.

The analysis of the artificial added mass effect in [CGN05] and [FWR07] allows to conclude, that weakly, sequentially staggered coupling schemes are only conditionally stable in simulations involving incompressible fluid flow. Typically, an upper limit of ρ^F / ρ^S can be found as instability condition.

In the application of wind-membrane interaction, in which the wind is modeled as incompressible air flow, no significant influence of the added mass effect is expected and observed. This can be reasoned by the relatively low density of air compared to the structural density. The worsening effect of the small structural stiffness is neutralized by the applied prestress. In contrast to the analysis found e.g. in [CGN05], [FWR07], which is related to the simulation of blood flow, in the simulation of wind-membrane interaction, the fluid has access to both sides of the structure. To the author's knowledge, the effects due to artificial added mass for cases of a structure with fluid on both sides have yet to be analyzed.

4.4 Computational Aspects of Partitioned Analysis

After the discussion of coupling methods for the simulation of surface coupled problems of fluid-structure interaction, in the following, certain aspects of fsi coupled simulations shall be introduced. These aspects are essential for the setup of a computational environment, which is suitable for the simulation of wind-membrane interaction.

4.4.1 Non-matching Interface Discretization

In section 4.2, the usage of different spatial discretizations of the fluid-structure interface Γ was named as an advantage of a partitioned fsi approach, as the best suited spatial discretization can be applied for all physical domains. By using individual discretization in the different domains, the spatial surface discretization of the common interface is likely to vary as well. In the most general case, this results in differences in discretization of the common fsi interface, which can be in the density of the discretization or / and in the type of surface elements. In the following, the spatial discretization of the fsi interface shall also be simply named as interface mesh. Thereby, the case of individual interface discretization is referred to as *non-matching interface meshes*. An example for non-matching fsi interface meshes is given in fig. 4.3, which shows the surface mesh of a four-point tent, both in the structural and fluid domain.

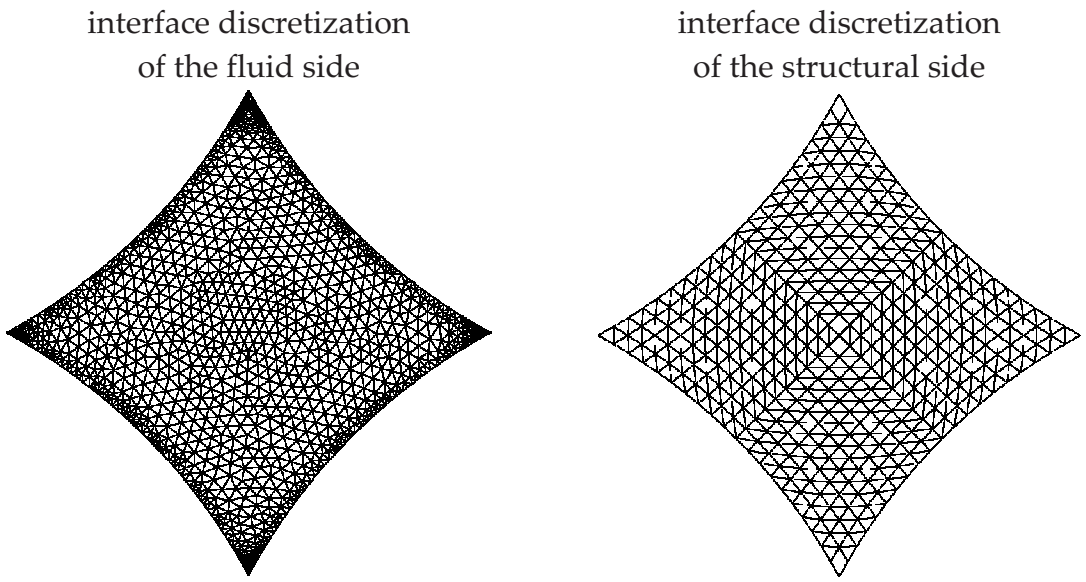

Figure 4.3: Non-matching interface discretization upper side of a four-point tent structure.

To realize the physical coupling, the transfer of the coupling quantities has to be performed. In case of non-matching interface meshes, this requires methods to transfer data between various discretizations. The criteria for the data transfer methods can be derived from the coupling conditions formulated in section 4.3, which were derived for the case of matching interface discretizations. In the context of this work, these criteria are the conservation of interface loads, as well as displacements and thus, energy at the interface. This conservation has to be fulfilled locally, as well as globally for the summation of loads and energy over the interface. Furthermore, the transfer method has to be sufficiently computationally efficient, since for every inter-field operation, the data transfer between the non-matching meshes has to be performed at least twice.

Different methods for the data exchange on non-matching interface discretizations are discussed in the following:

◇ **Next-Neighbor interpolation**

The Next-Neighbor interpolation is a fast and simple method, in which the each node on one side of the interface is linked to the closest node on the other side of the interface [TBU00]. This method provides reasonable results only for interface discretizations that are almost identical, especially with respect to the interpolation of displacements. While the sum of loads is interpolated in a conservative manner, the spatial distribution of the loads can change significantly trough this data exchange method.

◇ **Projection based methods**

In projection based methods, a point of the target interface discretization is projected onto the source mesh. Based on the position within the source mesh, the data is interpolated onto the projected point and this data can be used in the original point [FLL98]. Alternatively to the projection of nodal values, [CL97, CL05] suggest the projection of quadrature points. Similar to point-based projections, also whole elements from the target mesh can be interpolated into the source mesh and the size of the area of intersection can be used for interpolation [JH04],[fAC03]. A comparison of three most common projection schemes can be found in [JJGL05].

◇ **Spline based methods**

Spline-based interpolation methods originate in the fields of computer graphics and medical imaging. The idea is to approximate the interface data on both sides by sum of shape functions, which are fitted to the interface geometry. This sum of shape functions is used to define a transformation matrix for data transfer between the two interface discretizations. Thereby, no projection and search algorithms are needed [dBvZB07]. Especially radial basis functions are of interest, as they were found to be well-suited for problems of fluid-structure interaction [BW01, SHC00, RA08].

◇ **Weighted residual based methods**

Weighted residual based methods aim to ensure a consistency of the transferred quantity in an integral sense. Similar to the Galerkin method presented in section 2.2.1.5, the coupling quantity is multiplied with a test function and integrated over the interface. This leads to a linear system of equation, which includes all interface degrees of freedom of the coupling quantity. The method can be enhanced by an appropriate choice of the test function, typically the basis function from one interface side. As the same test function has to be used on both interface discretizations, weighted-residual based methods often necessitate projection and / or interpolation. Similar methods can be derived based on Lagrangian multiplier methods [PFO01]. A particular technique is the Mortar method [BMP94, Baa01].

Interpolation based data exchange method for non-matching interface discretization used within this work

Within this work, an interpolation based method is used for the data transfer between non-matching interface discretizations. It proved to be sufficiently accurate not to limit the stability of the computation and is easy to implement. Most importantly, it can be applied to

interpolate data on curved surfaces with reasonable computational effort. To simplify the further discussion, the terms of source and target mesh are introduced. The source mesh is the spatial interface discretization, on which the coupling quantity data is located and the target mesh is the interface discretization onto which the data shall be transferred.

To assess the relations between the two non-matching interface meshes, the so-called *neighborhood-search* is preceding the data interpolation. In the neighborhood-search, each node of the source mesh is projected onto the target mesh. The element on the target mesh, in which the projected node is located, is identified and the position of the projected node is expressed in the local coordinates of the specific element on the target mesh. This projection is performed twice, firstly, with the interface mesh of the structural side as source mesh and the interface mesh of the fluid side as target mesh and secondly, vice versa.

In the scope of this work, the fluid and the structure interfaces are assumed to stick together. Sliding of domains in tangential direction to the interface surfaces is not permitted. Therefore, the relations between interface discretization will remain constant and the neighborhood-search has to be performed only once at the beginning of the simulation.

In order to fulfill the requirements of global and local conservation of coupling quantities, the interpolation scheme needs to be separated into two types of exchanged data: coupling quantities of field-type, such as deformations or pressure, and quantities of flux-type, such as nodal forces.

◇ **Interpolation of field quantities**

For field type quantities, the interpolation is performed based on the type and shape functions of the source element. This is explained in the example of interpolation of displacements.

The interface displacements shall be interpolated from the source interface mesh of the structural side to the target mesh on the fluid side, which is illustrated in fig. 4.4(a) . Therefore, the projection of fluid node i onto the structural source mesh is considered. In the respective structural element e_S with n nodes and n shape functions $N^e_{S,r}(\xi,\eta)$, $\xi_{S,i}$ and $\eta_{S,i}$ are the local coordinates of node i. The interpolated displacement $\mathbf{d}_{F,i}$ for fluid node i is computed as:

$$\mathbf{d}_{F,i} = \sum_{r=1}^{n} N^e_{S,r}(\xi_{S,i},\eta_{S,i})\mathbf{d}_{S,r} \tag{4.39}$$

An identical procedure can be applied to transfer the pressure from the fluid to the structural side, which is illustrated in fig. 4.4(b) . Now, a node j from the structural side is projected to the fluid side and is located in fluid interface element e_F with m nodes and m shape functions $N^e_{F,l}(\xi,\eta)$. Accordingly, based on the local coordinates $\xi_{F,j}$ and $\eta_{F,j}$ of the projected structural node within the fluid element, the pressure p on the structural node can be computed by:

$$p_{S,j} = \sum_{l=1}^{m} N^e_{F,l}(\xi_{F,j},\eta_{F,j})p_{F,l} \tag{4.40}$$

The presented transfer of displacements and / or pressure by a linear or bilinear interpolation does not guarantee the conservation of energy or displacement. However, for moderately different interface meshes, the author observed no significant decrease in accuracy or stability comparing fsi simulations with matching interface discretization to those with data transfer by linear interpolation for non-matching interface discretization.

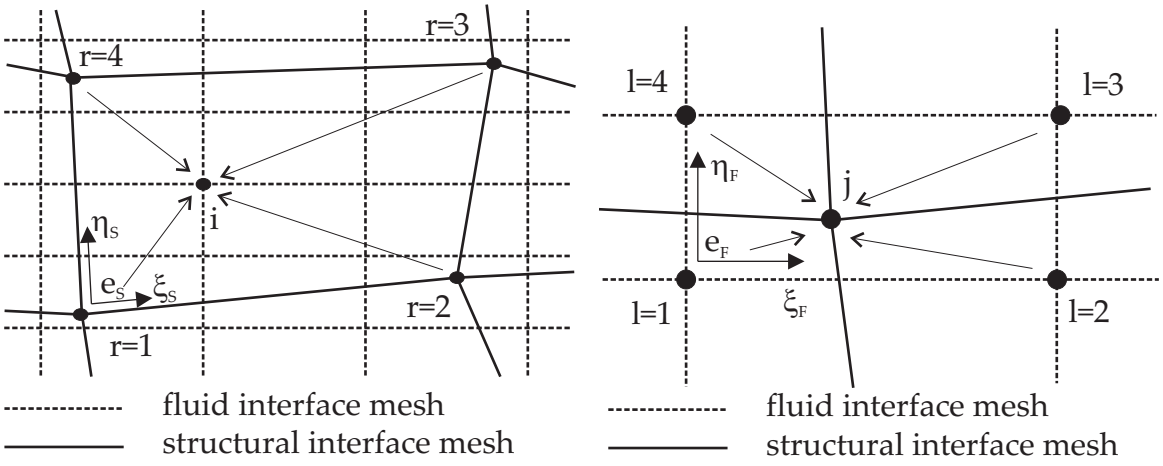

(a) Interpolation of displacements form a structural surface element e_S onto a fluid node i.

(b) Interpolation of pressure form fluid surface element e_F onto a structural node j.

Figure 4.4: Interpolation of field-based quantities.

◇ **Interpolation of flux quantities**

For the transfer of nodal loads from the fluid to the structural side, the conservative interpolation strategy is applied [FLL98], which is illustrated in fig. 4.5. Here, a fluid node i from the source mesh is projected onto the structural element e_S of the target mesh. Within the element e_S of the target mesh, the projected node i has again the local coordinates $\xi_{S,i}$ and $\eta_{S,i}$. Now, the nodal load $\mathbf{f}_{F,i}$ of node i is transferred to the n nodes of the element e_S according to:

$$\mathbf{f}_{S,r} = N^e_{S,r}(\xi_{S,i}, \eta_{S,i})\mathbf{f}_{F,i} \tag{4.41}$$

Eq. 4.41 is used for all n nodes of element e_S. This projection and transfer of nodal loads is repeated for all fluid nodes of fluid interface mesh.

For linear shape functions $N^e_{S,r}(\xi, \eta)$ holds:

$$\sum_{r=1}^{n} N^e_{S,r}(\xi, \eta) = 1 \tag{4.42}$$

which leads to the fact, that fluid node i transfers its complete nodal load to the n nodes of structural element e_s:

$$\mathbf{f}_{F,i} = \sum_{r=1}^{n} \mathbf{f}_{S,r} \tag{4.43}$$

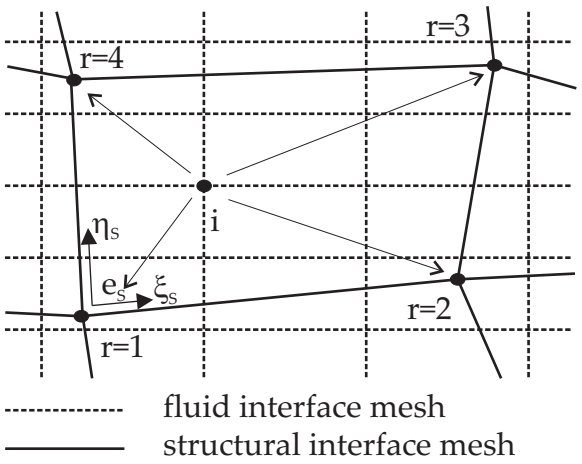

Figure 4.5: Interpolation of flux-based quantities.

As this procedure is performed for all fluid nodes, the sum of nodal loads on the structural interface equals those on the fluid interface, which establishes a conservative type of interpolation with respect to global conservation of interface loads.

Consideration about the used interpolation method

As with most interpolation methods, the result of the method used in this work is best, if the two interface discretizations are quite similar. In case of larger differences in element sizes, this interpolation method will perform with reduced accuracy. In case of flux quantities, such as nodal loads, this will not affect the global conservation, e.g. the sum of forces before and after the interpolation, but will have an impact on the distribution of these forces, thus the local conservation. This can be easily explained using fig. 4.6.

Figure 4.6 shows a coarse discretization of the fluid side of the interface and a regular discretization of the structural interface. On the fluid side, a uniform pressure distribution is assumed. For these non-matching meshes, the uniform pressure load shall be consistently transferred from the source mesh on the fluid side to the target mesh on the structural side. Based on the regularity of the target mesh, as result of the interpolation of nodal loads representing a uniform pressure distribution on the source mesh, a uniform distribution of nodal loads on the target mesh is expected. At the beginning of the data transfer, the pressure on the fluid source mesh is transformed into nodal loads on the fluid source mesh. Then, these nodal loads are transferred to the structural side by the interpolation procedure described above. Due to the fact that the fluid interface discretization in the lower area is much coarser than the structure's discretization, not all nodes of the target mesh will have nodal forces assigned. Comparing the actual distribution of the nodal forces on the target mesh after the interpolation with the correct solution, the incorrect distribution of loads becomes obvious. However, the sum of interface nodal forces will still be equal on fluid and structural side.

While the relation of coarseness between fluid and structural side needs to be considered for plane interface geometries, for curve geometries, such as the surface of a cylinder,

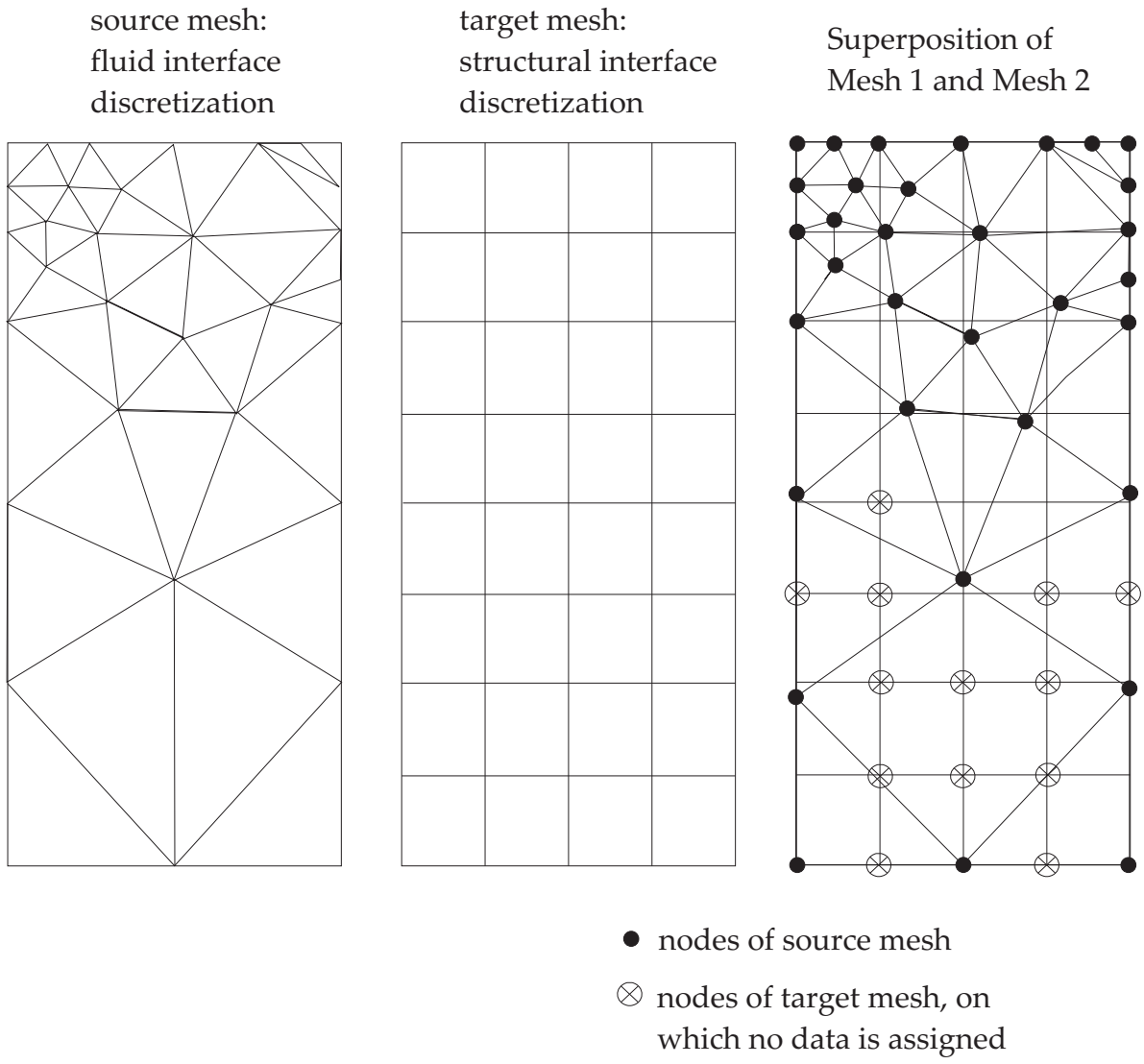

Figure 4.6: Interpolation of flux quantities for large difference in interface discretization.

problems with interpolation can result in a totally wrong interpolation, as not only the distribution, but also the direction of the nodal forces on the target mesh can be highly incorrect.

A simple remedy to this problem is to use a finer source mesh when transferring flux-based data. Fortunately, in the case of fluid-structure interaction, typically the fluid side features a finer discretization than the structural side, so this criteria is implicitly met.

Considering the linear or bilinear interpolation for field-based quantities on interface discretizations with highly differing coarseness, no un-physical distribution of the transferred quantities is expected. However, a loss of data and, therefore, a loss in accuracy occurs each time data is transferred from a finer to a coarser mesh. Additional attention has to be paid to non-matching interface discretization with curved fsi-interfaces. For field based quantities, which depend on the local coordinate system of the interface mesh, e.g. pressure acting always perpendicular to the interface surface, the difference in surface normal direction be-

tween source and target mesh at a specific point has to be respected.

4.4.2 Mesh Movement of the CFD Grid

As the structure is subject to deformations during the simulation of fluid-structure interaction, the fsi interface, which describes the boundary between structural and fluid domains, is deformed as well. In the simulation of wind-membrane interaction, large displacements of the membrane are expected. However, rigid body rotations and displacements are not analyzed, as the membrane structure is considered well grounded.

For the structural domain within this work, a Lagrangian approach is chosen. Therefore, the moving fsi boundary does not necessitate any modification. For the fluid domain, which is based on the Eulerian approach, the moving fsi boundary has to be explicitly respected. In the scope of this work, the ALE-approach was chosen to handle the moving boundaries in the fluid domain. The ALE approach has already been introduced in section 3.3.7. In contrast to fixed-grid methods, in an ALE-based approach, the fluid mesh is adapted to the moving fsi-boundaries. The challenge in adapting the computational grid of the fluid simulation is not to deteriorate the quality of the computational grid. Therefore, the local modification of the fluid domain at the fsi boundary is extended into the fluid domain. This adaptation of the fluid computational grid has to be performed for every step in the interfield iteration loop.

The most direct method to include the changes of the boundaries of the fluid domain in the coupled computation is to generate a new computational grid for the whole fluid domain or parts of it. This approach is known as *remeshing*. However, remeshing is computationally very expensive and can introduce various sources of inaccuracy. One source of possible inaccuracy is the interpolation, which is necessary, to transfer the mesh-based data of the fluid domain from the old to the new fluid grid. Additionally, a remeshed fluid domain necessitates a new setup of the interpolation method to transfer coupling data, e.g. to conduct a new neighborhood search. For CFD computation on multiple processors, a new domain decomposition has to be performed. Due to these considerations, remeshing of the fluid domain shall be restricted to cases, in which other methods of mesh adaption already have lead to an extremely distorted computational grid, e.g. due to large displacements, or cases in which a change of the mesh topology is necessary, e.g. when the fluid penetrates the structure at cracks. For all other cases, the usage of mesh moving methods is favorable, with respect to accuracy, stability, and computational effort.

Mesh moving methods are methods, which transfer the local deformation at the fsi interface into the computational grid of the fluid domain by changing the position of the grid nodes while the topology of the computational grid remains unchanged. The requirement to preserve the quality of the complex computational grid is not trivial. In order to resolve the flow boundary layer close to the fsi interface appropriately, the computational fluid grid is usually very fine at the fsi interface. Therefore, in the area, in which the greatest mesh deformations are expected, small size elements reside. Due to the difficulties of mesh moving, the ALE approach has been interpreted as three field "fluid"-"computational fluid grid"-"structure" problem, e.g. by [Wal99], [Far04].

Summarizing the considerations above, the main criteria for the mesh movement methods, with respect to arbitrary deformations within a certain range, is to:

- ◇ retain a good mesh quality to avoid problems with convergence and / or accuracy of the CFD solution.
- ◇ avoid the creation of control volumes with negative volume due to self penetration of the CFD grid.
- ◇ limit the additional computational effort.

Different methods for mesh movement computations are available, which try to distribute the mesh distortion introduced at the fsi interface into the fluid domain while retaining an acceptable mesh quality. In the following, the most widely used methods are divided into three groups:

- ◇ **Analytical and interpolation based methods**

  Analytical methods are easy to implement, fast to compute and reliable for geometrically simple situations [SHC00]. For block structured meshes, simple linear and transfinite interpolation proved to give good results, while no system of equations needs to be solved [GBD$^+$01, Glü02]. For unstructured meshes, e.g. with fine boundary resolution, basic interpolation methods are not applicable.

  A newer development in interpolation methods is the usage of radial basis function [vZdBB07], [dBvdSB07], same as those which can be used for data interpolation at the fsi interface. In order to derive the interpolation matrix, a linear system of equations has to be solved to invert the matrix of correlation between the boundary nodes. This method is reported to provide good results even for large displacements and rotations. Additionally, by the use of radial basis functions, aspects of the mesh moving can be combined with data interpolation for non-matching interface discretizations [RA08].

- ◇ **Methods based on mesh smoothing**

  Laplacian method [LY96] and bi-harmonic approaches [Hel03] are well known as mesh smoothing techniques, common in mesh generation in CFD and CSD. The solution of an elliptic problem is used to generate a smooth distribution of a certain quantity over a certain domain within the prescribed boundary conditions. In case of mesh movement, the quantities distributed over the fluid domain can be the displacements of the fsi interface. Compared to the Laplace method, the bi-harmonic approach has the advantage to control the mesh spacing better but at the cost of a four time higher computational effort.

  By assigning a non-uniform distribution of diffusiveness, depending on the element size and / or distance to the boundaries, within the fluid domain, the mesh deformation can be influenced. This is necessary to avoid, that smaller and larger size elements are subject to the same change in volume, which is very likely to lead to self-penetration of the CFD mesh. Self-penetration of the fluid mesh can also result due to shear deformations of the CFD elements. It is a disadvantage of basic mesh smoothing methods, such as the Laplacian method, that the control of mesh shear deformation is limited.

◇ **Methods based on structural analogy**

Methods based on structural analogy can be further subdivided into:

- Spring methods [Blo00], [DF02], [BDS05]
- Pseudo material approach [Wal99], [STB03], [STB04], [LQX06]

The idea for spring approach and the pseudo material approach is to use the principles of structural mechanics to determine the mesh deformation. The fluid grid is treated similar to a volume of material and the boundary deformation is typically introduced as a Dirichlet boundary condition for a structural problem. Most commonly, a pseudo static problem of the following type is produced:

$$\mathbf{K}_g \cdot \mathbf{d}_g = \mathbf{f}_g \tag{4.44}$$

$\mathbf{K}_g$ is the pseudo stiffness, which is derived based on pseudo material parameters or assumed springs. The load vector $\mathbf{f}_g$ is based on the Dirichlet boundary conditions, which represent the boundaries of the fluid domain, including the fluid-structure interface. The solution of this linear system of equations results in the displacements of nodes of the fluid grid $\mathbf{d}_g$. For the most general three-dimensional case, the system of equations needs to contain the three possible displacements of all nodes of the fluid grid which are subject to the grid adaption. For a large computational grid with up to several millions of fluid nodes, the setup of the system of equations and its solution can become computationally expensive.

Compared to the spring approach, in the pseudo material approach the distortion of control volumes in the CFD grid can be easier controlled. The pseudo material quantities, such as the Lamé-parameter [STB03], can be assigned to the CFD grid depending on the element size, and / or distance to the boundaries of the fluid domain. Thereby, the distortion of smaller elements can be avoided, as they can be found at the domain boundaries. In order to control mesh distortions in the spring methods, additional configuration or additional spring types have been introduced, e.g. torsional and diagonal springs.

An interesting suggestion to reduce the computational effort for adaptation of the fluid grid is to combine this method with interpolation techniques. Instead of the original CFD grid, a coarser mesh is used to solve the pseudo material problem. Based on the solution on the coarser mesh, the deformation of the finer original CFD mesh is determined via interpolation. This interpolation can be based on a Delaunay diagram [LQX06] or on shape function as used in CSD [Lef08].

For wind-membrane interaction, mainly deformations perpendicular to the pre-stressed membrane surface are expected. Therefore, except for simple interpolation techniques, any of the three mesh moving methods can be applied in this context. Details about the method used are given in section 4.5.2.

4.4.3 Convergence in Partitioned Analysis

The strongly coupled partitioned solution strategies, which were introduced above, use an iterative scheme to reach a state of equilibrium for the interaction of fluid and structure within each time step. By performing the inter-field iterations, the coupled solution converges to this state of equilibrium. In order to assess the convergence of the coupled solution, an appropriate convergence criteria has to be formulated.

Deparis [Dep04] suggests a criterion based on the velocity $\mathbf{u}$ in the whole fluid domain, the structural displacement $\mathbf{d}$ and velocity $\dot{\mathbf{d}}$ at the fsi interface. The check for convergence, L^2 or Euclidean norm $||\quad||$ is used together with two parameters:

$$||\left(\tilde{\mathbf{d}}^{n+1}_{\Gamma,k+1}, \dot{\tilde{\mathbf{d}}}^{n+1}_{\Gamma,k+1}\right) - \left(\mathbf{d}^{n+1}_{\Gamma,k}, \dot{\mathbf{d}}^{n+1}_{\Gamma,k}\right)|| \leq C_1\,\epsilon_{\text{Tol}} \tag{4.45}$$

$$||\mathbf{u}^{n+1}_{k+1} - \mathbf{u}^{n+1}_{k}|| \leq C_2\,\epsilon_{\text{Tol}} \tag{4.46}$$

The drawback of this approach is, that the relative error check in eq. 4.45 and 4.46 is not dimensionless and, therefore, additional to the tolerance limit ϵ_{Tol} the choice of the parameters C_1 and C_2 is problem depending.

Similarly, Küttler et al. [KW07, KW09] [Mok01] propose an convergence criterion based on an absolute value using the interface displacements. This criterion uses only the length scale norm of the residuum of the interface displacements $\mathbf{r}^{n+1}_{\Gamma,k+1}$ with a tolerance limit of ϵ_{Tol} and n_{eq} as the total number of degrees of freedom for the test quantity on the coupling interface:

$$\mathbf{r}^{n+1}_{\Gamma,k+1} = \tilde{\mathbf{d}}^{n+1}_{\Gamma,k+1} - \mathbf{d}^{n+1}_{\Gamma,k} \tag{4.47}$$

$$\frac{1}{\sqrt{n_{eq}}}||\mathbf{r}^{n+1}_{\Gamma,k+1}|| < \epsilon_{\text{Tol}} \tag{4.48}$$

Alternatively to using absolute values of the coupling quantities, relative values can be used to formulate a convergence criterion. In a relative convergence criterion, a reference value, e.g. a reference displacement d_{ref}, is defined, with which the value of the residuum can be normalized. The choice of d_{ref} is based on typical values expected for the specific application. Deparis [Dep04] suggests to perform the convergence test by using:

$$||\tilde{\mathbf{d}}^{n+1}_{\Gamma,k+1} - \mathbf{d}^{n+1}_{\Gamma,k}|| < d_{ref}\,\epsilon_{\text{Tol}} \tag{4.49}$$

$$\frac{||\dot{\tilde{\mathbf{d}}}^{n+1}_{\Gamma,k+1} - \dot{\mathbf{d}}^{n+1}_{\Gamma,k}||}{||\dot{\tilde{\mathbf{d}}}^{n+1}_{\Gamma,k+1}||} < \frac{d_{ref}\,\epsilon_{\text{Tol}}}{||\tilde{\mathbf{d}}^{n+1}_{\Gamma,k+1}||} \tag{4.50}$$

$$\frac{||\mathbf{u}^{n+1}_{k+1} - \mathbf{u}^{n+1}_{k}||}{||\mathbf{u}^{n+1}_{k+1}||} < \frac{d_{ref}\,\epsilon_{\text{Tol}}}{||\tilde{\mathbf{d}}^{n+1}_{\Gamma,k+1}||} \tag{4.51}$$

A similar approach is used by Gerbeau et al. [GV03] and Glück [Glü02], but applied only to the interface displacements.

Additionally to the convergence tolerance ϵ_{Tol}, the absolute and relative convergence criteria introduced above all necessitate the choice of a problem dependent parameter or

reference value. Here, an enhanced relative convergence criterion is proposed, which is used within this work.

In contrast to the convergence criterion presented, in the current approach, the reference value can be automatically determined based on the data of coupling quantities obtained during the inter-field iteration. As a first approach, the absolute change in two relevant coupling quantities, e.g. the interface displacement $\mathbf{d}_\Gamma$ and the interface load $\mathbf{f}_\Gamma$, since the end of the last time step is used to normalize the residuum:

$$\frac{||\tilde{\mathbf{d}}_{\Gamma,k+1}^{n+1} - \mathbf{d}_{\Gamma,k}^{n+1}||}{||\tilde{\mathbf{d}}_{\Gamma,k+1}^{n+1} - \mathbf{d}_{\Gamma}^{n}||} < \epsilon_{\text{Tol}} \tag{4.52}$$

$$\frac{||\tilde{\mathbf{f}}_{\Gamma,k+1}^{n+1} - \mathbf{f}_{\Gamma,k}^{n+1}||}{||\tilde{\mathbf{f}}_{\Gamma,k+1}^{n+1} - \mathbf{f}_{\Gamma}^{n}||} < \epsilon_{\text{Tol}} \tag{4.53}$$

with $\mathbf{d}_\Gamma^n$ as the interface displacement and $\mathbf{f}_\Gamma^n$ as the interface load at the end of the previous time-step. Both criteria have to be fulfilled to establish convergence within one time-step.

The advantage of this convergence criterion is to be able to omit the specification of a problem dependent parameter additionally to the tolerance limit. Furthermore, the convergence test is performed on all variables with the same accuracy. In case of small changes in the coupling quantities since the end of the last time-step, the requirement for establishing convergence is increased, compared to the methods presented above. By applying the convergence criteria to both, interface displacements and loads, it is ensured that the influence of under-relaxation on the convergence criterion is limited, which is discussed below. Monitoring the relative change of the coupling quantities at the interface during the inter-field iterations proved to be a valuable byproduct for the analysis of computational instabilities or failures. It provides the possibility to trace drastic changes in the coupling quantities to one single field solver and thus a separation into "cause and effect", which is otherwise difficult because of the interdependencies of the involved computation.

Remarks on convergence criteria for fixed-point iterations with under-relaxation

For methods based on fixed-point iteration with under-relaxation, the convergence criteria have to be applied to the non-under-relaxed quantities. In the discussion above, this is indicated by marking the non-under-relaxed values with a tilde. Based on the author's experience, it is highly suggested to consider that even by using the non-under-relaxed values for the convergence check, the influence of the under-relaxation is still existent in the convergence criteria due to the interdependency of the coupling quantities, which are used to judge the state of convergence.

An example is the usage of a very low under-relaxation factor, e.g. 10^{-3} for the interface displacements and a relatively high convergence limit of 10^{-2}. The convergence check after the first inter-field-iteration uses the non-under-relaxed values. Therefore, the low under-relaxation factor has no influence. However, due to a small change in the interface-displacements, the fluid solution is very likely to result only in a small change of the interface loads. The interface displacements, which are computed based on these only slightly modified interface loads, will only slightly differ from those at the end of the previous interface

displacements. Now, the convergence check for the interface displacements and the interface loadings will indicate convergence due to the small changes compared to the previous inter-field iteration step.

However, this convergence is only artificially achieved due to the high under-relaxation. For further time-steps, this can result in slower convergence within the inter-field iteration loop or even in the occurrence of instabilities in the coupled computation. These effects have been found to be more severe in case of the usage of predictors.

By dynamically determining the under-relaxation factor with the Aitken's method, considerations about very small under-relaxation factors could be omitted, as the under-relaxation factor increases when coupled computation converges. It shall be noted that this assumes a good convergence of the coupled simulation. For strongly coupled computations that face instabilities, e.g. due to the artificial added mass effect introduced above, even under-relaxation factors determined with the Aitken's method can easily be very low.

Concluding, for the usage of under-relaxation in fixed-point based methods, special care should be taken to avoid failures of the convergence criteria due to the under-relaxation. In the current work, the under-relaxation factor was limited to values larger than 10^{-2} for convergence limits typically in the range of 10^{-4}.

Convergence in the coupled simulation and in the single field solutions

Due to the strong physical coupling, the convergence of the coupled partitioned solution is depending on the convergence of the single field solvers. The single field solvers have to reach convergence for the respective current boundary conditions within every step of the inter-field iteration loop. The tolerance limit, which has to be met to establish a state of convergence for the coupled computation, was identified above by the value ϵ_{Tol}. In order to reach ϵ_{Tol} for the coupled computation, the tolerance limit for the convergence criteria of the single field solvers $\epsilon_{\text{Tol, single field}}$ has to be smaller than ϵ_{Tol}, since the accuracy of the coupled simulation will naturally be limited by the accuracy of the single field solvers. Deparis [Dep04] suggests to apply a similar convergence criteria for the single field solvers as for the coupled computation and to choose the tolerance limit for the single field solver to $\epsilon_{\text{Tol, single field}} = \epsilon_{\text{Tol}} / 10$. This corresponds with the author's recommendation to choose the convergence limit of fluid and structural solver one magnitude smaller than the convergence limit expected for the coupled computation. Strong fluctuations of the coupling quantities in the inter-field iteration, which start to occur below a certain limit, have been found as an indication of a too high convergence limit for one of the single field solvers.

4.5 Computational Concept

The previous sections discussed the different elements necessary to perform a fully-coupled fsi simulation. This section presents the implementation of the coupling approach in a software environment.

The highly demanding requirements for the simulation of wind-membrane interaction are met by using a partitioned approach. For this partitioned approach, the specialized

software codes CARAT for the structural computation and Ansys CFX 11 for the fluid computation are used. These single field solvers have already been introduced in the previous chapters.

Three software setup

For an efficient realization of a software environment for coupled simulation of wind-membrane interaction, it is advantageous to reuse existing single field solvers and to limit the necessary modifications as much as possible. This is especially important in the case of Ansys CFX, which is a commercial software, whose source code is not available. Therefore, all modifications in Ansys CFX have to be introduced using the User Fortran Programming interface.

To limit the modifications in the existing codes, the data exchange in the current environment is handled by a third software programm, which is called the *coupling tool* in the following. The main purpose of the coupling tool is to perform the data transfer of the coupling quantities for non-matching interface discretization. It is sufficient for each single field solver to just consider the data on its side of the fsi-interface based on its appropriate interface discretization. The coupling quantities are sent from one code based on the respective interface discretization to the coupling tool, which performes the data transfer and sends the coupling data based on the interface discretization of the second solver to the second solver. This data transfer between the three involved software codes, the structural solver, the coupling tool, and the fluid solver, is shown in fig. 4.7

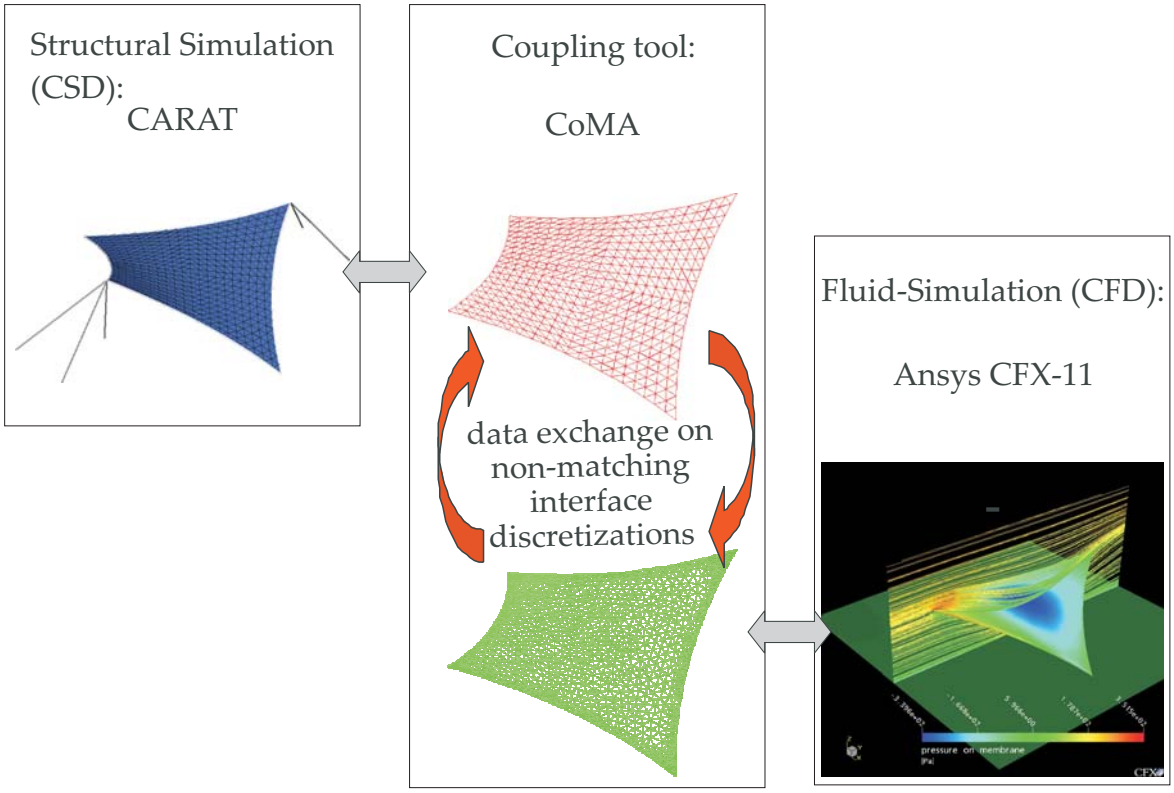

Figure 4.7: Exchange of coupling data using three software codes.

Additional advantages of using a separate software for the data exchange are:

- ◇ Different software codes for the simulation of the single field solvers can be used. The possible exchange of single field solver in the current environment necessitates that each solver has the specific software interface to communicate with the central coupling tool.
- ◇ The application of the central coupling tool is independent of the type of problem. Therefore, its application can be extended to other multi-field simulations, in which the data exchange based on the discretization of a common interface is necessary.
- ◇ The central coupling tool has all information about the degrees of freedom on the fsi interface. Thereby, the implementation of methods in the coupling tool is possible, to modify or interpret the interface data from the two coupling codes and thereby, to enhance the coupled simulation.
- ◇ Extending the functionalities of the central coupling tool further, a client server software environment setup is possible. In this setup, the central coupling tool manages the complete coupling simulation and activates the single field solvers as updated single field solutions are required. Possible applications are the optimization in context of multi-physics problems, especially, fluid-structure interaction. Another possible application would be the realization of the fsi coupling scheme using reduced order models, as introduced in section 4.3.3.2.

In order to realize these advantages, the central coupling tool CoMA was developed within this work. Details about the coupling tool are given in section 4.5.3.

Coupling scheme

To fully represent the strong coupling between wind flow and the deformation of the membrane structure, a strongly, iteratively staggered coupling scheme is necessary. As explained in section 4.3.3, this can be realized by using schemes based on fixed-point iteration or Newton-based schemes.

In the proposed software environment, the application of Newton-based coupling schemes is restricted by the lack of access to the source code of the commercial fluid solver Ansys CFX. Without the possibility to make major modifications in the fluid solver, the usage of Newton-based schemes is restricted to methods, which are not enhanced by the solution of a subproblem. Additionally, for the application of wind-membrane interaction, no experience is available, to which extent subproblems contain the necessary physical relations to sufficiently model the wind flow around a building or a membrane construction. Newton schemes based on the Jacobi-free Krylov method still have to prove their applicability to large scale problems and for the Newton-based methods based on the finite-difference schemes, no significant improvements are expected compared to the application of an advanced fixed-point iteration scheme. The only Newton-based method, which is of interest, is the one using a constructed fluid model.

Concluding, Newton-based methods are extremely difficult to realize with a black-box single field solver, while for possible Newton-based schemes no significant improvements

compared to schemes based on fixed-point iterations are expected. Therefore, within this work, a coupling scheme based on the fixed-point iteration is used with stabilization by adaptive under-relaxation based on the Aitken method, which has been presented in section 4.3.3.1. A flow-chart of the sequence of computations for the coupling scheme and the necessary data transfer is presented in fig. 4.8. This coupling scheme is a realization of the schemes presented in Algorithm 2 or Algorithm 3, depending whether the under-relaxation is applied to the interface displacements or interface loadings. As initial step, the surface mesh of the fsi interface discretization is sent from both solvers to the coupling tool, before the iteratively sequentially coupled computation starts.

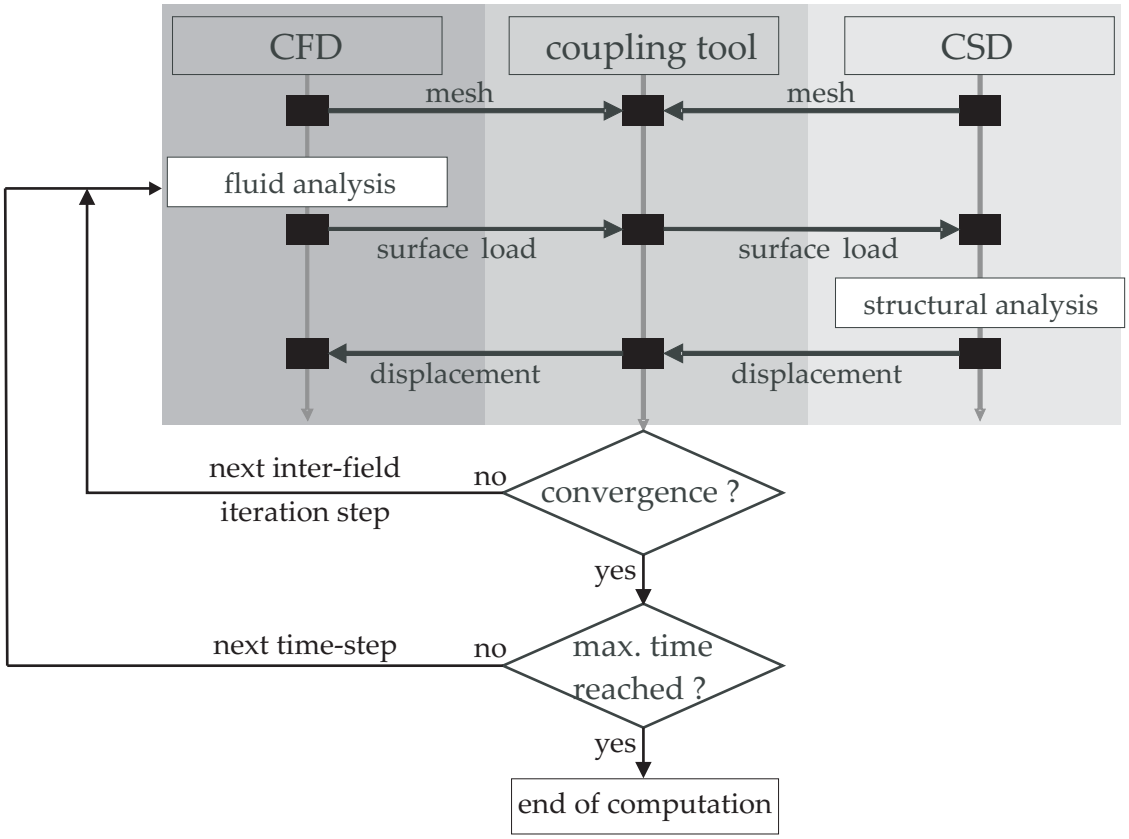

Figure 4.8: Flow-chart of computations and data exchange in the current approach.

The necessary modifications of the single field solvers CARAT and Ansys CFX for an application within this coupling scheme are presented in the following sections.

Geometrical models in fluid and structural domains

Surface coupled multi-physics problems, such as simulation of fluid-structure interaction, requires special consideration about the type of the computational and geometrical models used in the single field solvers. This can be easily explained at the example of aero-elastic analysis of an aircraft wing. From the structural point of view, the wing can be sufficiently represented by a beam or plate type computational model. The structural model can be connected to the geometrical model by projection schemes . For correct modeling of the fluid

flow around the wing, the complete three-dimensional geometry of the wing is necessary in the fluid domain. Therefore, the computational model of the wing in the fluid domain has to be identical to the geometrical model. The possible difference between the computational models used in structural and fluid domain needs to be considered, when setting up fsi analysis.

In the case of membrane structure-wind interaction, considerations about dimension of the used structural and fluid models can be separated into those concerning the membrane itself and the supporting structure. As explained in section 3.5.2, the influence of the supporting structure is neglected in the fluid simulation within this work. Accordingly, the supporting structure is not represented in the fluid domain.

The geometry of a prestressed membrane by itself is a curved surface with a very small thickness compared to the lateral dimensions. In structural simulations, including the form finding computation, the thickness of the membrane is treated as a constant parameter. Thereby, the membrane's geometry can be reduced to an infinitely thin plane, to a two-dimensional structure in a three-dimensional space. This two-dimensional surface is used as the structural computational model.

In the fluid simulation, the membrane structure can be modeled as an infinitely thin surface as well, as no significantly different flow effects are expected whether the membrane is modeled with or without considering its thickness. To be able to distinguish the flow conditions on the upper and lower side of the membrane, the membrane geometry needs to have two sides in the fluid simulation. Thus, the two-dimensional membrane has to be described by two separate surfaces in the geometric and computational model of the membrane in the fluid domain.

To create a compatible geometrical model in the structural domain, the surface used in the structural model is doubled. The orientation of the normal vector of the two surfaces are adjusted so, that they point in opposite directions into the fluid domain. The mapping from the computational structural model to the geometry model is straightforward, as the same surface discretization is used for both models, thus only the different orientation of the surface normal vector has to be considered.

4.5.1 Structural Solver: CARAT

The extension of the structural solver CARAT for coupled problems is straightforward. For static, geometrically non-linear analysis, the respective solution algorithm is enhanced by a staggering procedure. For dynamic, time-dependent geometrically non-linear analysis, each time-step can be repeated multiple times during the inter-field iteration loop [BWK06].

The surface loads on the fsi interface, which are computed by the fluid solver and transferred by the coupling tool, are treated as ordinary surface loads. Forces are directly used as nodal loads, while surface pressure and traction are integrated to nodal loads based on the discretization of the fsi interface and the form functions used in the structural model. The resulting nodal loads are exclusively used on the right hand side of eq. 2.59. Therefore, they

are not treated as follower loads in the classical sense. However, by iterating in the inter-field iteration loop and therefore, by repeating the structural computation for geometries, with small changes in deformation as the coupled computation converges, the effects of the follower forces is fully included in the current setup.

In the current setup, the modification of the coupling quantities, the interface load and interface displacements, are performed inside CARAT. The used method of adaptive under-relaxation based on the Aitken's method has already been introduced in section 4.3.3.1, as well as the convergence check for the inter-field iteration in section 4.4.3. The convergence check is performed within CARAT using the change of the coupling quantities on the structural fsi interface discretization.

Central geometrical model

As explained in section 2.1, for pre-stressed membrane structures, the initial geometry can not be assessed directly. It is the result of a form finding computation, which computes the geometry, for which the inner forces due to prestress and initial loading conditions are in equilibrium. In the simulation of prestressed membrane structures, the form finding computation has to precede the 'real' structural analysis.

In the current environment, the initial geometry of the membrane is computed using the structural analysis programm CARAT. According to considerations about the consistency of computational and geometrical models in fluid and structural domains, the initial membrane geometry is described by two surfaces with identical surface discretization and identical position of the nodes, but with opposite directions for the surface normal vectors. The two surfaces are stored in facetted description in the stereolithography (STL) file format. The STL-file format contains only the surface geometry of a three dimensional object. The STL-files describing the membrane's upper and lower sides are used to model the membrane in both the structural and the fluid domain. Thereby, a consistency of the geometrical models in both domains is ensured and the facetted geometrical representation of the membrane serves as the central geometrical model for the coupled problem.

4.5.2 Fluid Solver: Ansys CFX

Within this work, the numerical simulation of wind flow is performed by the commercial CFD-package Ansys CFX 11 of Ansys Inc. The basic flowchart of the solution algorithm of CFX has been presented in fig. 3.8 in section 3.5.1.

For the simulation of fluid-structure interaction, additional routines have been implemented via the User Fortran Programming Interface. Ansys CFX provides the possibility to call User Fortran Routines at specified points during the CFD solution, e.g. at the beginning or end of every time step or every coefficient iteration step of the solver. In order not to interfere with the MPI and VPM environment used by CFX for parallelization, the data exchange for fsi simulation is file-based. Therefore, the interface loading and control sequences are written into ascii-files, while interface displacements and further control sequences are read from ascii-files.

Realization of a weak, simply staggered coupling scheme

Figure 4.9 presents the realization of a simple staggered coupling scheme in Ansys CFX, which requires only little modification of the CFX solution scheme. The boundary conditions are exchanged at the end of the fluid time-step. For this exchange, first the interface loads and control flags are transferred to the coupling tool. Then the Ansys CFX solver waits until it receives the interface displacements and further control flags. Afterwards, it updates the computational mesh according to the new boundary conditions and starts a new time-step.

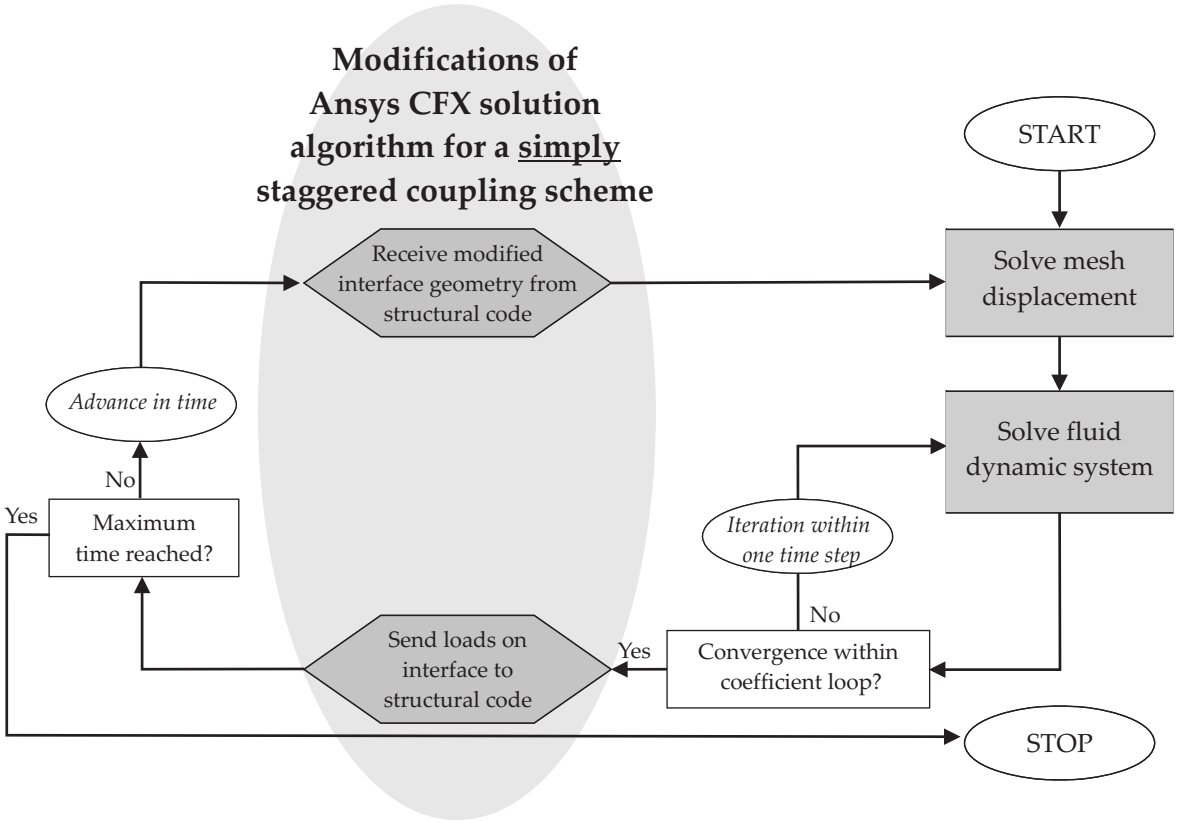

Figure 4.9: Modified CFX solution scheme for weak, simply staggered fsi coupling.

Realization of a strong, iteratively staggered coupling scheme for steady-state fsi problems

The feature to solve the mesh displacements and, therefore, to adapt the computational CFD grid to the changed boundary conditions is only available for transient computations. For some applications with constant flow conditions, a steady-state behavior of the structure can be expected as result from a computation of fluid-structure interaction. An exemplary case is a flexible plate as an obstacle in a channel with laminar flow, which will bend due to the fluid pressure on its surface. For constant flow conditions, a static behavior of this plate is expected. To model this application of fluid-structure interaction, a transient, time-dependent simulation can be used. It will model the dynamic, oscillating behavior of the structure until the oscillation settles.

In the scope of this work, modeling a steady-state solution is performed in a more efficient way. By using the implementation presented in fig. 4.9 and choosing a time-step size, which is larger than the period of the smallest eigenfrequency of the structure in the coupled system, the time dependency of the computation can be circumvented. The transient fluid solution resembles a series of snapshots of the fluid solution, separated by a considerably long time interval. Thereby, the transient effects of the fluid solution are neglected. However, this implies the usage of a time integration scheme, which converges for time-step sizes clearly violating the CFL condition.

This approach shows a much more stable computational behavior compared to a fully transient simulation. Furthermore, fewer steps of the inter-field iteration loop are necessary to reach the steady-state solution compared to the transient analysis with declining oscillations. Thereby, the computational effort can be greatly reduced. An evaluation by comparing this iteratively-staggered steady-state solution scheme with a completely transient scheme is presented in section 4.6.2 on the example of the ARIES membrane structure.

Realization of a strong, iteratively staggered coupling scheme for transient fsi problems

For transient, time-depending fsi simulations with strong, iteratively staggered coupling schemes, as presented in section 4.3.3, the fluid solver has to be capable to run solutions of the same time-step multiple times. If there is no convergence within the coupled solution after one inter-field iteration, the time-step is repeated with updated boundary conditions. Therefore, at the beginning of each iteration step in the inter-field iteration loop, the state of the CFD solver has to be reset to the one at the end of the previous time-step. This reset of the state of the solution was not available in Ansys CFX in the scope of this work .

A different implementation of the implicit coupling scheme was chosen within this work, which is visualized in fig. 4.10. It is implemented by modifying the coefficient iteration loop. Until the solution within the coefficient iteration loop is converged, the solution algorithm remains unchanged. Once the convergence criterion for the solution of the coefficient loop iteration is satisfied, the computed interface loads are sent to the structural solver. The fluid solver stops until it receives updated boundary displacements from the structural solver. Additionally, the fluid solver receives notifications, if the convergence for the coupled solution is reached. If it is not, the fluid mesh is updated with the new interface displacements and the computation is continued within the coefficient iteration loop. Once convergence for the coupled solution is reached, the simulation code proceeds in time.

The advantage of this approach is that the complete FSI inter-field iteration loop is implemented within the structure of the coefficient loop. Considering all additional FSI-specific steps of the inter-field iteration loop as functions which can be skipped, if the convergence criterion within the coefficient loop is not fulfilled, the coefficient loop remains unchanged during most of the computation. Therefore, the solution algorithm of the fluid solver "does not know or need to know" of the existence of an additional inter-field iteration loop. From the point of view of the solver, only additional cycles in the coefficient iteration loop are performed. This extension of the solution scheme is applicable for FSI-implementations in CFD-Codes, which do not support "time step repetition".

As the coupled solution converges, the change in the interface displacement between two cycles in the inter-field iteration loop becomes very small. This results in a quick conver-

gence of the coefficient iteration loop within one inter-field iteration. Through the ongoing iteration in the coefficient iteration loop, while converging towards the coupled solution, the accuracy of the fluid solution is increased as well. It can be interpreted as reusing the previous solutions reached within the inter-field iteration loop, in order to accelerate the convergence of the coefficient iteration loop. This is an advantage over the standard iteratively staggered fsi implementation, in which at the beginning of a step in the inter-field iteration loop the fluid solution is reset to the state at the end of the last time-step, and thus, the information of the previously computed converged inter-field iteration steps is lost.

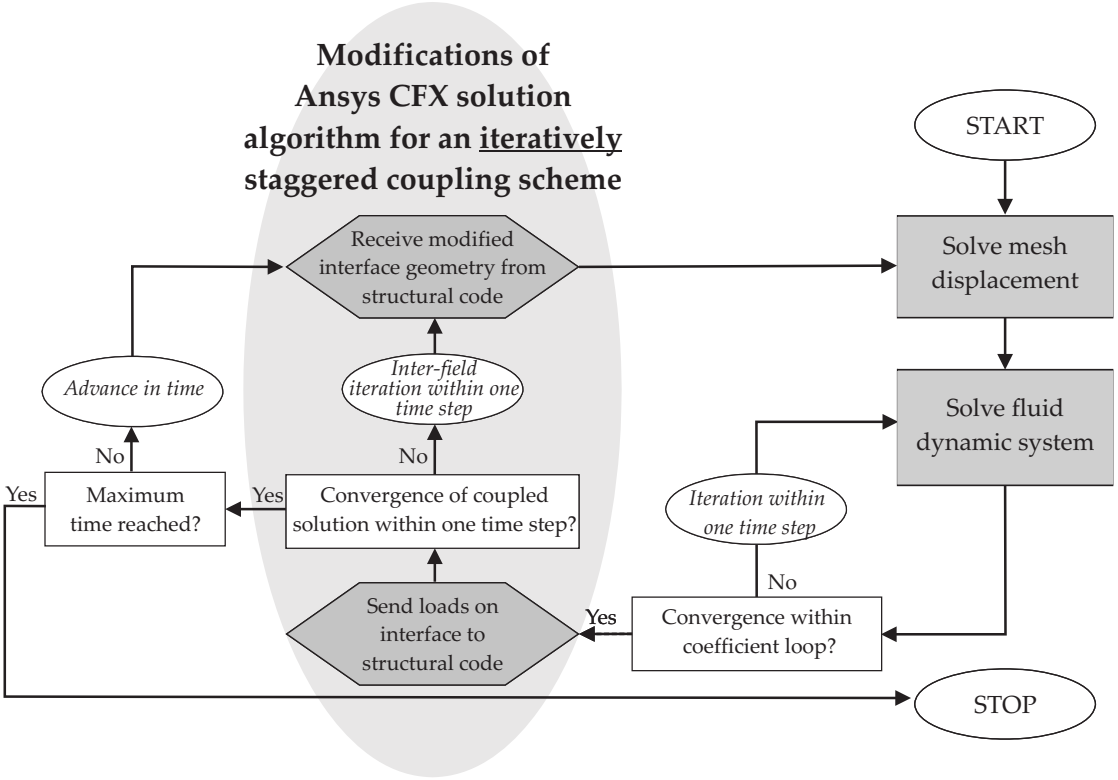

Figure 4.10: Modified CFX solution scheme for strong, iteratively staggered fsi coupling.

Mesh movement scheme used in Ansys CFX

By applying the above mentioned ALE approach, Ansys CFX offers the possibility of moving and deforming grids such as they are necessary for the deformation of a FSI interface during a coupled simulation [CFX06]. The adaptation of the CFD grid to the updated boundary conditions is performed by solving a diffusion problem. This resembles a special case of the mesh moving model proposed in [JT94], [STB03].

$$\begin{aligned} &\frac{\partial}{\partial x}\left(K_{Mesh}\frac{\partial}{\partial x_i}d_i\right) = 0 \\ &\text{with } x\Big|_{\Gamma_{fsi}} = x_b \text{ for deformed surfaces} \\ &\text{and } x\,|_{\Gamma_0} = 0 \text{ for undeformed surfaces} \end{aligned} \tag{4.54}$$

with d_i as the displacement of the CFD mesh in i-th direction and K_{Mesh} as the diffusion coefficient, which has the function of a the mesh stiffness. In order to prevent self penetration of the finite volume elements in the adapted computation grid, it has been proven useful to increase the "mesh stiffness" of especially small finite volume cells by determining the parameter K_{Mesh} depending on the volume of the cells to:

$$K_{Mesh} = \left(\frac{1}{V_{FVE}} \right)^m \tag{4.55}$$

where V_{FVE} is the volume of a specific finite volume cell and m a natural number. For numbers m greater than 3, depending on the volume of the smallest finite volume cell and the computational precision, floating point exceptions are likely to occur.

Using $m = 3$, the mesh moving algorithm provides smooth computational grids, while preserving the boundary layer discretization for interface deformations perpendicular to the fsi interface. For shear type of deformations, modifying the "mesh stiffness" K_{Mesh} does not diminish the susceptibility of the finite volume cells towards distortion. Therefore, large shear deformations can result in overlapping of the computational grid close to the fsi interface, thus making the grid unusable and stopping the computation.

An important aspect of mesh movement in Ansys CFX is that the mesh deformation is based on the difference between the new mesh and the previously used mesh. In case of an iteratively coupled scheme, the reference mesh is the one of the previous inter-field iteration step. This is advantageous in the case of known interface displacements, which are applied gradually.

In the case of unknown interface displacements, such as in fsi, this gradual mesh update is problematic. Since no fixed reference mesh is used, all distortions introduced during inter-field iteration in the coupled simulation remain within the mesh. For coupled computations, which involve a large number of inter-field iterations, and thus, a large number of mesh deformation operations, the mesh quality quickly decreases. This results in less accurate fluid computations, less accurate interface loading, and therefore, even higher disturbances in the interface displacements computed by the structural solver.

4.5.3 Coupling and Data Transfer Tool: CoMA

In the scope of this work, the data exchange was handled by a third program, which manages the setup of the computation and the communication between the codes.

For this type of application, the commercial software package MpCCI is available. MpCCI stands for Mesh-based parallel Code Coupling Interface and was developed by the Fraunhofer Institute for Algorithms and Scientific Computing SCAI as a standardized tool for the coupling of multiple solvers [fAC03]. MpCCI supports the data exchange for different discretizations of the fsi-interface. Communication of MpCCI is based on the common Message Passing Interface-Library (MPI). It is available on different platforms and allows coupled simulations with codes across diverse platforms.

The in-house coupling tool CoMA (Coupling for Multiphysics Analysis) was developed at the Chair of Structural Analysis, Technische Universität München, based on the experiences with MpCCI and the aim to realize additional functionalities. It has an object-oriented, C++ based implementation and is able to run on different platforms and in various software environments. In the development of CoMA, special focus was put on a high modularity of the software. Therefore, a very flexible tool was created, which is applicable for a large variety of multi-physics problems as well as diverse software environments.

The key features in the concept of the coupling tool CoMA are:

- ◇ Support of different single field solvers
- ◇ Support of different communication concepts
- ◇ Support of parallelization of the single field solvers
- ◇ Flexible data exchange for various multi-physics simulations
- ◇ Support of multiple data transfer methods for non-matching grids
- ◇ Support of overlapping interface patches
- ◇ Possibility to include key components of the coupled computation in the central coupling tool.

Within this thesis, the main features of the coupling tool CoMA are discussed further. The implementation of the functionalities is to some degree straightforward, in other cases, complicated by details. Where available, references providing more details about the implementation are given.

Support of different single field solvers

In the first version, CoMA was used for the communication between the in-house structural code CARAT and the commercial fluid solver Ansys CFX 11 as well as the open source fluid solver OpenFOAM [GKI+09]. The implementation in the fluid solver FASTEST (Flow Analysis Solving Transport Equations with Simulated Turbulence) is in progress.

Support of different communication concepts

Methods for data exchange between the central coupling tool and the single field solvers are implemented in a modular way in CoMA. Thereby, different communication concepts can be supported. depending on the current software environment.

As a basic communication concept, a file based data interface was used within this work. This implementation was chosen as a flexible data interface, which does not interfere with communication methods used for the parallelization of the single field solvers. During the coupled computation, the sending program writes to disk an ascii-file containing the data of a coupling quantity or of control flags. This file is read in by the receiving program. Each code waits, until the data file necessary to proceed is available. The availability of a data file is indication by the existence of an additional blank file. The format for the files used

for the exchange of coupling quantities was chosen in such a way, that the files can be easily visualized using GID as a postprocessing tool.

Meanwhile, the communication concept in CoMA has been enriched by a communication concept based on the Message Passing Interface (MPI) [GKI+09].

Support of parallelization of the single field solvers

For the computation of wind-membrane interaction, fluid simulations with high computational effort have to be performed. This necessitates the possibility to parallelize the fluid solver. In an arbitrary decomposed domain, the patches of the fsi interface are likely to be scattered among different processes. For an efficient parallelization strategy in the coupled computation, it is therefore advantageous, if the data transfer is possible between CoMA and the various parallel fluid processes, among which the fluid solution is split up.

To enable this individual communication, CoMA provides the possibility to handle an interface surface, which is split into multiple surfaces called (interface) partitions. This is visualized in fig. 4.11, which shows two surface discretizations, used by code 1 and code 2, and each split into different partitions. This approach provides the necessary flexibility to work with parallel solvers, as each partition can be assigned to one process of the solver.

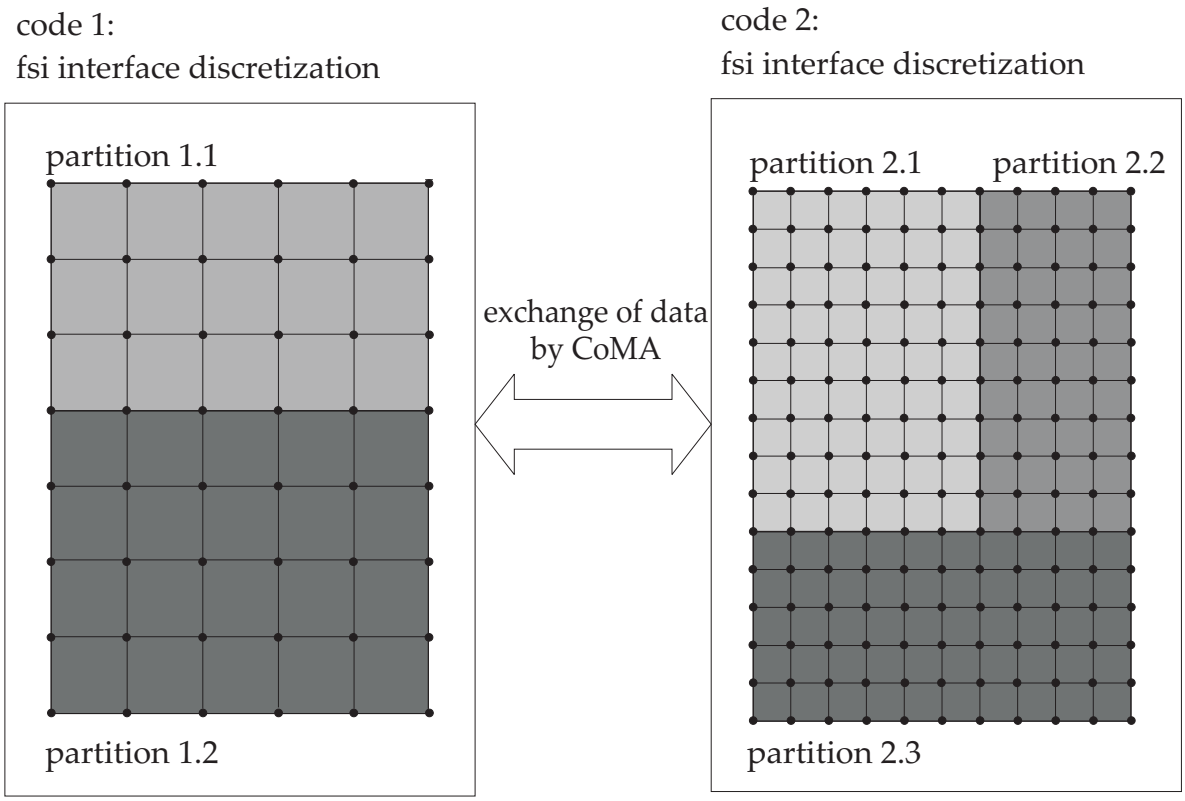

Figure 4.11: Data transfer scheme based on partitions of the fsi interface surface.

Flexible data exchange for various multi-physics simulations

The functionality of exchanging data between arbitrary surfaces with non-matching discretization is necessary for many numerical multi-field simulations. To extend the usage of CoMA beyond fluid-structure interaction, the exchange of mesh-based data has to be flexible with respect to the type of the exchanged data. In the current setup, the data exchange is possible for flux and field based data, which can be scalars or vectors.

Additionally to the flexibility regarding the type of exchanged data, CoMA is flexible regarding the point in time, in which the data is exchanged. This is realized by a concept of exchange points, which are specified in the input-file of CoMA. For each exchange point the code acting as data source, the code receiving data, and the data type are specified.

Fig. 4.12 gives an example for a fsi simulation between one structural solver (CSD) and a fluid solver consisting of two fluid solver processes (CFD1 and CFD2). As initial step, the fsi-interface mesh of each code is sent to CoMA to establish the relations between the interface discretizations. At exchange points 1 and 2, surface pressure is transferred from the fluid code's processes to the structural solver via the coupling tool CoMA. In exchange point 3 and 4, the interface displacement is sent from the structural solver to the two fluid processes. As final control step within one inter-field iteration loop, the simulation status of each code is sent to CoMA, which compiles these and sends instructions how to proceed with the computation.

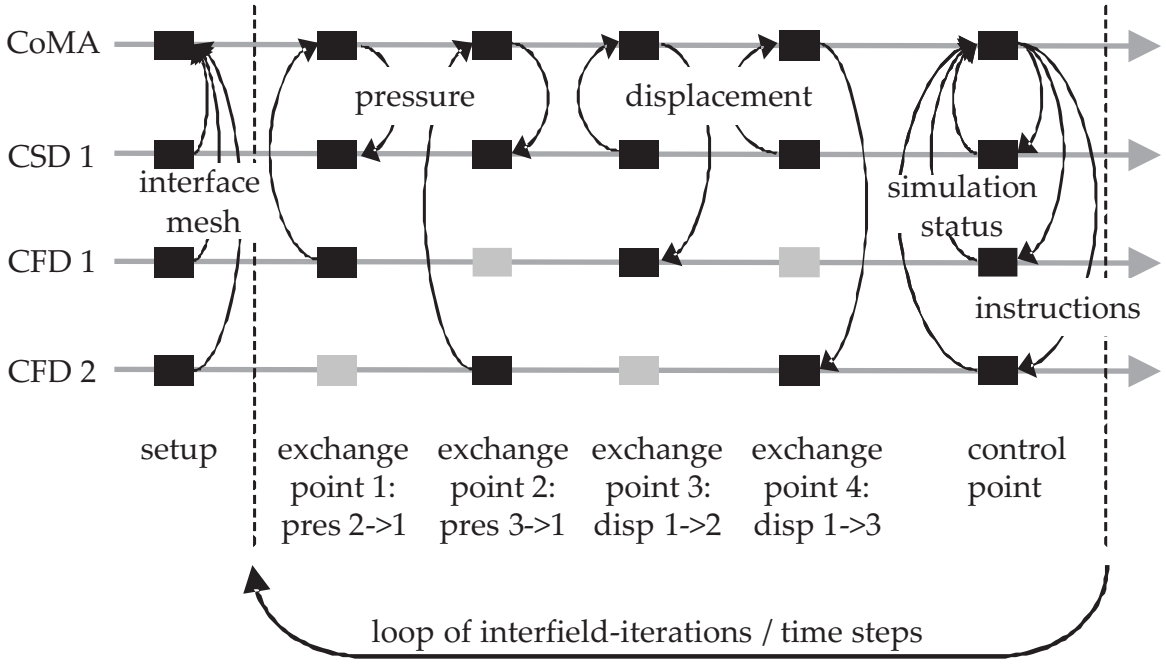

Figure 4.12: Data transfer scheme using exchange points.

In the example presented in fig. 4.12, the data transfer is organized by the interface partitions, as each fluid code is assigned to certain partitions of the fsi interface (e.g. referring to fig. 4.11: partition 2.1 and 2.2 for fluid process 1 and partition 2.3 for fluid process 2),

while the complete fsi surface is assigned to the only structural code process (e.g. reffering to fig. 4.11: partition 1.1 and 1.2 of the structural solver). With the combination of the concept of surface patches and exchange points, a great flexibility for different application with multiple involved single field solvers is achieved.

Support of multiple data transfer methods for non-matching grids

In section 4.4.1 different methods for data transfer between non-matching interface discretizations were introduced. Due to its modular setup, CoMA provides the flexibility to implement any of these methods in the proposed environment. Currently, linear and bilinear interpolations for field-based quantities and the conservative interpolation for flux-based quantities is implemented. These interpolation-based methods are described in section 4.4.1. Supported discretizations are linear triangular and bilinear quadrilateral surface meshes. Details about the implementation can be found in [IKL+07].

In future work the basic data transfer methods will be enhanced. This will be necessary due to the need for exchange of different coupling quantity types, e.g. sensitivities, or due to different shape functions used in the single field solver, e.g. for isogeometric analysis.

Support of overlapping interface patches

In section 4.5, the geometrical model of the fluid-structure interface for membrane-wind interaction is deduced as two sides on an infinitely thin membrane, which are modeled by two identical surfaces with identical or different discretization. These two surfaces represent the fsi-interface in the structural and in the fluid model. Establishing a neighborhood search, which is necessary for the interpolation-based data transfer methods as introduced in section 4.4.1, is not trivial. The two surfaces in the structural and fluid domain are lying on each other and in case of an identical discretization, such as for the structural domain, even the nodal coordinates of the surface meshes are identical. Therefore, for a correct matching of these overlapping surfaces it is necessary to distinguish between upper and lower surface in the fluid and structural model. This can be achieved by using the direction of the surface normals. Within CoMA, a more general approach is used, in which tags are assigned to the interface partitions. Only partitions with identical patches are related to each other.

As an example, the fsi interface in the structural domain, and analog in the fluid domain, can be described as one surface consisting of two partitions. The partitions represent the surfaces describing the upper and lower side of the interface. Now, an identical tag is assigned to the upper side partition in both, the fluid model and the structural model. The same is done for the lower sides. Thereby, the two upper sides of the models can be identified by CoMA and will be related to each other. Same holds for the lower sides. This selective pairing of interface partitions enables the usage of a standard neighborhood search in CoMA, while using overlapping partitions.

Possibility to include key components of the coupled computation in the central coupling tool.

By transferring functionalities from the single field solvers to the central coupling tool CoMA, the flexibility of the software environment is enhanced. By not only performing data transfer for the current values of the coupling quantities, but also retaining a history

of quantities on the interface, the convergence of a coupled simulation can be monitored. Furthermore, stabilizing methods, such as adaptive under-relaxation, or methods enhancing the computational efficiency, such as the use of predictors, can be implemented in the central coupling tool. These methods are then available for any multi-physics application using CoMA.

Functionalities, such as the error estimation of the transferred coupling quantities, are only possible for a code, which has access to all discretizations of the fsi-interface and the coupling quantities based on these surface discretizations. This makes the coupling tool, which actually performs the data transfer between the non-matching meshes, an ideal platform to assess this error.

4.6 Example: Wind Effects on ARIES Membrane Structure in Coupled Computation

The methods of fluid-structure interaction, which have been described in this chapter and implemented in the software environment, are now applied to analyze the interaction between the ARIES membrane structure and wind flow.

4.6.1 Setup of the Coupled Computational Model

The coupled computational model essentially consists of the numerical fluid and structural modeling that have been described in the previous chapters. The purpose of the proposed software environment is to combine these numerical models for a coupled analysis.

The fully prestressed configuration of the ARIES structure, which was computed in section 2.4, is used as the numerical structural model. The structural part of the coupled computation is carried out by the finite element program CARAT.

The CFD model consists of a finely discretized inner domain and an outer domain with a coarser computational grid. This model has been discussed in section 3.5. For an appropriate simulation of the neutrally stratified ABL flow, same turbulence models, wall treatment, and boundary conditions, as presented in section 3.5.2.2 and section 3.5.2.3, are applied.

As the ARIES structure is completely included in the inner domain, moving boundaries have to be considered only in the inner domain. Same as in section 3.5.2.1, the ARIES structure is represented by the membrane surface within the fluid model. The surface is separated into an upper and a lower part, in order to compute the pressure difference between both sides of the membrane.

As initial solution for the fluid part of the coupled computation, the flow field results from previous analysis of the rigid ARIES structure are used. Thereby, the computational time of the first fluid solution in the first inter-field iteration step can be significantly reduced.

The fsi interface is represented by the upper and lower sides of the membrane. Each upper and lower interface surface is discretized by 17328 triangular elements on the fluid side and 3450 quadrilateral elements on the structural side. In the coupling tool CoMA, the two membrane sides are treated as two surface partitions. In the fluid as well as in the structural model tags are assigned to the two partitions, in order to establish the correct relations (see section 4.5.3). The exchanged coupling quantities are the surface pressure and interface displacements. For both quantities, the bilinear interpolation method described in section 4.4.1 is applied. Based on the structural discretization of the fsi interface, the surface pressure is transferred to nodal loads within the structural solver. Thereby, the tangential shear stresses induced by the fluid on the membrane are neglected. This is considered as acceptable because the tangential shear stresses were two magnitudes smaller, as compared to the pressure. Furthermore, the membrane structure is susceptible to loads acting perpendicularly to the surface, which makes forces resulting from surface pressure the decisive loads.

The control of the coupled computation is performed by CoMA as well. For all computations, an iteratively staggered, fixed-point iteration based coupling scheme, as described in section 4.3.3.1, is applied. Adaptive under-relaxation according to the Aitken's method was applied in all simulations in order to stabilize the computation and decrease the computational effort.

Convergence of the coupled simulations within the inter-field iteration loop is checked by using the convergence criterion introduced in section 4.4.3. The tolerance limit for the coupled simulation is 10^{-4}. For the single field solvers, a Root Means Square (RMS) criterion was used with a tolerance limit of 10^{-9} for the structural computation and 10^{-5} for the fluid computation.

4.6.2 Simulation of Steady-State Solution

Firstly, steady-state response of the structure is analyzed for two different reference wind speeds and each for two wind directions. In this steady-state simulation, a time-wise constant inflow velocity distribution and time averaged turbulence is assumed. The distribution of velocity and the turbulence quantities is prescribed according to eqs. 3.118, 3.119, and 3.120.

Due to the constant flow conditions, the structure is expected to reach a static state of deformation. In this static state, effects of inertia of the structure can be neglected, as no displacement over time and thus no acceleration is occurring.

Evaluation of the proposed method for steady-state solutions in coupled computations

For the iteratively staggered, coupled analysis of steady-state situations, a special coupling approach was described in section 4.5.2. Here, this approach is evaluated on the example of the steady-state response of the ARIES structure for wind from the front with a reference wind speed of 25 m / s.

With the suggested approach for iteratively staggered, steady-state computations, the effects of inertia in the structural computation are neglected. Thereby, the structural problem

can be solved in a static, geometrically non-linear computation. For the solution of the fluid field, a large time step is chosen.

For comparison, an iteratively staggered, fully transient coupled simulation was carried out for the same constant inflow velocity. The transient simulation models the declining oscillation of the structure until it reaches the steady-state condition.

In fig. 4.13 the time-displacement curve of the transient simulation and the result of the steady-state modeling strategy are compared using two points A and B located on the ARIES membrane surface (see fig. 4.14). Both approaches result in the same deformation state of the structure. For a comparison of the computational effort, the number of inter-field operations, which are necessary to reach a state of convergence in the inter-field iteration loop, are considered. This number provides a good estimation of the computational effort, as for every inter-field iteration step, the solution of one structural simulation and one fluid simulation needs to be performed. For the transient analysis, a total of 192 inter-field iteration steps were necessary. In contrast, the steady-state approach required only 66 inter-field iterations. Thus, for this application, the computational effort can be reduced by a factor of about 3, if the presented iteratively staggered steady-state approach is applied.

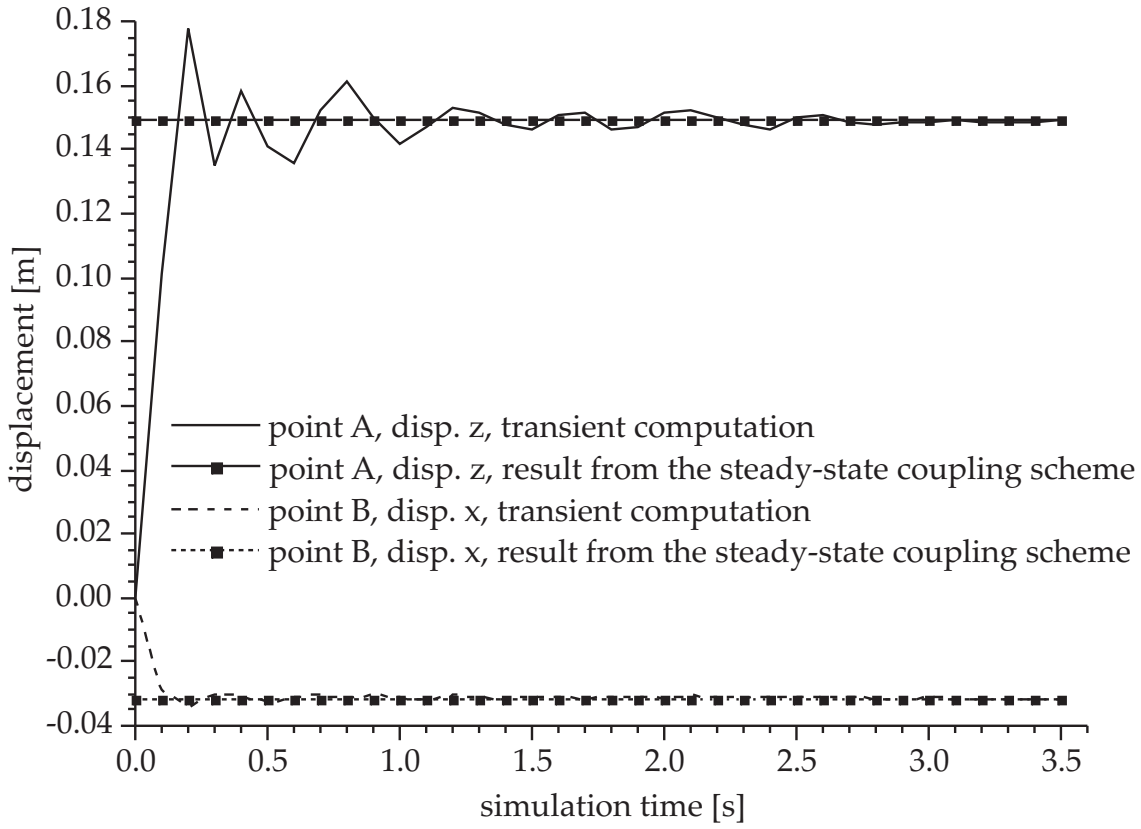

Figure 4.13: Comparison of results from transient and steady-state coupling schemes.

Results of the steady-state computation

In the following, the coupled simulations are performed using the iteratively staggered, steady-state approach. Wind from the front and the back side of the structure are modeled.

The definition of the wind directions is identical to those used throughout section 3.5 and indicated in fig. 4.14. Both directions were analyzed for wind speeds of 15 m/s and 25 m/s.

The results are visualized for a reference wind speed of 25 m/s by showing the absolute deformation of the ARIES structure in fig. 4.15 for wind from the back side and in fig. 4.17 for wind from the front side.

For a more quantitative analysis, the displacements at two points on the ARIES structure shall be considered. Point A is located at the top part of the membrane, behind the cone shape, in the membrane's symmetry axis. Point B is located at the back of the membrane. Both locations are presented in fig. 4.14.

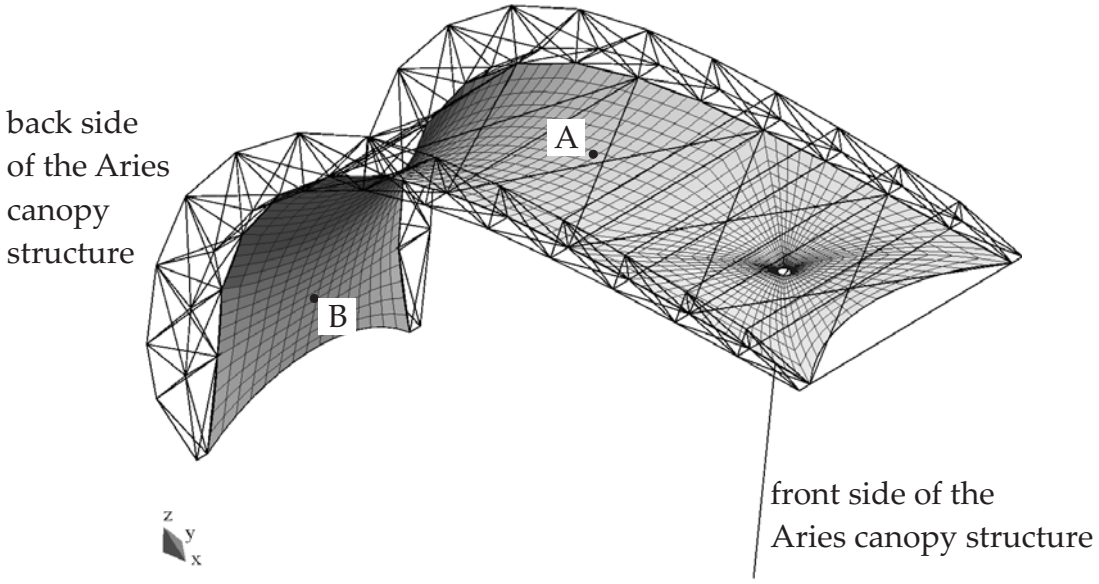

Figure 4.14: Location of points A and B on the ARIES membrane.

In fig. 4.16 and fig. 4.18, the vertical displacements of node A and the horizontal displacements of node B are plotted over the number of inter-field iterations.

Again, the number of necessary inter-field iterations can be used to evaluate the coupled computations. Comparing fig. 4.16 and fig. 4.18, it can be observed, that the situation for wind from the front side is the more difficult to simulate in coupled simulation, as more inter-field iteration steps are needed to reach convergence for both reference wind speeds considered.

Steady-state effects for wind from the back side

For wind from the back side, the reaction of the membrane structure is observed as being uncritical for a constant wind speed up to 25 m/s. The membrane in the back of the structure, close to the mounting points of the cantilever beams at the ground, is pushed inwards to some degree, which increases its curvature. The only critical effect which could arise, is a possible contact of membrane and tribune. However, since the stiffness of the membrane increases as it is pushed inwards, this effect is not expected.

At the top part of the ARIES construction, behind the cone shape, the suction caused by the flow separation of the wind flow moves the membrane upwards. This could lead to a possible contact between the membrane and the strut cables, which are crossed in between the two lattice beams. However, the vertical displacements are sufficiently small, so that this effect is unlikely to occur for moderately high wind speeds. Nevertheless, by the upward deformation, the prestress in the membrane is reduced, which makes the membrane more susceptible to oscillations.

Steady-state effects for wind from the front side

For wind from the front side, the membrane shows deformations according to a general uplifting effect. In the front, at the cone-shape part of the membrane, the membrane's inner stresses and the tension in the tie-down cable are increased. Same as for wind from the back side, the membrane at the top of the canopy structure moves upwards. Compared to the setup with wind from back side, the upwards deformations are larger. In the back part of the structure, the membrane is deformed outwards by the pressure acting on its inside. This results in a backwards movement of the membrane towards the strut cables between the lattice beams.

Compared to the setup with wind from the back side, the observed deformations are generally larger. Both deformations at the back and the top of the membrane show critical tendencies towards possible contact between the membrane and the strut cables spanning between the lattice beams. Furthermore, the prestress of the membrane is greatly reduced in these parts, which makes the membrane susceptible to further deformations and oscillations. Concluding, the setup with wind from the front side is the decisive case of these two setups.

Above a certain wind speed, a snap-through tendency of the membrane can be expected at the top and the back side of the construction. In case of a snap-through, the membrane will change its curvature from inwards to outwards the construction. Thereby, the membrane will hit the strut cables, which has to be absolutely avoided. Possible consequences would be a damage in the membrane and a great change to the load carrying behavior of the construction. Additionally, a dynamic contact of the membrane and the strut cables can lead to noise and vibrations in the whole structure.

4.6.3 Transient Computation

In the results from the steady-state coupled analysis, the wind flow situation with wind from the front side was identified as critical. In the following, this setup is used in a transient simulation with the aim to obtain a first assessment of the dynamic wind-membrane structure interaction.

For the transient fluid simulation, an URANS turbulence model is used, which is based on the k-ω SST turbulence model described in section 3.2.3.1. Therefore, the requirements towards spatial and time-wise resolution of the wind fluctuations, which are necessary to accurately describe the neutrally stratified ABL flow in a dynamic simulation, are not fulfilled. Thus, this simulation is not applicable for the computation of design wind loads,

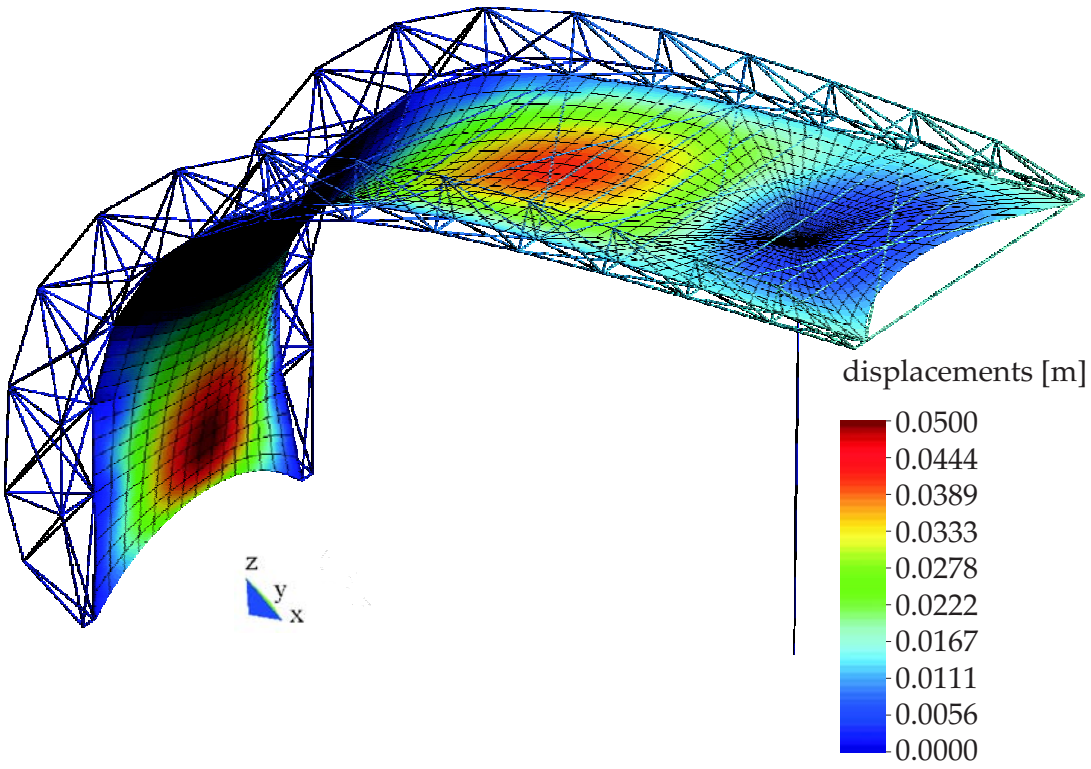

Figure 4.15: Deformation of the ARIES structure, wind from the back side, $u_{ref} = 25$ m / s.

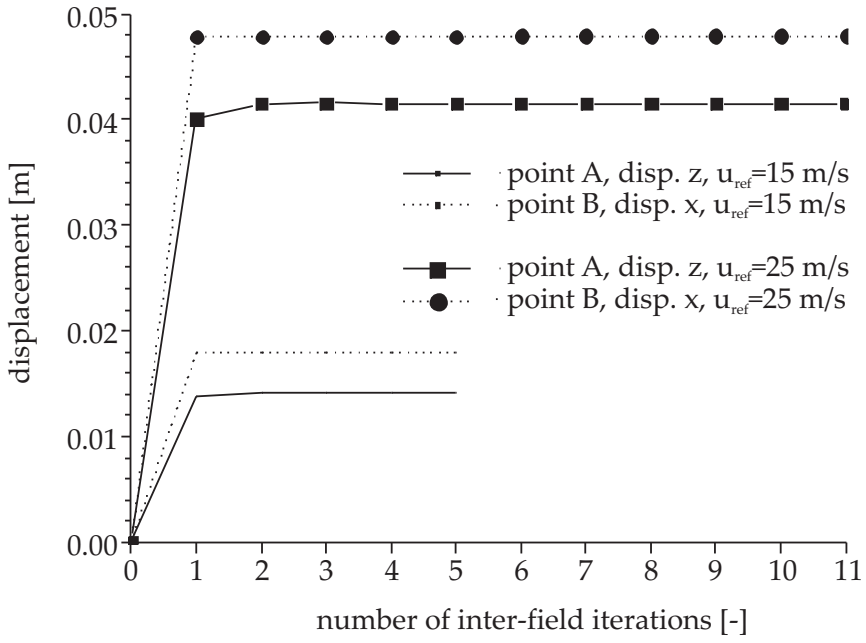

Figure 4.16: Plot of deformations of points A and B, wind from the back side.

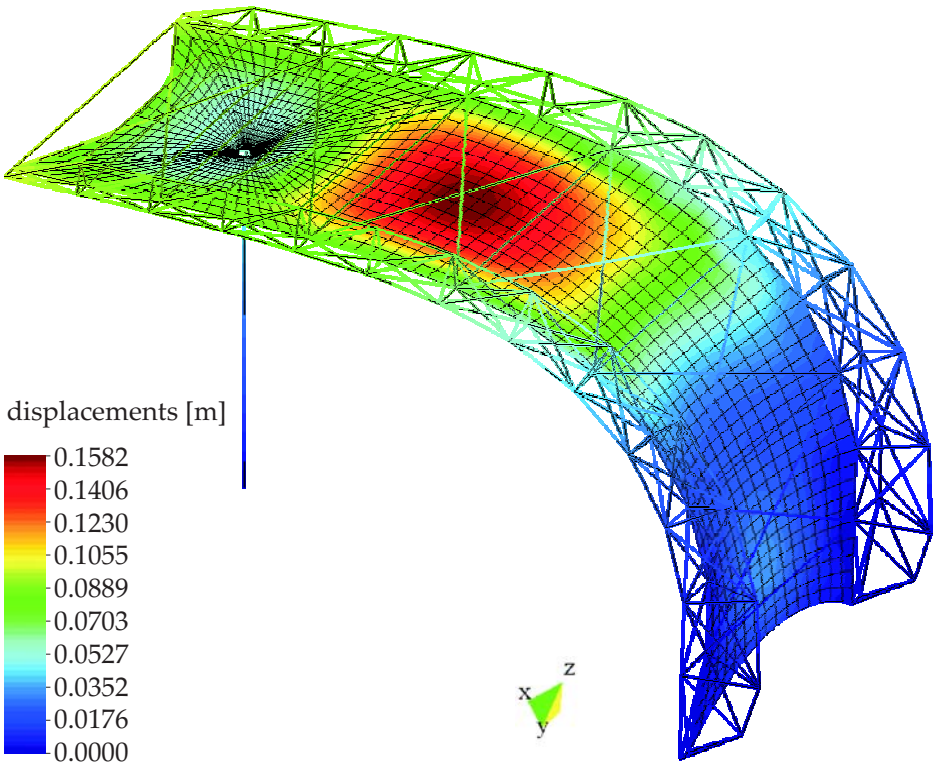

Figure 4.17: Deformation of the ARIES structure, wind from the front side, $u_{ref} = 25$ m / s.

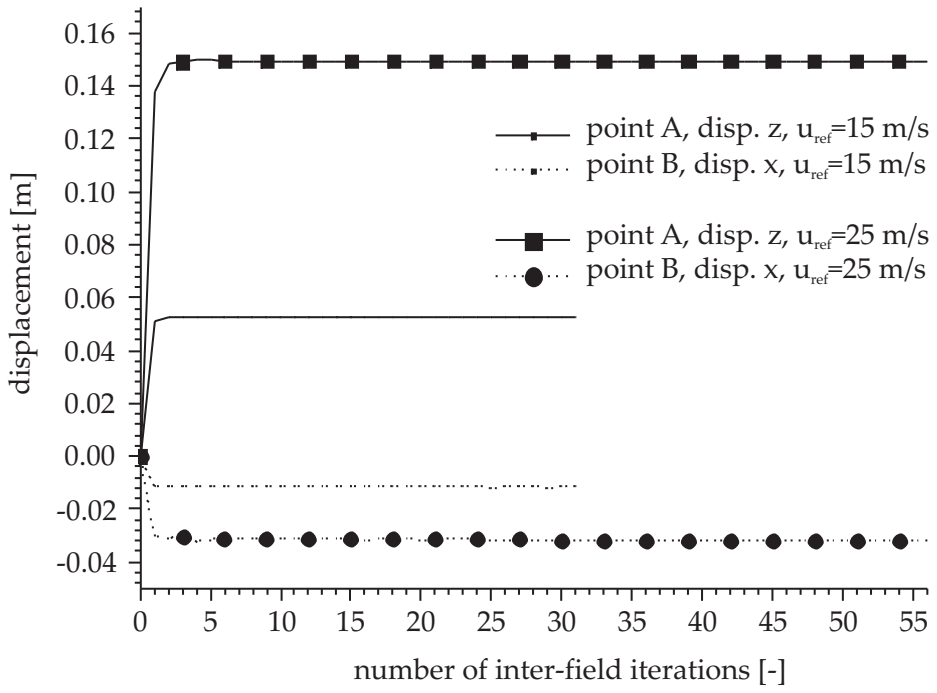

Figure 4.18: Plot of deformations of points A and B, wind from the front side.

as discussed in section 3.4.2. However, in the context of this work it is used to give a first assessment of the dynamic wind effects on the ARIES structure.

As time integration schemes, the generalized-α scheme was used in the structural domain and a second order Euler Backwards scheme in the fluid domain. The time-step was chosen to be 0.1 s and the total simulated time interval was 7.0 s. All effects of inertia were respected in the structural and fluid simulation. The results of the steady-state coupled analysis presented above have been used as initial conditions, for the structural and the fluid solution.

The simulation was carried out by using the general, iteratively staggered coupling scheme presented in algorithm 3 in section 4.3.3.1 with its specific implementation in Ansys CFX according to fig. 4.10. Adaptive under-relaxation was applied on the interface loads to stabilize the simulation and increase the overall efficiency.

In order to imitate a gust-like effect, the reference wind speed is varied between 15 m/s and 35 m/s. Fig. 4.19 shows the variation of the reference wind speed over the simulation time. The wind speed distribution and the distribution of the turbulent quantities are related to the reference wind speed through eq. 3.118 - eq. 3.120.

Results

The deformations of points A and B, as specified in fig. 4.14, are plotted in fig. 4.19 for the simulated time interval. Comparing the variation of the wind speed and the deformation of the structure in fig. 4.19, it can be observed, that the structural deformation follows the variation of the wind speed without significant delay. This can be explained by the membrane's pre-stress, its small mass, and the small mass of the lattice cantilever beams, which result in little inertia effects for the whole construction.

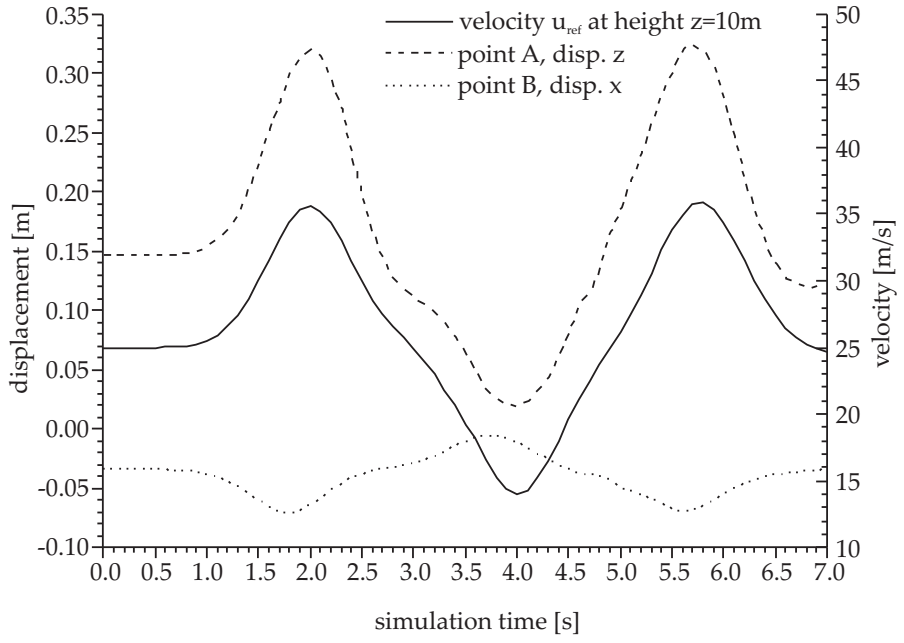

Figure 4.19: Plot of u_{ref} and deformations of points A and B, wind from the front side.

Fig. 4.20 presents a series of pictures, which depict the structural deformation at specified points in time during the coupled simulation. The left side of the figure shows the absolute displacement of the structure. On the right side of the figure, a side view of only the membrane is given. For comparison, the membrane edge at the beginning of the transient computation, so for a reference velocity of 25 m / s, is shown as a thin black line on the right side.

The danger of a snap-trough behavior of the membrane at the top and in the back part of the structure and, thereby, its contact with the strut cables, was already discussed in the scope of steady-state analysis. The transient analysis shows this effect at time $t = 1.9$ s and $t = 5.5$ s, which can be observed in fig. 4.20. [1] Resulting from this computation, a recommendation to the designers can be given that care has to be taken to avoid contact between the membrane and the cables by either constructive means or by increasing the membrane prestress.

Concluding, the transient, URANS-based results of fluid-structure interaction provides a first assessment of the structure's behavior under wind loading, both with respect to the magnitude of the deformation and the involved frequencies of the structural response.

4.7 Summary

Within this chapter, the classification of wind-membrane interaction as a surface coupled, multi-physics problem was discussed. For the solution of multi-physics problems, different approaches were presented. A partitioned approach was chosen to solve the coupled problem, since it provides the potential to include all necessary features for the simulation of wind-structure interaction and the possibility to reuse existing solvers.

The basic requirements for coupled partitioned simulations with respect to conservation of mass, momentum, and energy were formulated. Simple and iteratively staggered coupling schemes have been introduced. Selected aspects for the coupled simulation in partitioned approaches have been discussed and an overview of the appropriate methods was provided.

For the implementation of the simulation of wind-membrane interaction, a flexible software environment was suggested. The necessary modifications to include the single-field solvers CARAT and Ansys CFX into this environment were presented. Special effort was made to implement these modifications into the commercial blackbox fluid solver Ansys CFX. The concept, the features, and the implementation of the central coupling tool CoMA were presented.

Finally, the software environment was used to combine the numerical models, which have been derived in the two previous chapters, into a coupled computation.

[1] Since in the structural solution no contact algorithm was used to detect the contact between the membranes and the cable, the membrane would penetrate the cables without resistance in this simulation.

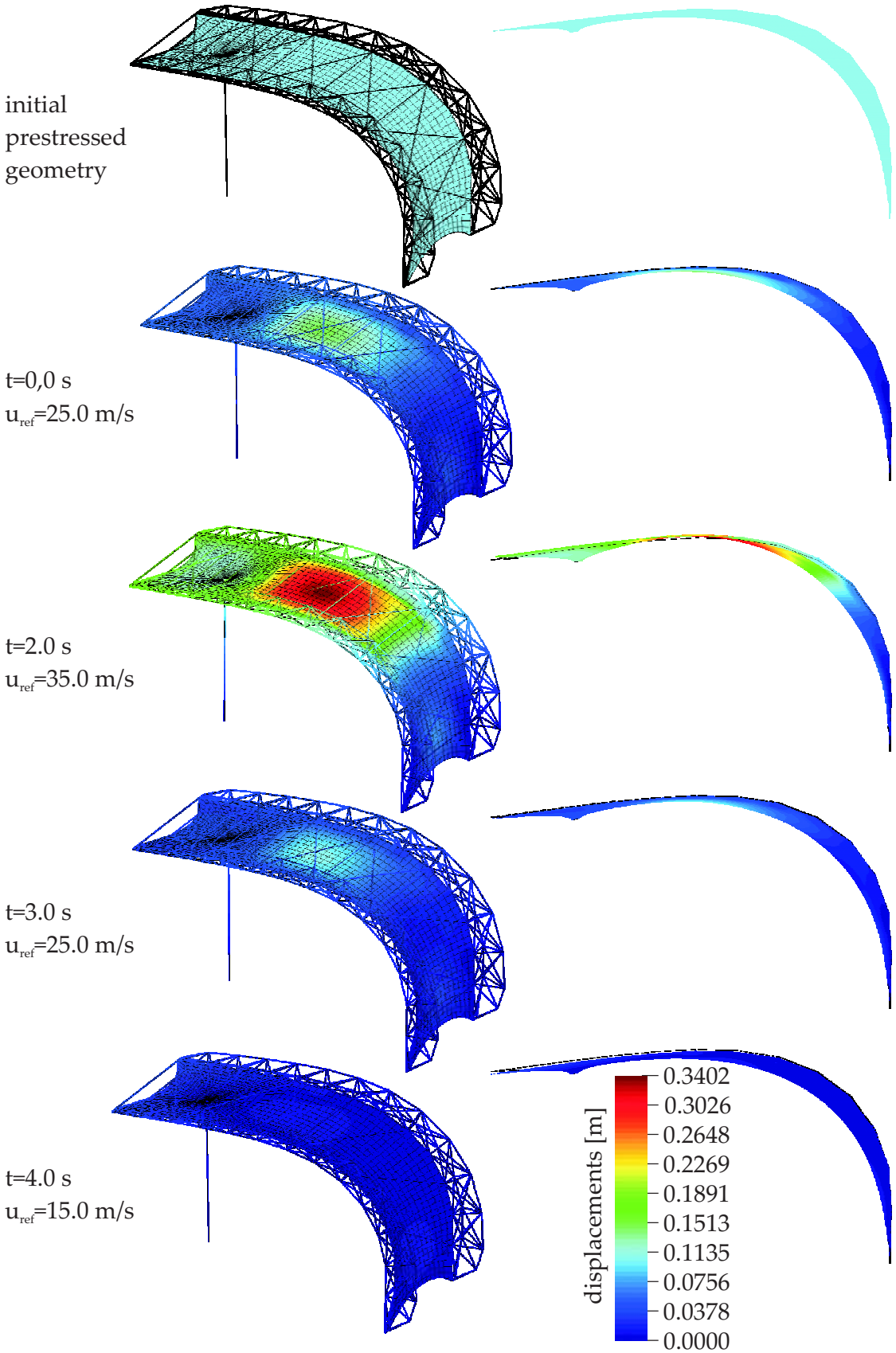

Figure 4.20: Deformations of the ARIES structure at specific points in time.

Chapter 5

Summary and Conclusion

5.1 Summary

In this thesis, a framework for the numerical analysis of the interaction between wind and membrane structures was developed. The need for an appropriate method to analyze these light-weight, flexible structures was motivated by the complex characteristics of the structural behavior of membranes, which can lead to dynamic, wind induced effects. Moreover, in case of large structural deformations, an interaction between membrane structures and wind flow has to be considered. This membrane structure-wind interaction results in an aeroelastic problem, which closes itself to accurate modeling in small-scale wind tunnel experiments.

Considerations about the complexity and characteristics of the relevant physics inherent to the complex aeroelastic coupled problem were presented. In the structural simulation of membrane constructions, a focus has to lie on modeling the geometrically non-linear behavior. Additionally, form finding methods have to be applied to derive the initial equilibrium shape of the membrane. In the numerical simulation of wind flow, or more specifically, of neutrally stratified Atmospheric Boundary Layer (ABL) flow, the emphasis has to be put on an appropriate combination of turbulence modeling and boundary conditions to derive a CFD model, which is able to represent and maintain the essential flow characteristics.

In order to account for all relevant physics in the numerical simulation of wind-membrane interaction, a partitioned simulation approach was chosen. By applying a partitioned approach, the multi-physics problem can be separated into the involved physical fields. In case of wind-membrane structure interaction, these are the structural simulation of the membrane construction and the fluid simulation, which describes the air flow around the construction.

The physical fields of structural and fluid mechanics have been discussed in detail. Based on the fundamentals of each field, appropriate methods for the numerical simulation of the single fields have been introduced. For the structural simulation, including the form finding computations, the Finite Element Method was used and the in-house research code CARAT was applied. The fluid simulations were conducted using the Finite Volume Method and Ansys CFX 11 was used as simulation program. Special considerations about numerical modeling strategies for neutrally stratified ABL flows were discussed.

In order to represent the strong physical coupling between structure and fluid, requirements of and methods for partitioned coupled simulations have been introduced. For the coupled solution of wind-membrane structure interaction, an iteratively staggered coupling approach was chosen. Dynamic under-relaxation by the Aitken's method has been used to increase robustness and efficiency of the coupled computation. Selected aspects for the numerical simulation of fluid-structure interaction problems were presented in detail.

The coupling methods were implemented in a flexible software environment, which is open to a large variety of multi-physics simulations. As an essential part of the simulation environment, the central coupling tool CoMA was developed, and its concept, advantages, and features were presented. Within the coupled computation, communication and data exchange on non-matching interface discretization are handled by CoMA. Thereby, the necessary modifications in the single field solvers can be reduced. The remaining important changes in the single field solvers for an application in coupled analysis, both with respect to exchange of boundary conditions and to the solution schemes, were presented. For the use of Ansys CFX 11 in fsi simulations as a black box fluid solver, functional as well as efficient modification schemes were presented.

The computational environment was applied to simulate the wind-membrane interaction for the mobile canopy structure ARIES. Firstly, a consistent structural model was derived. The geometry of this structural model was used to setup a numerical model for the simulation of neutrally stratified ABL wind flow. Results for the numerical fluid simulation of the rigid structure were compared with those from wind tunnel experiments. Finally, by using the software environment developed and implemented within this thesis, the interaction between the structural model of ARIES and the CFD model was established. This enabled the assessment of the basic interaction effects between wind and the ARIES membrane structure for wind directions from two sides. Steady-state and transient effects of wind-membrane structure interaction have been analyzed and presented.

5.2 Relevance of the Presented Methods for Wind Engineering

This thesis strongly focuses on methodological and modeling aspects. With the developed software environment in use, the question arises, how and to what extent, the methods presented here can be applied in the field of wind engineering.

Consideration about the role of CFD in wind engineering

According to Simiu and Scanlan [SS96], the designer needs the following information to design a structure for wind loading:

1. Information about the wind environment.
2. Information about the relation between that environment and the forces it induces on the structure.
3. Information about the behavior of the structure due to these forces.

The software environment developed within this work covers point 2, however, within the limitations that CFD simulations face in modeling the wind flow. The strength of the tool lies in the coverage of point 3, since the interaction between structure and air flow can be modeled explicitly and, moreover, the effect of the structure's behavior on the air flow can be taken into account. However, due to the deterministic nature of the numerical methods used, the prime application of the software environment is the analysis of wind flow around structures for specific setups.

The open question remains, how to step beyond the mere analysis of wind induced effects into using these methods for the computation of design loads for light-weight and flexible structures.

This discussion can be based on fig. 5.1, which has already been used in section 3.4.2 to determine the target values of the CFD analysis of the ARIES structure.

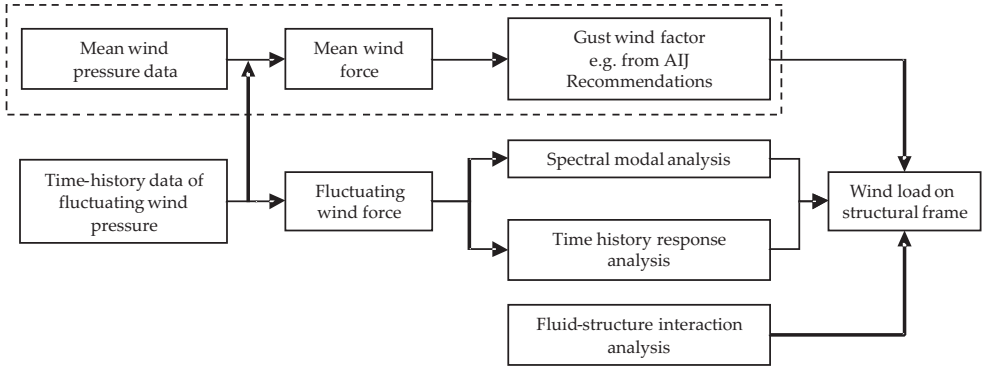

Figure 5.1: Procedure for estimating wind loads on structural frames using CFD. [TNK08]

In fig. 5.1, for the computation of loading on the structural frame, two main approaches can be distinguished:

- In an approach using averaged turbulence quantities, the mean wind loads can be computed. This is done within this work in section 3.5. Here, the mean wind load on the membrane structure was derived by the surface pressure using RANS methods. Based on the surface pressure, a distribution of c_p values over the membrane surface was computed. However, in order to use c_p values to compute design wind loads, the c_p values have to be derived in a way which is sufficient in the context of a building code, such as EN 1991-1-4:2005 [CEN05] or DIN 1055-4:2005-3 [Nor05a]. This can be achieved by using higher time and space resolution together with appropriate modeling to derive statistically representative answers, similar to those suggested in the next bullet point.

  Then, the results from the fsi computation can be included in the framework of c_p-based wind load assessment by computing c_p values, which depend on the maximum wind speed. For an appropriate analysis of possible wind speeds, the worst case c_p value can be computed for each point of the structure. Thereby, effects due to the quasi-static deformation of the structure are included in the design wind loads.

- ◇ For the analysis of wind flow, which includes the correct description of the ABL flow turbulence, transient CFD methods have to be used. This is possible with advanced LES or VLES methods, which can simulate the necessary time scale inherent to turbulent wind flow. With this approach, the use of numerical methods can be regarded as imitating wind tunnel testing, thus creating a "numerical wind tunnel". However, same as in wind tunnel experiments, special effort has to be made in order to correctly include the relevant scales of turbulence fluctuation into the "numerical wind tunnel". Furthermore, in order to compute a statistically representative answer, same as for wind tunnel experiments, certain time intervals have to be analyzed. Considering the small time-step size needed to resolve the necessary time scales, very high computational effort is necessary to cover these considerably long time intervals.

Common to both approaches is the need to analyze wind loads for winds approaching from different directions. Depending on symmetry properties of the building, several simulations for different wind directions are necessary.

Further consideration about numerical fsi simulation in wind engineering

In case of aeroelastic effects, the assumption that wind loads are related to the square of the wind speed by a constant factor is not valid anymore. Here, depending on the magnitude of the wind speed, the structure changes its shape, and therefore, the load distribution on its surface changes. For deriving design loads based on computations of fluid-structure interaction, these dependencies require that not only different wind directions, but also different wind speeds have to be analyzed. Depending on the problem, this leads to an increase by a magnitude in the number of necessary computations.

Methods of fluid-structure interaction have been presented in fig. 5.1 as suitable to compute the loading of the structural frame. However, no information is given about the procedure of deriving design-loads based on fsi computations. Based on the considerations above, deriving design loads based on fsi computation leads to an extremely high computational effort. This effort results from the requirement to analyze multiple combinations of possible wind speeds and wind directions, each computed for a sufficiently long time interval.

A possible remedy to avoid an extensive number of computations with varying combinations of parameters is to define one or more worst case combinations of parameters and analyze those. This is a more general approach to the suggestion of deriving wind speed dependent c_p values and combining those to derive the worst case c_p value for each point of the surface.

However, if the choice of worst case situations with respect to wind loading should include transient effects, a deep understanding of all possible critical wind induced effects is required. Such knowledge about possible effects can be taken from literature or experience. Only by knowing about possible effects, the approximations and simplifications in the CFD simulation can be adjusted accordingly, so that these effects are included in the model. A simple example is an appropriate choice of the time-step size for the analysis of higher frequency oscillations: if the time-step is not small enough to resolve these oscillations, no higher frequency oscillating behavior is present in the numerical simulation.

Therefore, the author concludes that the deterministic nature of numerical simulations requires either a large number of computations or detailed knowledge about the decisive wind induced effects in order to derive design loads with fsi based numerical methods. Currently, fsi based methods are regarded as an excellent tool for the analysis of expected wind induced effects, e.g. the fluttering of a bridge cross section. For the design of complex structures, for which not all dynamic wind induced effects are understood or analyzed, e.g. for large scale umbrellas, fsi based methods should only be applied with utmost consideration. Otherwise, critical wind induced effects are possibly not revealed in a numerical simulation due to the simplifications and approximations of the numerical model and/or the missing combinations of simulation parameters.

5.3 Conclusion and Outlook

The presented software environment is a valuable tool for a wind engineer, who has the experience to decide, which problems of wind-structure interaction are crucial for the design of a certain construction. Within the limits of the applied CFD model, the occurrence and the magnitude of wind induced effects can be analyzed, fully taking into account the interaction. Therefore, the method presented is a promising complement to and enhancement of existing methods of analytical, semi-analytical, or experimental approaches in wind engineering.

For further application to wind-structure interaction, improved turbulence modeling by LES and DES methods is available within Ansys CFX. The flexibility of the software environment allows to include alternative single-field solvers, which already has been done for the open-source CFD solver OpenFOAM.

Beyond the simulation of wind-membrane structure interaction, the flexibility of the partitioned coupling approach makes the developed software environment applicable for the numerical simulation of various, surface coupled multi-field problems. Applications can be found in biomechanics, e.g the simulation of blood in flexible veins, or in automotive and aeronautic industries, e.g. the analysis of the flexible roof of convertibles or wind flutter on aircrafts. For alternative applications and continuing enhancement of the software environment, the central coupling tool CoMA will be developed further at the Chair of Structural Analysis at the Technische Universität München.

Bibliography

[AAB74] J H. Argyris, T. Angelopoulos, and B. Bichat. A general method for shape finding of lightweight tension structures. *Computer Methods in Applied Mechanics and Engineering*, 3:135–139, 1974.

[AM88] J. Argyris and H.-P. Mlejnek. *Die Methode der Finiten Elemente - Band II: Kraft- und gemischte Methoden, Nichtlinearitäten*. Vieweg & Sohn, Braunschweig, 1988.

[And08] J.D. Anderson. *Introduction to Computational Fluid Dynamics*, chapter Introduction to Computational Fluid Dynamics, pages 1–267. von Karman Institute for Fluid Dynamics, 2008.

[Aps06] D. Apsley. Computational hydrolics. Technical report, University of Manchester, 2006.

[Arc04] Architectural Institute of Japan (AIJ). Recommondations for loads on buildings. Technical report, Architectural Institute of Japan, 2004.

[Arc05] Architectural Institute of Japan (AIJ). Guide for numerical prediction of wind loading on buildings. Technical report, Architectural Institute of Japan, 2005.

[Baa01] F.P.T. Baaijens. A fictitious domain / mortar element method for fluid-structure interaction. *International Journal of Numerical Methods in Fluids*, 35:743–761, 2001.

[Bag01] P.S. Baglin. Wind load assessment. Technical report, Arena Seating, 2001.

[Bar75] M.R. Barnes. Application of Dynamic Relaxation to the design and analysis of cable, membrane and pneumatic structures. In *Proceedings of the 2nd International Conference on Space Structures*, 1975.

[Bar99] M.R. Barnes. Form Finding and Analysis of Tension Structures by Dynamic Relaxation. *International Journal of Space Structures*, 14(2):89–104, 1999.

[Bat02] K.-J. Bathe. *Finite-Elemente-Methoden*. Springer-Verlag, Berlin, 2. edition, 2002.

[BB99] T. Belytschko and T. Black. Elastic crack growth in finite elements with minimal remeshing. *International Journal for Numerical Methods in Engineering*, 45(5):601–620, 1999.

[BBF07] P. Biagini, C. Borri, and L. Facchini. Wind response of large roofs of stadions and arena. *Journal of Wind Engineering and Industrial Aerodynamics*, 95:871–887, 2007.

[BBM+06] P. Biagini, C. Borri, M. Majowiecki, M. Orlando, and L. Procino. BLWT tests and design loads on the roof of the new olympic stadium in Piraeus. *Journal of Wind Engineering and Industrial Aerodynamics*, 94:293–307, 2006.

[BCS07] B. Blocken, J. Carmeliet, and T. Stathopoulos. CFD evaluation of wind speed conditions in passages between parallel buildings - effects of wall-function roughness modification of the atmospheric boundary layer flow. *Journal of Wind Engineering and Industrial Aerodynamics*, 95:941 – 962, 2007.

[BCZH06] Y. Bazilevs, V.M Calo, Y Zhang, and T.J.R Hughes. Isogeometric fluid-structure analysis with applications to arterial blood flow. *Computational Mechanics*, 38(4-5):310–322, 2006.

[BD04] M. Balz and M. Dencher. *European Design Guide for Tensile Surface Structures*, chapter Design Loading Conditions, pages 191 – 204. TensiNet, 2004.

[BDS05] C.L. Bottassoa, D. Detomib, and R. Serrab. The ball-vertex method: a new simple spring analogy method for unstructured dynamic meshes. *Computer Methods in Applied Mechanics and Engineering*, 194(39-41):4244–4264, 2005.

[Bel83] T. Belytschko. An overview of semidiscretization and time integration procedures. In T. Belytschko and T.J.R. Hughes, editors, *Computational Methods for Transient Analysis*, pages 1–64. North-Holland, Amsterdam, 1983.

[BG05] N. Burford and C. Gengnagel. *A Very Rapid Deployable Canopy System*, pages 158 – 171. Taylor & Francis, 2005.

[BHC97] J.E. Bardina, P.G. Huang, and T.J. Coakley. Turbulence modeling validation. Technical report, AIAA-1997-2121, 1997.

[Bis99] M. Bischoff. *Theorie und Numerik einer dreidimensionalen Schalenformulierung*. PhD thesis, Universität Stuttgart, Stuttgart, 1999.

[Bis03] M. Bischoff. Advanced Finite Element Methods. Technical report, Technische Universität München, 2003.

[BJM03] M. Breuer, N. Jovičić, and K. Mazaev. Comparison of DES, RANS and LES for the separated flow around a flat plate at high incidence. *International Journal for Numerical Methods in Fluids*, 41:357 – 388, 2003.

[Ble97] K.-U. Bletzinger. Form finding of tensile structures by the updated reference strategy. In Chilton J W et al., editor, *Proceedings of the IASS International Colloquium Structural Morphology - Towards the New Millenium*. University of Nottingham, UK, 1997.

[Ble98] K.-U. Bletzinger. Form finding and optimization of membranes and minimal surfaces. Technical report, Universität Karlsruhe, Institut für Baustatik, 1998.

[BLM00] T. Belytschko, W.K. Liu, and B. Moran. *Nonlinear finite elements for continua and structures*. John Wiley & Sons Ltd., Chichester, 2000.

[Blo00] F.J. Blom. Considerations on the spring analogy. *International Journal for Numerical Methods in Fluids*, 32(6):647 – 668, 2000.

[BMP94] C. Bernardi, Y. Maday, and A.T. Patera. *Nonlinear partial equations and their applications*, chapter A new nonconforming approach to domain decomposition: the mortar element method, pages 13–51. Longman, 1994.

[BR99] K.-U. Bletzinger and E. Ramm. A general finite element approach to the form finding of tensile structures by the updated reference strategy. *International Journal of Space Structures*, 14(2):131–145, 1999.

[Bre02] M. Breuer. *Direkte Numerische Simulation und Large-Eddy Simulation turbulenter Strömungen auf Hochleistungsrechnern, Habilitationsschrift*. Shaker Verlag, Aachen, 2002.

[BSC07] B. Blocken, T. Stathopoulos, and J. Carmeliet. CFD simulation of the atmospheric boundary layer: wall function problems. *Atmospheric Environment*, 41:238–252, 2007.

[BSMM00] I.N. Bronstein, K.A. Semendjajew, G. Musiol, and H. Mühlig. *Taschenbuch der Mathematik*. Verlag Harri Deutsch, 2000.

[BW00] Y. Başar and D. Weichert. *Nonlinear continuum mechanics of solids - Fundamental mathematical and physical concepts*. Springer-Verlag, Berlin, 2000.

[BW01] A. Beckert and H. Wendland. Multivariant interpolation for fluid-structure-interaction problems using radial basis functions. *Aerospace Science and Technology*, 5 (2):125–134, 2001.

[BWK06] K.-U. Bletzinger, R. Wüchner, and A. Kupzok. *Fluid-Structure Interaction - Modelling, Simulation, Optimisation; Lecture Notes in Computational Science and Engineering vol. 53*, chapter Algorithmic treatment of shells and free form-membranes in FSI, pages 336–355. Springer, 2006.

[CEN05] CEN - Comité Européen de Normalisation. EN 1991-1-4:2005 Eurocode 1: basis of design and actions on structures-Part 1-4: actions on structures-wind actions. Technical report, 2005.

[CFX06] CFX-11 Manual. Technical report, Ansys, Inc., 2006.

[CGN05] P. Causin, J.F. Gerbeau, and F. Nobile. Added-mass effect in the design of partitioned algorithms for fluid-structure problems. *Computer Methods in Applied Mechanics and Engineering*, 194:4506–4527, 2005.

[CH93] J. Chung and G.M. Hulbert. A time integration algorithm for structural dynamics with improved numerical dissipation: the generalized-α method. *Journal of Applied Mechanics*, 60:371–375, 1993.

[CL97] J.R. Cebral and R. Löhner. Conservative load projection and tracking for fluid-structure interaction. *AIAA Journal*, 35 (4):687–692, 1997.

[CL05] J.R. Cebral and R. Löhner. On the loose coupling of implicit time-marching codes. Technical report, 2005.

[CLS96] T.J. Craft, B. E. Launder, and K. Suga. Developement and application of a cubic eddy-viscosity model of turbulence. *International Journal of Heat and Fluid flow*, 17:108–115, 1996.

[CLYS03] Y. Cheng, F.S. Lien, E. Yee, and R. Sinclair. A comparison of large Eddy simulations with a standard k-e Reynolds-averaged Navier-Stokes model for the prediction of a fully developed turbulent flow over a matrix of cubes. *Journal of Wind Engineering and Industrial Aerodynamics*, 91:1301–1328, 2003.

[Coo85] N.J. Cook. *The designer's guide to wind loading of building structures, part 1*. Building Research Establishment and Butterworths, 1985.

[Coo90] N.J. Cook. *The designer's guide to wind loading of building structures, part 2*. Building Research Establishment and Butterworths, 1990.

[Cri91] M.A. Crisfield. *Non-linear finite element analysis of solids and structures - Vol. 1, Essentials*. Wiley, Chichester, 1991.

[Cri97] M.A. Crisfield. *Non-linear finite element analysis of solids and structures - Vol. 2, Advanced Topics*. Wiley, Chichester, 1997.

[DB04] M. Dencher and M. Balz. *European Design Guide for Tensile Surface Structures*, chapter c_p values for simple tension structures, pages 259 – 270. TensiNet, 2004.

[dBvdSB07] A. de Boer, M.S. van der Schoot, and H. Bijl. Mesh deformation based on radial basis function interpolation. *Computers and Structures*, 85(11-14):784–795, 2007.

[dBvZB07] A. de Boer, A.H. van Zuijlen, and H. Bijl. Review of coupling methods for non-matching meshes. *Computational Methods in Applied Mechanical Engineering*, 196:1515–1525, 2007.

[Dep04] Simone Deparis. *Numerical analysis of axisymmetric flows and methods for fluid-structure interaction arising in blood flow simulation*. PhD thesis, École Polytechnique Fédérale de Lausanne, 2004.

[DF02] C. Degand and C. Farhat. A three-dimensional torsional spring analogy method for unstructured dynamic meshes. *Computers & Structures*, 80:305–316, 2002.

[DHPRF04] J. Donea, A. Huerta, J.-Ph. Ponthot, and A. Rodríguez-Ferran. *Encyclopedia of Computational Mechanics, Volume 2: Solids and Structures*, chapter Arbitrary Lagrangian-Eulerian methods, pages 413–438. Wiley, Chichester, 2004.

[DP88] I. Demirdzic and M. Perić. Space conservation law in finite volume calculations of fluid flow. *International Journal for Numerical Methods in Fluids*, 8:1037–1050, 1988.

[Dur96] P.A. Durbin. On the k-ϵ stagnation point anomaly. *International Journal of Heat and Fluid Flow*, 17:89–90, 1996.

[Eas00] G. Easom. *Improved Turbulence Models for Computational Wind Engineering*. PhD thesis, University of Nottingham, 2000.

[EKM00] J. Ehrhard, R. Kunz, and N. Moussiopoulos. On the performance and applicability of nonlinear two-equation turbulence model for urban air quality modeling. *Environmental Monitoring and Asessment*, 65:201 – 209, 2000.

[ERC02] ERCOFTAC. Best practice guidelines (bpg) for industrial computational fluid dynamics. Technical report, European Research Community on Flow, Turbulence And Combustion, 2002.

[fAC03] Fraunhofer Institute for Algorithms and Scientific Computing. MpCCI specification, version 2.0. Technical report, 2003.

[Far04] C. Farhat. *Encyclopedia of Computational Mechanics, Volume 3: Fluids*, chapter CFD based Nonlinear Computational Aeroelasticity, pages 459–480. Wiley, Chichester, 2004.

[FGG07] M.A. Fernández, J.-F. Gerbeau, and C. Grandmont. A projection semi-implicit scheme for the coupling of an elastic structure with an incompressible fluid. *International Journal for Numerical Methods in Engineering*, 69(4):794–821, 2007.

[FHJ+04] J. Franke, C. Hirsch, A.G. Jensen, H.W. Krüs, M. Schatzmann, P.S. Westbury, S.D. Miles, J.A. Wisse, and N.G. Wright. Recommendations on the use of CFD in predicting pedestrian wind environment. Technical report, COST Action C14 - "Impact of Wind and Storms on City Life and Built Environment"- Working group 2 - CFD techniques, 2004.

[FHSC07] J. Franke, A. Hellsten, H. Schlünzen, and B. Carissimo. Best practise guideline for the CFD simulation of flows in the urban environment. Technical report, COST Action C732 - "Quality Assurance and Improvement of Microscale Meteoroligical Models", 2007.

[FKB+08] M. Fathali, M. Klein, T. Broeckhoven, C. Lacor, and M. Baelmans. Generation of turbulent inflow and initial conditions based on multi-correlated random fields. *International Journal for Numerical Methods in Fluids*, 57 (1):93 – 117, 2008.

[FL00] C. Farhat and M. Lesoinne. Two efficient staggered algorithms for the serial and parallel solution of three-dimensional nonlinear transient aeroelastic problems. *Computer Methods in Applied Mechanics and Engineering*, 182(3-4):499–515, 2000.

[FLL98] C. Farhat, M. Lesoinne, and P. LeTallec. Load and motion transfer algorithms for fluid / structure interaction problems with non-matching discrete interfaces: Momentum and energy conservation, optimal discretization and application to aeroelasticity. *Computer Methods in Applied Mechanics and Engineering*, 157:95–114, 1998.

[FLM95] C. Farhat, M. Lesoinne, and N. Maman. Mixed explicit / implicit time integration of coupled aeroelastic problems: Three-field formulation, geometric conservation and distributed solution. *International Journal for Numerical Methods in Fluids*, 21:807–835, 1995.

[FM04] B. Forster and M. Mollaert. *European Design Guide for Tensile Surface Structures*. Tensinet, 2004.

[FM05] M.A. Fernandez and M. Moubachir. A Newton method using exact Jacobians for solving fluid-structure coupling. *Computer and Structures*, 83:127–142, 2005.

[FP99] J.H. Ferziger and M. Perić. *Computational methods for fluid dynamics*. Springer-Verlag, Berlin, 2. edition, 1999.

[Fra06] J. Franke. *Wind Effects on Buildings and Design of Wind-Sensitive Structures*, chapter Introduction to the Prediction of Wind Loads on Buildings by Computational Wind Engineering (CWE), pages 67–104. Springer Vienna, 2006.

[Fra07] J. Franke. Richtlinien und Empfehlungen guter fachlicher Praxis für den Einsatz numerischer Strömungsmechanik im Windingenieurwesen. *Bauingenieur*, 4 / 2007:Fachteil WtG, 6–8, 2007.

[FWR07] C. Förster, W.A. Wall, and E. Ramm. Artificial added mass instabilities in sequential staggered coupling of nonlinear structures and incompressible viscous flows. *Computational Methods in Applied Mechanics and Engineering*, 196:1278–1293, 2007.

[Gao05] Chow W.K. Gao, Y. Numerical studies on air flow around a cube. *Journal of Wind Engineering and Industrial Aerodynamics*, 93:115–135, 2005.

[GBD+01] M. Glück, M. Breuer, F. Durst, A. Halfmann, and E. Rank. Computation of fluid-structure interaction on lightweight structures. *Journal of Wind Engineering and Industrial Aerodynamics*, 89:1351–1368, 2001.

[GBD+03] M. Glück, M. Breuer, F. Durst, A. Halfmann, and E. Rank. Computation of wind-induced vibrations of flexible shells and membranous structures. *Journal of Fluids and Structures*, 17:739–765, 2003.

[Gen04] C. Gengnagel. Mobile Tribünenüberdachung. Die Entwickung von A.R.I.E.S. *Umrisse - Zeitschrift für Baukultur*, 3:44 – 51, 2004.

[Gen05] C. Gengnagel. *Mobile Membrankonstruktionen*. PhD thesis, Lehrstuhl für Tragwerksplanung, Fakultät für Architektur, Technische Universität München, 2005.

[GKI+09] T. Gallinger, A. Kupzok, U. Israel, K.-U. Bletzinger, and R. Wüchner. *International Workshop on Fluid-Structure Interaction. Theory, Numerics and Application*, chapter A computational environment for membrane-wind interaction, pages 97–114. Kassel University Press, 2009.

[Glü02] M. Glück. *Ein Beitrag zur numerischen Simulation von Fluid-Struktur-Interaktionen*. PhD thesis, Universität Erlangen - Nürnberg, 2002.

[GMSS00] L. Grundig, E. Moncrieff, P. Singer, and D. Strobel. A history of the principle developments and applications of the Force Density method in Germany 1970 - 1999. In *Proceedings of the IASS-IACM 2000 Fourth International Colloquium on Computation of Shell and Spacial Structures*, 2000.

[Gra03] V. Gravemeier. *The Variational Multiscale Method for Laminar and Turbulent Incompressible Flows*. PhD thesis, University of Stuttgart, Institut für Baustatik, 2003.

[GV03] J.F. Gerbeau and M. Vidrascu. A quasi-Newton algorithm based on a reduced model for fluid-structure interaction problems in blood flows. *ESAIM: Mathematical Modelling and Numerical Analysis*, 37(4):631–647, 2003.

[GW06] A. Gerstenberger and W.A. Wolfgang. *European Conference on Computational Fluid Dynamics ECCOMAS CFD 2006*, chapter An extended finite element method based approach for large deformation fluid-strcture interaction. TU Delft, 2006.

[Hal02] A. Halfmann. *Ein geometrisches Modell zur numerischen Simulation der Fluid-Struktur-Interaktion windbelasteter, leichter Flächentragwerke*. PhD thesis, Technische Universität München, München, 2002.

[Hei04] M. Heil. An efficient solver for the fully coupled solution of large-displacement fluid-structure interaction problems. *Computer Methods in Applied Mechanics and Engineering*, 193:1–23, 2004.

[Hel03] B.T. Helenbrook. Mesh deformation using the biharmonic operator. *International Journal for Numerical Methods in Engineering*, 56:1007–1021, 2003.

[HK07] K. Holschemmacher and Y. Klug. *Lastannahmen nach neuen Normen*. Bauwerk Verlag GmbH, 2007.

[HL97] A. Hellsten and S. Laine. Extension of the k-omega-SST turbulence model for flows over rough surfaces. Technical report, AIAA-1997-3577, 1997.

[Hol00] G. A. Holzapfel. *Nonlinear solid mechanics*. John Wiley & Sons Ltd., Chichester, 2000.

[Hol01] J.D. Holmes. *Wind Loading on Structures*. SponPress, London, U.K., 2001.

[Hol04] J.R. Holton. *An Introduction To Dynamic Meteorology*. Elsevier Academic Press, 4th edition edition, 2004.

[HP72] E. Haug and G. H. Powell. Finite element analysis of nonlinear membrane structures. Technical report, Berkeley, 1972.

[Hüb03] B. Hübner. *Simultane Analyse von Bauwerk-Wind-Wechselwirkungen*. PhD thesis, Technische Universität Carolo-Wilhelmina zu Braunschweig, Braunschweig, 2003.

[Huc02] W.-H. Hucho. *Aerodynamik der stumpfen Körper - Physikalische Grundlagen und Anwendungen in der Praxis*. Vieweg, Braunschweig, 2002.

[Hug00] T. J. R. Hughes. *The finite element method - Linear static and dynamic finite element analysis*. Dover Publications, Inc., Mineola, 2000.

[Hul04] G. M. Hulbert. Computational structural dynamics. In E. Stein, R. de Borst, and T.J.R. Hughes, editors, *Encyclopedia of Computational Mechanics*, pages 169–194. John Wiley & Sons, Ltd., Chichester, 2004.

[HW06] D. M. Hargreaves and N. G. Wright. On the use of the k-ϵ model in commercial CFD software to model the neutral boundary layer. *Journal of Wind Engineering and Industrial Aerodynamics*, 95:355–369, 2006.

[HWD04] B. Hübner, E. Walhorn, and D. Dinkler. A monolithic approach to fluid-structure interaction using space-time finite elements. *Computer Methods in Applied Mechanics and Engineering*, 193(23-26):2087–2104, 2004.

[IKL+07] U. Israel, A. Kupzok, A. Lähr, T. Gallinger, R. Wüchner, and K.-U. Bletzinger. Eine flexible Kopplungsschnittstelle für partitionierte Berechnungen von Mehrfeldproblemen. In *19. Forum Bauinformatik*, 2007.

[IT69] B. Irons and R.C. Tuck. A version of the AItken's accelerator for computer implementation. *International Journal for Numerical Methods in Engineering*, 1:275–277, 1969.

[JH04] X. Jiao and M.T. Heath. Overlay Surface Meshes, Part I: Algorithms. *International Journal of Computational Geometry and Applications*, 14(6):379–402, 2004.

[JJGL05] R.K. Jaiman, X. Jiao, P.H. Geubelle, and E. Loth. Assessment of conservative load transfer for fluid-solid interface with non-matching meshes. *International Journal for Numerical Methods in Engineering*, 64:2014–2038, 2005.

[JT94] A.A. Johnson and T.E. Tezduyar. Mesh update strategies in parallel finite element computations of flow problems with moving boundaries and interfaces. *Computer Methods in Applied Mechanics and Engineering*, 119:73–94, 1994.

[Kai03] U. Kaiser. *Windwirkung auf schwach vorgespannte Membrankonstruktionen am Beispiel eines 30M-Membranschirms*. PhD thesis, Universität Stuttgart, 2003.

[KAT03] J.Y. Kim, N.R. Aluru, and D.A. Tortorelli. Improved multi-level Newton solvers for fully coupled multi-physics problems. *International Journal for Numerical Methods in Engineering*, 58:463–480, 2003.

[Kaz98] M. Kazakevitch. The aerodynamics of a hangar membrane roof. *Journal of Wind Engineering and Industrial Aerodynamics*, 77 & 78:157 – 169, 1998.

[KMM97] K. Kondo, S. Murakami, and A. Mochida. Generation of velocity fluctuations for inflow boundary conditions of LES. *Journal of Wind Engineering and Industrial Aerodynamics*, 67-68:51 – 64, 1997.

[Kna07] G.A. Knapp. *Improved Methods for Structural Wind Engineering*. PhD thesis, University of Nottingham, 2007.

[Kov94] I. Kovacs. Synthetic wind for investigations in time-domain. In *American Society of Civil Engineers - Structures Congress XII 1994*, 1994.

[KW07] U. Küttler and W. A. Wall. Fixed-point fluid-structure interaction solvers with dynamic relaxation. *Computational Mechanics*, 43 (1):61–72, 2007.

[KW09] U. Küttler and W.A. Wall. Vector extrapolation for strong coupling fluid-structure interaction solvers. *Journal of Applied Mechanics*, 76, 2009.

[LAF08] J.B.R. Loureiro, A.T.P. Alho, and A.P.S. Freire. The numerical computation of near-wall turbulent flow over a steep hill. *Journal of Wind Engineering and Industrial Aerodynamics*, 96:540 – 561, 2008.

[Law80] T.V. Lawson. *Wind effects on buildings, Vol. 1 & 2*. Applied Science Publisher, London, 1980.

[LCB06] A. Legay, J. Chessa, and T. Belytschko. An Eulerian-Lagrangian method for fluid-structure interaction based on level sets. *Computer Methods in Applied Mechanics and Engineering*, 195:2070–2087, 2006.

[Lef08] E. Lefrançois. A simple mesh deformation technique for fluid-structure interaction based on a submesh approach. *International Journal for Numerical Methods in Engineering*, 75(9):1085 – 1101, 2008.

[LF96] P. Lesoinne and C. Farhat. Geometric Conservation Laws for Flow Problems with Moving Boundaries and Deformable Meshes, and their Impact on Aeroelastic Computations. *Computer Methods in Applied Mechanics and Engineering*, 134:71–90, 1996.

[Lin99a] K. Linkwitz. About formfinding of double-curved structures. *Engineering Structures*, 21(8):709–718, 1999.

[Lin99b] K. Linkwitz. Formfinding by the 'direct approach' and pertinent strategies for the conceptual design of prestressed and hanging structures. *International Journal of Space Structures*, 14(2):73–87, 1999.

[LM92a] M.L. Levitan and K.C. Mehta. Texas Tech field experiments for wind loads part I: building and pressure measuring system. *Journal of Wind Engineering and Industrial Aerodynamics*, 43:1565–1576, 1992.

[LM92b] M.L. Levitan and K.C. Mehta. Texas Tech field experiments for wind loads part II: meteorological instrumentation and terrain parameters. *Journal of Wind Engineering and Industrial Aerodynamics*, 43:1577–1588, 1992.

[Lóp02] S. López. *Numerische Modellierung turbulenter Umströmungen von Gebäuden*. PhD thesis, Alfred-Wegener-Institut für Polar- und Meeresforschung, 2002.

[LQX06] X Liu, N. Qin, and H. Xia. Fast dynamic grid deformation based on Delaunay graph mapping. *Journal of Computational Physics*, 211:405–423, 2006.

[LRR75] B. E. Launder, G. J. Reece, and W. Rodi. Progress in the development of Reynolds-turbulence closure. *Journal of Fluid Mechanics*, 68(3):537–566, 1975.

[LTM01] P. Le Tallec and J. Mouro. Fluid structure interaction with large structural displacements. *Computer Methods in Applied Mechanics and Engineering*, 190:3039–3067, 2001.

[Lum70] J. Lumley. Towards a turbulent constitutive relation. *Journal of Fluid Mechanics*, 41:413, 1970.

[LY96] R. Löhner and C. Yang. Improved ALE mesh velocities for moving boundaries. *Communications in numerical Methods in Engineering*, 12:599–608, 1996.

[Man08] L. Mangani. *Development and Validation of an Object Oriented CFD Solver for Heat Transfer and Combustion Modeling in Turbomachinery Applications*. PhD thesis, Università degli Studi di Firenze, 2008.

[MCB+07] M. Mamou, K.R. Cooper, A. Benmeddour, M. Khalid, J. Fitzsimmons, and R. Sengupta. Correlation of CFD predictions and wind tunnel measurements of mean and unsteady wind loads on a large optical telescope. *Journal of Wind Engineering and Industrial Aerodynamics*, in press, 2007.

[Mea02] F. Menter and et al. CFD Best Practice Guidelines for CFD Code Validation for Reactor-Safety Applications, Report EVOL-ECORA-D 01. Technical report, 2002.

[Men93] F.R. Menter. Zonal two equation k-ω turbulence models for aerodynamic flows. Technical report, AIAA Paper 93-2906, 1993.

[Met04] Meteorologisches Institut - Universität Hamburg. CEDVAL - Compilation of Experimental Data for Validation of Microscale Dispersion Models. Technical report, Universität Hamburg, 2004.

[MHvBdB04] C. Michler, S.J. Hulshoff, E.H. van Brummelen, and R. de Borst. A monolithic approach to fluid-structure interaction. *Computers & Fluids*, 33(5):839–848, 2004.

[MI05] R. Mittal and G. Iaccarino. Immersed boundary methods. *Annual Review of Fluid Mechanics*, 37:239–261, 2005.

[Mic05] C. Michler. *Efficient numerical methods for fluid-structure interaction*. PhD thesis, Technische Universiteit Delft, Delft, 2005.

[MKL03] F.R. Menter, M. Kuntz, and R. Langtry. *Turbulence, Heat and Mass Transfer 4*, chapter Ten Years of Industrial Experience with the SST Turbulence Model. Begell House, Inc., 2003.

[MM98] B. Maurin and R. Motro. The surface stress density method as a form-finding tool for tensile membranes. *Engineering Structures*, 20(8):712–719, 1998.

[MMK+98] S. Murakami, A. Mochida, K. Kondo, Y. Ishida, and M. Tsuchiya. Development of new k-ϵ turbulence model for flow and pressure fields on bluff bodies. *Journal of Wind Engineering and Industrial Aerodynamics*, 67&68:169–182, 1998.

[MNS06] H.G. Matthies, R. Niekamp, and J. Steindorf. Algorithms for strong coupling procedures. *Computational Methods in Applied Mechanics and Engineering*, 195:2028–2049, 2006.

[Mok01] D.P. Mok. *Partitionierte Lösungsansätze in der Strukturdynamik und der Fluid-Struktur-Interaktion*. PhD thesis, Universität Stuttgart, Stuttgart, 2001.

[MR95] R. Münsch and H.-W. Reinhardt. Zur Berechnung von Membrantragwerken aus beschichteten Geweben mit Hilfe genäherter elastischer Materialparameter. *Bauingenieur*, 70:271–275, 1995.

[MS03] H.G. Matthies and J. Steindorf. Partitioned strong coupling algorithms for fluid-structure interaction. *Computers & Structures*, 81(805-812), 2003.

[MTB+08] M. Mamou, A. Tahi, A. Benmeddour, K.R. Cooper, I. Abdallah, M. Khalid, and J. Fitzsimmons. Computational fluid dynamics simulations and wind tunnel measurements of unsteady wind loads on a scaled model of a very large optical telescope: A comparative study. *Journal of Wind Engineering and Industrial Aerodynamics*, 96:257–288, 2008.

[Mur97] S. Murakami. Current status and future trends in computational wind engineering. *Journal of Wind Engineering and Industrial Aerodynamics*, 67&68:3–34, 1997.

[Mur98] S. Murakami. Overview of turbulence models applied in CWE 1997. *Journal of Wind Engineering and Industrial Aerodynamics*, 74-76:1–24, 1998.

[MvBdB05] C. Michler, E.H. van Brummelen, and R. de Borst. An interface Newton-Krylov solver for fluid-structure interaction. *International Journal for Numerical Methods in Fluids*, 47:1189–1195, 2005.

[MW01] D.P. Mok and W.A. Wall. Partitioned analysis schemes for the transient interaction of incompressible flows and nonlinear flexible structures. In W.A. Wall, K.-U. Bletzinger, and K. Schweizerhof, editors, *Trends in Computational Structural Mechanics*, pages 689–698, Barcelona, 2001. CIMNE.

[MWBR99] D. P. Mok, W. A. Wall, M. Bischoff, and E. Ramm. Algorithmic aspects of deformation dependent loads in non-linear static finite element analysis. *Engineering Computations*, 16(5):601–618, 1999.

[Nat00] J. Marighetti; A. Wittwer; M. De Bortoli; B. Natalini; M. Paluch; M. Natalini. Fluctuating and mean pressure measurements on a stadium covering in wind

tunnel. *Journal of Wind Engineering and Industrial Aerodynamics*, 84:321 – 328, 2000.

[New59] N. M. Newmark. A method of computation for structural dynamics. *Journal of the Engineering Mechanics Division, ASCE*, 85:67–94, 1959.

[Nob01] F. Nobile. *Numerical approximation of fluid-structure interaction problems with application to haemodynamics*. PhD thesis, Ecole Polytechnique Fédérale de Lausanne, 2001.

[Nor05a] Normenausschuss Bauwesen im DIN. DIN 1055-4:2005-3 Einwirkung auf Tragwerke, Teil 4: Windlasten. Technical report, DIN Deutsche Institut für Normierung e.V., 2005.

[Nor05b] Normenausschuss Bauwesen im DIN. DIN EN 13782:2005 Fliegende Bauten - Zelte - Sicherheit. Technical report, DIN Deutsche Institut für Normierung e.V., 2005.

[NT02] K. Nozawa and T. Tamura. Large eddy simulation of the flow around a low-rise building immersed in a rough-wall turbulent boundary layer. *Journal of Wind Engineering and Industrial Aerodynamics*, 90:1151 – 1162, 2002.

[Par03] H. Parisch. *Festkörper-Kontinuumsmechanik - Von den Grundgleichungen zur Lösung mit Finiten Elementen*. Teubner Verlag, Stuttgart, 2003.

[Pes02] CS Peskin. The immersed boundary method. *Acta Numerica*, 11:479–517, 2002.

[PF01] S. Piperno and C. Farhat. Partitioned procedures for the transient solution of coupled aeroelastic problems. Part II: energy transfer analysis and three-dimensional applications. *Computer Methods in Applied Mechanics and Engineering*, 190:3147–4170, 2001.

[PFO01] K.C. Park, Carlos A. Felippa, and Roger Ohayon. Partitioned formulation of internal fluid-structure interaction problems by localized Lagrange multipliers. *Computer Methods in Applied Mechanics and Engineering*, 190:2989–3007, 2001.

[Pip97] S. Piperno. Explicit / implicit fluid / structure staggered procedures with a structural predictor and fluid subcycling for 2D inviscid aeroelastic simulations. *International Journal for Numerical Methods in Fluids*, 25:1207–1226, 1997.

[Pop75] S. B. Pope. A more general effective-viscosity hypothesis. *Journal of Fluid Mechanics*, 72 / 2:331–340, 1975.

[Pop00] S. B. Pope. *Turbulent flows*. Cambridge Univ. Press, 2000.

[PSN97] R. A. Pielke Sr. and M. E. Nicholls. Use of meteorological models in computational wind engineering. *Journal of Wind Engineering and Industrial Aerodynamics*, 67&68:363–372, 1997.

[QNE08] QNET-CFD. QNET-CFD Knowledge Base. Technical report, EU Network on Quality and Trust in the Industrial Application of Computational Fluid Dynamics, 2008.

[RA08] T.C.S. Rendall and C.B. Allen. Unified fluid-structure interpolation and mesh motion using radial basis functions. *International Journal for Numerical Methods in Engineering*, 74:1519–1559, 2008.

[Rai03] T. Raible. *Concepts for nonlinear orthotropic material modeling with applications to membrane structures*. PhD thesis, Universität Hannover, 2003.

[RH93] P.J. Richards and R.P. Hoxey. Appropriate boundary conditions for computational wind models using the k-ϵ turbulence model. *Journal of Wind Engineering and Industrial Aerodynamics*, 46,47:145 – 153, 1993.

[RHRF97] A.P. Robertson, R. P. Hoxey, P. J. Richards, and W. A. Ferguson. Full-scale measurements and computational predictions of wind loads on free-standing walls. *Journal of Wind Engineering and Industrial Aerodynamics*, 67&68:639–646, 1997.

[RHS01] P.J. Richards, R.P. Hoxey, and L.J. Short. Wind pressure on a 6m cube. *Journal of Wind Engineering and Industrial Aerodynamics*, 89:1553 – 1564, 2001.

[Rod97] W. Rodi. Comparison of LES and RANS calculations of the flow around bluff bodies. *Journal of Wind Engineering and Industrial Aerodynamics*, 69 - 71:55 – 75, 1997.

[RW07] H. Ruscheweyh and R. Windhövel. *Praktische Anwendungen in der Windingenieurtechnik*, chapter Winddruckverteilung an runden Zeltdächern, pages 31 – 38. WtG Windtechnologische Gesellschaft e.V., 2007.

[Sch99] M. Schäfer. *Numerik im Maschinenbau*. Springer Berlin, Heidelberg, New York, 1999.

[Sch04] G. Scheuerer. Lösungsalgorithmen für Finite-Volumen-Methoden. In *Numerische Berechnung turbulenter Strömungen in Forschung und Praxis*, 2004.

[Sch06] M. Schmidberger. Partitionierte Verfahren zur Lösung von Fluid-Struktur-Interaktion. Master's thesis, Technische Universität München, Institute for Computational Mechanics, 2006.

[SDB83] J. Steger, F.C. Dougherty, and J.A. Benek. *Advances in Grid Generation*, chapter A Chimera grid scheme, pages 59–69. ASME, 1983.

[SH97] K. Saberi-Haghighi. *Zur Ermittlung der verformungsabhängigen Windbelastung bei Hängedächern*. PhD thesis, Universität Hannover, Hannover, 1997.

[SHC00] M.J. Smith, D.H. Hodges, and C.E.S. Cesnik. Evaluation of computational algorithms suitable for fluid-structure interactions. *Journal of Aircrafts*, 37 (2):282–294, 2000.

[SJSA97] P. Spalart, W. Jou, W.-H. Strelets, and S. Allmaras. *Advances in DNS/LES*, chapter Comments on the feasibility of LES for wings and on the hybrid RANS/LES approach. Greyden Press, 1997.

[SL85] G. Schwarz and H. Lienhart. Umströmung von Membranen und ihre Simulation im Windkanal. In *3. Internationales Symposium "Weitgespannte Flächentragwerke", SFB 64*, 1985.

[SLS+95] T.-H. Shih, W.W. Liou, A. Shabbir, Z. Yang, and J. Zhu. A new k-ϵ Eddy-viscosity model for high Reynolds number turbulent flows - model development and validation. *Computers and Fluids*, 24(3):227–238, 1995.

[SM00] J. Steindorf and H.G. Matthies. Numerical efficiency of different partitioned methods for fluid-structure interaction. *ZAMM*, 80:557–558, 2000.

[Soc94] H. Sockel. *Wind-Excited Vibrations of Structures*, chapter Fundamentals of Wind Engineering, pages 85–160. Springer, New York, 1994.

[Spe87] C.G. Speziale. On non-linear k-ϑ and k-ϵ models of turbulence model. *Journal of Fluid Mechanics*, 178:459–475, 1987.

[SR04] E. Stein and M. Rüter. *Encyclopedia of Computational Mechanics, Volume 2: Solids and Structures*, chapter Finite Element Methods for Elasticity with Error-controlled Discretization and Model Adaptivity, pages 5 – 58. Wiley, Chichester, 2004.

[SRK+97] S.-H. Suh, H.-W. Roh, H.-R. Kim, K.-Y. Lee, and K.-S. Kim. Application of computational techniques for studies of wind pressure coefficients around an odd-geometrical building. *Journal of Wind Engineering and Industrial Aerodynamics*, 67&68:659–670, 1997.

[SS96] E. Simiu and R.H. Scanlan. *Wind effects on structures - Fundamentals and applications to design*. John Wiley & Sons, Inc., New York, 3. edition, 1996.

[SSG91] C.G. Speziale, S. Sarkar, and T.B. Gatski. Modeling the pressure-strain correlation of turbulence: an invariant dynamical systems approach. *Journal of Fluid Mechanics*, 227:245–272, 1991.

[Sta97] T. Stathopoulos. Computational wind engineering: past achievements and future challenges. *Journal of Wind Engineering and Industrial Aerodynamics*, 67,68:509–532, 1997.

[Sta03] T. Stathopoulos. Windloads on low buildings: in the wake of Alan Davenport's contributions. *Journal of Wind Engineering and Industrial Aerodynamics*, 91:1565–1585, 2003.

[STB03] K. Stein, T. Tezduyar, and R. Benney. Mesh moving Techniques for Fluid-Structure Interactions With Large Displacements. *Journal of Applied Mechanics*, 70:58–63, 2003.

[STB04] K. Stein, T. Tezduyar, and R. Benney. Automatic mesh update with the solid-extension mesh moving technique. *Computer Methods in Applied Mechanics and Engineering*, 193:2019–2032, 2004.

[Ste02] J. Steindorf. *Partitionierte Verfahren für Probleme der Fluid-Struktur Wechselwirkung*. PhD thesis, Technische Universität Braunschweig, Braunschweig, 2002.

[SvBRO02] A.P.G. Sagrado, J. v. Beeck, P. Rambaud, and D. Olivari. Numerical and experimental model of pollutant dispersion in a street canyon. *Journal of Wind Engineering and Industrial Aerodynamics*, 90:321 – 339, 2002.

[TBU00] P. Thévenaz, T. Blu, and M. Unser. Interpolation revisited. *IEEE TRANSACTIONS ON MEDICAL IMAGING*, 19 (7):739 – 758, 2000.

[Tez07] T.E. Tezduyar. Finite elements in fluid: stabilized formulations and moving boundaries and interfaces:. *Computers & Fluids*, 36:191–206, 2007.

[TL79] P.D. Thomas and C.K. Lombard. Geometric conservation law and its application to flow computations on moving grids. *AIAA Journal*, 17 No. 10:1030–1037, 1979.

[TMP06] Y.-H. Tseng, C. Meneveau, and M.B. Parlange. Modeling Flow around Bluff Bodies and Predicting Dispersion Using Large Eddy Simulation. *Environmental Science & Technology*, 40:2653 – 2662, 2006.

[TMY+08] Y. Tominaga, A. Mochida, R. Yoshie, H. Kataoka, T. Nozu, M. Yoshikawa, and T. Shirasawa. Aij guidelines for practical applications of cfd to pedestrian wind environment around buildings. *Journal of Wind Engineering and Industrial Aerodynamics*, 96 (10-11):1749–1761, 2008.

[TNK08] T. Tamura, K. Nozawa, and K. Kondo. AIJ guide for numerical prediction of wind loads on buildings. *Journal of Wind Engineering and Industrial Aerodynamics*, Article in Press, 2008.

[TSKS06] T.E. Tezduyar, S. Sathe, R. Keedy, and K. Stein. Space-time finite element techniques for computation of fluid-structure interactions. *Computer Methods in Applied Mechanics and Engineering*, 195:2002–2027, 2006.

[TSS06] T.E. Tezduyar, S. Sathe, and K. Stein. Solution techniques for the fully discretized equations in computation of fluid-structure interaction. *Computer Methods in Applied Mechanics and Engineering*, 195:5743–5753, 2006.

[Unh04] S. A. Unhale. *Application and Analysis of RANS based turbulence models for bluff body aerodynamics*. PhD thesis, Texas Tech University, 2004.

[UO99] T. Uchida and Y Ohya. Numerical simulation of atmospheric flow over complex terrain. *Journal of Wind Engineering and Industrial Aerodynamics*, 81:283–293, 1999.

[vBdB05] E.H. van Brummelen and R. de Borst. Interface-GMRES(R) Acceleration of Subiteration for Fluid-Structure-Interaction Problems, Report DACS-05-001. Technical report, TU Delft, 2005.

[Ver05] Verein Deutscher Ingenieure. *VDI 3783 Part 9: Environmental meteorolgy - Prognostic microscale wind field model - Evaluation of Flow around Buildings and Obstacles*. Beuth Verlag Berlin, 2005.

[Ver06] J.W. Veraik. Introduction to atmospheric boundary layers. In *von Karman institute for Fluid Dynamics: Lecture Series 2006-02 - Introduction to Wind Technology*, 2006.

[vLAdHB05] R. van Loon, A.D. Anderson, Jürgen de Hart, and FPT Baaijens. A three-dimensional fluid-structure interaction method for heart valve modelling. *Compter Rendus Mecanique*, 333(12):856–866, 2005.

[VLDV07] J. Vierendeels, L. Lieve, J Degroote, and P. Verdonck. Implicit coupling of partitioned fluid-structure interaction problems with reduced order models. *Computers & Structures*, 85:970–976, 2007.

[vZdBB07] A.H. van Zuijlen, A. de Boer, and H. Bijl. Higher-order time integration through smooth mesh deformation for 3d fluid-structure interaction simulations. *Journal of Computational Physics*, 224(1):414–430, 2007.

[Wal99] W.A. Wall. *Fluid-Struktur-Interaktion mit stabilisierten Finiten Elemente*. PhD thesis, Universität Stuttgart, Institut für Baustatik, 1999.

[WB05] R. Wuechner and K.-U. Bletzinger. Stress-adapted numerical form finding of pre-stressed surfaces by the updated reference strategy. *International Journal for Numerical Methods in Engineering*, 64:143–166, 2005.

[Wüc07] R. Wüchner. *Mechanik und Numerik der Formfindung und Fluid-Struktur-Interaktion von Membranbauwerken*. PhD thesis, Technische Universität München, 2007.

[WE99] N. G. Wright and G. J. Easom. Comparison of several computational turbulence models with full-scale measurements of flow around building. *Wind and Structures*, 2(4):305–323, 1999.

[Wen01] H. Wengle. Numerische Berechnung turbulenter Strömungen - Vorlesungsmanuskript. Technical report, München, 2001.

[Wev08] C. Wevers. Validierung eines CFD-Programms zur Simulation von Windfeldern unter der Verwendung des Standard k-ϵ Turbulenzmodells anhand der VDI Richtlinie 3783. Master's thesis, Lehrstuhl für Aerodynamik und Strömungsmechanik im Bauwesen, Ruhr-Universität Bochum, 2008.

[WGG+06] W.A. Wall, A. Gerstenberger, P. Gamnitzer, C. Förster, and E. Ramm. *Fluid-Structure-Interaction: Modelling - Simulation - Optimization, Lecture Notes in*

Computational Science and Engineering (53), chapter Large Deformation Fluid-Structure Interaction - Advances in ALE Methods and New Fixed Grid Approaches., pages 195–232. Springer Berlin, Heidelberg, New York, 2006.

[Wil95] C.J.K. Williams. *Wind Loading on Temporal Structures - Conference Proceddings*, chapter Structural design of fabric structures to resist wind loading, pages 74 – 80. HSE Books, 1995.

[Wil06] D.C. Wilcox. *Turbulence Modeling for CFD - 3rd edition*. DCW Industries, 2006.

[WKB07] R. Wüchner, A. Kupzok, and K.-U. Bletzinger. A framework for stabilized partitioned analysis of thin membrane wind interaction. *International Journal for Numerical Methods in Fluids*, 54:945–963, 2007.

[WMR99] W.A. Wall, D.P. Mok, and E. Ramm. Partitioned analysis approach for the transient, coupled response of viscous fluids and flexible structures. In *European Conference on Computational Mechanics*, 1999.

[WMR00] W. A. Wall, D. P. Mok, and E. Ramm. Simulation of nonlinear shell interaction with instationary flows. In *4th International Colloquium on Computational Shell and Spatial Structures*, 2000.

[XC06] Z. Xie and I.P. Castro. LES and RANS for Turbulent Flow over Arrays of Wall-Mounted Obstacles. *Flow, Turbulence and Combustion*, 76:291 – 312, 2006.

[YO86] V Yakhot and S.A. Oszag. Renormalization group analysis of turbulence. *Journal of Scientific Computing*, 1(1):1–51, 1986.

[YQX+08] W. Yang, Y. Quan, J. Xinyang, Y. Tamura, and M. Gu. Influences of equilibrium atmospheric boundary layer and turbulence parameter on wind loads of low-rise buildings. *Journal of Wind Engineering and Industrial Aerodynamics*, Article in Press, 2008.

[ZGZ05] A. Zhang, Cuilan G., and L. Zhang. Numerical simulation of the wind field around different building arrangements. *Journal of Wind Engineering and Industrial Aerodynamics*, 93:891 – 904, 2005.

[Zha05] Yu Zhaosheng. A DLM / FD method for fluid / flexible-body interactions. *Journal of Computational Physics*, 207(1):1–27, 2005.

[ZTZ05] O. C. Zienkiewicz, R. L. Taylor, and J. Z. Zhu. *The finite element method: its basis and fundamentals*. Elsevier Butterworth-Heinemann, Burlington, 6. edition, 2005.

[Zur69] J.A. Zuranski. *Windbelastung von Bauwerken und Konstruktionen*. Verlagsgesellschaft Rudolf Müller, Köln-Braunsfeld, 1969.